TESIS DE LA UNIVERSIDAD DE ZARAGOZA
2017
7

Patricia Villar Gómez

Background evaluation of the ANAIS dark matter experiment in different configurations: towards a final design

Departamento
Física Teórica

Director/es
Sarsa Sarsa, Maria Luisa
Cebrián Guajardo, Susana

http://zaguan.unizar.es/collection/Tesis

ISSN 2254-7606

Prensas de la Universidad
Universidad Zaragoza

Reconocimiento – NoComercial – SinObraDerivada (by-nc-nd): No se permite un uso comercial de la obra original ni la generación de obras derivadas.

© Universidad de Zaragoza
Servicio de Publicaciones

ISSN 2254-7606

Universidad Zaragoza
1542

Tesis Doctoral

BACKGROUND EVALUATION OF THE ANAIS DARK MATTER EXPERIMENT IN DIFFERENT CONFIGURATIONS: TOWARDS A FINAL DESIGN

Autor

Patricia Villar Gómez

Director/es

Sarsa Sarsa, Maria Luisa
Cebrián Guajardo, Susana

UNIVERSIDAD DE ZARAGOZA

Física Teórica

2016

Repositorio de la Universidad de Zaragoza – Zaguan http://zaguan.unizar.es

Universidad Zaragoza
1542

Tesis Doctoral

Título de la tesis:

Background evaluation of the ANAIS dark matter experiment in different configurations: towards a final design

Autor

Patricia Villar Gómez

Director/es

María Luisa Sarsa Sarsa
Susana Cebrián Guajardo

Facultad de Ciencias

2016

Repositorio de la Universidad de Zaragoza – Zaguan http://zaguan.unizar.es

Background evaluation of the ANAIS dark matter experiment in different configurations: towards a final design

Memoria presentada por

Patricia Villar Gómez

para optar al grado de

Doctora en Física

Laboratorio de Física Nuclear y Astropartículas
Área de Física Atómica, Molecular y Nuclear
Departamento de Física Teórica
UNIVERSIDAD DE ZARAGOZA

Octubre 2016

Contents

Introduction

Latest impressive measurements on cosmological parameters (like those of Planck [1]) support a flat Universe, in accelerated expansion with a 27% of non–baryonic dark matter and a 68% of dark energy content, according to the ΛCDM model of the Universe. However, and despite the success of the ΛCDM model, many unknowns still remain, in particular the nature of the dark matter and dark energy.

There exist substantial evidences (see section 1.2), from galactic to cosmological scale, suggesting that most matter in the Universe is dark, and there are compelling reasons to believe that it consists mainly of non–baryonic particles. The solution to the dark matter problem requires the existence of beyond the Standard Model particle physics: one solution is the incorporation of a new massive, neutral and weakly interacting particle into the model (see section 1.3), but also more complex scenarios are possible, as the mirror dark mater framework (see subsection 1.5.2).

Different experimental strategies have been applied in order to detect this unknown, non–luminous matter, filling the galactic halos (see section 1.4). On one hand, by identifying the products of the dark matter annihilation in the galactic halos or galaxy clusters and on the other, by searching for interactions of dark matter particles with the nuclei of a convenient detector in dedicated experiments carried out at underground laboratories.

Sodium iodide crystals doped with Tl have been widely used as radiation detectors and, in particular, they have taken part in the direct search of galactic dark matter for a long time [2–8]. Among the several experiments using NaI(Tl) crystal detectors, DAMA/LIBRA (see section 1.5) in the Gran Sasso National Laboratory (LNGS), in Italy, is the most relevant one, having reported the observation of a modulation in the signal compatible with that expected for galactic halo WIMPs with a large statistical significance [9] [10]. Results obtained in other experiments with different target materials and detection techniques (like those from CDMS [11],

CRESST [12], EDELWEISS [13], KIMS [14], LUX [15], PICO [16] [17] or XENON [18] collaborations) have been ruling out for years the most plausible compatibility scenarios.

The ANAIS (Annual modulation with NaI Scintillators) project [19] (see chapter 2) is intended to search for dark matter annual modulation with ultrapure NaI(Tl) scintillators at the Canfranc Underground Laboratory (LSC) in Spain; the aim of the experiment is to provide a model–independent confirmation of the annual modulation positive signal reported by DAMA/LIBRA using the same target and technique, but different experimental conditions (affecting systematics). Projects like DM–Ice [20], KIMS [21] and SABRE [22] also envisage the use of large masses of NaI(Tl) for dark matter searches. The joint collaboration between KIMS and DM–Ice groups has made possible to put their detectors together in a common array of NaI(Tl) crystals: the 100 kg of COSINE–100 experiment that could start the data taking at Yangyang laboratory in Korea along 2016 [23].

ANAIS aims at the study of the annual modulation in the dark matter signal using a NaI(Tl) mass of 112.5 kg at the LSC. To be able to confirm DAMA/LIBRA results, ANAIS detectors performance and radiopurity should be comparable to those of the italian group, in particular, in terms of energy threshold and radioactive background: energy threshold lower than 2 keVee[1] and background at a few counts/(keV kg day) in the region of interest, below 6 keVee. A long expertise has been acquired in the University of Zaragoza group since the nineties of the past century in the operation of NaI(Tl) scintillators, using BICRON and Saint–Gobain crystals (see section 2.2). In the last years, several prototypes for ANAIS have been developed. Among them, the so-called ANAIS–0 detector [24–27], a 9.6 kg Saint–Gobain crystal similar to those of DAMA experiment, has to be highlighted due to its successful background model [24] that has been the starting point for the ANAIS background understanding and modeling, which is the main goal of the work presented in this dissertation. Some other interesting results, as very slow scintillation in NaI(Tl) [26] or an anomalous fast event population attributable to quartz light emission [28] were also obtained from first prototypes. Over the years, the main challenge for ANAIS has been the achievement of the required low background level, being contaminations in the bulk of the crystal the dominant contribution in the region of interest (see section 3.1).

[1] keVee is used to refer to an energy deposition equivalent to 1 keV deposited by an electron

The latest ANAIS prototypes, in which this work is focused on, have been built by Alpha Spectra Inc. (AS), Colorado (US) [29]. Every module consists of a 12.5 kg NaI(Tl) crystal, housed in OFE (Oxygen Free Electronic) copper and coupled through quartz windows to two Hamamatsu photomultipliers (PMTs) at the LSC clean room in a second step. They have been fully tested and characterized at the LSC since the end of 2012, obtaining very promising results (see section 2.10).

ANAIS initial goal was to reproduce DAMA/LIBRA experiment using the same detection mass, 250 kg of NaI(Tl). However, several reasons led to a modified experimental configuration for ANAIS: a total active mass of 112.5 kg of NaI(Tl) divided into nine modules. On one hand, improved purification procedures of the raw materials at AS developed to tackle the ^{40}K and ^{210}Pb radiopurity of the modules increased strongly the price of the modules. Moreover, on the other hand, excellent light collection in AS modules allows an achievable energy threshold at 1 keVee (see subsection 2.10.2) improving the sensitivity. Comparison of the sensitivities for the annual modulation in the different experimental configurations and background conditions will be presented in section 5.2.

The full ANAIS experiment set–up will be installed at LSC at the beginning of 2017. The shielding will consist of 10 cm of archaeological lead, 20 cm of low activity lead, 40 cm of neutron moderator, an anti-radon box (to be continuously flushed with radon-free air), and an active muon veto system made up of plastic scintillators designed to cover top and sides of the whole ANAIS set–up (see section 2.8). The hut that will house the experiment at the Hall B of LSC (under 2450 m.w.e.) is already operative, and shielding materials and electronic chain components are prepared for mounting [30][31]. Different PMT models were tested in order to choose the best option in terms of light collection and background [31] [32]. The Hamamatsu R12669SEL2 PMT was selected, and all the required units are already available at the LSC.

A large effort has been carried out in order to characterize the background of sodium iodide crystals within the ANAIS project. The main goals of this work, presented through this dissertation thesis, have been the development of detailed background models for the first three 12.5 kg NaI(Tl) detectors produced by Alpha Spectra and operating at the LSC (see chapter 3), together with an evaluation of the background prospects for the final ANAIS experiment considering different scenarios and experimental configurations (see chapter 4). Monte Carlo simulations

have been carried out to assess the different background contributions after identifying and quantifying most of the relevant radioactive contaminations in the different components of the set–up and detectors by different complementary techniques. In addition to the expectations for the foreseen ANAIS design with a lead shielding, the achievable improvement thanks to the operation of the crystals matrix inside a liquid scintillation veto system has been also evaluated.

The structure of this memory is the following:

- A brief introduction on the history of the Universe (section 1.1), dark matter evidences (section 1.2) and the search for candidates of this unknown kind of matter (section 1.3) in direct or indirect detection experiments (section 1.4) are presented in chapter 1. At the end of this chapter, a detailed description and the most relevant results of the only experiment claiming for a positive signal on the annual modulation of dark matter, DAMA/LIBRA (section 1.5), are given. A corollary study of this result in the frame of the symmetric mirror dark matter models, carried out in a research stage at the Università di Roma "Tor Vergata", is presented (subsection 1.5.2).

- In chapter 2, a complete description of the ANAIS experiment is made: goals and requirements (section 2.1), previous prototypes (section 2.2), all the elements of the experimental set–up like crystals and photomultipliers, electronics and data acquisition, slow control or the muon veto system (sections 2.3 to 2.8), the set–ups already operated at LSC (section 2.9) and the general detector performance (section 2.10).

- A detailed study of the background models developed for the Alpha Spectra ANAIS detectors is presented in chapter 3; including a description of the sources used in the simulation (section 3.1), of the background modeling and its validation (sections 3.2 and 3.3) and an analysis of the detector optimum design (section 3.4). The particular background models, including the comparison with data and the estimate of the different background contributions, are discussed for D0/D1 (section 3.5) and D2 (section 3.6) detectors. Preliminary results for D3 are also shown (section 3.7).

- ANAIS background prospects using results derived from the simulation and comparison with data of chapter 3 for different configurations are presented in

chapter 4: considered background sources are detailed (section 4.1), results for a set–up with either 112.5 or 250 kg are discussed (section 4.2) and the study of the inclusion of a liquid scintillor veto is shown (section 4.3).

- Finally, the sensitivity projections in the search for the annual modulation effect in the dark matter signal in different scenarios for the ANAIS experiment are shown in chapter 5 before drawing the final conclusions.

Chapter 1

Dark matter in the Universe

1.1 The Standard Cosmological Model of the Universe

Understanding the Universe has been a fundamental issue in all cultures since the very beginning of human history. First theories considered the Earth as the center of the Universe, and then the Copernican revolution showed that it was not so. Furthermore, later studies showed that the Solar System and the Milky Way galaxy are a negligible corner of the Universe.

Cosmology aims to describe the global dynamics and contents of the Universe. High–precision observational data obtained since the last decade of the past century allowed to test different cosmological models and conclude that the Universe is well described by the so–called ΛCDM cosmological model, composed by four fundamental elements: dark energy, non–baryonic cold dark matter, baryonic matter and radiation. As most of the cosmological models, it is based on the Cosmological Principle, stating that the Universe is homogeneous and isotropic.

The discovery of the Cosmic Microwave Background (CMB) radiation was an important evidence supporting a hot early Universe (Big Bang model) and introduced a major development in cosmology. Although predicted by earlier theoretical works in 1948 [33], it was first discovered accidentally by two American radio astronomers, Arno Penzias and Robert Woodrow Wilson in 1964 [34] while they were using the Holmdel Horn Antenna. The CMB radiation was soon identified as a relic radiation from the epoch of recombination or photon decoupling in Big Bang cosmology.

When the temperature of the Universe dropped to 3000 K, neutral atoms could form: the Universe, filled with a plasma opaque to photons, changed into a gas of neutral atoms, transparent to photons. After their decoupling from matter, they travelled freely through the space, being red–shifted as the Universe expanded; they are observed today at a temperature of 2.73 K, in the microwave frequency range, and thus, it is named CMB radiation.

Previously to the CMB discovery, the Big Bang model was already strongly supported by observational data, in particular, by the Universe expansion. The first evidence of an expanding Universe came from Hubble in 1929, finding out that galaxies moved away following the Hubble's law:

$$v = H_0 r \tag{1.1}$$

where H_0 is the Hubble's constant, v the galaxy velocity and r its distance from the Earth.

Measuring precisely the Hubble constant was for decades a major challenge for astronomers, trying to study the most distant objects in the Universe. Distant supernovae type Ia proved to be very interesting objects: having a known intrinsic luminosity allowed to determine precisely the distance to the hosting galaxy from its apparent brightness. In 1998 unexpected results were obtained independently by Supernova Cosmology Project and High–Z Supernova Search Team, pointing at an acceleration in the expansion of the Universe [35]. Because General Relativity predicts that the expansion of the Universe should slow down at a rate determined by its density of matter and energy, this accelerated expansion implies the presence of a new kind of energy able to produce repulsive effects, the dark energy. Thus, in fact the Universe is currently in a dark–energy–dominated era.

The Standard Cosmological Model describes the dynamics of the Universe in the General Relativity Theory frame, in which the gravitational interaction has a geometrical meaning, being considered as a distortion of the space–time. The resolution of Einstein's equation, allowing a cosmological constant term, leads to the ΛCDM model in an isotropic and homogeneous Universe, where geometry is defined by the Friedmann–Lemaître–Robertson–Walker metric (FLRW metric, eq. 1.2).

The overall geometry and the evolution of the Universe in the ΛCDM model is described with two cosmological parameters: the spatial curvature, k and the time

dependent scale factor, $a(t)$:

$$ds^2 = g_{\mu\nu}dx^\mu dx^\nu = -dt^2 + a^2(t)[\frac{dr^2}{1-kr^2} + r^2(d\theta^2 + sin^2\theta d\phi^2)] \tag{1.2}$$

The k parameter can be equal to 1, 0 or –1, corresponding to a closed, flat or open Universe respectively.

Relation between space-time, its geometry and its content is stated by the Einstein's field equations:

$$R_{\mu\nu} - \frac{1}{2}g_{\mu\nu}R = 8\pi G T_{\mu\nu} + \Lambda g_{\mu\nu} \tag{1.3}$$

where Λ is the cosmological constant, $R_{\mu\nu}$ is the Ricci tensor, $R = g^{\mu\nu}R_{\mu\nu}$ is the Ricci scalar and $T_{\mu\nu}$ is the energy–momentum tensor:

$$T_{\mu\nu} = (p + \rho)u_\mu u_\nu + p g_{\mu\nu} \tag{1.4}$$

considering the Universe as a perfect fluid without viscosity or heat flux, with u_μ the four–velocity of the fluid element, p the pressure and ρ the density. The term with Λ in equation 1.3 was introduced by Einstein to allow an statical Universe solution, and later dismissed as soon as the expansion of the Universe was beyond doubt, to be recovered and included as essential in the ΛCDM model, when the acceleration in the expansion of the Universe was measured.

Combining these relations, the Friedmann's equations are obtained:

$$(\frac{\dot{a}}{a})^2 + \frac{k}{a^2} = \frac{8\pi G}{3}\rho \tag{1.5}$$

$$\frac{\ddot{a}}{a} = \frac{-4\pi G}{3}(\rho + 3p) \tag{1.6}$$

Assuming an ideal fluid model for the Universe, the equation of state is defined as:

$$p_i = \rho_i \omega_i \tag{1.7}$$

where i represents the matter, radiation, dark energy or any other component contributing to the energy density of the Universe. By solving Friedmann equations,

the temporal evolution of the energy density for each component results:

$$\rho_i(t) \propto a(t)^{-3(\omega_i+1)} \tag{1.8}$$

where ω_i is 0 for matter, 1/3 for radiation, and for dark energy, there are two different models: $\omega = -1$ (corresponding to a cosmological constant), or, more generally, any $\omega <$ -1/3 value, where a dependence $\omega(t)$ is possible.

Equation 1.5 can be used to define the critical density, ρ_c, which corresponds to the energy density considering a flat Universe ($k = 0$):

$$\rho_c = \frac{3H_0^2}{8\pi G} \tag{1.9}$$

where H_0 is the present value of the Hubble's constant. Consequently, a dimensionless parameter can be built to indicate the contribution of each component to the Universe energy:

$$\Omega_i = \frac{\rho_i}{\rho_c} \tag{1.10}$$

Along the years, this cosmological model has been refined by adding components, as the dark energy. However, only very recently precision measurements have been available allowing, from the comparison of the model predictions with the observational data, to fit the model parameters. WMAP (Wilkinson Microwave Anisotropy Probe, launched in 2001 by NASA) has played a keyrole in establishing the ΛCDM model as the current Standard Model of cosmology [36]. Planck satellite was launched in 2009 by ESA with the main goal of improving the sensitivity and angular resolution of the CMB fluctuations measurements (see figure 1.1). The presently best estimates for the parameters, according to the Particle Data Group are mostly dominated by Planck data, with a very little effect if other observational inputs (as Baryon Acoustic Oscillations (BAO), supernova constraints, etc.) are considered in the fit.

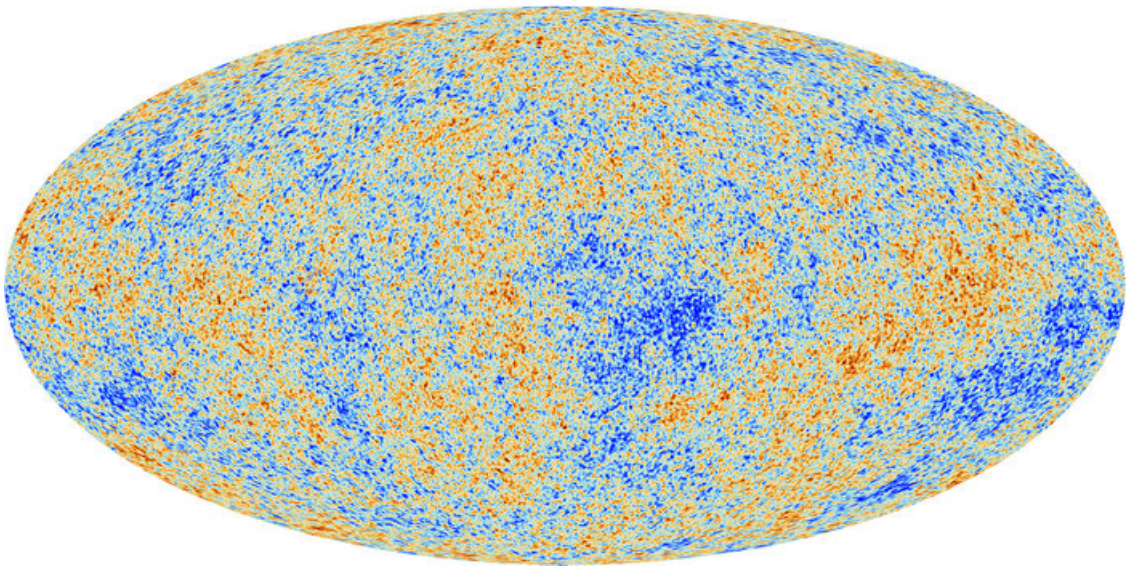

Figure 1.1: *All–sky picture of the infant Universe created from over 1500 days of Planck data. The image reveals 13.7 billion year old temperature fluctuations (shown as color differences) that correspond to regions of slightly different densities, representing the seeds of all future structure. The signal from our Galaxy was subtracted using the multifrequency data. ESA and the Planck Collaboration [37].*

	Planck+lowP	Planck+lowP+lensing	Planck+lowP+lensing+ext
$\Omega_B h^2$	0.02222 ± 0.00023	0.02226 ± 0.00023	0.02227 ± 0.00020
$\Omega_c h^2$	0.1197 ± 0.0022	0.1186 ± 0.0020	0.1184 ± 0.0012
$100\theta_{MC}$	1.04085 ± 0.00047	1.0410 ± 0.0005	1.0411 ± 0.0004
n_s	0.9655 ± 0.0062	0.968 ± 0.006	0.968 ± 0.004
τ	0.078 ± 0.019	0.066 ± 0.016	0.067 ± 0.013
$ln(10^{10}\Delta^2_R)$	3.089 ± 0.036	3.062 ± 0.029	3.064 ± 0.024
t_0 (Gyr)	13.813 ± 0.038	13.799 ± 0.038	13.796 ± 0.029
H_0 (km s^{-1} Mpc^{-1})	67.31 ± 0.96	67.81 ± 0.92	67.90 ± 0.55
Ω_m	0.315 ± 0.013	0.308 ± 0.012	0.306 ± 0.007
Ω_Λ	0.685 ± 0.013	0.692 ± 0.012	0.0694 ± 0.007

Table 1.1: *Fitted values for the ΛCDM cosmological model parameters (68% C.L.) from Planck CMB power spectra, in combination with lensing reconstruction (lensing) and external data. Above the line there are the six parameter combinations actually fitting to the data; those below the line are derived from these. For more detail about the assumptions to derive the cosmological parameters see [1]. (Table reproduced from [1]).*

Table 1.1 summarizes the present status of the estimates of the six parameters of the cosmological model: $\Omega_B h^2$ and $\Omega_c h^2$ stand for the current baryon and cold dark matter density, respectively, H_0 is the Hubble constant, h is the reduced Hubble constant $h = H_0$ / (100 km s^{-1} Mpc^{-1}), Ω_m is the matter density and Ω_Λ is the present dark energy density; σ_8 is the density perturbation amplitude (fluctuation amplitude at $8h^{-1}$ Mpc). θ_{MC} is a measure of the sound horizon at last scattering, n_s is the scalar spectrum power–law index, τ is the scattering optical depth and $ln(10^{10}\Delta_R^2)$ is the primordial perturbation amplitude and t_0 corresponds to the age of the Universe.

According to these results, the energy content of the Universe is dominated by the unknown dark energy (Ω_Λ about 68%) and baryonic matter only amounts to 4.4% ($\Omega_B h^2$ about 0.02), being required a large contribution from dark matter about 27% ($\Omega_c h^2$ about 0.12). In section 1.2, a more detailed analysis on the CMB anisotropies supporting that the Universe is composed by a large amount of non–baryonic, neutral, massive and non–interacting matter, beyond the Standard Model, the *dark matter*, will be commented.

The baryonic content of the Universe compatible with CMB anisotropies (see table 1.1) is also fully consistent with the predictions of the primordial Big Bang Nucleosynthesis (BBN) and the measured abundances of light nuclei [38]. This consistency of observational data coming from so different fields has been for long considered as a strong support for the presently accepted ΛCDM cosmological model. However, studying the halos dwarf stars, it has been observed that ^{7}Li abundance shows a definite discrepancy with previous observational determinations [39]. To date, no solution has been found or it requires substantial departures from the Standard Model. Attempts to find a solution include modifications of the nuclear rates, inclusion of new resonant interactions, stellar depletion, lithium diffusion in the post–recombination Universe, new particles beyond the Standard Model decaying around the time of BBN, axion cooling or variations in the fundamental constants.

1.2 Dark matter evidences

The first reference to dark matter comes from 1933, when Fritz Zwicky inferred the existence of an unseen matter (*dunkle Materie*) by studying the redshifts of galaxies within the Coma cluster [40].

Using the virial theorem, Zwicky compared kinetic and gravitational energies in the cluster, finding that the cluster mass should be much larger than the observed in form of galaxies and hot gas. Since then, more evidences of the presence of dark matter have arosen; as it will be shown in this section, measurements from galactic to cosmological scale show anomalies that can only be explained by the existence of a large amount of unseen (dark) matter.

1.2.1 Galaxies rotation curves

In the galactic scale, the most direct and convincing evidences of dark matter existence are the galactic rotation curves first measured by Vera Rubin in 1975 [41].

According to newtonian dynamics and assuming spherical symmetry of the galactic mass distribution, the rotational velocity of stars or gas clouds as a function of the distance to the galactic centre is:

$$v(r) = \sqrt{\frac{GM(r)}{r}} \tag{1.11}$$

where r is the distance to the centre of the galaxy, G is the Newton gravitational constant and $M(r)$ is the mass content in a radius r.

This velocity should decrease as $r^{-\frac{1}{2}}$ in the outskirts of the galaxies. However, $v(r)$ was observed to reach an almost constant value up to the most outlying objects in spiral arms of galaxies allowing the measurement (see figure 1.2). The most direct interpretation of these measurements is that the galactic mass distribution did not follow the visible mass distribution [41] and thus, the existence of larger amount of invisible mass was necessary, that is, a dark matter halo, extending further beyond the limits of the visible galaxy.

This study has also been extended to elliptical galaxies, where dark matter proportion is lower than that of spiral galaxies and to low surface brightness galaxies where dark matter proportion is higher. In both cases dark matter is required, although dark matter distribution seems to be different than in the spiral galaxies, specially in the innermost regions [42].

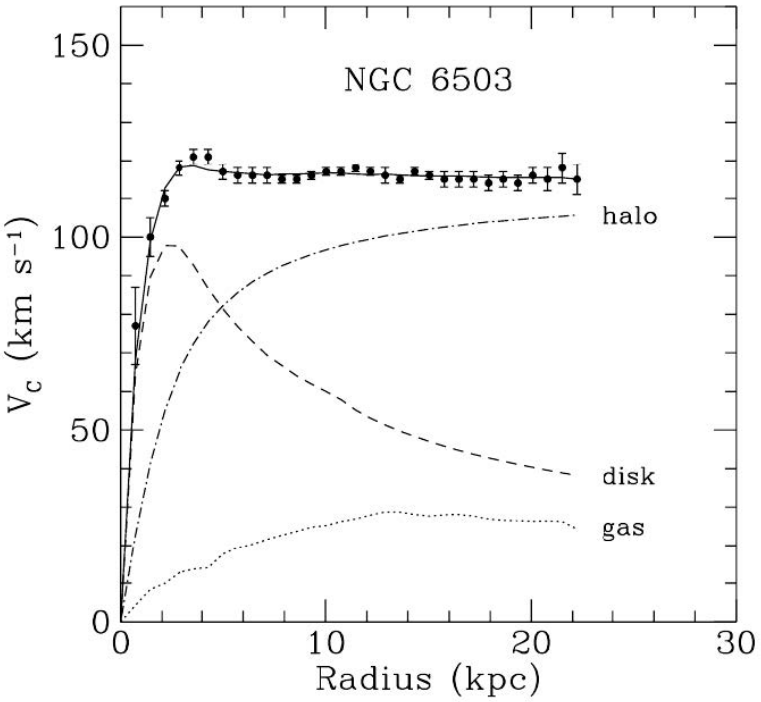

Figure 1.2: *Example of a typical galactic rotation curve. The gas (dotted), disk (dashed) and halo matter (dash-dotted) rotation velocity contributions are shown. From [43].*

1.2.2 Galaxy clusters dynamics and gravitational lens effect

Light follows geodesics, which are the generalization of straight lines in any curved space, as is the space–time in the presence of mass according to General Relativity. Then, the observed light coming from a far source is deflected by massive galaxy clusters placed between the source and the observer, leading to the appearance of multiple images of the source (see figure 1.3).

The analysis of the gravitational lens effect allows the determination of the mass distribution of the interposed object, giving always larger cluster masses than those estimated from the luminosity. Moreover, X–ray measurements reveal that the temperatures of the hot gas trapped in the galaxy clusters should have lead to the clusters evaporation long time ago, lacking from enough gravitational pull to keep it bound if only visible matter is considered. Same argument would prevent clusters from being stable structures given the high velocities observed for the galaxies they contain.

Figure 1.3: *Gravitational lens effect in galaxy cluster Abell 2218. Multiple deformed images of a few background galaxies are clearly observed after the lensing effect of the cluster. From [44]*

The Bullet Cluster provided a new insight into the dark matter problem: distribution of hot gas in the cluster does not follow neither the distribution of galaxies, nor the distribution of matter evidenced by the gravitational lens effect (see figure 1.4). This cluster can be understood as the result of the collision of two clusters, but requires a different nature for most of the clusters unseen matter, which should interact much weakly than the hot gas they contained.

1.2.3 Anisotropies in the CMB radiation

In the cosmological scale, the CMB can be interpreted as a map of the density of the early Universe. Perturbations in this density were the seeds for the growing of the structures we observe at present in the Universe.

The first measurements pointed at a high isotropy in this radiation and the study and characterization of the CMB signal has been improving since then revealing anisotropies at 10^{-5} level. In 1992, spatial satellite COBE (Cosmic Background Explorer) obtained the first data about cosmic radiation anisotropies [45]. These

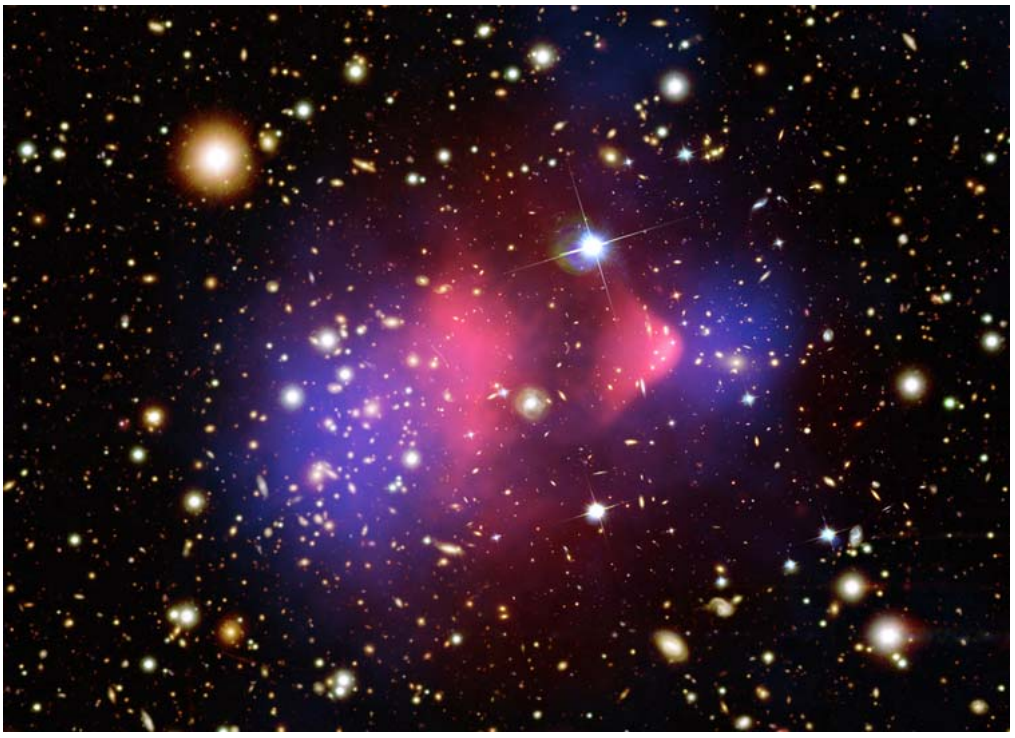

Figure 1.4: *Galaxy cluster 1E 0657–556 (also known as the Bullet cluster) composite image. Hot gas detected by Chandra X–ray telescope is shown in pink. Galaxies are seen in orange and white from Magellan and Hubble Space Telescope images in the optical range. The mass distribution deduced by gravitational lensing is shown in blue. From [46].*

anisotropies have been studied by WMAP and Planck satellites, greatly improving the angular resolution and sensitivity.

This anisotropy is expressed through the spherical harmonic expansion of the CMB temperature map:

$$T(\theta, \phi) = \sum_{lm} a_{lm} Y_{lm}(\theta, \phi) \tag{1.12}$$

With this expansion, it is easier to compare the features of the resultant power spectrum defined as:

$$l(l+1)\frac{C_l}{2\pi} \tag{1.13}$$

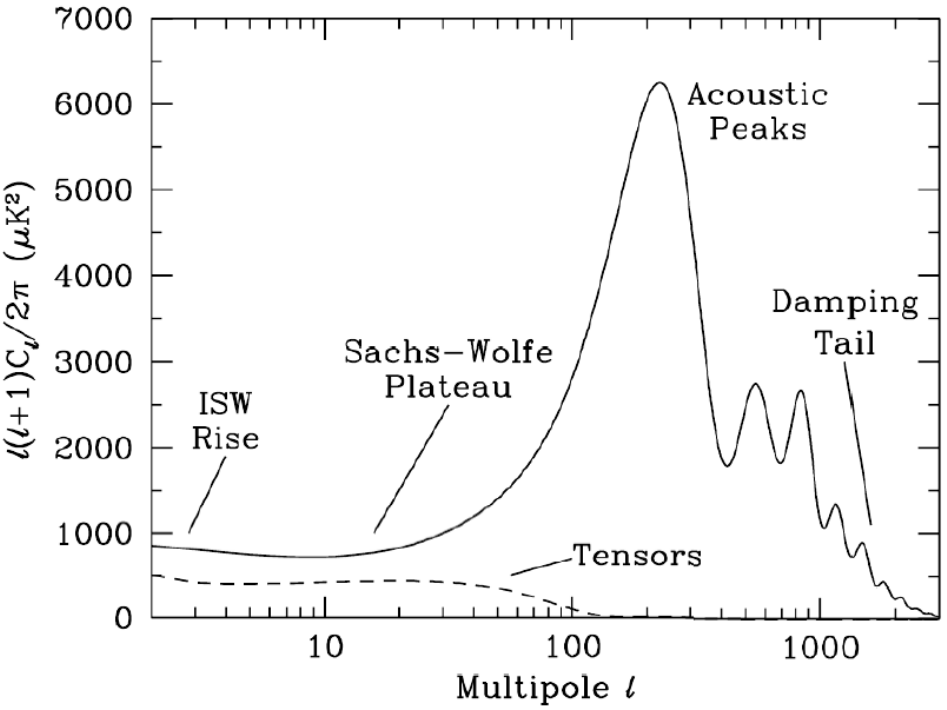

Figure 1.5: *Theoretical CMB anisotropy power spectrum, using a Standard ΛCDM Model. From [47].*

being

$$C_l = \frac{1}{2l+1} \sum_m a_{lm}^2 \tag{1.14}$$

Baryons and photons were tightly coupled in the early Universe. In such a hot plasma medium, density perturbations produced oscillations, similar to sound waves. At the recombination time, the baryons lost the pressure moving them outwards and stayed in a shell around overdense regions at a radius dependent on the Universe properties (the sound horizon). Subsequent gravitational interaction of dark matter and baryons resulted in the conservation of this feature in the clustering of the galaxies in the present time. Then, BAO are observed in the CMB as acoustic peaks (see figure 1.5) and in the number of galaxy pairs at the sound horizon distance (as measured, for instance, by BOSS [48]). The angular position of these acoustic peaks in the CMB power spectra and their amplitude is very sensitive to the Universe composition, and it cannot be explained by including only baryonic matter in the model.

The CMB has a mean temperature of 2.725 ± 0.008 mK which can be considered as the monopole component ($l = 0$), whereas the largest anisotropy is in the dipole

component ($l = 1$). This is interpreted as the result of the Doppler shift caused by the motion of the solar system relative to the nearly isotropic black–body field. Data shown in the plots (as is done in figure 1.1) subtract the dipole term corresponding to our reference frame motion with respect to the CMB, not relevant to understand the perturbations in the density of the early Universe. Also the galactic contribution has been subtracted from these plots before analysing the power spectrum, combining *multifrecuency* information. The expected CMB power spectrum at higher–order multipoles predicted in the frame of the ΛCDM cosmological model shows peculiar features, as shown in figure 1.5: the Sachs–Wolfe plateau, acoustic peaks and a damping tail. Different polarization modes in the CMB photons can also show their own anisotropies and power spectra C_l^E, C_l^B, C_l^{TE} for E–modes, B–modes and correlations between density and velocity perturbations at last scattering surface, respectively, providing complementary model parameters constraints (see figures 1.6 and 1.7). All this information derived from the study of the CMB anisotropies allows a fine-tuning of the ΛCDM model parameters. Present best fit parameters values have been shown in table 1.1.

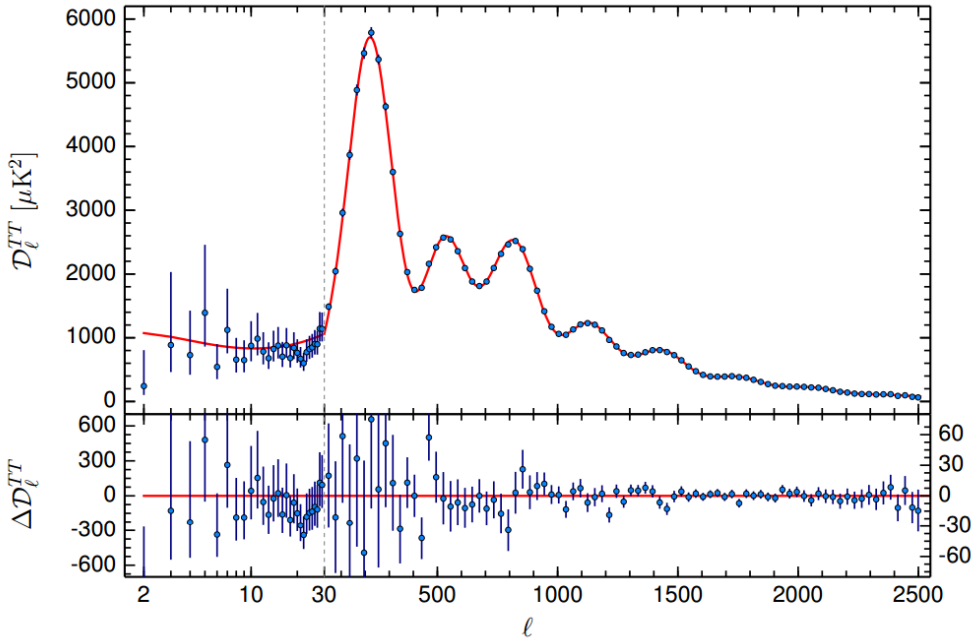

Figure 1.6: *Planck 2015 temperature power spectrum and best fit to ΛCDM theoretical spectrum. Residuals are also shown. Parameters derived from this fit have been shown in table 1.1. Figure from [1] and details therein.*

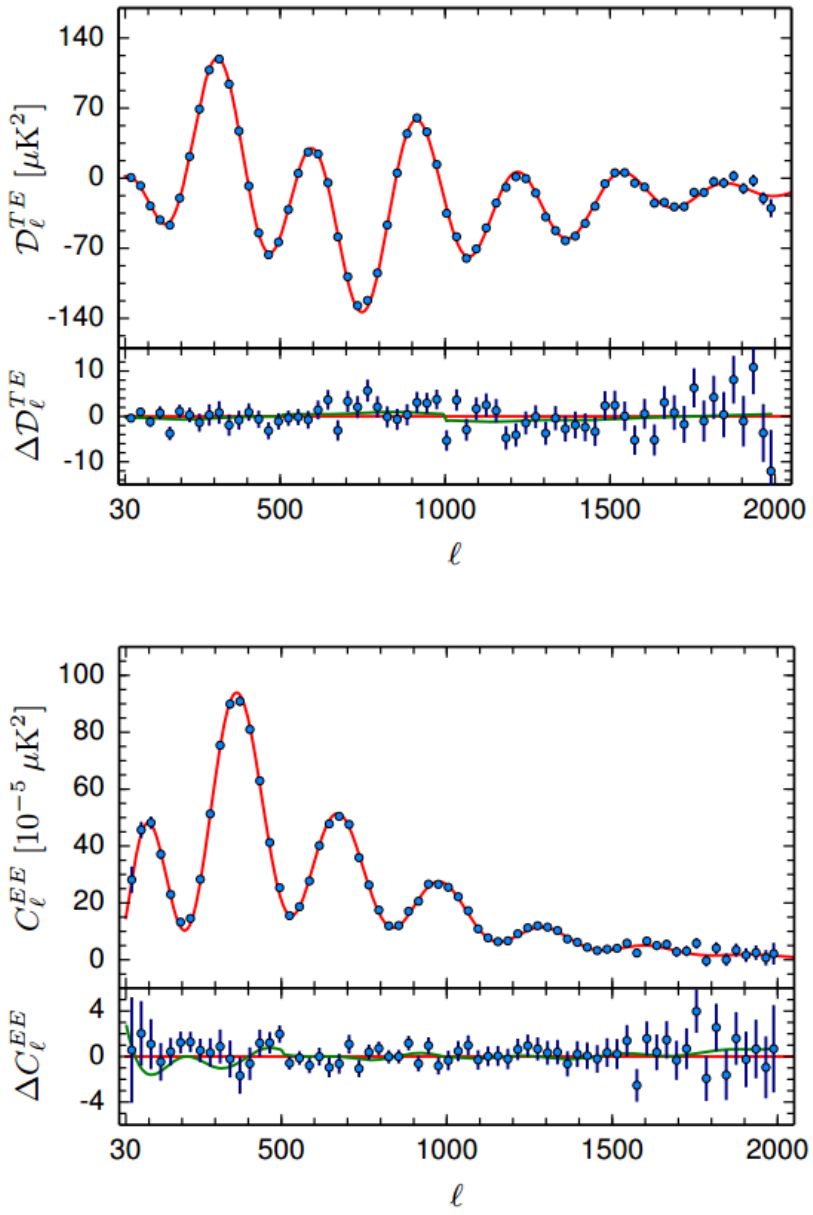

Figure 1.7: *Planck 2015 frequency–averaged TE and EE spectra and best fit to the ΛCDM model (without fitting for temperature–to–polarization leakage). Residuals are also shown. Figure from [1] and details therein.*

As shown in table 1.1, recent results from Planck satellite presented a value of $\Omega_B h^2 = 0.02227 \pm 0.00020$, that corresponds to a fractional uncertainty of less than 1% [1]. When compared to the total matter density the conclusion is that less than 20% of the matter of the Universe is baryonic and therefore there is a need of an important fraction of non–baryonic matter in the Universe, which means unknown matter (see section 1.3).

1.2.4 If not dark matter...

The existence of dark matter has been questioned since its proposal. Alternative hypotheses to explain the observed anomalies in the Universe have been proposed. The most promising theories are MOND (MOdified Newtonian Dynamics) [49] and their relativistic generalization TeVeS (tensor–vector–scalar gravity) [50]. For instance, rotation curves in spiral galaxies could be matched by slightly modifying (but *ad hoc*) the gravity force, without requiring the presence of dark matter halos around them. These theories do not explain consistently all the observations; for instance, in galaxy clusters dark matter is still required. TeVeS has been capable to explain some effects as strong gravitational lensing and some features of the CMB anisotropy without requiring any additional matter but always in an incomplete way and giving inaccurate predictions. Moreover, there are plenty of theoretical difficulties: ad–hoc additions are required to allow for a non–Newtonian non–relativistic limit of gravity fields.

1.3 Dark matter candidates

Dark matter describes whatever particle species which does not emit or interact with electromagnetic radiation and takes part of the present density content of the Universe. These dark matter candidates are required to be stable or long-lived on the cosmological time scales, weakly interacting with ordinary matter, non–relativistic at the time of the galaxy formation, neutral and massive.

Dark matter particles are expected to have been in thermal equilibrium in the early Universe within the primordial *soup*. Then, depending on the particle mass, they can be classified as hot or cold dark matter. Hot dark matter (very light particles) travelled very fast at their decoupling of the rest of the Universe contents, being relativistic and preventing small structures from forming. On the other hand, cold dark matter (particles in the GeV range) allowed the gravitational growing of structures at the scales observed in the Universe.

1.3.1 Standard Model candidates

Looking at the Particle Physics Standard Model, only neutrinos partially fulfill the previous requirements as they are stable (or long-lived) and do not experience nei-

ther electromagnetic nor strong interactions. Neutrinos were considered dark matter candidates as soon as their mass was discovered, but neutrinos were relativistic at the time of decoupling and, thus, were not able to produce as much small scale structures as observed in the Universe. Simulations and observations are incompatible with neutrinos being the only particle composing dark matter. Neutrino physics is well–known and a fossil density of neutrinos should contribute to the Universe density, as thermal relics of the very hot primordial Universe. These fossil neutrinos would be hot dark matter, because they decoupled from the rest of the Universe contents very soon, as their interaction rate is very low, and the Universe temperature was still much higher than the neutrino mass. However, structure formation favors strongly CDM candidates [51]. Even if neutrinos are known to take part in the composition of the dark matter of the Universe, it is in a very small percentage of the required missing mass. Therefore, a non-baryonic candidate beyond the Standard Model must be searched for. Anyway, neutrinos served as an important gateway particle, leading physicists to begin their experimentation with a variety of other, more viable, particle dark matter candidates.

1.3.2 Beyond the Standard Model candidates

Since 1984 the more widely accepted hypothesis in the scientific community has been that the mass of the Universe is composed by cold and non-baryonic particles. An hypothetical non–baryonic particle that would fulfill all the requirements for dark matter is being investigated. It is worth noting that the number of particles types contributing to dark matter is unknown and there is not any reason to believe it is not multi–component (see figure 1.8).

There are arguments supporting the extension of the Standard Model into a more complete theory. One of them is the supersymmetric extension of the Standard Model (SUSY) [52]. SUSY states that for every fermion, a boson must exist with the same quantum numbers (and vice versa) and therefore it predicts the existence of several new electrically neutral and non-baryonic particles that, in case of being stable, could be cosmologically abundant, and may have played an important role in the evolution of the Universe. Since these new SUSY particles have not been detected yet in particle accelerators, they must be heavy and/or extremely weakly–interacting particles [53] [54].

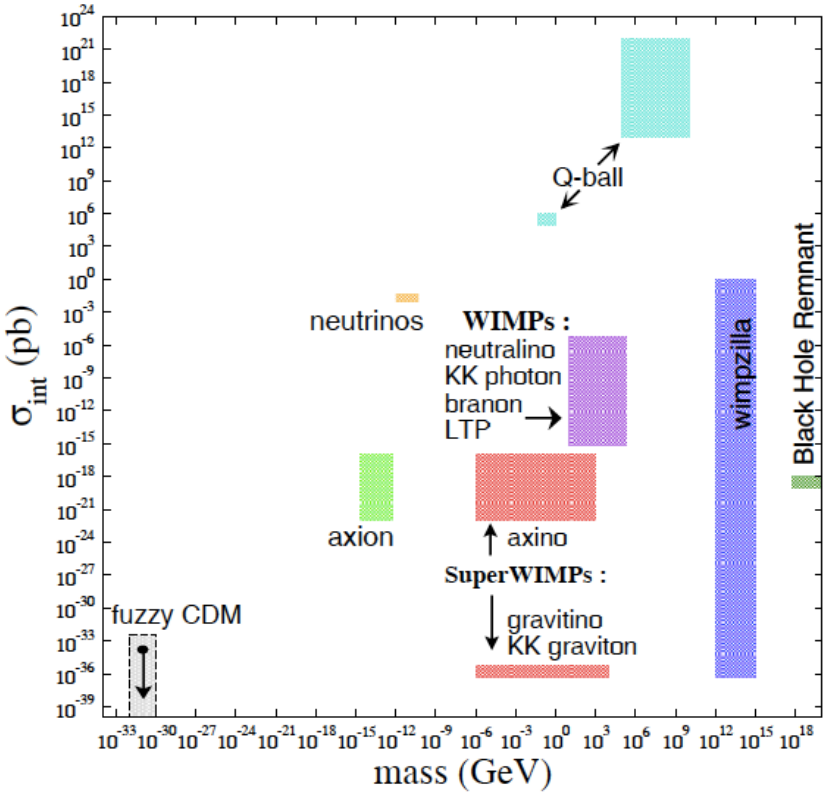

Figure 1.8: *Some dark matter candidates as a function of their mass and interaction cross-section. From [57].*

The two leading candidates for dark matter beyond the Standard Model are axions and Weakly–Interacting Massive Particles (WIMPs). Axions were proposed by Peccei and Quinn in 1977 in order to solve the strong CP problem in QCD (quantum chromodynamics) [55]. The axion is only a viable dark matter candidate in a small mass range; several constraints from experiments and astrophysical observations establish the mass of the axion below $3 \cdot 10^{-3}$ eV, if heavier than ≈ 1 eV would lead to the very fast cooling of red giant stars, in contradiction with the observations [56]. These light axions can have very interesting consequences for cosmology as they are stable over cosmological timescales. Therefore, axions produced in the early Universe would have survived until our days and could be able to constitute the dark matter.

WIMPs are hypothetical particles that are massive, neutral, non-relativistic, they interact weakly with ordinary matter and up to date, have an unknown nature. WIMPs are, as opposed to axions, very massive (from a few GeV to a few TeV). Assuming thermal production in the early Universe of particles having masses in

that range, and having interaction cross–section at the electroweak scale, the right relic abundance to explain the dark matter of the Universe is derived [58]; it is the so–called WIMP–miracle. The number of WIMPs in a volume expanding with the universe (comoving density) first decreases exponentially due to the Boltzmann factor $e^{-m/T}$ and then *freezes out* to a constant value when the WIMP annihilation rate fell below the expansion rate (see figure 1.9). This scheme is also especially attractive for experimentalists, as these particles interact with matter other than gravitationally, allowing their detection (see section 1.4). Also the natural emergence of this kind of particles in supersymmetric theories is another strong support to consider WIMP as a solid dark matter candidate.

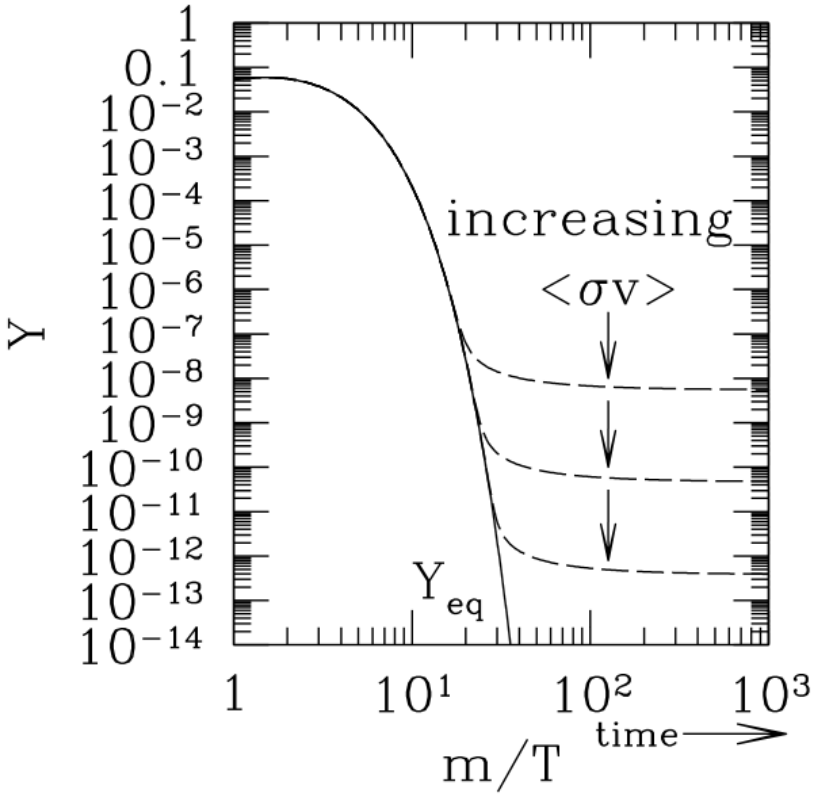

Figure 1.9: *Evolution of the number of WIMPs in a volume expanding with the Universe (comoving density) in the early Universe during the epoch of WIMP chemical decoupling, where $< \sigma v >$ is the thermally averaged total annihilation cross–section. The larger this annihilation cross-section, the lower the relic WIMP density.*

Beyond WIMPs and axions, many other "exotic" dark matter candidates have been proposed: black hole remnants, wimpzillas, fuzzy cold dark matter, etc. Another interesting possibility is that dark matter might be a consequence of the ex-

istence of extra spatial dimensions: in some models, ordinary particles traveling through an extra dimension of space can appear to us as stationary, but very heavy particles, called Kaluza–Klein modes, which could be stable and then, constitute the dark matter of our Universe. Similarly, a parallel or hidden Universe could explain the dark matter: the so-called mirror matter has been considered and analyzed in section 1.5.2. If this kind of matter exists in large abundances in the Universe, interacting with ordinary matter via photon–mirror photon mixing, this matter could be detected in direct dark matter detection experiments (see section 1.4.2).

1.4 Dark matter detection

The search of the dark matter of the Universe and the nature of the particles that it is made of is a challenge for astrophysics, cosmology, particle and nuclear physics.

For the detection of this kind of matter there are three main established research lines; the search in big particle accelerators, the indirect search through dark matter particle–antiparticle pair annihilation products and the direct search through the interaction of dark matter with ordinary matter. Impressive improvement in sensitivity along the last decades has been achieved in these three research lines. In this section, the fundamental aspects and results for direct detection will be presented together with a brief description of indirect searches.

Dark matter particles candidates could be produced at colliders [59] such as the Large Hadron Collider (LHC) and many information about the nature of dark matter could be obtained in the case of finding new physics below the TeV scale. However, no hints of physics beyond the Standard Model have been observed yet in accelerators but mass and cross–section limits have been established by Tevatron CDF [60] and LHC CMS [61] [62] and ATLAS [63–66] experiments.

1.4.1 Indirect dark matter detection

A non–negligible fraction of WIMPs can remain gravitationally confined around massive objects. Where WIMP density is high they can self–annihilate producing ordinary matter such as quarks or gauge bosons that induce photons, protons, antiprotons, electrons, positrons and neutrinos. The flux of this radiation is pro-

portional to the annihilation rate that depends on the square of the density of dark matter particles and the annihilation cross–section.

The search of dark matter through indirect detection hunts for an excess of ordinary matter in cosmic rays that cannot be explained by any other mechanism. This excess must be searched for in sources with high dark matter particles density, that is, in dense regions of the galactic halo (such as the galaxy center, dwarf galaxies satellites of the Milky Way, or even the center of the Sun) or very massive clusters of galaxies.

Gamma rays annihilation signal plays an outstanding role as a possible messenger of dark matter because of their nature; they propagate almost unperturbed and pointing directly to their source. Therefore, gamma rays are searched for directly, with satellites, or indirectly with ground–based Cerenkov telescopes. Due to the small area on satellites available for the installation of detectors, higher energies can be only detected by ground–based telescopes. HESS [67], MAGIC [68] (see figure 1.10) or VERITAS [69] have not found any excess attributable to dark matter self–annihilation coming from dwarf galaxies, satellites of the Milky Way. The future CTA (Cherenkov Telescope Array) [70] could improve significantly the sensitivity in this search. The Fermi gamma–ray Space Telescope was launched in 2008 carrying the Large Area Telescope (LAT). LAT is an imaging high–energy gamma–ray telescope that covers an energy range from about 20 MeV to more than 300 GeV. Although claims of an observation of a 130 GeV line near the galactic center were published [71] [72], this interpretation was disfavoured after further analyses carried out by the collaboration, that reported upper limits at 95% C.L. from the absence of signal excess between 7 and 200 GeV [73].

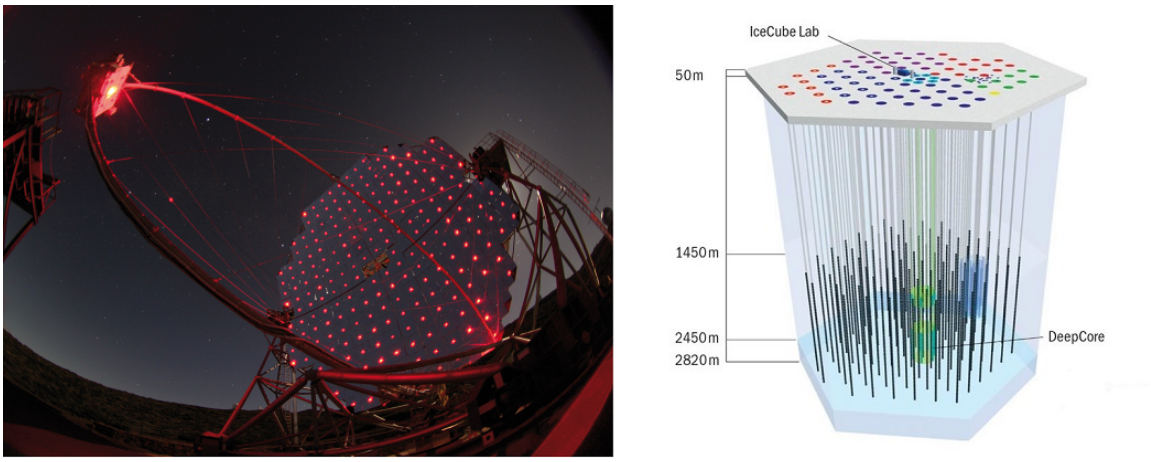

Figure 1.10: *MAGIC and IceCube telescopes.*

Neutrinos can also play a role in dark matter annihilation signature. Due to the rare interaction of neutrinos and the distance to their sources, indirect detection focuses on the detection of near annihilation sources. The Earth or the Sun could scatter WIMPs and bound them gravitationally allowing their annihilation and producing a signature of high energy neutrinos coming from the center of the Earth or the Sun [74]. However, no excess of neutrinos coming from the Sun, nor from the Earth, has been detected by the IceCube Neutrino Observatory, located at the geographic South Pole [75] (see figure 1.10).

Also the presence of antimatter, as positrons and antiprotons, can be a signature of dark matter annihilation. AMS–01 (Alpha Magnetic Spectrometer) [76] confirmed an excess of positrons previously reported by PAMELA [77] and more recent results of AMS–02 [78] are inconclusive about the clear excess of positrons that could be produced in the annihilation of dark matter particles or attributed to astrophysical backgrounds [79].

1.4.2 Direct dark matter detection

Dark matter direct detection experiments aim at the conversion of some of the halo dark matter particles energy into a visible signal through their coupling to ordinary matter or fields. Experimental approach is quite different depending on the dark matter candidate searched for. The fundamental factor to be considered in order to design a direct dark matter detection experiment is the expected interaction rate, which however, is strongly dependent on the dark matter halo and particle models.

Among the preferred dark matter candidates, showing favorable perspectives for its direct detection, are not only WIMPs but also axions. Many experiments are searching for astrophysical axions through the Primakoff effect [80], in which the axion is converted into a detectable photon under the presence of a strong electromagnetic field. None of the experiments searching for axions from galactic origin and those produced in the Sun's core have obtained yet a positive result. IAXO (International Axion Observatory) is a new generation axion helioscope, aiming at the detection of axions emitted from the Sun [81]. IAXO experiment will use a 20 m long toroidal superconducting magnet, with eight coils and eight 60 cm diameter bores placed in between the coils. This magnet will be placed on a conventional telescope–like moving structure in order to make the magnet point to the Sun. ADMX (Axion Dark Matter eXperiment) uses a resonant microwave cavity within a large superconducting magnet to search for galactic halo axions by detecting the very weak conversion of dark matter axions into microwave photons. It is located at the Center for Experimental Nuclear Physics and Astrophysics (CENPA) at the University of Washington (US) [82].

On the other hand, WIMPs are expected to interact weakly with ordinary matter mainly through elastic scattering with detector nuclei. In these collisions only a small nuclear recoil kinetic energy (under 100 keV) is released. Experiments searching for WIMPs are carried out in underground laboratories and using very massive and ultrapure detectors in order to fight against the very low expected interaction rates.

1.4.2.1 Calculation of rates

This interaction rate can be calculated in a one–type of nucleus of mass m_N target detector as [83]:

$$\frac{dR}{dE_R} = N_N \frac{\rho_0}{m_W} \int_{v_{min}}^{v_{max}} v g(\vec{v}) \frac{d\sigma_{WN}}{dE_R} d\vec{v} \tag{1.15}$$

where m_W is the WIMP mass, ρ_0 is the local WIMP density, $g(v)$ the WIMP speed distribution in the detector reference system and $\frac{d\sigma_{WN}}{dE_R}$ the WIMP–nucleus differential cross–section.

Considering the isotropic, isothermal and non–rotating spherical standard halo model, WIMPs follow a Maxwellian velocity distribution in the halo reference frame, $f(v)$, being v_0 the most probable value of the velocity, that can be written as:

$$f(v) = \frac{1}{v_0^3 \pi^{\frac{3}{2}}} exp(-\frac{v^2}{v_0^2}) \tag{1.16}$$

taking into account that this distribution is truncated by the existence of an escape velocity (v_{esc}).

In the WIMP–nucleus scattering, the recoiling nucleus receives an energy:

$$E_R = \frac{\mu_{WN}^2 v^2 (1 - cos\theta^*)}{m_N} \tag{1.17}$$

where θ^* is the scattering angle in the center of mass reference frame and μ_{WN} is the WIMP–nucleus reduced mass:

$$\mu_{WN} = \frac{m_W m_N}{(m_W + m_N)} \tag{1.18}$$

To produce a recoil energy E_R the minimum velocity of the WIMP, v_{min}, in equation 1.15 is:

$$v_{min} = \sqrt{\frac{m_N E_R}{2\mu_{WN}^2}} \tag{1.19}$$

whereas the maximum WIMP velocity, v_{max} in equation 1.15 is related with the halo escape velocity, after transformation into the detector reference frame.

In order to compute the WIMP–nucleus cross-section starting from the particle model parameters (WIMP couplings to SM particles) it is necessary to describe first the nucleon content in terms of quarks and gluons through hadron matrix elements and then, to build the nuclear matrix elements. A more direct approach is usually followed: although a new theoretical framework generalizes WIMP interaction with nucleons by including 14 WIMP–nucleon interaction operators (all

Galilean–invariant operators up to quadratic order in momentum transfer arising from exchange of particles of spin 1 or less [84]), this interaction is usually decribed by two terms, an spin–independent (SI) term (coherent sum of the dispersion amplitudes with the individual nucleons) and a spin–dependent (SD) term (WIMP is coupled to the total nuclear spin),

$$\frac{d\sigma_{WN}}{dE_R} = (\frac{d\sigma_{WN}}{dE_R})_{SI} + (\frac{d\sigma_{WN}}{dE_R})_{SD} = \frac{m_N}{2\mu_{WN}^2 v^2}(\sigma_0^{SI} F_{SI}^2(E_R) + (\sigma_0^{SD} F_{SD}^2(E_R)) \quad (1.20)$$

In this equation, $F(E_R)$ are the nuclear form factors which account for the finite size of the nucleus and depend strongly on the interaction momentum transfer. $\sigma_0^{SI,SD}$ are the WIMP–nucleus cross–sections in the limit of zero momentum transfer, which can be written in quite a general form:

$$\sigma_0^{SI} = \frac{4\mu_{WN}}{2}\pi[Z \cdot f_p + (A - Z) \cdot f_n]^2 \quad (1.21)$$

$$\sigma_0^{SD} = \frac{32\mu_{WN}}{2}\pi G_F^2 \frac{J+1}{J}[a_p < S_p > + a_n < S_n >]^2 \quad (1.22)$$

where f_p, f_n, a_p, and a_n are the effective WIMP couplings to neutrons and protons in the SI and SD case, respectively. In the SI interaction scheme, coupling to neutrons and protons of WIMPs is usually considered the same ($f_p = f_n$). $< S_{p,n} >$ are the expectation values of proton and neutron spin operators in the limit of zero momentum transfer in the target nucleus, N, and they can be determined using detailed calculations, specific for each nuclear species. Figure 1.11 shows an example of expected dark matter rates calculated for Na and I nuclei and two different WIMP masses.

In order to be able to compare the results of experiments using different target nuclei, N, it is necessary to relate WIMP–nucleus cross–sections with WIMP–nucleon cross–sections. Under the assumption of equal coupling intensity of WIMPs to protons and neutrons in SI interactions, the relation between WIMP cross–sections with nuclei (σ_0^{SI}) and nucleons (σ_{Wn}^{SI}) is:

$$\sigma_0^{SI} = (\frac{\mu_{WN}}{\mu_{Wn}})^2 \cdot A^2 \cdot \sigma_{Wn}^{SI} \quad (1.23)$$

being A the atomic mass number of the target nuclei and μ the reduced masses.

As it has been said before, when interacting with ordinary matter, WIMPs produce a small recoil in one of the target nuclei. Energy released can be detected as photons, phonons or electric charge, depending on the detector characteristics. The expected signal can be easily shadowed by the radioactive background. The main contributions to the background come from the environmental radioactivity, primordial radioactive isotopes present in the materials of the detector itself and cosmic radiation as well as cosmogenic activation in the detector materials due to exposure to cosmic rays.

Low background techniques are used in this kind of experiments in order to achieve as much sensitivity as possible. Dark matter direct detection experiments are carried out in underground laboratories in order to protect the detectors from cosmic radiation and avoid the cosmogenic activation in the detector materials. The detectors are built from high radiopurity materials and to minimize radioactive environmental background, active and passive shieldings are installed in order to protect from beta and gamma radiations and neutrons. Whenever possible, nuclear recoil discrimination techniques are applied in order to remove most of the usual backgrounds.

Comparing the experimentally measured residual rates in a given detector with the estimated rates for a specific WIMP candidate and halo model, allows to rule out such a candidate if the measured rate is below the estimates. However, this exclusion is halo model, dark matter particle model, and target dependent, and it has to be cautiously compared with results from other targets. It is impossible to distinguish an individual energy deposition produced by an hypothetical dark matter particle from that produced by a neutron, for instance, and then, only negative results can be derived from such a comparison. A distinctive behaviour must be searched for WIMPs that would allow a positive identification of a dark matter signal unambiguously. This could be achieved by searching for the annual modulation expected in the signal rate due to Earth's motion around the Sun which changes the relative velocity WIMP–nucleus [85]; by determining the direction of the recoiling nucleus, which is correlated with the direction of the impinging WIMP (WIMP wind seems to come from Cygnus constellation, due to Earth movement inside the galaxy) and changes along the day with a very specific pattern [86]; and by profiting that WIMP

interaction rate depends strongly on the target nuclei (mass and spin content) and in a different way as other backgrounds, as neutrons, do [87] [88].

As the energetic deposition is produced by the elastic dispersion of the WIMPs with the nuclei of the detector, the signal generated concentrates in the low energy region (below 100 keV). Due to the exponential shape of the searched signal, the rate is much higher close to the detection threshold (see figure 1.11).

An ideal detector for direct dark matter detection should fulfill the following characteristics:

- Low energy threshold.
- Good energy resolution in the energy region below 100 keV.
- Very low radioactive background.
- High nuclear recoil discrimination power.
- Large mass.
- High sensitivity to nuclear recoil energy.
- Sensitivity to nuclear recoil direction.
- Stability for long time measurements.
- Possibility of combining different target nuclei in the same set–up.

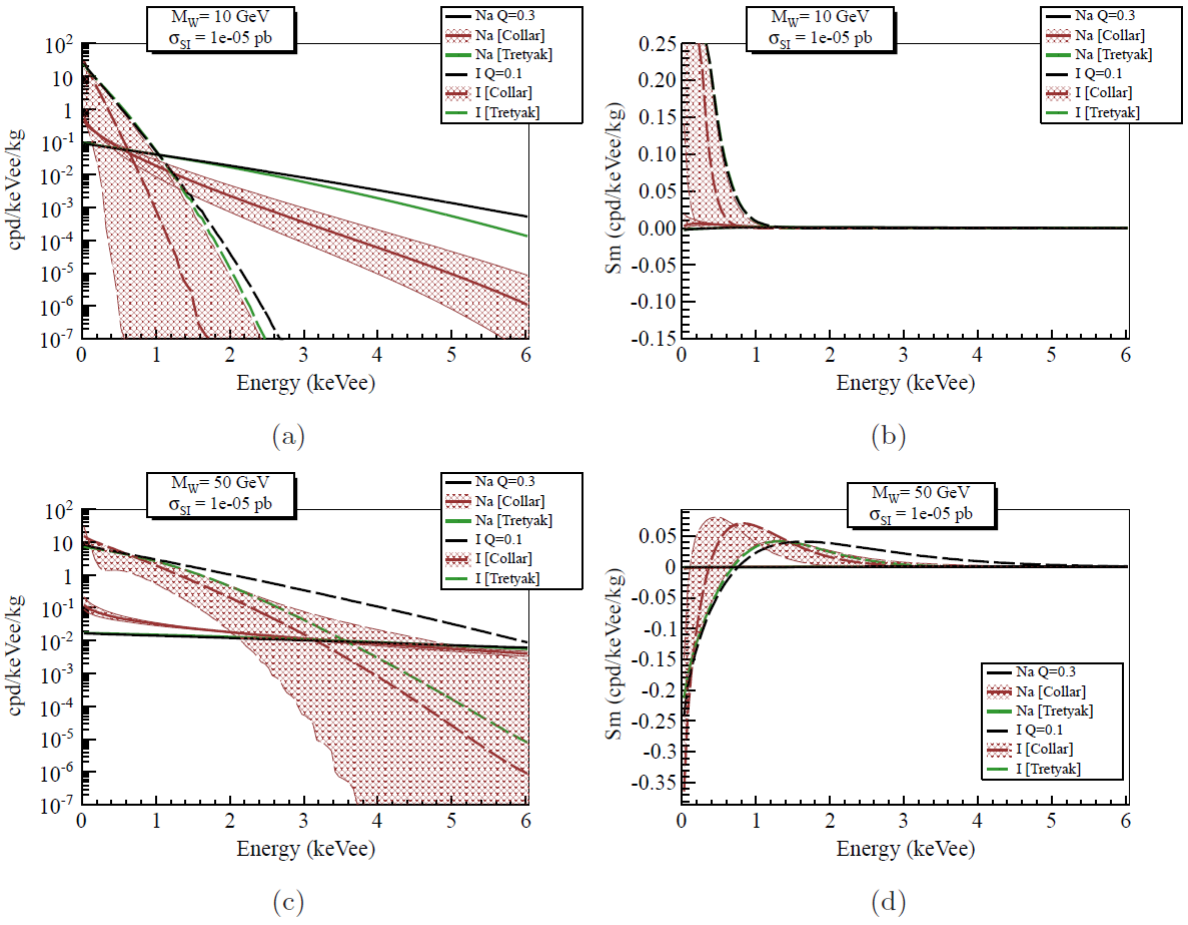

Figure 1.11: *Expected dark matter rates and modulation amplitude in NaI. Different signals for WIMPs of $m_W = 10$ GeV and $m_W = 50$ GeV with $\sigma^{SI}_{Wn} = 10^{-5}$ pb, and different values of Na and I nuclear recoils quenching factors, as reported on [90] and [91] [92], have been considered. Figure from [32].*

Unfortunately, it does not exist a detector satisfying all of these requirements, but new detection techniques are being continuously under development and strong improvement in sensitivity and performance of the detectors has been achieved in the last years. In the rest of the section an updated review of the most relevant experiments in the field of dark matter direct searches will be presented.

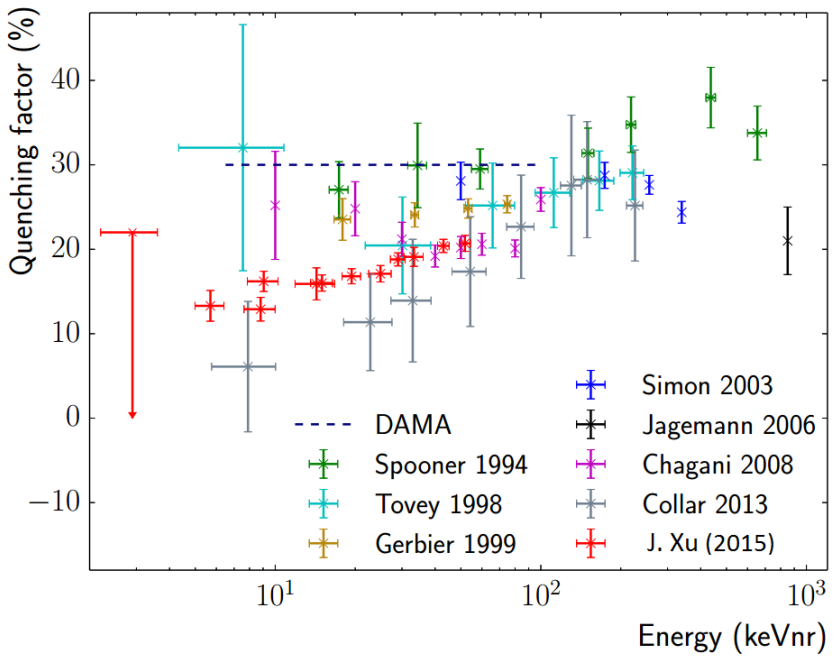

Figure 1.12: *Na–recoil quenching factors measured by several experiments. Figure from [97].*

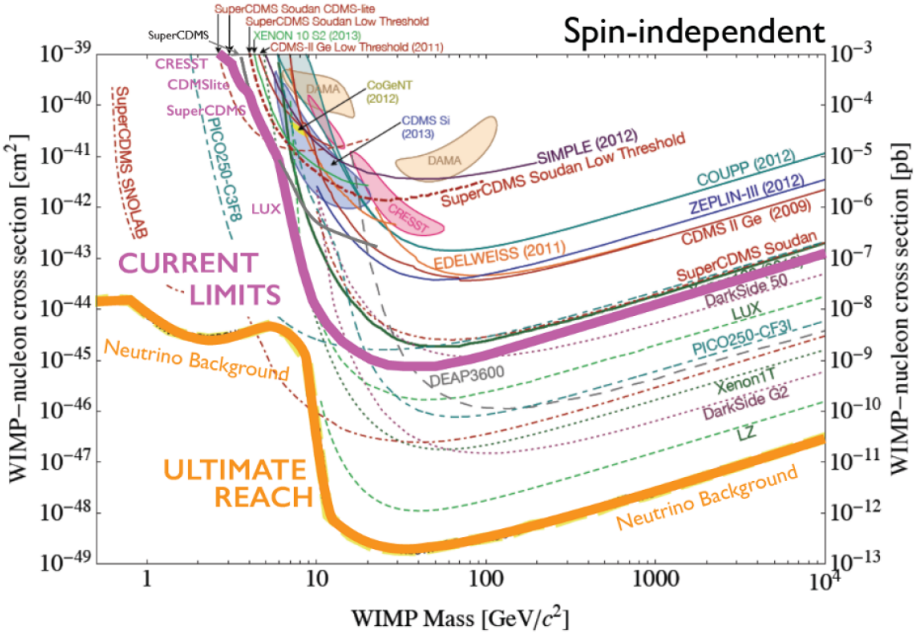

Figure 1.13: *Exclusion plot (for SI interactions) with current better limits (in pink), current experimental individual results (solid lines) and projections (dashed lines). From [89].*

The so–called Relative Efficiency Factor (REF or quenching factor, Q) measures the conversion of the energy deposited by nuclear recoils into visible signal. The REF is an important feature for all techniques, but it is specially relevant in scintillator materials as it is well–known that the scintillation yield strongly depends on the type of interacting particle and it is much lower for nuclear recoils than for electron/gamma events. Therefore, knowing precisely the value of the quenching factor is mandatory for the correct recoil energy calibration of the experiments.

Most of the detectors devoted to the search for dark matter are calibrated in energy with the photopeaks of β/γ sources. These calibrations produce an energy scale valid for electron recoil events, named typically as *electron equivalent energy (keVee)*, but not for nuclear recoil events. Uncertainties in quenching factors have an important impact on the conversion of the expected spectra of WIMPs (in recoil energy) into visible energy (keVee) (see figure 1.11).

In ANAIS, ultrapure NaI(Tl) crystals are used as target material. As it will be explained in section 2.3, NaI presents several advantageous features in the search for dark matter. A low energy threshold can be achieved thanks to the high light yield of NaI and it combines light and heavy nuclei, ensuring good sensitivity in the low and high mass WIMP ranges. Moreover, both Na and I isotopes have spin, and are sensitive to SD WIMP–nucleus interactions. The main disadvantage of using NaI(Tl) as target material in a experiment searching for dark matter is the low REF.

Quenching factor values of ~ 0.3 for Na and ~ 0.1 for I are reported [4] [5] [94] [95]. Energy independent behaviour of Q at low energies is compatible with these results, whereas other results show a slight increase of Q when lowering the energy [91] [92] [96]. However, recent measurements point to a stronger dependence with energy and much lower values of Q for Na in the low energy region [90] [97]. This result would lead to an important shift in the WIMP parameter within reach of the ANAIS experiment and therefore, a better knowledge of Q is required in order to compare results from NaI(Tl) experiments with those of experiments using other target material. Figure 1.12 summarizes the status of quenching factor measurements for Na.

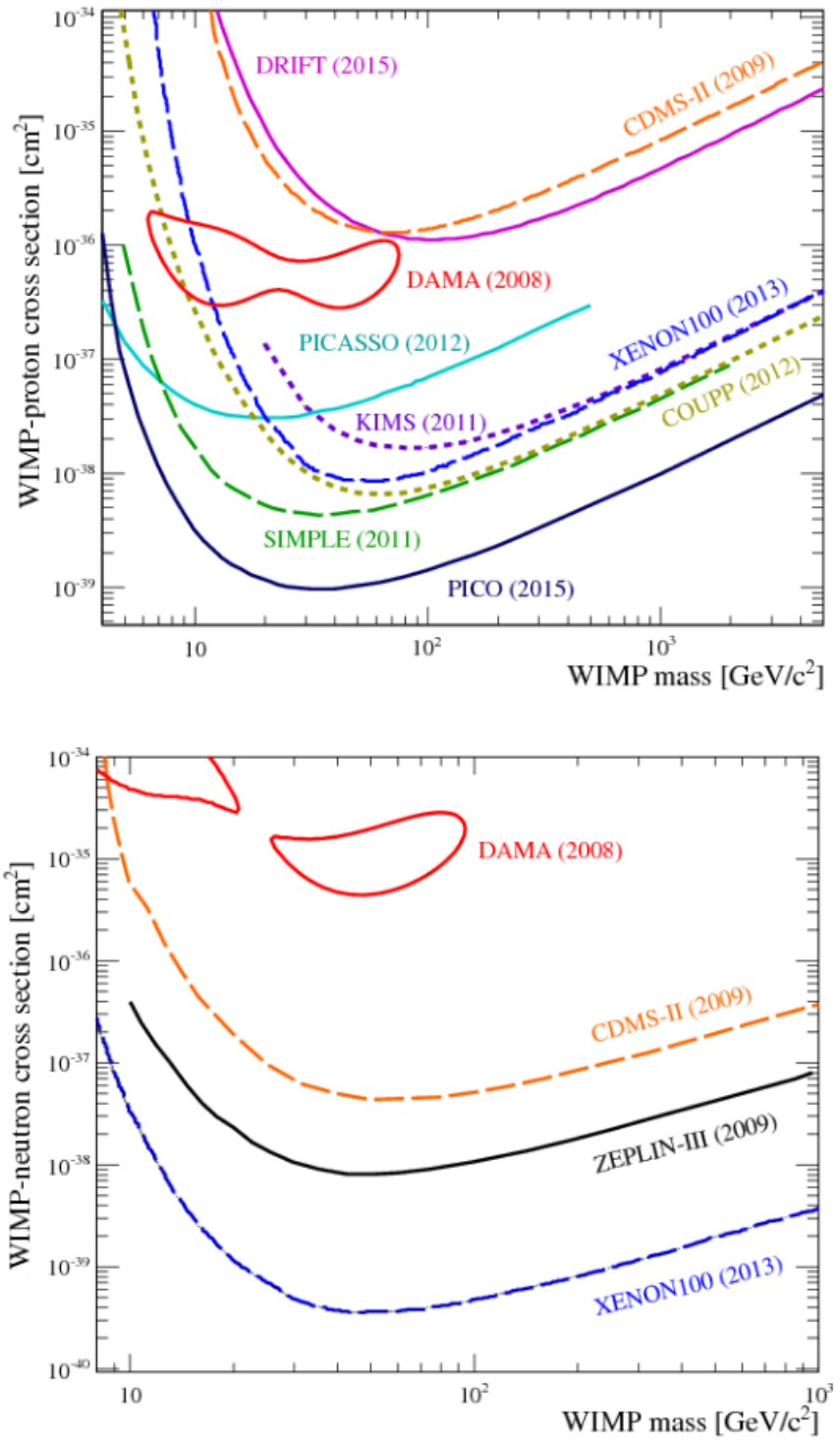

Figure 1.14: *Exclusion plots (for SD interactions) assuming pure proton coupling (top) and pure neutron coupling (bottom). From [93].*

1.4.2.2 Results from experiments

Several experiments have been devoted to the search of dark matter since the eighties, profiting from the low background techniques developed for investigating the neutrinoless double beta decay. Since the nineties, NaI scintillators have been chosen due to their sensitivity to spin–dependent interactions and feasibility of big mass detectors together with hyperpure Ge detectors, having higher radiopurity but smaller detection mass. More recently, solid–state detectors and detectors using liquids of noble gases with better sensitivity because of their ability to discriminate nuclear from electronic recoils, have been used.

Among the different techniques devoted to the direct dark matter detection, solid–state cryogenic detectors (operating at sub–Kelvin temperatures) offer low threshold (< 10 keV), excellent resolution ($< 1\%$ at 10 keV) and ability to discriminate nuclear from electronic recoils [98]. Following this technique, CDMS collaboration has developed several experiments based on semiconductors operating at 40 mK, reporting an excess of three events in Si detectors [99] and no excesses nor modulation in the Ge detectors. Latest results have been obtained from the low ionization threshold experiment [100]. SuperCDMS, an upgrade at Soudan Underground Laboratory, United States, using 9 kg of Ge detectors has presented first results [101]. SuperCDMS next goal is to install 100 kg of Ge and 10 kg of Si detectors [102].

EDELWEISS [13] experiment in the Modane Underground Laboratory, France, uses cryogenic germanium detectors. An upgrade consisting of 4 kg of Ge detectors, EDELWEISS–II, found 5 events with a background estimate of 3, giving limits on the SI cross–section [103]. The next upgrade, EDELWEISS–III consisting of 40 detectors with improved technology and radiopurity with 24 kg of fiducial mass, has presented first exclusion results [13].

CRESST [12] at the LNGS, uses now $CaWO_4$ scintillating bolometers. The collaboration has operated several cryogenic detectors with simultaneous phonon and photon detection. The upgrade, CRESST–II consisting of 8 detectors, 300 g each, reported 67 events in the nuclear recoil region that could not be explained by known backgrounds [104]. More recent results with a new detector design have not confirmed this issue [105]. A high scale cryogenic experiment called EURECA [106] following EDELWEISS and CRESST experience and know–how in this technique is

in design phase.

Germanium ionization detectors can reach sub–keV energy threshold and very low backgrounds [107] but, as for NaI, they are not capable to distinguish electronic from nuclear recoils. CoGeNT [108] is the only p–type point contact germanium experiment that has reported the presence of an annual modulation in the event rate [108] [109], however, recent analyses result in contradictory conclusions [110] [111].

Liquid Xenon (LXe) and liquid Argon (LAr) are also used in several experiments devoted to the search of dark matter [112]. Simultaneous detection of scintillation and ionization allows the identification of the primary interacting particle in the liquid and by using Time Projection Chambers (TPCs), the 3D position of an interaction can be determined. The feasibility to build detectors with large mass, highly radiopure and allowing to define fiducial cuts convert LXe and LAr into very sound targets for WIMP searches. Double phase liquid/gas Xe TPC experiments as LUX at Sanford Underground Research Facility [15] [113], XENON–100 [18] [114] [115][116], and the proposed XENON1T [117] at LNGS, PandaX [118] at China Jin-Ping underground Laboratory (CJPL); double phase liquid/gas Ar TPC experiments like ArDM [119] at the LSC; single phase Ar TPC as DarkSide [120] [121] at LNGS; single phase Ar scintillator as CLEAN [122] and DEAP [123] at SNOLab and single phase Xe scintillator as XMASS [124] at the Kamioka Observatory are a few experiments searching, with noble liquids, for dark matter. None of them has reported a deviation from background expectations and XENON and LUX have set very stringent limits on WIMP interaction cross–sections.

To be sensitive to SD interactions, a target nuclei with uneven total angular momentum is required. ^{19}F is a very convenient target nucleus for SD interaction which is present in WIMP detectors using superheated liquids as SIMPLE [125], COUPP [126] and PICASSO [127] experiments. Recently, COUPP and PICASSO collaborations have joined efforts in the PICO project [16]. They have already obtained competitive results. Searches using other isotopes have been carried out, like ^{127}I by DAMA [4] and KIMS [128] and ^{129}Xe and ^{131}Xe by XENON [115].

Among experiments using scintillation detectors it is worth taking into account those using NaI(Tl) as, in addition to ANAIS, KIMS [128][129], in Korea (using CsI and NaI detectors), COSINUS [130], SABRE [22], PICO–LON [131], DM–Ice [20] or DAMA/LIBRA (see section 1.5) in Italy.

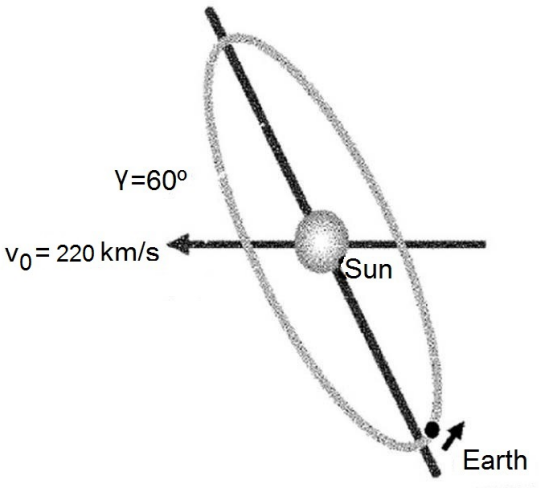

Figure 1.15: *Schematic representation of the Earth's motion around the Sun and the Sun's motion in the GRS.*

As a summary of the latest results in the direct detection of WIMPs, figures 1.13 and 1.14 show the updated exclusion plots derived from different experiments for SI and SD interactions, respectively.

1.4.2.3 Annual modulation of dark matter

Dark Matter attached to our galaxy is distributed in the called dark halo and, in the simplest model, it can be supposed as isotropic in the galactic reference system (GRS). The WIMP interaction rate with the target nuclei depends on the relative velocity WIMP–nucleus, i.e. the velocity of the WIMP in the laboratory reference system, (equation 1.20). The Earth, in its motion around the center of the galaxy together with the Solar System, is moving with a velocity v_E in the GRS. A transformation of the type $v = v_W - v_E$ has to be performed, where v_W is the velocity of the WIMP in the GRS. The Earth's motion produces a distinctive periodic pattern in the detection rate of dark matter particles from the galactic halo, so that it allows distinguishing it from another background signals.

The Earth moves around the Sun with a periodicity of 1 year and a velocity v_{orb} of about 30 km/s. In its motion, the Earth follows an almost circular orbit whose plane has an inclination angle $\gamma \approx 60^o$ with respect to the galactic plane (see figure 1.15). In summer the Earth's velocity in its motion around the Sun is added to

the rotation velocity of the Sun around the galactic center ($v_0 \approx 220$ km/s), while in winter, Earth's orbital velocity is opposite to that of the Sun. Thus, the relevant component of the Earth's velocity for WIMP annual modulation is the projection in the direction of the Sun velocity that can be described as $v_{rot} = v_{orb} cos\gamma \cos\omega(t - t_0)$ where $\omega = 2\pi/T$ and t_0 is the time for which v_{rot} reaches its maximum, around June, 2^{nd} [132]. Concerning the Sun, its velocity can be expressed as $v_S = v_0 + v_\odot$, being $v_\odot$ the peculiar velocity of the Sun. Figure 1.16 shows the variation of the Earth's velocity in the GRS obtained summing v_S and v_{rot}.

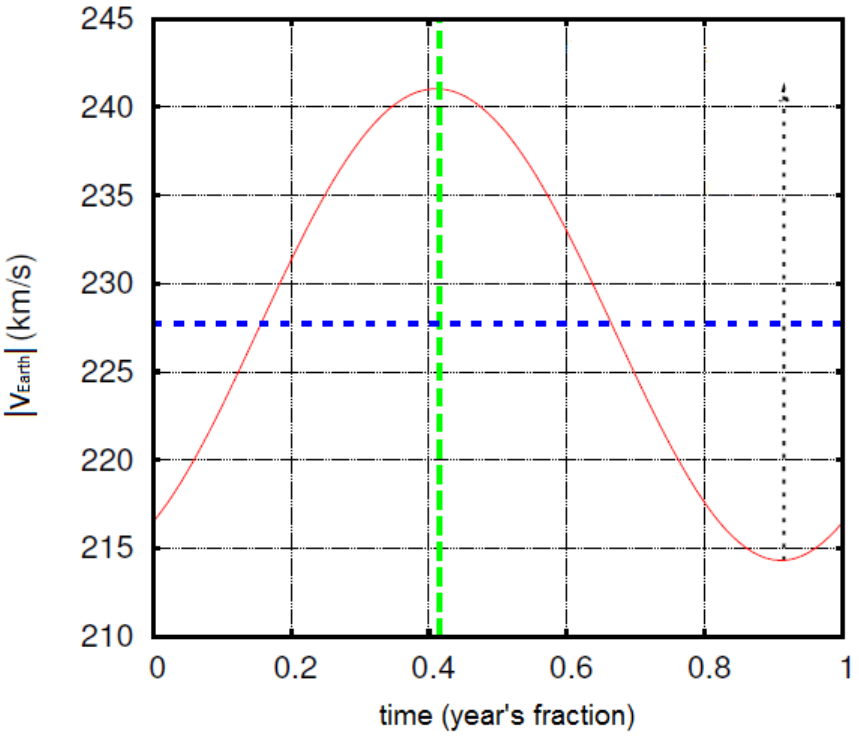

Figure 1.16: *Variation of the Earth's velocity (in module) in the GRS along the year with a maximum around June 2^{nd}. From [133].*

Detection rate in the detector depends on the velocity of the WIMPs in the reference system of the Earth. As the variation $\Delta v_E \approx 12$ km/s is a small percentage of v_E ($\Delta v_E / v_E \approx 7\%$) the expression can be approximated for a determined k–th energy interval as a Taylor series development cut at the first order, S_k:

$$S_k = S_{0,k} + S_{m,k} cos\omega(t - t_0) \tag{1.24}$$

where $S_{0,k}$ is the mean rate and $S_{m,k}$ is the amplitude of the modulated term. In these conditions, when the relative velocity WIMP–nucleus is higher, WIMPs are more energetic on average and leave more energy in the detector, changing the shape of the differential spectrum, which implies that the rate in June can be greater or smaller than in December depending on the analysed energetic range.

The characteristics of the dark matter searched signal are:

- Sinusoidal behaviour of the rate as a function of time.
- A one-year periodicity signal.
- Presence of the signal modulation phase at around June 2^{nd}.
- Small amplitude signal ($\approx 7\%$).
- Only appreciable in single–hit events and in a very small energy range, depending on the WIMP mass and the detector (target nucleus and relative efficiency factor). For example, for NaI detectors, the signal is only distinguishable for energies below 6 keVee.

On the other hand, for an annual modulation search experiment exceptional conditions of stability of all parameters of the experiment that could induce a variable behaviour in time must be guaranteed. Very good background understanding is required too because some backgrounds could produce similar effects to the signal searched for. For instance, muon flux is correlated at high depth with the atmospheric variations of temperature and could induce a modulation with an annual periodicity in the background of an underground experiment at low energy through neutrons induced by muons. This effect has been analyzed in [134–136].

1.5 The DAMA/LIBRA experiment

DAMA/LIBRA experiment [9] [137] [138], at the LNGS, under 1400 meters of rock, has shown evidence with high statistical significance, of the presence of an annual modulation in the detection rate at low energy, compatible with the expected for an hypothetical dark matter halo. The DAMA collaboration considers that this effect cannot be explained by any systematic effect nor other known background and that it could be attributable to a dark matter signal [139] [140]. In this sense, in

Figure 1.17: *DAMA/LIBRA experiment in the LNGS, in Italy.*

section 1.5.2 a corollary study relating the measured annual modulation signal and symmetric mirror dark matter is presented.

DAMA/NaI experiment (DArk MAtter Experiment) [3] [10] with NaI(Tl) radiopure scintillators (100 kg of mass) was the first experiment to announce an annual modulation signal. In 2003 DAMA detectors were upgraded and detection mass was increased to about 250 kg, this new experiment was called LIBRA and confirmed with higher statistical significance DAMA/NaI results.

1.5.1 Description and results

DAMA/LIBRA consists of 25 NaI(Tl) scintillating radiopure crystals produced by Saint Gobain company [141] of 9.7 kg each in a 5×5 matrix. Each crystal is coupled to two low background photomultipliers with 10–cm–long quartz light guides acting as optical windows. Modules operate inside a sealed copper box flushed with highly pure nitrogen placed within a low activity shield of Cu/Pb/Cd/polyethylene/paraffin (see figures 1.17 and 1.18). In addition, 1 m of concrete from Gran Sasso rock material, almost fully surrounds this passive shield as neutron moderator. The installation has a 3–level sealing system which prevents environmental air from reaching the detectors. The whole installation is air–conditioned and several operation parameters are continuously monitored and recorded.

Software designed for DAMA/LIBRA, as the one designed for DAMA/NaI, has the capability of registering single–hit (detected by a single detector) and multiple–hit (detected by more than one detector) events and the energy threshold of the experiment has been established at 2 keVee.

As shown in figure 1.19, several annual cycles of data seem to confirm this annual modulation for single–hit events in the 2–6 keVee region satisfying the requirements for a dark matter signal. In fact, the measured period (0.998 ± 0.002) y and phase (144 ± 7) d, are both compatible with expectations. Modulation appears in the 2–6 keVee region and it does not in other energy regions and multiple–hit events, attributable to background, do not show any modulation. The estimated modulation amplitude in the 2–6 keVee region is (0.0112 ± 0.0012) counts/(keV kg day) with 9.3 σ C.L.[9].

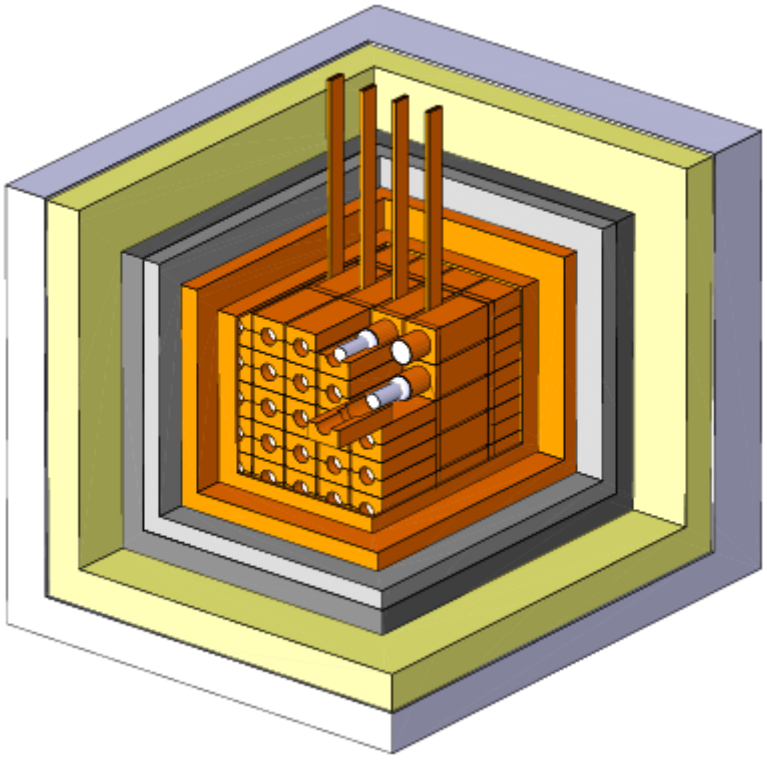

Figure 1.18: *Schematic view of the passive shield of the DAMA/LIBRA set–up.*

No other experiment up to date has found such modulation in the detection rate, even with higher sensitivity detectors. Results have been recently presented by XENON [18], XMASS [124] and DM–Ice [20].

However, comparison among experimental results derived from different targets and techniques is model dependent, and this is the main reason why experiments using NaI as target and with the same detection technique as DAMA/LIBRA are required to solve this controversy (see section 1.4.2). Among them, ANAIS, carried out at the LSC, becomes a crucial experiment, with the same target (NaI) and experimental technique as DAMA/LIBRA.

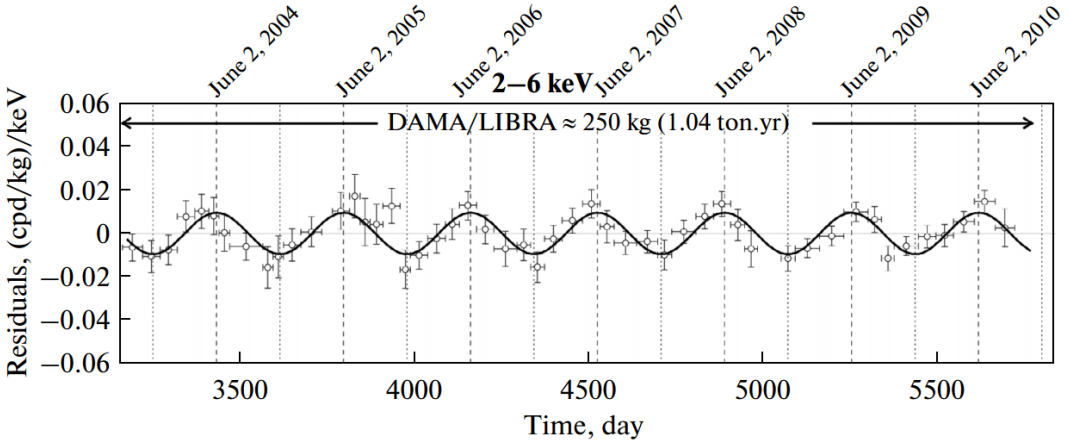

Figure 1.19: *DAMA/LIBRA experiment residual rate of single-hit scintillation events in the 2-6 keV region (from [138]).*

1.5.2 Annual modulation effect in DAMA experiment and symmetric mirror matter

The DAMA group has carried out several studies of the model independent annual modulation effect in different dark matter scenarios [142–146]. In this section, one specific interpretation of the annual modulation signal observed by DAMA/LIBRA in terms of symmetric mirror matter is presented as example. This work was done during the research stage of this thesis author at University of Rome "Tor Vergata" in 2015 [147].

Mirror matter is an exact duplicate of ordinary matter from a parallel hidden sector with a chemical composition dominated by mirror helium, but that can also contain significant fractions of heavier elements as mirror carbon or oxygen. Mirror atoms from these "dark", "hidden" or "shadow" sector could interact with ordi-

nary matter as result of kinetic–mixing between mirror and ordinary photons. In this assumption, dark atoms would interact with nuclei of the target detector via Rutherford-like scattering.

In this section, results of kinetic–mixing parameter range able to explain the DAMA/LIBRA annual modulation signal in the frame of different scenarios for the chemical composition of the Milky Way dark sector are presented. Uncertainties from nuclear and particle physics have been taken into account in the analysis.

1.5.2.1 The mirror world

The idea of dark matter particles coming from a hidden sector has become increasingly popular in the last years. This sector may consist of elementary leptons (as our electron) and composite baryons (similar to our proton or neutron) which can be combined in atoms by long–range forces mediated by dark photons. Stability of dark proton follows from the shadow baryon number conservation, as the stability of our proton is guaranteed by the conservation of our baryon number. On the other hand, the cosmological fraction of shadow dark matter should be related to the dark baryon asymmetry induced by the primordial baryogenesis mechanisms, similar to the popular mechanisms for the baryogenesis in the observable sector. Such type of dark matter is also known as asymmetric dark matter.

A mirror world was introduced some time ago by reasons related to parity conservation rather than purposes of explaining the dark matter. Standard Model particles respect rotation and translation symmetries, but do not respect parity (mirror reflection symmetry), in fact, only weak interactions breaks parity conservation. However, parity symmetry can be restored by assigning a mirror partner (right–handed) to every ordinary particle (left–handed) [148–150].

Thus, as far as our sector is described by the Standard Model SU(3)× SU(2)× U(1), all ordinary particles (electron e, proton p, neutron n, photon γ, neutrinos ν, etc.) should have mirror twins (e', p', n', γ', ν', etc.), which are sterile to our strong, weak and electromagnetic interactions but have instead their own gauge interactions SU(3)' × SU(2)' × U(1)' with exactly the same coupling constants.

Mirror matter is coupled gravitationally to ordinary matter, and then, it is a sound dark matter candidate as far as it is invisible, not being coupled through

strong, weak or electromagnetic interactions. Mirror world is expected to be very similar to ordinary world, being ruled by very similar physical laws. However, mirror matter was not considered as a serious candidate for dark matter for a long time [150] [151] [152]. In fact, the mirror world having the same temperature as the ordinary one, $T' = T$, is excluded by the BBN limits on the effective amount of light degrees of freedom: the contribution of mirror particles in the expansion rate of the Universe at the BBN epoch would be equivalent to the amount of extra neutrinos $\Delta N_{eff} = 6.15$, while at most $\Delta N_{eff} \simeq 0.5$ is allowed by the present constraints. On the other hand, once baryon asymmetry in the mirror sector is generated by the same physics as in the ordinary one, then the cosmological fractions of the mirror and ordinary baryons would be expected to be equal, $\Omega'_B = \Omega_B$. This would not be enough to explain the whole amount of dark matter. However, all problems can be settled assuming that, after inflation, both sectors were heated to different temperatures, and the temperature of the mirror sector, T', remained below that of the ordinary one, T, over all stages of the cosmological evolution [153]. This condition can be realized by adopting the following paradigm: at the end of inflation, ordinary and mirror sectors were (re)heated in an non–symmetric way, with $T > T'$. Then, both systems evolved almost adiabatically and the temperature asymmetry T'/T remained nearly invariant in all subsequent epochs until the present days.

In order to have a cosmologically plausible mirror dark matter, satisfying present BBN limits, the temperature ratio should be $T'/T \lesssim 0.5$, equivalent to $\Delta N_{eff} = 0.5$. It is worth noting that the stronger limit, $T'/T \lesssim 0.3$, comes from cosmological considerations, by requiring the early enough decoupling of mirror photons which makes mirror baryons practically indistinguishable from the canonic Cold Dark Matter (CDM) in observational tests related to the large scale structure formation and CMB anisotropies [153–157]. These limits apply independently whether mirror baryons constitute dark matter entirely, or only about 20% of the dark matter, which is the case corresponding to $\Omega'_B \simeq \Omega_B$ [155] [156]. In this case the remaining 80% of dark matter should be composed from other component, presumably some kind of dark matter represented by particles belonging to the so–called WIMP class candidates, axions or other sort of hidden gauge sectors with heavier *shadow* baryons [158–160] as in the case of asymmetric mirror matter [142], where it is assumed that mirror parity is spontaneously broken and the electroweak symmetry breaking scale in the mirror sector is much larger than that in the Standard Model.

Mirror matter can interact with ordinary matter via different portals, for exam-

ple, via *kinetic mixing* of mirror and ordinary photons, or mass mixing of mirror and ordinary pions or π-mesons. In the context of $G_{SM} \times G'_{SM}$ gauge factors, where ordinary particles belong to G and mirror particles to G', the kinetic mixing between gauge bosons, $\frac{\tilde{\epsilon}}{2} B^{\mu\nu} F'_{\mu\nu}$ is allowed. After the electroweak symmetry breaking, it transforms into photon–mirror photon kinetic mixing term with an effective coupling $\epsilon = \tilde{\epsilon} cos^2\theta_W$, where θ_W is the Weinberg angle. As far as both, ordinary and mirror photons, are massless, this mixing does not induce oscillation between them. However, it makes mirror particles mini–charged with respect to ordinary electromagnetic interactions: the mirror particles acquire electric charges ϵq. Generically, in this case dimensionless parameter ϵ could be of order 1. However, there are stringent experimental constraints on ϵ which come from the limits on ortopositronium oscillation into mirror ortopositronium [161] [162]. The latest limit on the experimental search points to $\epsilon < 4 \cdot 10^{-7}$ [163] while cosmological limits are even stronger [164]. Namely, the condition T'/T < 0.3 implies $\epsilon \lesssim 3 \cdot 10^{-9}$ [165].

As far as at the mirror BBN epoch the expansion rate of the Universe was dominated by ordinary matter density, the weak interaction's freezing in mirror sector occured earlier and frozen ratio of neutrons to protons was larger than in ordinary nucleosynthesis. As a result, primordial chemical content of the mirror sector was helium dominated, with ^{4}He' constituting up to 80% of mass fraction of mirror baryons in the limit $T'/T \to 0$ [153].

The primordial chemical content in mirror sector should also have larger metallicity that in ordinary one, but the primordial mass fraction of the heavier elements is anyway negligible. However, heavier elements should be produced in stars and thrown in the galaxy via supernova explosions in ordinary and mirror sectors. In ordinary sector, the chemical elements with A ~ 16 as oxygen, carbon, nitrogen and neon account for about a few per cent of mass fraction, and heavier elements are less abundant, accounting for about 4 per mille of mass fraction while in the mirror sector these proportions can be quite different (see table 1.2).

Experimental direct searches of dark matter should be concentrating on the detection of mirror helium as the most abundant mirror matter particles. In fact, the region of dark matter masses below 5 GeV is practically unexplored, although existing experimental indications favour light dark matter particles (see figure 1.13).

1.5.2.2 DAMA signal and mirror dark matter

In this study, the annual modulation observed by DAMA is analyzed in the framework of mirror dark matter, exploiting the interaction portal related to kinetic mixing $\frac{\epsilon}{2}F^{\mu\nu}F'_{\mu\nu}$ between the ordinary photon and mirror photon [166]. As mixing renders the mirror nuclei mini–charged with respect to ordinary electromagnetic force, it mediates the mirror atom scattering off the ordinary target nuclei, the Na and I nuclei at the DAMA/LIBRA detectors, with the Rutherford–like interaction cross sections [167] [168]. As mirror atoms have radii as large as the ordinary ones, at the recoil energies of the DAMA observed effect, the Rutherford scattering of the mirror nuclei off ordinary target ones is the leading order (with cross–section proportional to Z^2).

In this analysis, only scenarios compatible with the annual modulation phase experimentally measured by DAMA/LIBRA were studied (see section 1.5.1).

Isotope	(Z, A)	Mass fraction (%)	Atom fraction (%)
H	(1, 1)	70.57	91.0
He	(2, 4)	27.52	8.87
C	(6, 12)	0.30	0.032
N	(7, 14)	0.11	0.010
O	(8, 16)	0.59	0.048
Ne	(10, 20)	0.15	0.010
Si	(14, 28)	0.065	0.0030
Fe	(26, 56)	0.117	0.0027

Table 1.2: *Abundance of elements in the Solar System. From [169]*

Cosmological abundances of the mirror atoms are assigned directly rescaling from the abundances in ordinary sector, as shown in table 1.2. Table 1.3 shows the mirror matter abundances for three representative scenarios considered in this analysis.

Mirror Halo composition	H' (%)	He' (%)	C' (%)	O' (%)	Fe' (%)
H', He', Fe'	24.0	75.0	-	-	1.0
H', He', C', O'	12.5	75.0	7.0	5.5	-
H', He', C', O', Fe'	20.0	74.0	0.9	5.0	0.1

Table 1.3: *Halo compositions of the mirror dark matter scenarios considered in this analysis; the mass fraction of different mirror atoms is reported.*

In section 1.4.2.3 a simplified description of the dark matter halo has been considered, assuming it at rest in the galactic frame. There are many possible halo models. In this work, in the framework of a mirror symmetric dark matter model, dark matter particles are expected to form clouds and *bubbles* with diameter which could be even as the size of the Solar System. In this model, a dark halo, at the present epoch, could be crossing a region close to the Sun with an arbitrary velocity. Each *bubble* would be composed by dark atoms of different species having a Maxwellian velocity distribution in the frame where the halo is at rest. Assuming thermal equilibrium in a halo at temperature, T, the root mean square velocity of the j–type atom would be $v^2_{j,rms} = \frac{3KT}{m_j}$ where K is the Boltzmann constant and m_j if the mass of the j–type atom. In the following such local *bubbles* will be named simply as halo.

The annual modulation effect phase depends on the module of such a velocity and on the relative direction of the halo with respect to the Earth velocity, described by the angle α, $\cos\alpha = \hat{v}_E \cdot \hat{v}_{halo}$, where v_E is the velocity of the Earth in the galactic frame. When the velocity of the halo, v_{halo}, is anti–parallel to the velocity of the Earth ($\alpha \simeq \pi$) the phase of the annual modulation is June 2^{nd} for any module of v_{halo}. For parallel halo velocity ($\alpha \simeq 0$) depending whether or not v_{halo} is larger than v_S the phase of annual modulation can be even reversed.

1.5.2.3 Analysis procedures

In this study, a fraction, f, of the dark matter halo in the galaxy is assumed to be composed by mirror atoms of various species and two type of temperature regimes are considered, a cold one (T$\simeq 10^4 - 10^5 K$) and a hot one ((T$\gtrsim 10^6 - 10^8 K$). The direction of the velocity of the halo with respect to the velocity of the Sun changes the phase of the annual modulation, and thus a detailed study of the behaviour of

the phase as a function of the velocity of the halo in the galactic frame has been made.

Some discrete cases have been considered to account for the uncertainties on the measured quenching factors and on the parameters used in the nuclear form factors (referred as set A, see [147] for more scenarios). Results presented here are obtained by considering the mean values of the parameters of the used nuclear form factors and quenching factors from [10].

Data analysis in the considered mirror dark matter framework model allows the determination of the range of the $\sqrt{f}\epsilon$ parameter compatible with the observed annual modulation in DAMA/LIBRA experiment for the different scenarios. The allowed regions for dark matter can be calculated by comparing (in 1 keV energy bins from 2 to 4 keV) the measured dark matter annual modulation amplitude $S^{exp}_{m,k}$ with the expectation in the considered scenario $S^{th}_{m,k}$. In this procedure it must be taken into account that the measured counting rate in the cumulative energy spectrum (given by the sum of the constant background contribution, b_k, and $S_{0,k}$) is $\sim$ 1 count/(keV kg day) in the lowest energy bins; but, as discussed e.g. in [170], the constant background, b_k, is estimated to be not lower than $\sim$ 0.75 counts/(keV kg day) in the 2–4 keV energy region; thus, an upper limit on S_0 of $\sim$ 0.25 counts/(keV kg day), $S_{0,max}$, is derived. In order to compare the expectations with the experimental results, the χ^2 quantity can be computed as:

$$\chi^2 = \sum \frac{(S^{exp}_{m,k} - S^{th}_{m,k})^2}{\sigma_k^2} + \frac{(S_{0,max} - S^{th}_{0,2-4})^2}{\sigma^2_{2-4}} \Theta(S^{th}_{0,2-4} - S_{0,max}) \tag{1.25}$$

where σ_k is the error associated to the modulation amplitudes in the k–th energy bin determined from the annual modulation independent analysis and the second term encodes the experimental bound about the unmodulated part of the signal, Θ is the Heaviside function, $S^{th}_{0,2-4}$ is the average expected signal counting rate in the (2–4) keV energy interval and $\sigma_{2-4} \simeq 10^{-3}$ counts/(keV kg day).

In the mirror dark matter model considered in this study, the χ^2 quantity is a function of only one parameter, $\sqrt{f}\epsilon$, thus:

$$\Delta\chi^2\{\sqrt{f}\epsilon\} = \chi^2\{\sqrt{f}\epsilon\} - \chi^2\{\sqrt{f}\epsilon = 0\} \tag{1.26}$$

where $\Delta\chi^2$ follows a χ^2 distribution with one degree of freedom and can be used to determine the allowed interval for the $\sqrt{f}\epsilon$ parameter at 5σ from the *null signal*

hypothesis.

In case of low mass dark matter particles producing nuclear recoils it is also necessary to account for the Migdal effect; this effect is known since long time and is described in [171] [172]. It consists in the ionization and the excitation of bound atomic electrons induced by the presence of a recoiling atomic nucleus. In the case of mirror nuclei interacting with the target nuclei the recoiling nucleus can *shake off* some of the atomic electrons, and an electromagnetic contribution is present together with a recoil signal. Since this contribution is not quenched, this part could play a role, mainly when low mass dark matter candidates are considered; however, in the present case of mirror matter, only second order corrections (of an order not exceeding 10% on the expected counting rate) are foreseen when the Migdal effect is accounted for.

Another important issue to take into consideration is the *channeling* effect of low energy ions along axes and planes of the NaI(Tl) crystals. The channeling effect in crystals implies that a fraction of nuclear recoils are channeled producing a much larger ionization signal than that expected if quenching factors derived from neutron calibrations are taken into account. Since the channeling effect cannot be generally pointed out with neutron measurements [173], only modeling can be considered. Although some amount of blocking effect could be present, because of the difficulties of experimental measurements and of theoretical estimate of this channeling effect, in the following it will be either included or not in order to give idea on the related uncertainty.

Table 1.4 summarizes all the scenarios considered when analysing DAMA/LIBRA experiment data in the symmetric mirror dark matter framework.

1.5.2.4 Results

Some results obtained in this study with the different scenarios presented are shown here. The constant part of the signal and the annual modulation amplitude evaluated under different assumptions are depicted in figures 1.20 and 1.21, respectively. Figures 1.22 to 1.25 show the allowed regions of the $\sqrt{f}\epsilon$ parameter as a function of the temperature and the halo velocity, considering different scenarios.

Scenario	Quenching factor	Channeling	Migdal
a	[4]	no	no
b	[4]	yes	no
c	[4]	no	yes
d	[92]	no	no
e	[92]–normalized	no	no

Table 1.4: *Summary of the scenarios considered when analysing DAMA/LIBRA experiment data in the symmetric mirror dark matter framework (from [147]).*

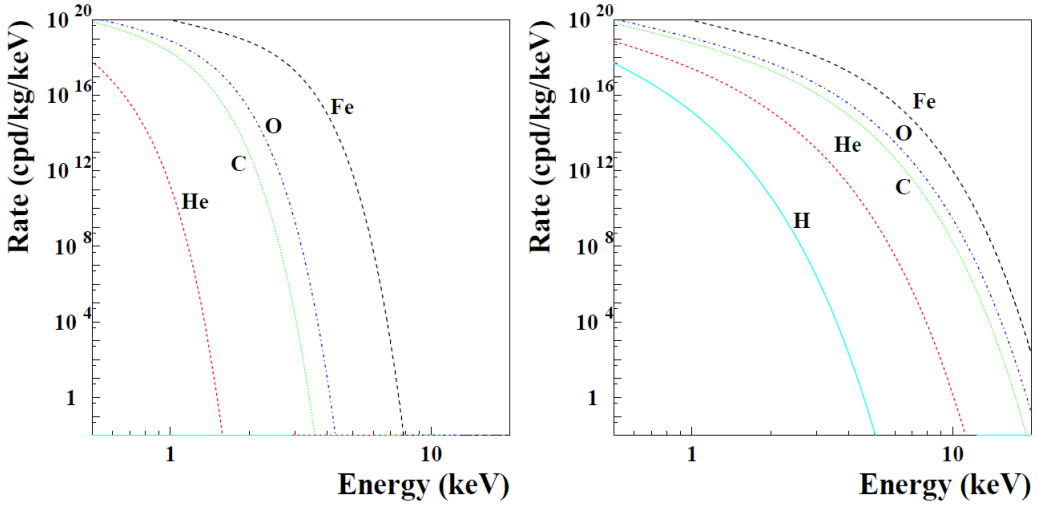

Figure 1.20: *Annually averaged event rate expected for different mirror atoms in a NaI(Tl) detector, considering* $\sqrt{f}\epsilon = 1$*. Two cases are shown here: a cold halo* ($T \sim 10^4$ *K) (left) and hot halo* ($T \sim 10^7$ *K) (right) with* $v_{halo} = 100$ *km/s. The considered scenario is the case (a) of table 1.4 in set A. From [147].*

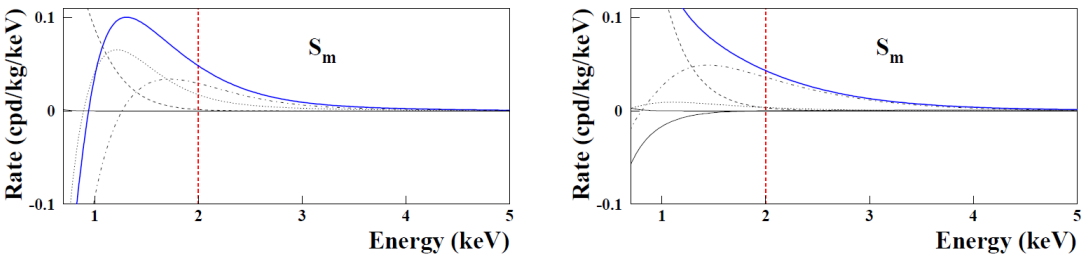

Figure 1.21: *Examples of expected modulation amplitude of the signal, S_m, for the mirror dark matter candidates in the scenario (a) of table 1.4, for two different halo models. Left: composite dark halo: H'(12.5%), He'(75%), C'(7%), O'(5.5%), with halo velocity v_{halo} = 30 km/s, temperature $T = 10^6$ K, v_0 = 220 km/s and parameters in set A. The contributions to the signal (blue line) of the different dark atoms are depicted: H' (not visible), He' (dashed), C' (dotted), O' (dashed–dotted). Right: composite dark halo: H'(20%), He'(74%), C'(0.9%), O'(5%), Fe'(0.1%), with halo velocity v_{halo} = 0 km/s and temperature $T = 10^7$ K, v_0 = 220 km/s and parameters in set A. The contributions to the signal (blue line) of the different dark atoms are depicted: H' (solid line), He' (dotted), C' (dashed), O' (dashed–dotted), Fe' (solid, with tail above 3 keV). From [147].*

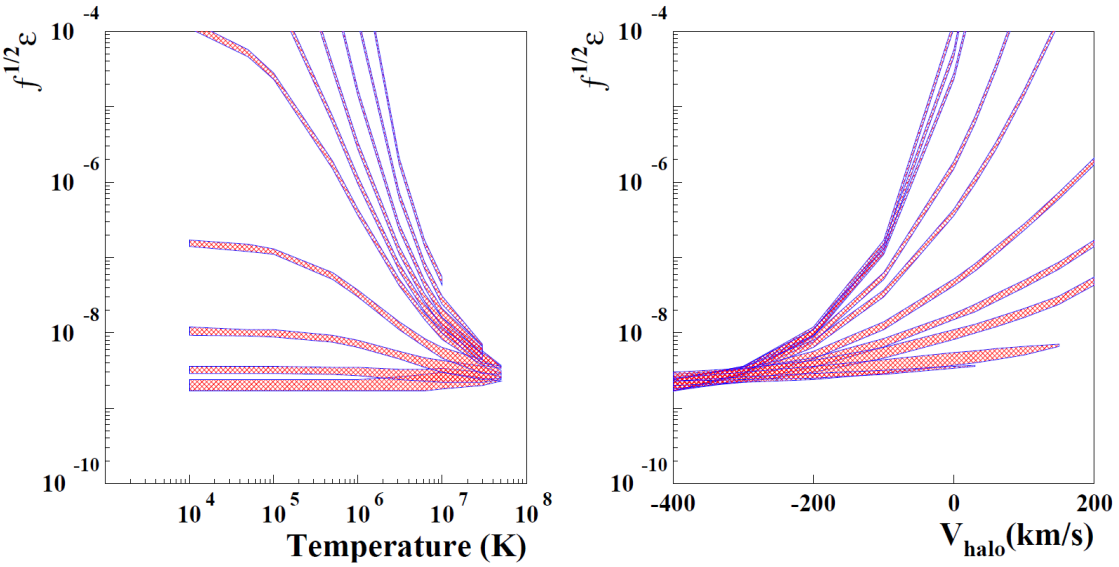

Figure 1.22: *Halo composed by pure He' dark atoms in the scenario (a) of table 1.4 with v_0 = 220 km/s and parameters in set A. Left: allowed regions for the $\sqrt{f}\epsilon$ parameter as function of the halo temperature for different values of the velocity of the halo in the galactic frame; when increasing the halo velocity from -400 km/s to 300 km/s the allowed regions e.g. at a fixed temperature of 10^4 K move to higher values of $\sqrt{f}\epsilon$ parameter. Right: allowed regions for the $\sqrt{f}\epsilon$ parameter as function of the velocity of the halo in the galactic frame for different halo temperatures. The considered temperatures spam in the range 10^4 – 10^8 K; when increasing the temperature the allowed region at large positive v_{halo} move to smaller values of $\sqrt{f}\epsilon$ parameter. These allowed intervals identify the $\sqrt{f}\epsilon$ values corresponding to C.L. larger than 5σ from the null annual modulation hypothesis, that is $\sqrt{f}\epsilon = 0$. From [147].*

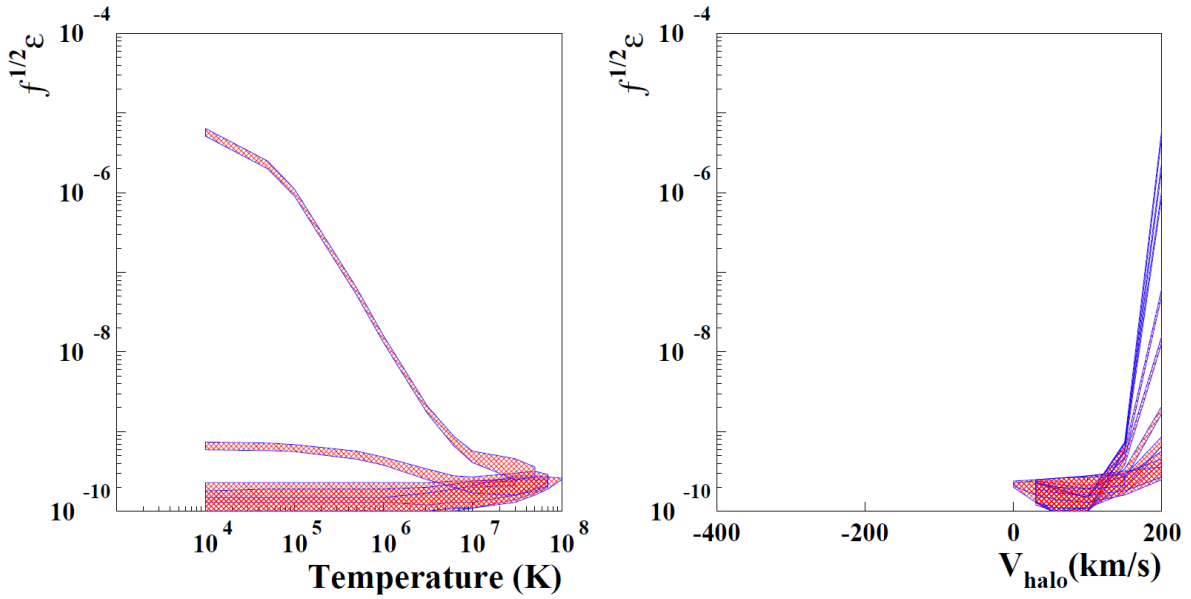

Figure 1.23: *As figure 1.22, but for a halo composed by pure Fe' dark atoms. From [147].*

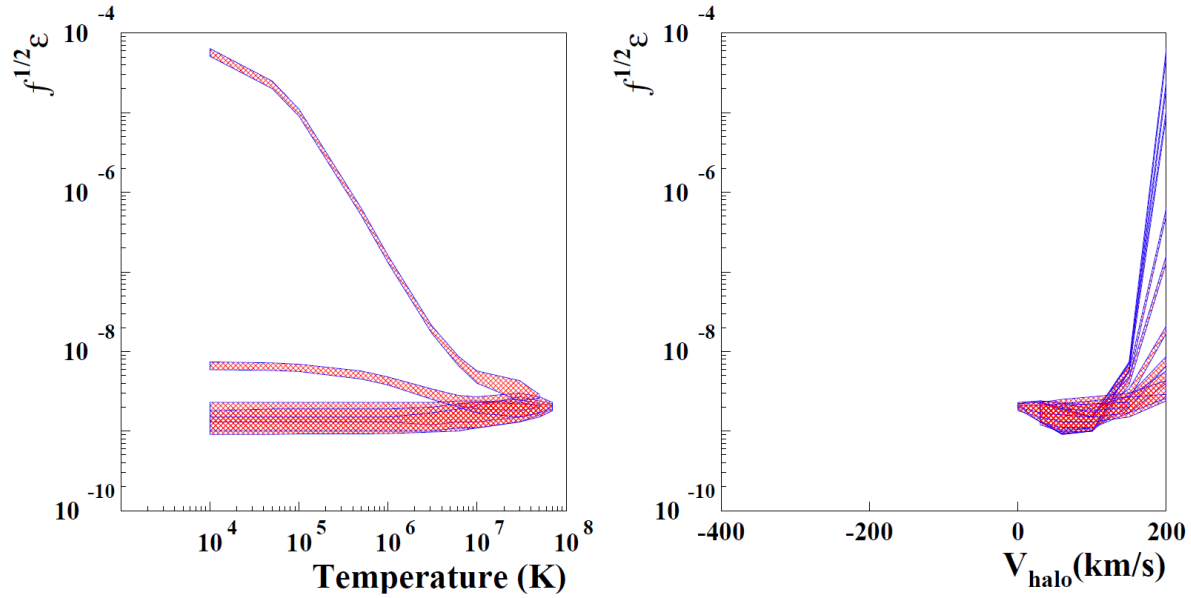

Figure 1.24: *As figure 1.22, but for a halo composed of H'(24%), He'(75%) and Fe'(1%). From [147].*

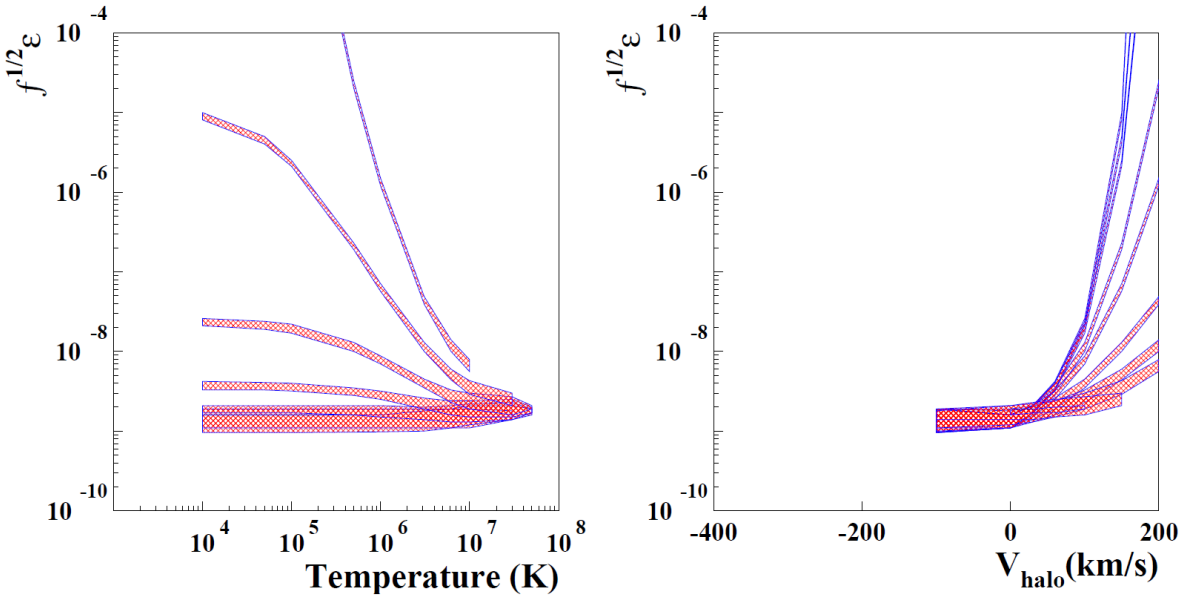

Figure 1.25: *As figure 1.20, but for a halo composed of H'(12.5%), He'(75%), C'(7%) and O'(5.5%). From [147].*

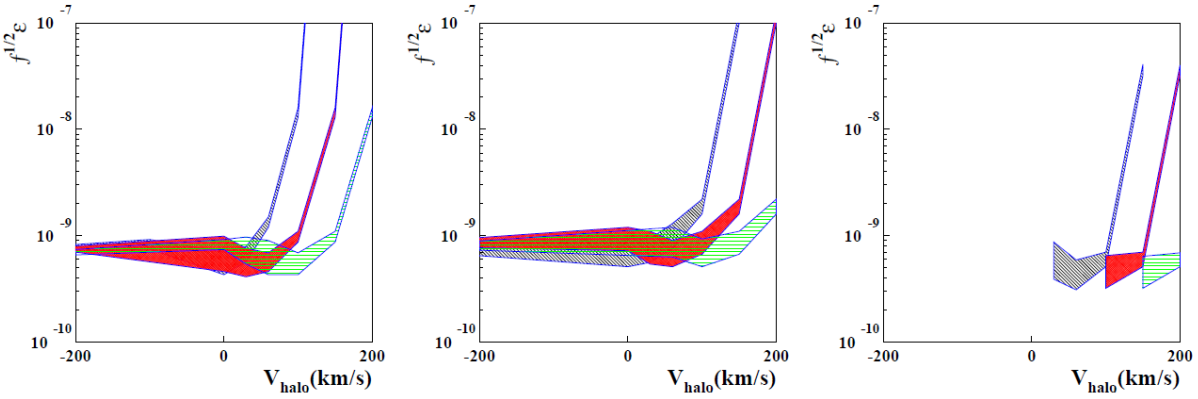

Figure 1.26: *Allowed regions for the $\sqrt{f}\epsilon$ parameter as function of v_{halo}. The three graphs refer to different dark halo compositions with the same temperature $T = 10^4$ K, the same set A and the same scenario (d): Left: composite dark halo H'(12.5%), He'(75%), C'(7%), O'(5.5%). Center: composite dark halo H'(20%), He'(74%), C'(0.9%), O'(5%), Fe'(0.1%). Right: composite dark halo H'(24%), He'(75%), Fe'(1%). The three contours in each plot correspond to $v_0 = 170$ km/s (area with diagonal lines, gray area on–line), $v_0 = 220$ km/s (shaded area, red area on–line), $v_0 = 270$ km/s (area with diagonal lines, gray area on–line), respectively. From [147].*

Figure 1.26 shows the allowed regions for the $\sqrt{f}\epsilon$ parameter as a function of the halo temperature for three different v_0 values considering different dark halo compositions. Only for low temperature halos the v_0 parameter has an impact on the allowed regions.

In the analysis, the fact that a fraction, f, of the dark matter halo in the Milky Way is composed by mirror atoms of various species has been assumed and allowed physical intervals for the parameter $\sqrt{f}\epsilon$ in different scenarios have been derived. It is worth noting that some of the existing uncertainties (in particular those corresponding to quenching factors, channeling and Migdal effect) have been taken into account.

From this study, it can be concluded that the mirror matter model is well compatible with the model–independent annual modulation effect observed by the DAMA/LIBRA collaboration using 250 kg NaI(Tl). Results demonstrate that different halo models (composition, temperature, etc.) and experimental parameters choices reproduce the DAMA annual modulation effect for $\sqrt{f}\epsilon$ values compatible with cosmological bounds.

Chapter 2

The ANAIS experiment

The ANAIS (Annual modulation with NaI(Tl) Scintillators) experiment aims at the confirmation, in a model-independent way, of the DAMA/LIBRA annual modulation signal using the same target and technique at the LSC, in Spain. The smallness of this effect ($< 10\%$ of the total signal) makes necessary to accumulate as much statistics as possible, combining both, long exposure and large detection mass. The initial design of ANAIS full experiment consisted of 250 kg of ultrapure NaI(Tl) crystals in a 5×4 matrix. However, the increase in the price of the crystals, due to improvements made by the manufacturer company (see section 2.3.1) in order to reach the ANAIS radiopurity level target, led the Zaragoza group to find the optimum configuration, with less NaI(Tl) mass, that could satisfy ANAIS goals. The evolution of the results of the different prototypes, improvement of the energy threshold and background understanding, presented in this memory, led the experiment to its present design: 112.5 kg of ultrapure NaI(Tl) crystals in a 3×3 matrix configuration.

In this chapter, the goals and experimental requirements of ANAIS will be described (section 2.1) as well as previous prototypes (section 2.2), all the elements of the experimental set–up like crystals and photomultipliers, electronics and data acquisition, slow control or the muon veto system (sections 2.3 to 2.8), the set–ups already operated at LSC (section 2.9) and the general detector performance (section 2.10).

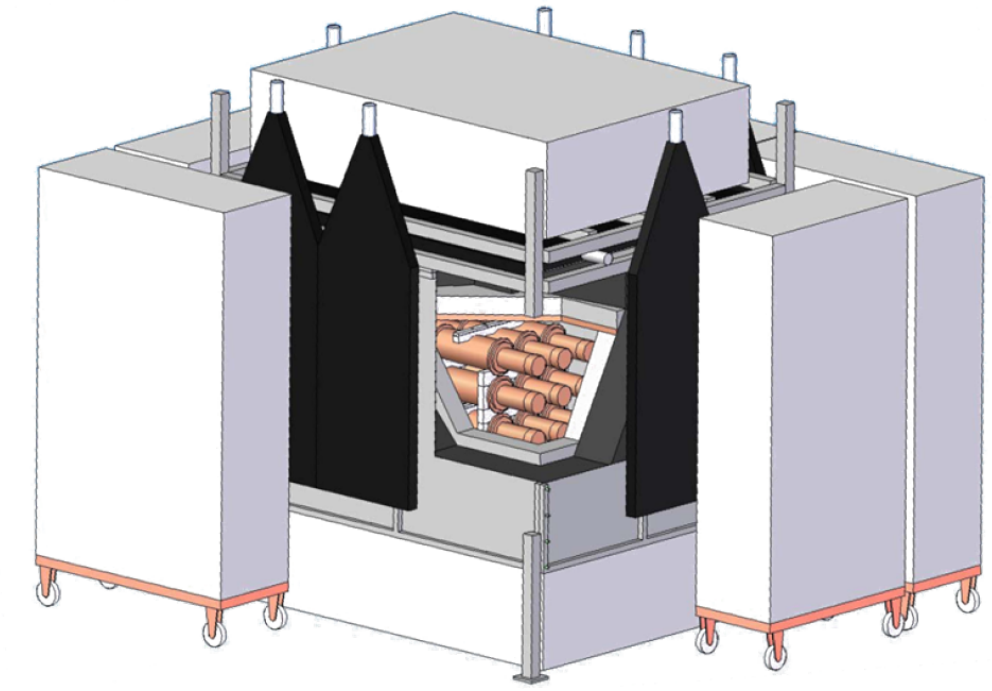

Figure 2.1: *Artistic view of the ANAIS experimental set-up.*

2.1 ANAIS goals and experimental requirements

An experiment devoted to the search of the dark matter annual modulation must fulfill a few requirements in order to achieve its goal, according to the properties of the searched signal. As it is expected to appear in the very low energy region and it is very small, an energy threshold as low as possible is desirable and any background that could mask it must be reduced. Large exposure time and stability are also an important issue in order to have enough statistical significance in a search for a seasonal variation.

2.1.1 Energy threshold

WIMPs are expected to produce nuclear recoils in I and Na nuclei below about 100 keV, depending on the WIMP mass, but the visible energy is even lower (see section 1.4.2). The energy threshold depends on experimental aspects as the light collection efficiency (that depends on the optical quality of the crystal, the light collection sytem of the modules, and the quantum efficiency of the photomultipli-

ers) and the trigger level. Due to the nature of the low energy events (consisting on few separate photons), triggering strategy is very important as it has to ensure the acquisition of all relevant events. The first triggering step is then to trigger each PMT signal at photoelectron level, in order to allow a high trigger efficiency for very low energy events. In a second step, since dark events would dominate the trigger rate, they have to be prevented by triggering each module in logical AND mode between the two PMTs signals. Moreover, robust noise filtering protocols are mandatory in order to guarantee the quality of low energy events. ANAIS goal is to reach an energy threshold at or below 2 keVee.

2.1.2 Background in the region of interest

The rate of interaction between dark and ordinary matter is low and the annual modulation is expected to be less than a 10% of the total dark matter rate, but in a much lower percentage of the total events rate if other backgrounds are present in the region of interest. The expected modulation amplitude, according to DAMA/LIBRA result (see section 1.5) is of the order of 0.05 counts/(keV kg day) above 1 keVee [174]. This is the reason why background in this range of energies must be kept as low as possible; rates at or below a few counts/(keV kg day) are necessary below 10 keVee in ANAIS detectors. Special care has to be taken with the radiopurity of the NaI(Tl) crystal itself. For example, isotopes ^{40}K and ^{22}Na in NaI(Tl) crystals were identified to be specially harmful for dark matter search experiments as they produce a line at 3.2 keV and 0.9 keV, respectively, corresponding to the K–shell electron binding energy released following EC, and falling in the region of interest for the annual modulation analysis [32].

Besides internal, external contaminations have to be also under control. For that, a passive shield made of lead (20 cm of low activity lead and 10 cm of archaeological lead in the inner part) together with a 40–cm–thick neutron moderator made of boron–loaded water and polyethylene will be installed for ANAIS. A sealed anti–radon box with continuous boil–off nitrogen flux will also contribute to avoid the entrance of airborne radon inside the set–up. By installing ANAIS at the LSC, under 2450 m.w.e. (meter water equivalent), cosmic radiation is suppressed although a residual muon flux still survives and could be able to induce neutrons and other particles that could contribute to the background in the region of interest. Therefore, plastic scintillators placed on the top and lateral faces of the set–up will act as

active vetoes to tag muon interactions in the detectors and shielding, allowing the removal of related events (see figure 2.1).

2.1.3 Stability and exposure maximization

Due to the fact that ANAIS searches for the dark matter annual modulation and thus, measurements of various cycles will be performed, stability is one of the main requirements for the experiment. Consequently, in order to detect any anomalous behaviour or seasonal variation that could affect to the gain, threshold, background, or trigger efficiency of the experiment, as many parameters as possible must be controlled. A slow–control system was designed in order to monitor these parameters (see section 2.7).

Once the target mass is fixed, the exposure of the experiment is set by the effective measurement time, the *live time*. The system has to maintain as low as possible the *dead time* after each event, while the system is not able to record another event due to different reasons. Both times should be precisely known. In present ANAIS acquisition system both are determined by using specific counters (see [31]).

2.2 Previous prototypes and ANAIS set–ups

Along the years at the Zaragoza University group, experience has been acquired from the tests with different prototypes for ANAIS. NaI32 experiment, carried out at the LSC, was the precursor of ANAIS. It was operating for two years and consisted of three BICRON hexagonal NaI detectors with a total mass of 32.1 kg. No positive signal was found in the first published results in the search for the annual modulation effect but bounds to WIMP mass and cross–section were established [7] [8] [175].

Later, one of the NaI32 detectors was used as ANAIS Prototype–I [176] and after decoupling the photomultiplier and removing the original encapsulation, the crystal was used to build ANAIS Prototype–II and Prototype–III [133]. The main purposes of these prototypes were the implementation of pulse shape discrimination techniques, the optimization of light collection, and testing of different PMT models, together with the measurement of the potassium content of the bulk crystal. After dedicated measurements, all the available BICRON crystals were found to have too high potassium content (at the level of 0.5 ppm [25]) as well as a high

^{210}Pb contamination for a dark matter search experiment and thus, were disregarded.

ANAIS–0 set–up (see figure 2.2) consisted of a NaI(Tl) ultrapure crystal of 9.6 kg, made by Saint-Gobain and encapsulated in OFHC copper in the University of Zaragoza. It had the same size and shape as those of DAMA/LIBRA [137] and was designed to characterize and fully understand the background at low energy, optimize NaI scintillation events selection, to determine the calibration method and test the electronics. Although it presented a much lower level of ^{210}Pb than BICRON crystals, its high potassium content, at the same level than that found in the latter [25], was again the reason why it was disregarded.

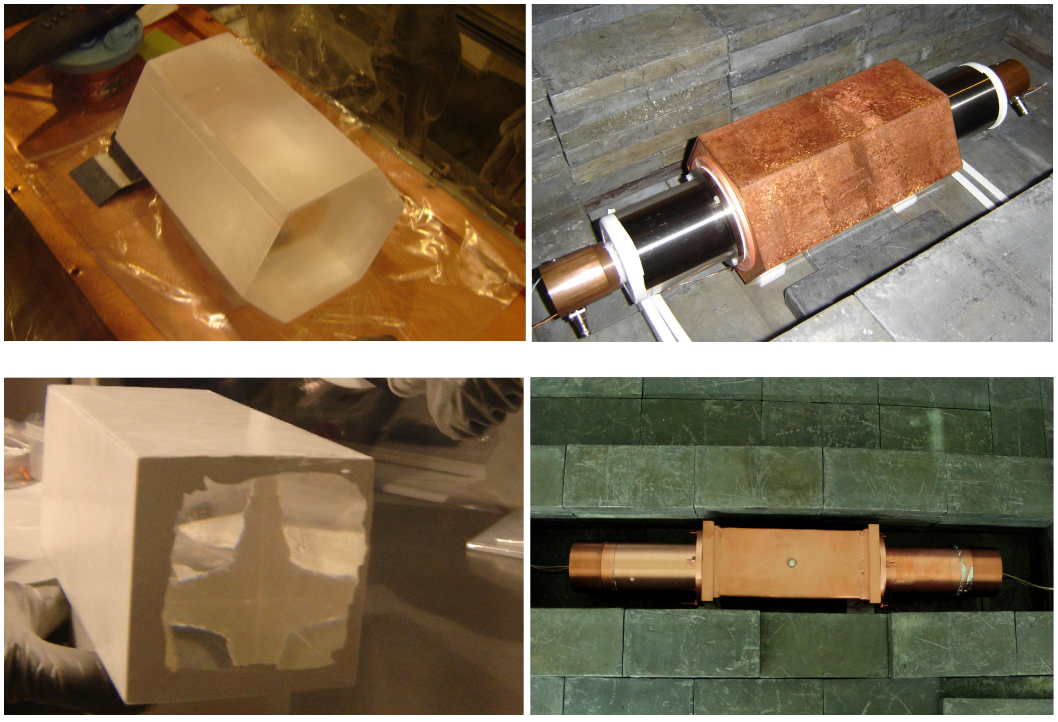

Figure 2.2: *Nude NaI(Tl) crystals (left) and detectors in set-up (right) for BICRON (top) and ANAIS–0 prototypes (bottom).*

Backgrounds at low, medium and high energy were quite well understood for ANAIS–0 prototype [24], very slow scintillation in NaI(Tl) [26] or an anomalous fast event population attributable to quartz scintillation [28] were studied, and the bulk NaI(Tl) scintillation low energy events selection procedure was proposed and tested [27]. Other technical aspects of the set–up and data taking system were established to be used in next ANAIS prototypes.

2.3 NaI(Tl) crystals

As pointed out in section 1.4.2.2, scintillators are one of the detector types used in direct dark matter detection experiments. Choosing the scintillator material for a direct dark matter search is very important. This material must fulfill a few properties:

- It should convert the kinetic energy of the nuclear recoil into visible light with a high scintillation efficiency to be easily detectable.
- It should have a scintillation time as fast as possible.
- It should have good optical quality and the medium should be transparent to the emitted wavelength.
- It should behave linearly with the deposited energy.
- It would be also desirable that the scintillator emission band would overlap appropriately with the quantum efficiency peak of the PMTs.

The two most commonly used types of scintillator materials are inorganic crystals and organic-based liquid and plastic scintillators, although there exist other kind of materials used in dark matter experiments, as liquids of noble gases (see section 1.4.2.2) which are also proficient scintillators. The scintillation mechanism is different for each type.

Organic material scintillators have a faster response compared to that of the inorganic ones but have a lower light yield. In organic scintillators the radiative transitions can be observed independently of the material physical state because they arise from the energy level structure of a single molecule. In ANAIS, the muon vetoes surrounding the shielding consist of plastic organic scintillators, and are used to tag muons.

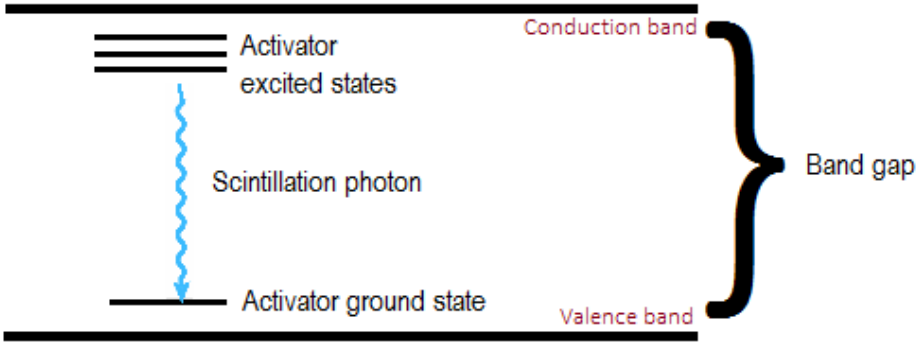

Figure 2.3: *Energy band structure of an inorganic activated crystalline scintillator.*

In inorganic materials, the scintillation mechanism usually depends on the existence of radiative decays of some of the states in the gap of the crystal band structure, which can be filled by excited electrons from the valence band after energy depositions from charged particles in the material, not being the recombination of the electron–hole pairs with emission of a photon the dominant process for energy relaxation in most of the materials. Only a few photons are released by this mechanism and band gap widths in pure crystals are such that the emitted photons are too energetic to lie within the visible range. Therefore, this type of materials is usually doped with small amounts of impurities, called activators (see figure 2.3), in order to enhance the probability of UV–visible photon emission during the de–excitation process. These activators create special sites within the forbidden gap modifying the normal band structure of the pure crystal. Electrons can de–excite back to the valence band emitting photons with a wide range of half–lives from 10^{-9} to 10^{-7} s.

The most widely used scintillator materials are inorganic alkali halide crystals, as NaI. This material presents an excellent light output and good linearity but the response is slower than that of the organic scintillators. In the case of NaI Thallium is usually added as activator. Fine–tuning of Tl concentration is able to achieve high light yield, while preserving high transparency to its own light emission, because photons produced in the decay of the activator excited state are not absorbed by electrons in the valence band. The spectral distribution of the scintillation photons in NaI(Tl) has its maximum around 410 nm [177].

NaI(Tl) scintillators have been widely used in gamma spectrometry field. The disadvantages of NaI(Tl) are its long scintillation decay time (230 ns), its fragility and its highly hygroscopic nature that requires a tight encapsulation.

2.3.1 Alpha Spectra NaI(Tl) crystals

After disregarding BICRON and Saint–Gobain crystals because of the high potassium content (see section 2.2), for the final ANAIS design, several providers of purified NaI were contacted in order to find a crystal that would fulfill the requirements of ANAIS [32].

Alpha Spectra, Inc.[29] in the United States provided a NaI powder sample compatible with the potassium required content (having <90 ppb, following the measurements at LSC with HPGe [25]) and therefore, two 12.5 kg NaI crystals were grown with that powder and installed for testing in the ANAIS–25 set-up [178] (see section 2.9).

Alpha Spectra (AS) crystals (see figure 2.4) are cylindrical, 4.75" diameter and 11.75" length. They are housed in OFE copper, with two synthetic quartz windows for PMTs coupling at LSC clean room in a second step. Very low energy calibration can be performed thanks to a Mylar window in the lateral face of each module.

Figure 2.4: *ANAIS–25 NaI(Tl) crystals prepared for encapsulation. Courtesy of Alpha Spectra Inc.*

2.4 Photomultipliers

Photomultiplier tubes, are extremely sensitive detectors of light in the ultraviolet, visible, and near–infrared ranges of the electromagnetic spectrum. Photomultipliers are typically constructed with an evacuated glass housing, with an input window, a photocathode with a sensitive layer, several electron multipliers (dynodes), focusing electrodes and an anode.

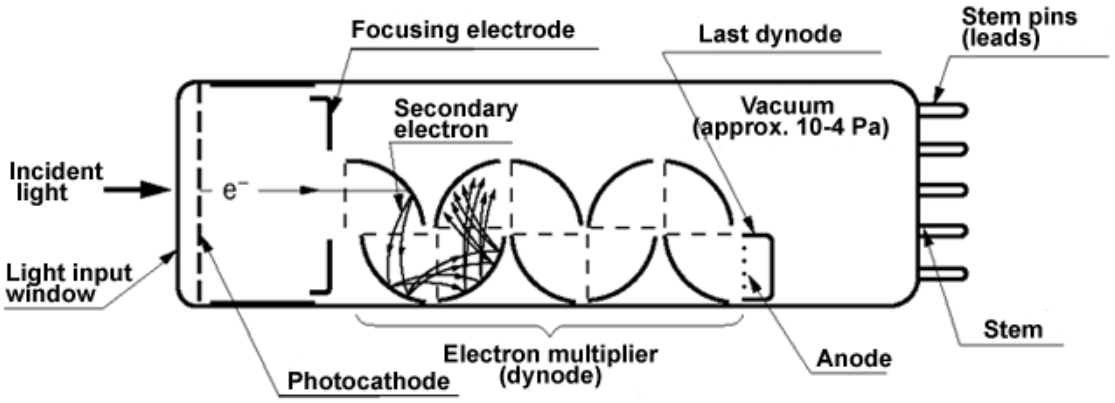

Figure 2.5: *Photomultiplier operating method scheme. From [179].*

Photomultipliers convert the incident light into a measurable electrical signal (see figure 2.5). Light passes through the input window and excites the photocathode, consequently, and depending on the quantum efficiency of the tube, photoelectrons are emitted into the vacuum via photoelectric effect. Then, photoelectrons are accelerated in the vacuum and focused by an electric field onto the first dynode. Electron multiplication is then achieved by repeating this process at each dynode, biased through a HV divider circuit, and charge is finally collected usually in the last dynode.

There are different types of PMTs depending on the photocathode type and the geometric disposition and number of dynodes. In order to guarantee a correct operation of a photomultiplier tube, a stable high voltage supply is crucial to bias the dynodes in order to have an stable gain, a good housing system to shield the photomultiplier from external light and avoid electromagnetic interferences (that could deviate the electron cloud and affect the gain) and a proper signal processing set–up.

Photomultipliers require a previous characterization to test the following parameters:

- **Quantum efficiency:** It is the ratio between photoelectrons produced and incident photons at photocathode. It is dependent on the wavelength of the incident photons and photocathode material.
- **Gain:** It is the final number of collected electrons for each produced photoelectron in the photocathode.
- **Rise time:** It quantifies the time for going from 10% to 90% of a single photoelectron signal.
- **Transit time:** It is the time interval from the arrival of light to photocathode and the appearance of the output signal in the anode.
- **Dark current:** It is the rate of dark events produced without light excitation of the photocathode.
- **Single electron response (SER):** It is the output signal produced by a single photoelectron.

In ANAIS, low background PMTs, made of radiopure materials, are required in order to minimize their contribution to the background of the experiment. Low dark rate of the PMT is also important, otherwise it would lead to undesired high trigger rate, increasing dead time and making more difficult data analysis and selection of real bulk scintillation events in the NaI(Tl).

Hamamatsu R12669SEL2 PMT model, previously R6956MOD (see table 2.1), was selected for ANAIS. This model conveniently covers all the previously listed requirements. It has a Bialkali photocathode, high quantum efficiency (>33%), a maximal response at 420 nm, dark current below 500 Hz, ten dynode stages and a gain factor of 10^6 at the nominal voltage value.

42 units of Hamamatsu R12669SEL2 (see figure 2.6) were received at LSC and soon tested by HPGe spectroscopy to verify the radiopurity levels and the homogeneity of all the units (see table 2.2). For most of the units, SER, gain, relative quantum efficiency and dark rate were measured in the University of Zaragoza. A dedicated set–up was prepared to characterize all the PMTs. A periodically pulsed ultraviolet LED was used as light source and trigger for a MATACQ digitizer based acquisition (more information on details and results in [31]).

	Hamamatsu R12669SEL2
Characteristics:	
Diameter	3”
Spectral response	300–650 nm
λ of max. response	420 nm
Photocathode material	Bialkali
Photocathode min. effective	70 mm
Dynode structure	Box–and–grid + Linear focused
Number of stages	10
Operating ambient T	–30/+50°C
Max. supply voltage	1500 V
Max. avg anode current	0.1 mA
Characteristics at 25°C:	
Cathode luminous sens.	10 μA/lm
Quantum efficiency at peak	>33%
Anode luminous sens.	100 A/lm
Gain	10^6
Anode dark current (max.)	6 (60) nA
Dark current rate	<500 Hz
Anode pulse rise time	9.5 ns
Electron transit time T	60 ns
Transit time spread	13 ns
Pulse linearity	30 ($\pm$ 2 %) mA

Table 2.1: *Hamamatsu R12669SEL2 technical data.*

A good knowledge of the PMTs response with low light intensity is essential to understand the scintillation signal in the very low energy region. Particularly, a characterization of the SER allows to understand the most elementary PMT signal.

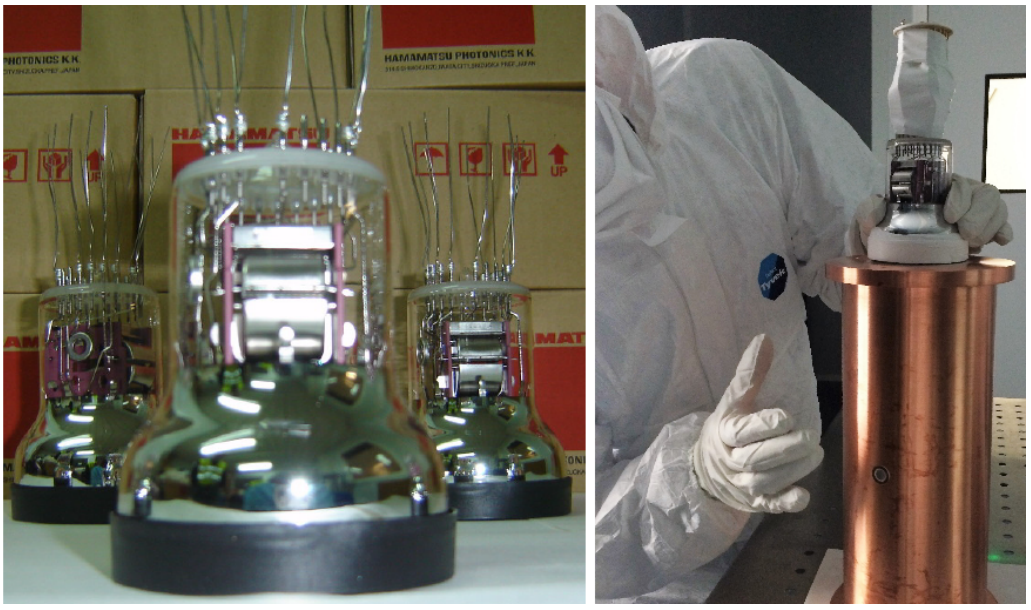

Figure 2.6: *Left: Hamamatsu R12669SEL2 photomultipliers. Right: Coupling the PMT to D3 module at LSC clean room.*

Pulses corresponding to single photoelectrons were obtained by sending a very small amount of light produced by an UV–LED in the before mentioned testbench (see figure 2.7). Trigger was done by the LED excitation and light filters were used to attenuate the light emission until the average number of photoelectrons per event seen by the PMT was very low (in the particular case shown in figure 2.8, less than 0.04). Hence, the contribution of two or more photoelectrons in the output signal can be taken as negligible.

SER pulse area distribution is fitted, taking also in consideration the population of events for which no light reached the PMT, to two Gaussian functions (parameters resulting of the fit are also shown, for example, in figure 2.8).

By increasing the light received at the PMT, the PMT signal can be modelled as addition of the response functions for one, two, three, and more photoelectrons.

Model	Reference	^{232}Th (mBq/PMT)	^{238}U (mBq/PMT)	^{262}Ra (mBq/PMT)	^{40}K (mBq/PMT)
R6959MOD	ZK5902	20 ± 2	128 ± 38	84 ± 3	97 ± 19
R6959MOD	ZK908	20 ± 2	150 ± 34	88 ± 3	133 ± 13
R12669SEL2	FA0010	18 ± 2	77 ± 42	78 ± 4	113 ± 18
R12669SEL2	FA0016	18 ± 2	179 ± 51	83 ± 4	123 ± 20
R12669SEL2	FA0018	21 ± 3	161 ± 58	79 ± 5	108 ± 29
R12669SEL2	FA0020	25 ± 4	260 ± 84	77 ± 6	95 ± 36
R12669SEL2	FA0022	18 ± 2	158 ± 53	77 ± 4	93 ± 19
R12669SEL2	FA0034	20 ± 2	144 ± 33	89 ± 5	155 ± 36
R12669SEL2	FA0035	22 ± 2	148 ± 29	79 ± 4	79 ± 14
R12669SEL2	FA0036	16 ± 2	139 ± 31	71 ± 4	95 ± 27
R12669SEL2	FA0037	19 ± 2	170 ± 37	78 ± 5	123 ± 32
R12669SEL2	FA0051	19 ± 2	133 ± 52	89 ± 4	94 ± 16
R12669SEL2	FA0053	25 ± 2	114 ± 29	87 ± 4	132 ± 19
R12669SEL2	FA0057	19 ± 2	153 ± 25	82 ± 3	128 ± 23
R12669SEL2	FA0058	22 ± 2	168 ± 31	84 ± 4	118 ± 27
R12669SEL2	FA0059	26 ± 2	171 ± 32	85 ± 4	104 ± 24
R12669SEL2	FA0060	22 ± 2	145 ± 29	88 ± 4	95 ± 24
R12669SEL2	FA0064	21 ± 2	180 ± 34	85 ± 4	131 ± 31
R12669SEL2	FA0066	19 ± 2	156 ± 31	82 ± 4	117 ± 29
R12669SEL2	FA0068	18 ± 2	185 ± 29	81 ± 4	138 ± 25
R12669SEL2	FA0069	18 ± 2	159 ± 29	79 ± 3	105 ± 15
R12669SEL2	FA0070	21 ± 2	127 ± 30	82 ± 4	103 ± 20
R12669SEL2	FA0072	27 ± 3	172 ± 35	91 ± 4	91 ± 27
R12669SEL2	FA0073	22 ± 2	181 ± 31	78 ± 4	112 ± 25
R12669SEL2	FA0074	20 ± 2	252 ± 61	73 ± 3	89 ± 21
R12669SEL2	FA0076	17 ± 2	234 ± 65	79 ± 3	88 ± 22
R12669SEL2	FA0081	21 ± 2	162 ± 31	87 ± 4	98 ± 24
R12669SEL2	FA0086	19 ± 2	300 ± 70	59 ± 3	104 ± 25
R12669SEL2	FA0088	26 ± 2	241 ± 46	64 ± 2	137 ± 19
R12669SEL2	FA0090	18 ± 2	187 ± 58	59 ± 3	136 ± 26
R12669SEL2	FA0094	18 ± 2	233 ± 60	55 ± 3	102 ± 23
R12669SEL2	FA0093	22 ± 1	209 ± 37	63 ± 2	153 ± 16
R12669SEL2	FA0099	23 ± 2	210 ± 48	65 ± 2	116 ± 19
R12669SEL2	FA0100	21 ± 1	244 ± 49	60 ± 2	90 ± 15
R12669SEL2	FA0101	26 ± 2	243 ± 57	63 ± 3	103 ± 19
R12669SEL2	FA0104	23 ± 1	207 ± 47	63 ± 2	127 ± 19
R12669SEL2	FA0106	21 ± 1	198 ± 39	65 ± 2	128 ± 16
R12669SEL2	FA0108	21 ± 2	199 ± 44	61 ± 2	124 ± 18
R12669SEL2	FA0111	20 ± 2	254 ± 48	60 ± 2	93 ± 17
R12669SEL2	FA0117	23 ± 2	238 ± 70	53 ± 3	83 ± 26
R12669SEL2	FA0118	24 ± 2	228 ± 52	67 ± 3	139 ± 21
R12669SEL2	FA0119	22 ± 2	259 ± 59	59 ± 3	105 ± 21
R12669SEL2	FA0121	38 ± 2	261 ± 39	71 ± 2	126 ± 14

Table 2.2: *Contamination levels of Hamamatsu (R6956MOD and R12669SEL2) units measured at low background HPGe test bench at LSC.*

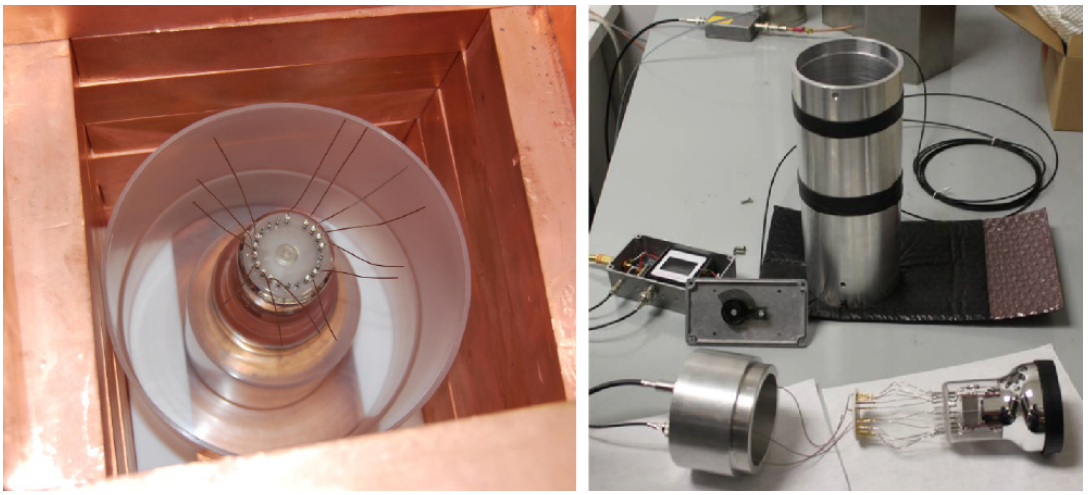

Figure 2.7: *Left: Hamamatsu R12669SEL2 radiopurity screening with a HPGe detector at LSC. Right: Set–up for PMT characterization at University of Zaragoza.*

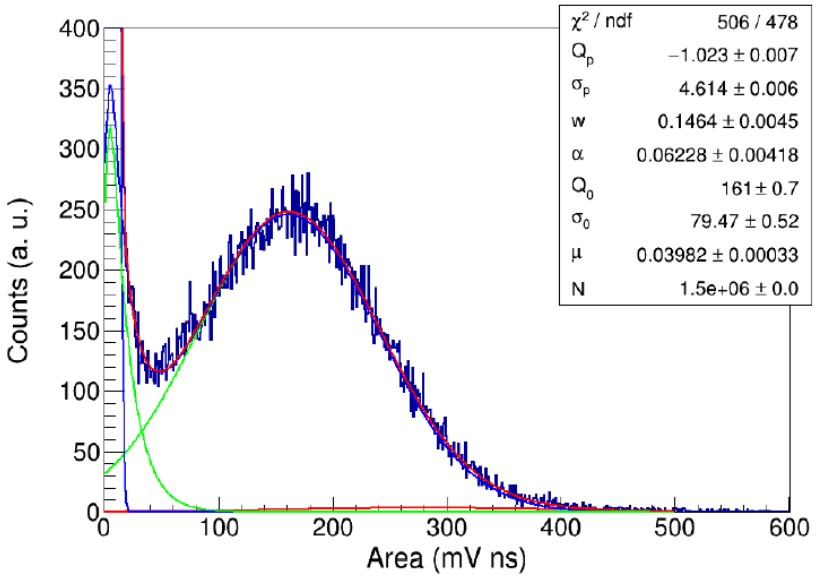

Figure 2.8: *SER pulse area distribution obtained from a population of events having a very low mean photoelectrons number ($\mu = 0.04$ is derived from the fit). From [31].*

Contamination levels measured in R12669SEL2 by HPGe (see table 2.2) show good homogeneity among units and are compatible with ANAIS requirements. These data have been used as an external contamination input for the background model of D0, D1, D2 and D3 modules, presented in chapter 3. The operational parameters (SER, gain, relative quantum eficiency and dark rate) were tested at the University of Zaragoza in order to understand R12669SEL2 response with low light intensity in the very low energy region and were found to follow the specifications.

2.5 Electronics and data acquisition

Design and characterization of the whole ANAIS acquisition system has been carried out in the frame of M.A. Oliván dissertation thesis [31]. ANAIS electronics has been tuned–up and tested through the different ANAIS set–ups (see section 2.9). ANAIS acquisition hardware and software design is robust and scalable. The electronic front–end has been designed taking into account the features of the scintillation signal described in section 2.3. Electronics has to be able to get information in a wide range of energies in order to understand the background of the experiment and a baseline as clean as possible is also needed to achieve a low energy threshold.

Hence, the design of the electronics of ANAIS has been made taking into account the following requirements:

- Trigger level must be done at photoelectron level with a good signal/noise ratio.
- Electronic noise must be minimized and controlled.
- Stability must be ensured during several annual cycles.
- The system must allow periodic energy calibrations to control the stability.
- The whole system must be robust and scalable.

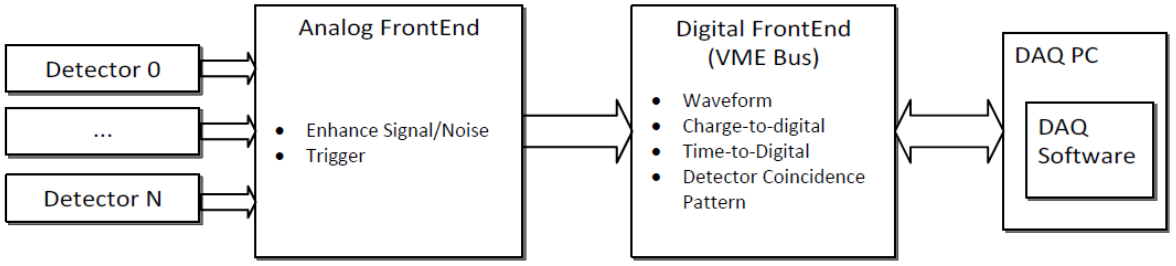

Figure 2.9: *DAQ system block diagram. From [31]*

In order to fulfill these requirements, the front–end (see figure 2.9) can be divided into two main stages:

- Analog stage: responsible for processing PMTs signals to achieve the trigger and signal/noise ratio goals. It consists of a preamplifier (placed very close

to the PMT output); Fan–In/Fan–Out module that produces several output signals from a given input, allowing the processing of the trigger signal line from one of the outputs, and the energy conversion/digitization of the signal from the others; and a Constant Fraction Discriminator (CFD), which produces the trigger for signals above the threshold at a given fraction of the signal maximum.

- Digital stage: responsible for digitizing the signal parameters:
  - –PMT signal waveform
  - –Charge generated at the PMTs
  - –Pattern of triggering for all detectors
  - –Triggering time for all the PMT signals
  - –Real time of the trigger and accumulated live time.

Acquisition system stores data depending on some configurable runtime conditions. It is important to reduce the dead time by avoiding the transfer of irrelevant data (as baselines from non–triggered detectors). This selection can be done by checking the trigger pattern, via Pattern Unit module (PU) and read the triggered data only. Precise estimate of the system dead time is crucial for ANAIS goals. ^{109}Cd calibrations have been performed in order to have enough statistical significance in those estimates at low energies leading to big improvements in both dead time and storage terms. High acquisition rate has been also tested by running with radon inside the shielding.

Each photomultiplier charge output signal is separately processed in order to obtain the trigger, pulse shape digitization and energy at different ranges (see figure 2.10). Triggering is done by the coincidence (logical AND) of the two PMT signals of any detector at photoelectron level in a 200 ns window, enabling digitization and conversion of these two signals. The building of the spectra is done off–line by software by adding the signals from both PMTs, and Pulse Shape Analysis is applied in order to select bulk scintillation events in the NaI crystals and to distinguish alpha interactions from beta/gamma ones. Filtering protocols for PMT noise similar to those described at [27] for ANAIS–0 prototype but optimized for these new detectors have been applied.

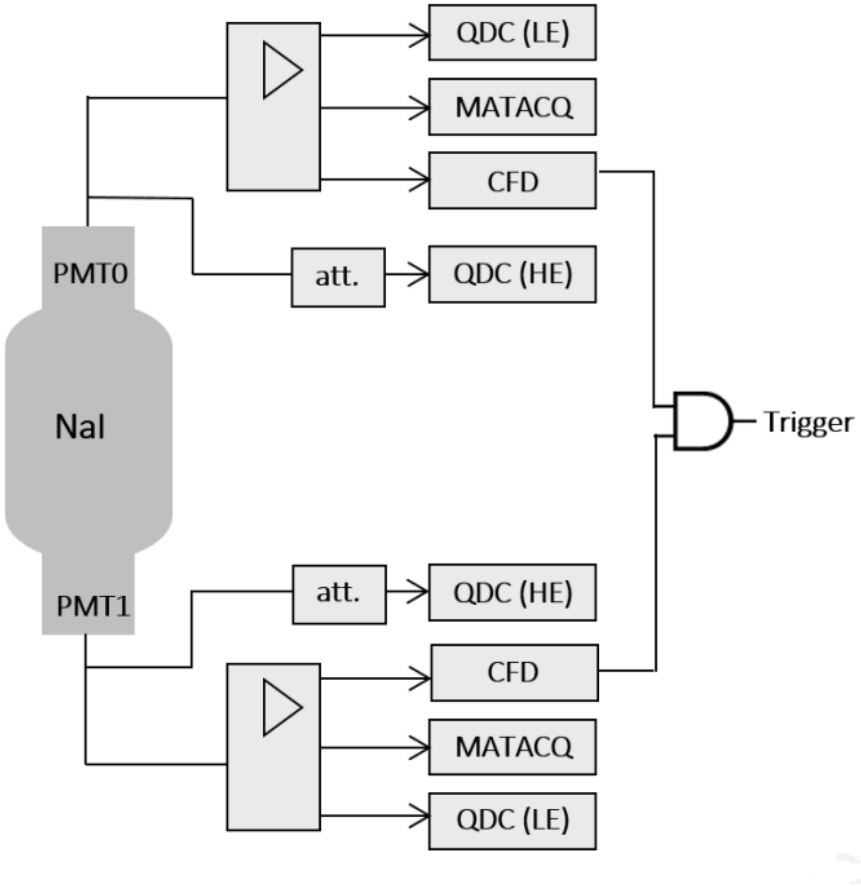

Figure 2.10: *Scheme of the ANAIS electronic acquisition system for one module.*

Along February 2016, ANAIS electronics was installed inside a temperature controlled space besides the ANAIS hut at LSC Hall B (see figure 2.11). This temperature control should allow to decouple the electronics temperature from the Hall B temperature fluctuations. Electronics temperature before and after the installation of the temperature control system are shown in figure 2.12. It can be observed that the fluctuation in temperature has been strongly reduced.

Figure 2.11: *Temperature controlled room for ANAIS electronics at Hall B of LSC.*

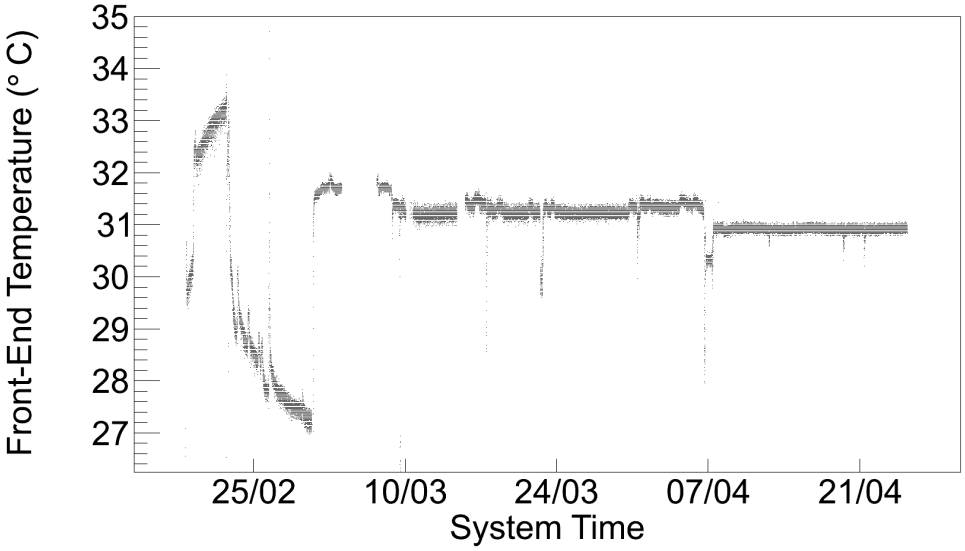

Figure 2.12: *Front–end temperature vs. time showing the effect of the new refrigeration system for ANAIS electronics.*

2.6 Calibration method

A few radioactive sources have been used to calibrate the different ANAIS set–ups (see table 2.3). Energy calibration is very important in any experiment. In the case of ANAIS, calibration also allows to get a reference of the NaI(Tl) scintillation events, to search for systematic effects in simulation, check the gain stability (con-

trolled through periodic calibrations), etc.

ANAIS modules are manufactured with a small Mylar window in order to allow the calibration at low energies. A good energy calibration near the threshold is crucial for ANAIS because the searched signal should appear in this energy region. In previous prototypes, and also in ANAIS–25 first months of operation, this calibration was made introducing, through an aperture in the anti–radon box and lead shielding, a tray with a disk–shaped source (see figure 2.13).

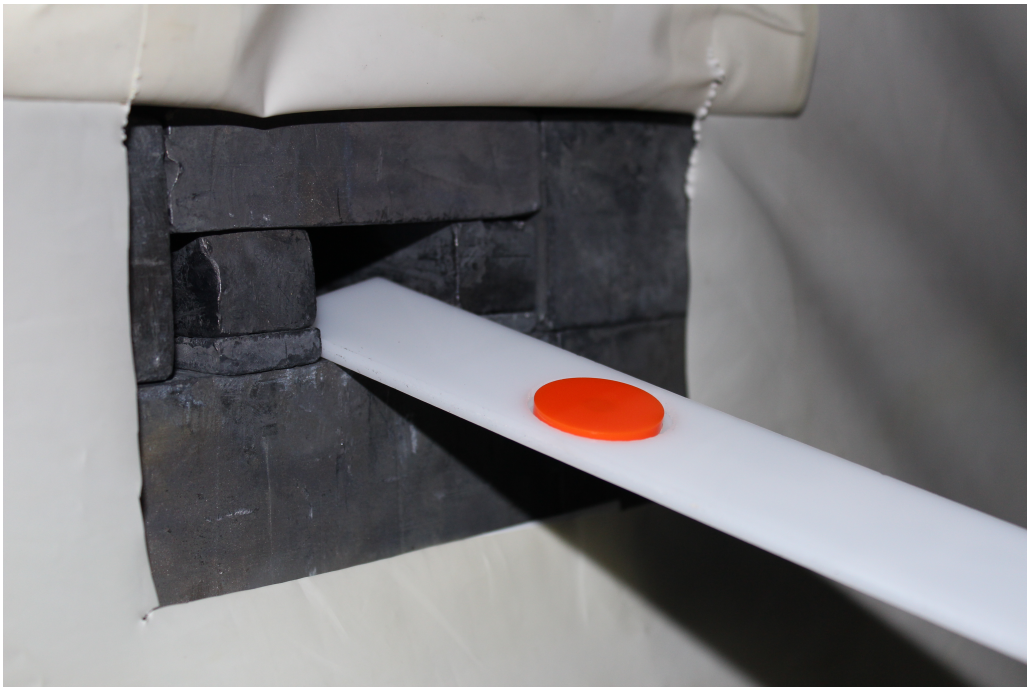

Figure 2.13: *Old disk–shaped calibration source.*

Since June 2014 two radioactive sources (^{57}Co and ^{109}Cd), specially designed for ANAIS, are mounted along a flexible wire that is introduced into the shielding through a closed tube and positioned in front of the Mylar window (see figure 2.14). This new system guarantees a closed radon–free calibration and is scalable to the full ANAIS experiment. In adjacent modules, Mylar windows are placed face to face in order to allow a simultaneous calibration when introducing the source. ^{57}Co and ^{109}Cd sources have been chosen for periodic calibration because of the low energy X and gamma emissions (see table 2.3).

Figure 2.14: *New calibration system with two radioactive sources (^{57}Co and ^{109}Cd) mounted along a flexible wire.*

Source	**Energy (keV)**	**Intensity (%)**
^{57}Co	6.4(*)	56.1 ± 1.0
	14.4	9.2 ± 0.2
	122.1	8.5 ± 0.1
	136.5	10.7 ± 0.2
^{109}Cd	22.6 (*)	101.5 ± 1.5
	88.0	3.6 ± 0.3
^{137}Cs	32.9 (*)	6.9 ± 0.2
	662	85.0 ± 0.2
^{22}Na	511	90.4 ± 0.2
	1275	99.9 ± 0.1
	1786 (A)	

Table 2.3: *Radioactive sources used for ANAIS calibration and their main gamma and X emissions (with intensities larger than 3%). Energies with (*) are average values that ANAIS set–ups are not able to resolve. Energies with an (A) correspond to the addition of two lines that are emitted in cascade, producing a peak in the energy spectrum and used for calibration.*

In the case of the ^{109}Cd source, it was covered by a heat–shrink tube as protection while building the new calibration system. This cover has some Br in its composition and then, it produces X–rays at 11.9 keV under irradiation of the ^{109}Cd gammas (see figure 2.15). This low energy line is also used for calibration purposes, although not included in table 2.3.

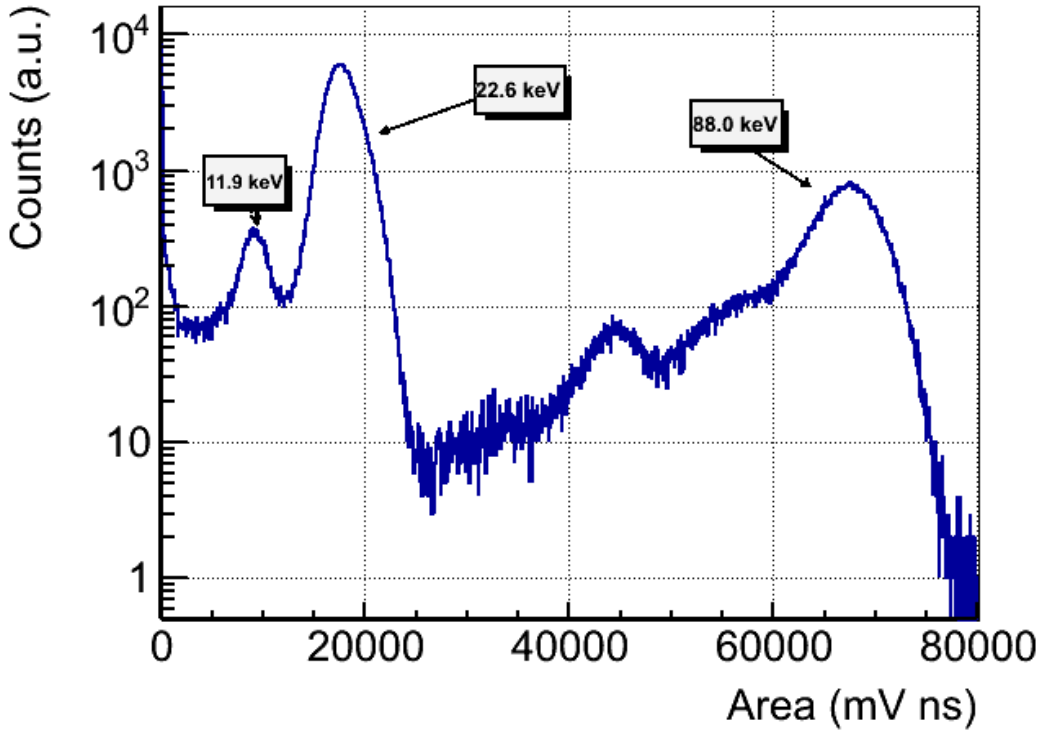

Figure 2.15: *Example of the pulse area spectrum using a ^{109}Cd source to get the energy calibration (data corresponding to D1 detector in ANAIS–37 set–up). 22.6 keV and 88.0 keV lines are clearly observed as well as the 11.9 keV of the Br K–shell X–ray mean.*

2.7 Slow–Control

As it has already been explained in section 2.1, stability of the operation parameters of an experiment searching for the annual modulation of the dark matter is a key feature. A slow–control system has been developed for ANAIS, as a LabVIEW program, to monitor and store any parameter that could have an effect in the stability of the system or background of the experiment (see figure 2.16).

The parameters monitored in ANAIS are:

- *Temperature:* Temperature is measured in different locations of the experiment as it can have a large effect in all the acquisition stages due to the observed relation between trigger rate and the temperature at the electronics rack, disturbing the acquisition.
  - Inside the shielding

– Inside the ANAIS hut

– At the electronics.

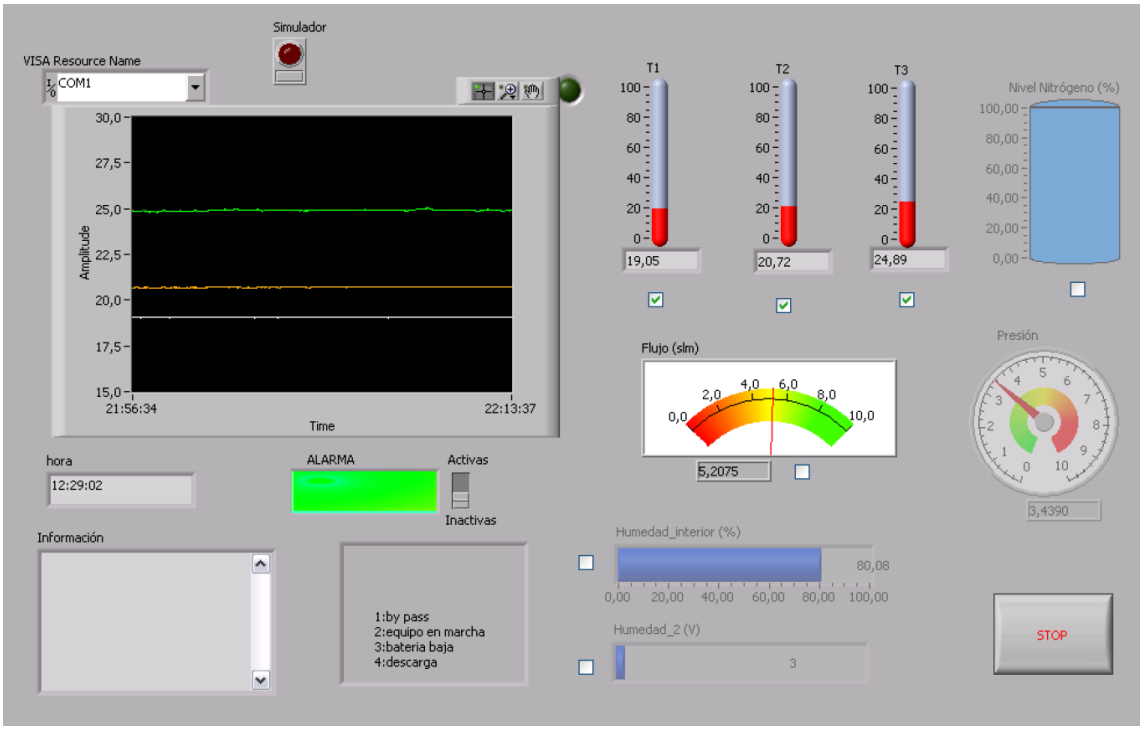

Figure 2.16: *ANAIS Slow–control interface.*

- *Nitrogen flux:* As it has been explained in section 2.1.2, ANAIS set–up is continuously flushed with boil–off N_2 flux in order to keep the inner space of the shielding as free as possible of radon. This flux is monitored to register any variation that could affect the experiment.

- *Radon concentration in the laboratory:* Radon concentration in the ambient that surrounds the experiment is also monitored by a Genitron (now Saphymo) AlphaGuard system that also records the pressure, humidity and temperature environmental parameters (see figure 2.17). It is worth to remark that ANAIS shielding is designed to prevent radon entrance and inner space is continuously flushed with radon–free gas, and thus, radon concentration in the ANAIS inner volume is below sensitivity. However, monitoring external environmental radon concentration levels is interesting in order to have under control possible systematics in the annual modulation analysis. In figure 2.17, behavior of humidity and radon concentration in LSC Hall B along three years and a half are shown. The best fit to a modulation in both parameters is also shown.

- *PMT bias voltage and crate parameters:* The electrical signal of the photomultipliers is very dependent on the high voltage applied and thus, it has to be very stable to assure the gain stability of the PMTs. PMTs current can also be monitored to detect any variation in its value. The CAEN crates used in ANAIS allow to monitor several temperatures (power supply and module section temperature, for instance) as well as fan behavior, voltages and intensity of the crate power supplies.

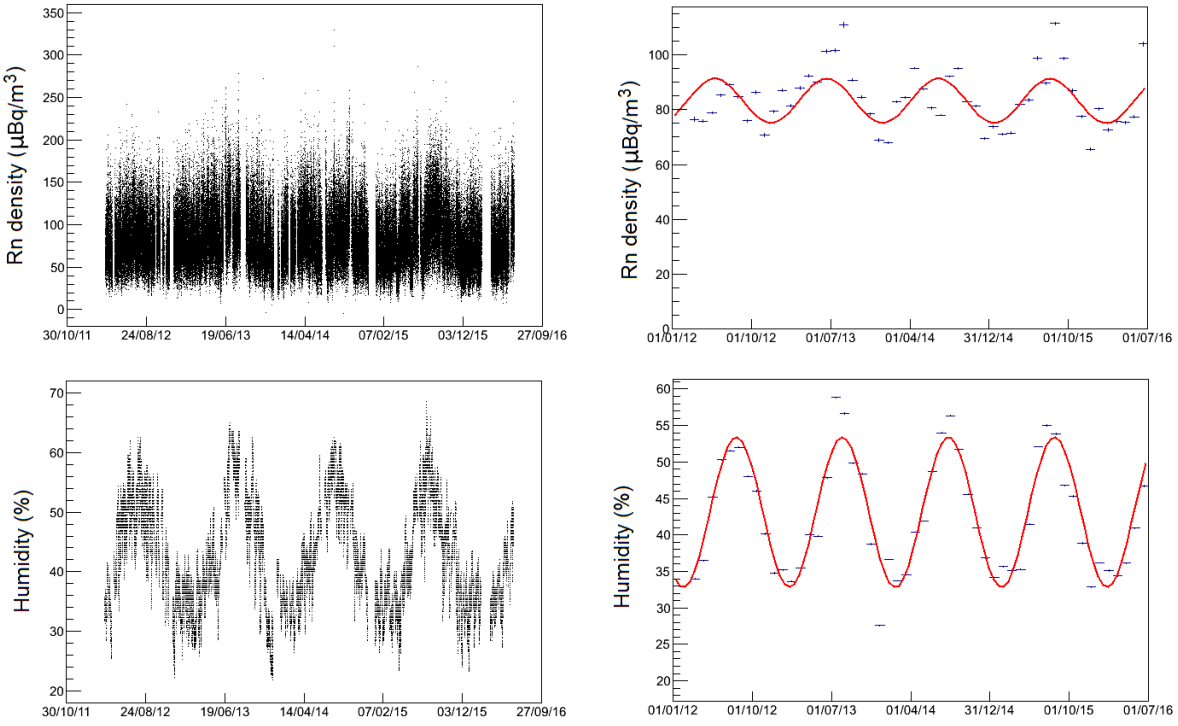

Figure 2.17: *Daily mean values (left) and monthly mean values (right) with modulation fit for radon concentration (top) and humidity (bottom).*

2.8 Muon veto system

Although most of the muon flux is avoided by placing the experiment underground, a residual flux is still present and contributes to the background of the experiment. Muons are expected to interact directly in the NaI(Tl) detector producing high energy depositions, but muon–related events, as secondary neutrons, produced in the shielding are expected to produce signals very similar to those expected for WIMP interactions and could mimic the dark matter signature.

At LSC, muon flux is small, of the order of $5 \cdot 10^{-3}\ \mu \cdot s^{-1} m^{-2}$, this is four orders of magnitude lower than the flux in surface but still enough to affect ANAIS detectors. Therefore, a veto system for ANAIS must be implemented in order to tag muons and then, veto all the possible muon–related events.

In the full ANAIS experiment, a veto system consisting of sixteen plastic scintillators covering all the faces of the ANAIS set–up, except the bottom one, will be installed (see figure 2.18).

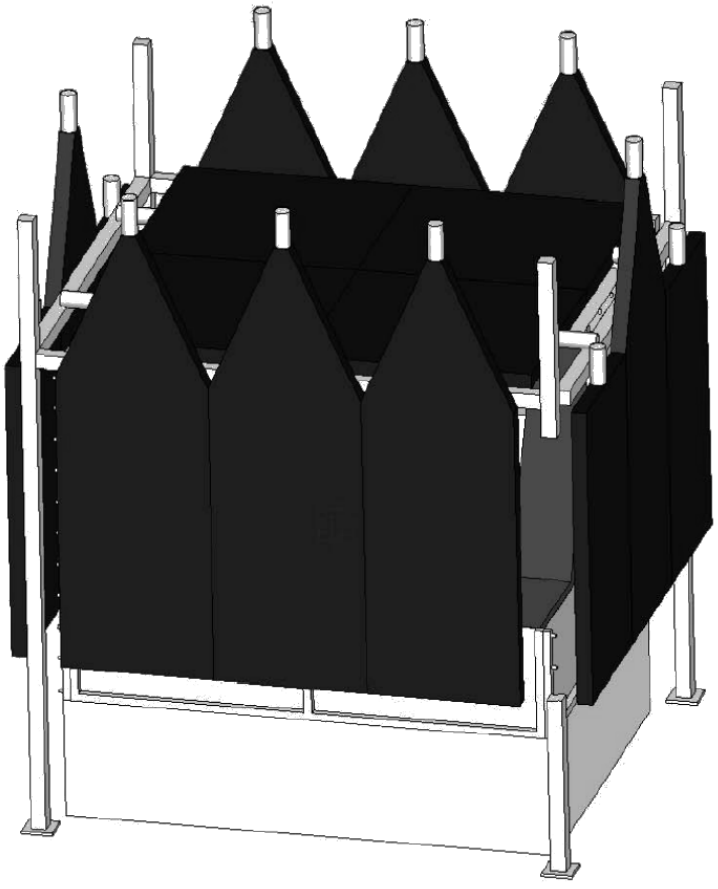

Figure 2.18: *Design of the sixteen plastic scintillators set–up to be installed as muon veto system in ANAIS full experiment.*

Plastic scintillators vetoes available for mounting in the ANAIS full experiment have different origin and dimensions (see table 2.4). Scionix vetoes were purchased for the full set–up and are still under test at LSC. Homemade vetoes were tested in ANAIS–0 and have been used since then covering the top face of the different set–ups. In ANAIS–37 and forward set–ups (see figure 2.19), eleven plastic scintillators are covering the lateral and top faces of the shielding. It has been observed

that top vetoes detect a higher muon flux than lateral vetoes, in agreement with the expected angular distribution, and that south and north faces have more events than east and west faces, compatible with the non–homogeneous rock overburden profile at the Hall B position [31] (see table 2.5).

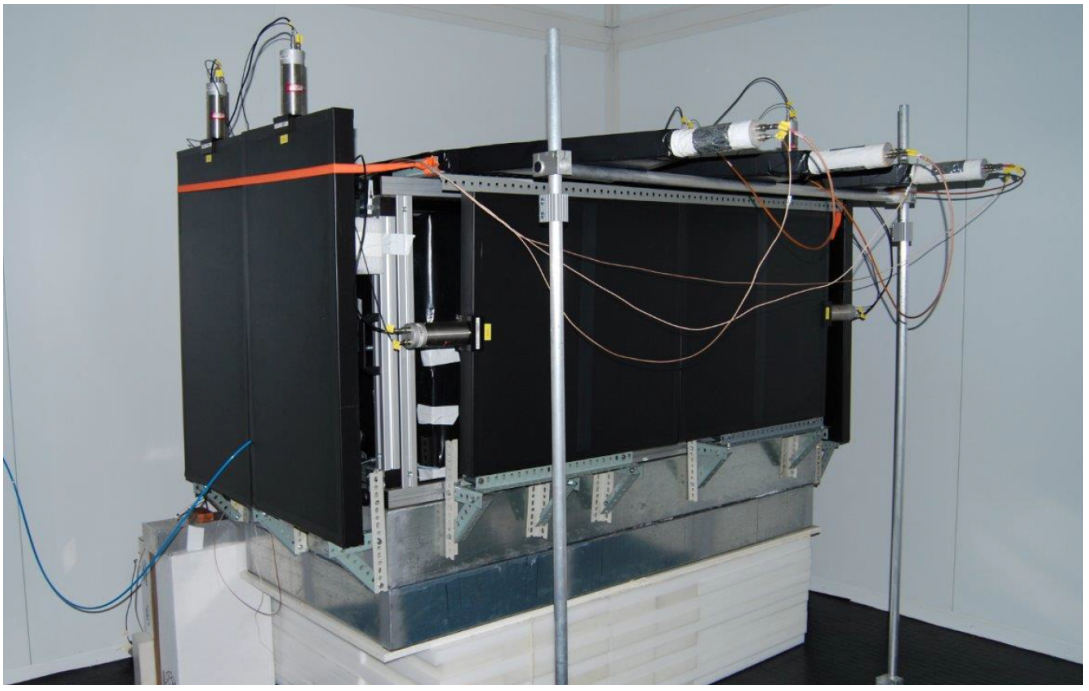

Figure 2.19: *Plastic scintillators in ANAIS–37 set–up.*

A test bench with two stacked plastic scintillators was installed at LSC facilities (external building and underground laboratory) in order to test the new Scionix vetoes (see figure 2.20). OR trigger between the two scintillators signals, digitizing both of them, allows the study of coincident and anti–coincident events. Non–coincident events come from natural radioactive background or have a PMT origin, while coincident events are mainly muons ionizing both detectors; the latter show the spectral features predicted by specific Geant4 simulations. The characterization of these populations was needed because the geometry of the ANAIS set–up (see figure 2.19) does not allow to use coincidences to select muons and Scionix scintillators in particular showed a too high anticoincident trigger rate, which had to be suppressed in order to guarantee the correct operation of the muon veto system. As result of these tests, a PSA procedure was implemented in order to discriminate muons from other background events in the Scionix scintillators. This PSA is carried out on–line, while data taking is ongoing, and only muon–origin events trigger the veto system.

Veto numbers	Vendor/Model	Dimensions (mm)
1, 2, 7, 8	Scionix/R500*50B1000–2ME2PX	1000×500×50
3, 4, 5, 6	Scionix/R700*50B550–2ME2PX	750×700×50
9, 10, 11, 12, 13, 14, 15, 16	Homemade	1000×500×50

Table 2.4: *Plastic scintillators models and dimensions for the ANAIS muon veto system.*

Face	Veto	Measured rate 10^{-3} ($\mu\ m^{-2}s^{-1}$)	Mean measured rate 10^{-3} ($\mu\ m^{-2}s^{-1}$)
South	#1	5.27 ± 0.10	5.43 ± 0.07
	#2	5.53 ± 0.10	
West	#3	4.88 ± 0.10	4.75 ± 0.07
	#4	4.61 ± 0.10	
East	#5	4.53 ± 0.10	4.54 ± 0.07
	#6	4.54 ± 0.10	
North	#7	5.05 ± 0.10	4.91 ± 0.07
	#8	4.77 ± 0.10	
Top	#9	7.23 ± 0.12	7.36 ± 0.07
	#10	7.54 ± 0.12	
	#11	7.32 ± 0.12	

Table 2.5: *Muon detection rate in each face of the plastic scintillator veto system. From [31].*

Figure 2.20: *Plastic scintillators test bench set–up at LSC.*

2.9 Set-ups

Most recent set–ups and prototypes aiming at the evaluation of the background, detector performance and the consequent expected sensitivity used to choose the final design for ANAIS experiment, as well as their main characterization results are presented in this section.

2.9.1 ANAIS–25

ANAIS–25 set–up consisted of two detector prototypes, amounting 25 kg of NaI(Tl), grown by AS and installed in the LSC (see figure 2.21). These two detectors (named D0 and D1) took data from December 2012 to March 2015.

The shielding consisted of 10 cm of archaeological lead plus 20 cm of low activity lead inside a radon exclusion box at Hall B of LSC. An active muon veto system made up of plastic scintillators covered the top and lateral faces of the shielding.

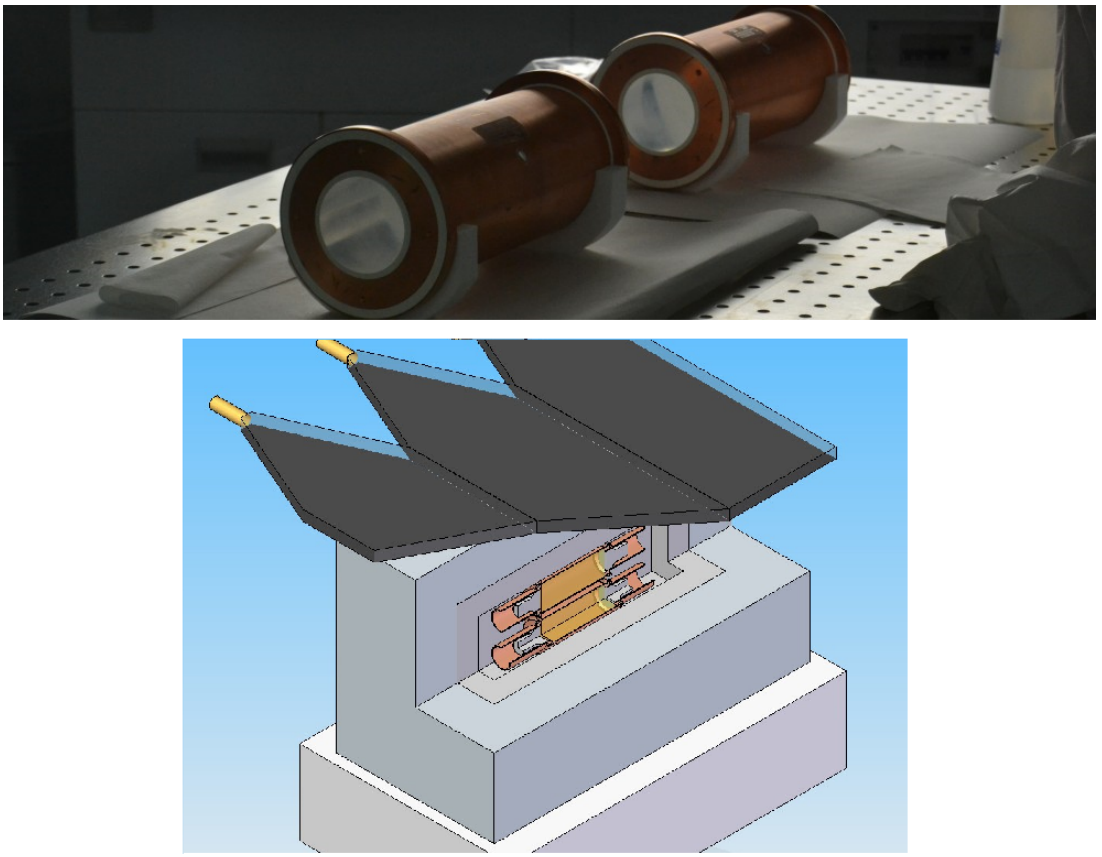

Figure 2.21: *ANAIS–25 crystals (top) at LSC clean room and ANAIS–25 set–up artistic view (bottom).*

The main goals were to measure the crystal internal contamination, determine light collection, fine tune the data acquisition and test the filtering and analysis protocols. As it will be shown in this chapter, D0 and D1 presented an excellent light collection (see section 2.10.1) and an acceptable ^{40}K content.

Figure 2.22 shows the low energy spectrum at the beginning of the data taking and after fifteen months underground. A high suppression of most of the lines, of cosmogenic origin, can be observed except the corresponding to ^{210}Pb. A more detailed study of this issue is presented in section 3.1.2.2. Alpha population events were selected by Pulse Shape Analysis (PSA) as alpha events are faster than beta–gamma–muon events, and can be distinguished by comparing the area and the amplitude of the pulse; a high alpha rate was observed, which could be due to ^{210}Po produced in ^{210}Pb decay series.

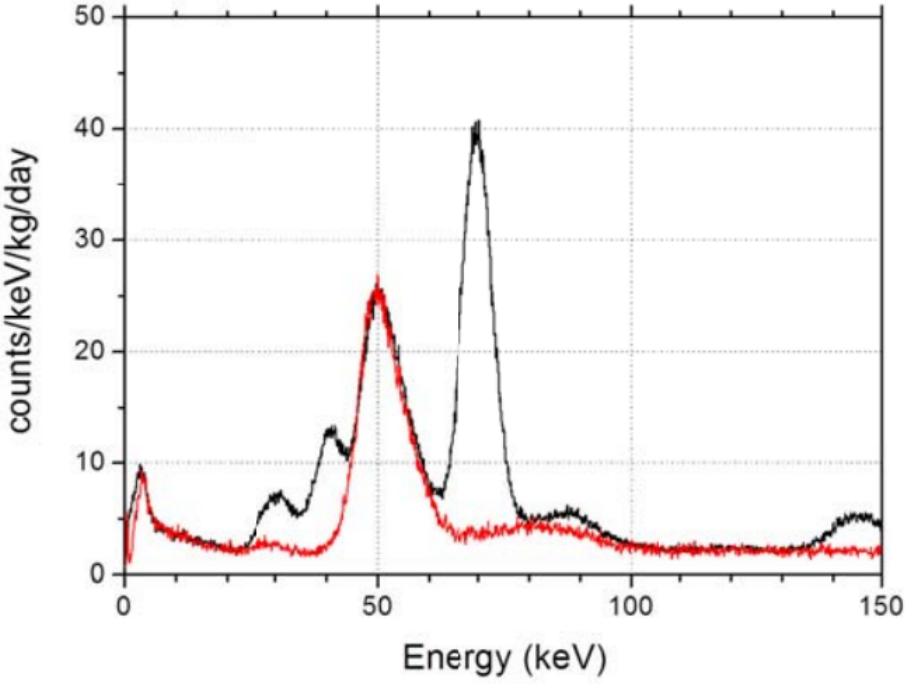

Figure 2.22: *Low energy spectra of D1 corresponding to the first month of measurements (black) and data taken after fifteen months underground (red). Most of the cosmogenically induced isotopes contributions at low energy have strongly decayed.*

2.9.2 AS1K

Conversations with Alpha Spectra about the possible origin of the very high ^{210}Pb–^{210}Po contamination in D0 and D1 modules started very soon after its discovery. As a result, a new bare crystal was ordered and very fast delivered. It was a 1–kg NaI(Tl) crystal prepared by Alpha Spectra and received at Zaragoza the first week of August 2013. This 1–kg crystal was coupled to two PMT units at the glove box available at the University of Zaragoza, under controlled atmosphere and inside a tightly sealed encapsulation. Then, it was moved to LSC and installed in a small shielding besides ANAIS–25. Measurements in low background environment at LSC started almost immediately. It was called AS1K set–up (see figure 2.23).

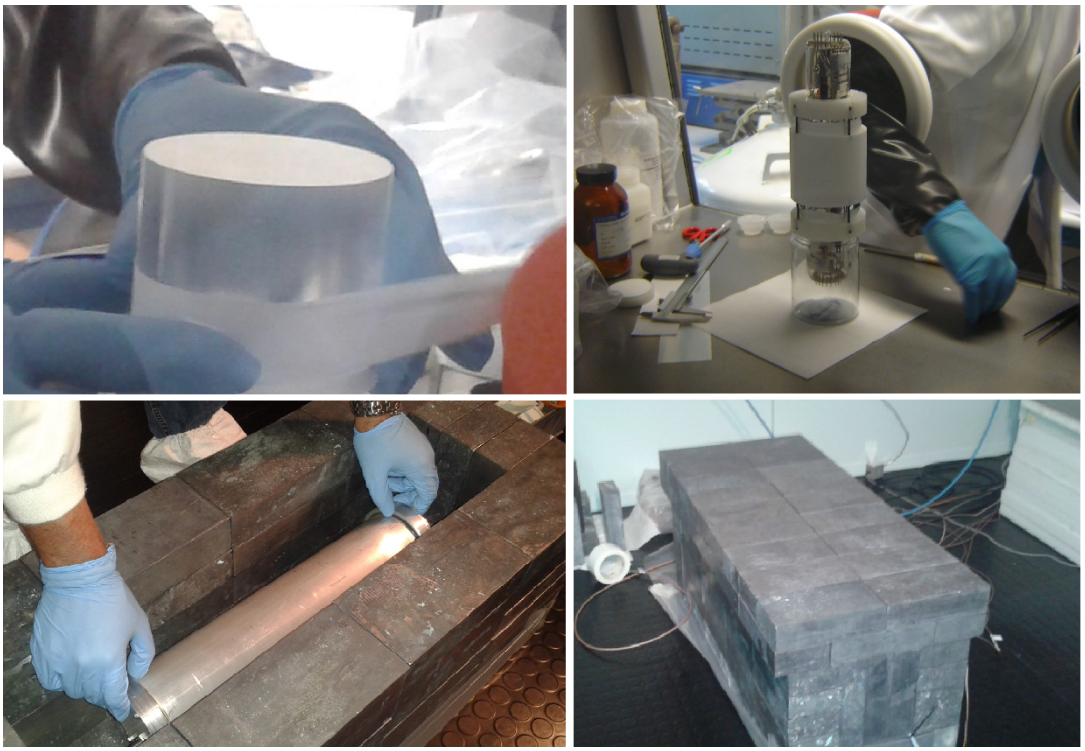

Figure 2.23: *Mounting of the 1–kg NaI(Tl) crystal from Alpha Spectra at the glove box at the University of Zaragoza (top) and installation of AS1K set–up at LSC (bottom).*

As in ANAIS–25, alpha population events were selected by PSA. Alpha rate evolution in time showed that equilibrium in the chain had not had time to recover (as it will be presented in the following chapter, see figure 3.5). Although AS1K was not an ultra–low background set–up, and for instance, low energy ^{210}Pb energy depositions were shadowed by other backgrounds, similar analysis to that used for ANAIS-25 at high energy was applied for AS1K data, and it could be confirmed that thorium chain and upper parts of uranium chain were not responsible of the high alpha rate, being again ^{210}Pb–^{210}Po the most plausible explanation for the contamination.

According to information provided by AS about dates of powder purification, crystal growing and machining, the observed increase in the rate could be explained by a contamination in the crystal growing (green line in figure 3.5). A thorough investigation of the possible mechanism responsible of the contamination was carried out at AS and changes were implemented in their protocols.

2.9.3 ANAIS–37

After these changes, a new module similar to D0 and D1 was ordered to be tested at LSC that, once incorporated to the set-up, formed ANAIS–37 (see figure 2.24) [180, 181]. This new detector, D2, grown using these new protocols to prevent radon contamination, presented a remarkable reduction of the ^{210}Pb content. It also presented an excellent light collection. The crystal was received the 6^{th} of March, 2015 and data taking started five days later. It was placed in between the two ANAIS–25 modules to maximize the coincidence efficiency for the potassium determination. Although in ANAIS–25 set-up the coverage of the muon vetoes was only partial, at the end of the ANAIS–37 data taking period the vetoes were fully operative.

The main goal of ANAIS–37 set-up was to characterize the new D2 module, in particular, to evaluate the reduction of ^{210}Pb contamination, to check the content of ^{40}K and ^{238}U and ^{232}Th chains and to assess also its general performance. Details on the achieved results will be presented in more detail in following chapters.

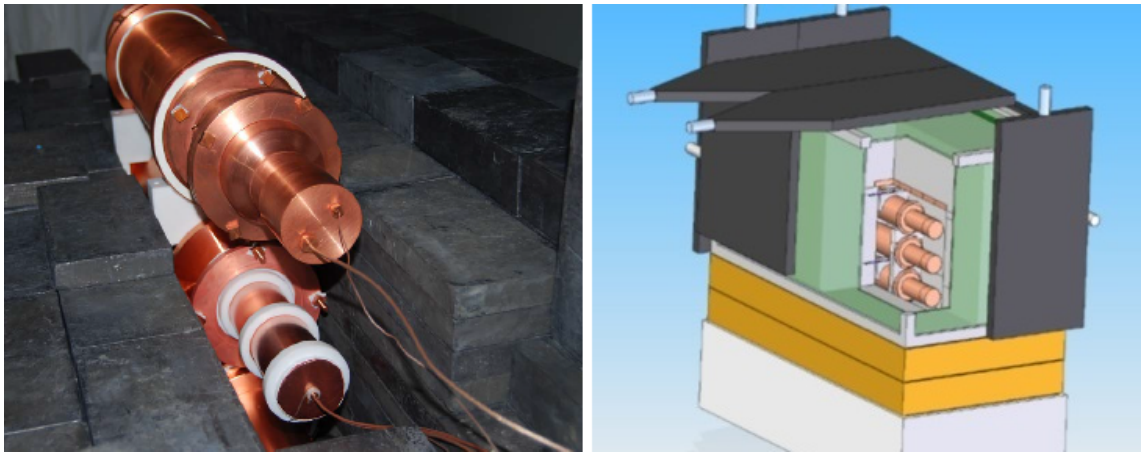

Figure 2.24: *ANAIS–37 set–up at LSC and artistic view.*

2.9.4 Blank module

A blank module, similar to AS modules, was prepared and mounted in the ANAIS–37 set–up replacing the D1 detector in September 2015. This blank module had no crystal nor quartz windows and was coupled to the two photomultipliers used in D1 (see figure 2.25).

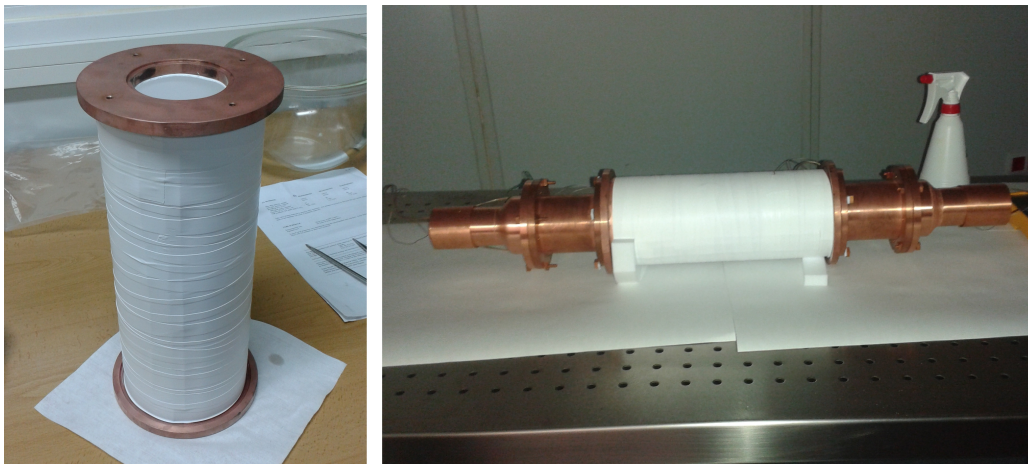

Figure 2.25: *Blank module installed in ANAIS–37 replacing D1 detector.*

The main goal of this set–up was to accumulate a population of pure photomultiplier events and to test the filtering protocols. Events with energies equivalent up to 20 keV were identified and most of the events were removed by applying the same filtering protocols that are used in the detectors (see section 2.10.4) and only a residual background of a few tenths of counts/(keV kg day) remained (see figure 2.26). Figure 2.27 shows the average of pulses above 10 keV, and figure 2.28 the average of events passing the cuts in the filtering procedure for the blank module data.

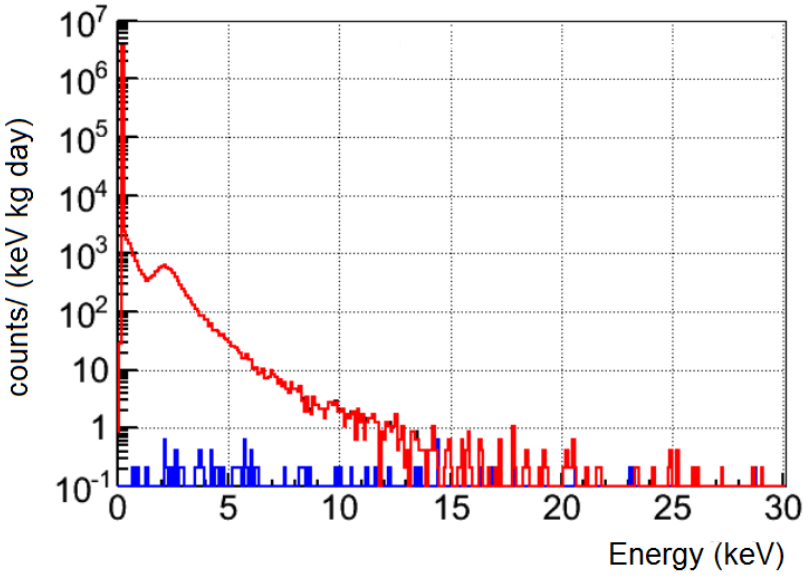

Figure 2.26: *Energy equivalent spectra corresponding to the blank module before (red) and after (blue) applying the filtering.*

There exists light coming out from the PMTs triggering in coincidence, not attributable to dark rate as pulses have high number of photons. Most of the events triggering are very fast events (see figure 2.27), being a possible origin the Cerenkov emission in the PMT glass. However, those events passing all cuts have a temporal distribution of photons emitted with a characteristic time of hundreds of ns. Further work is ongoing in order to fully understand the origin of these events.

On the other hand, a cut in the N_2 flux at the beginning of the data taking of the blank module in the ANAIS–37 set–up served to study the effect of the absence of N_2 flux in the triggering rate (see figure 2.29). Effect of N_2 flux on total trigger rates is much larger than expected due to the radon present in the air. This effect amounts an order of magnitude in the case of D0, but up to two orders of magnitude in the case of D2. Radon–origin events can be observed in figure 2.30 in the 200 to 400 keV energy region, at the 609 keV line, and also in figure 2.29 through coincidences between D0 and D2 modules. Moreover, it was found that the timing of the increase and decrease in the triggering rate after the change in the N_2 flux is not compatible with that observed for the radon-origin observed events. No explanation is available for this high increase in the triggering. Anyway, thanks to the installation of the blank module, it can be concluded that photomultipliers are not responsible (although contributing).

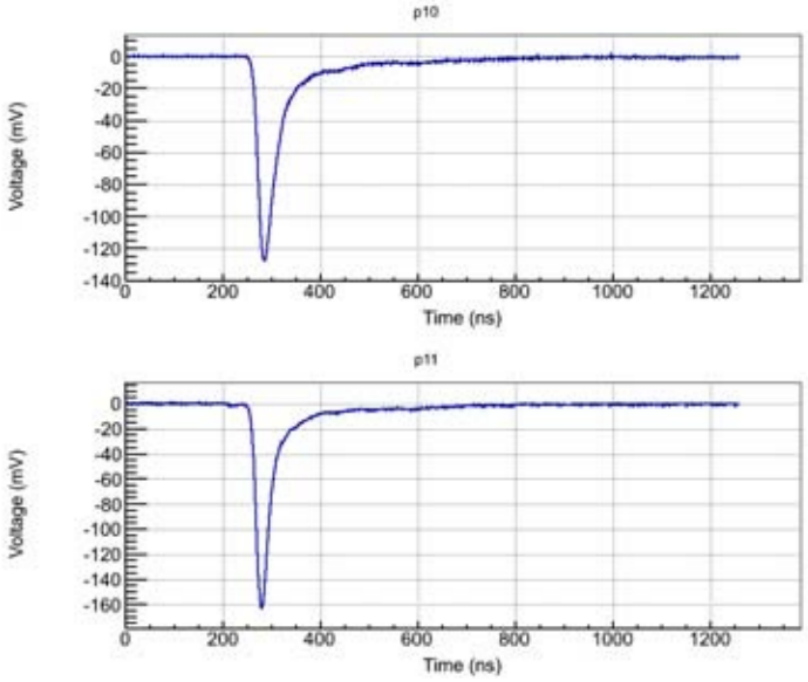

Figure 2.27: *Average of pulses from each PMT for blank module events above 10 keV.*

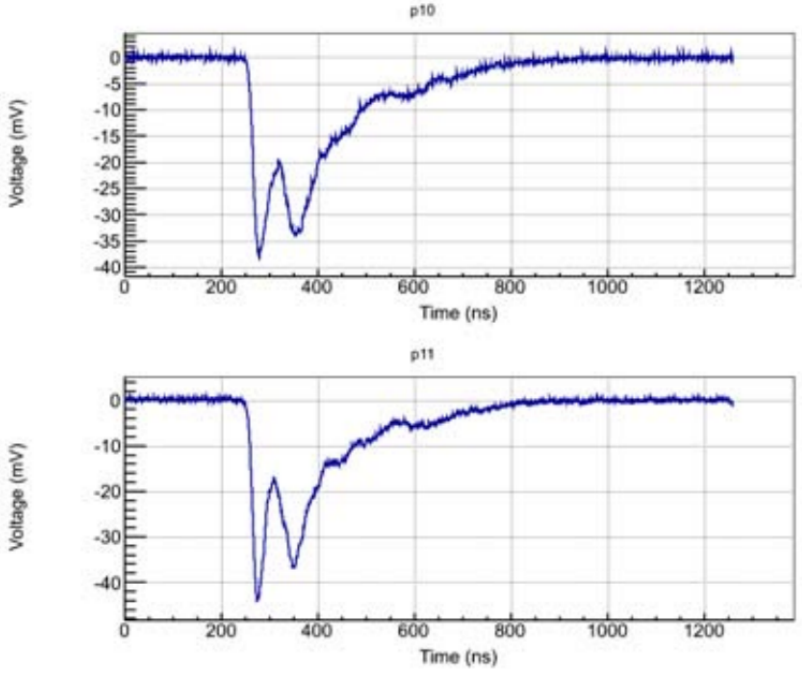

Figure 2.28: *Average of pulses from each PMT for blank module events passing all the cuts.*

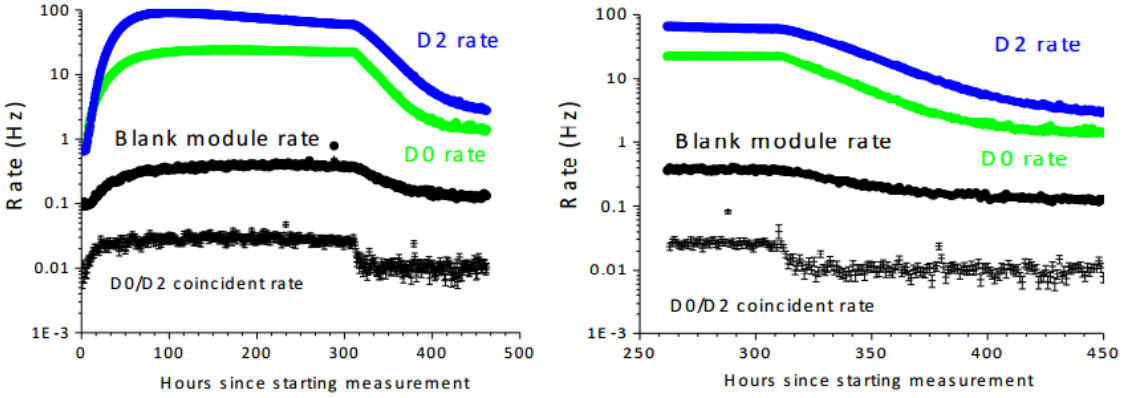

Figure 2.29: *Left: Total trigger rates in D0, D2 and blank module. Coincidence rate between D0 and D2 modules is also shown. N_2 flux was disconnected before starting taking data and resumed about 310 hours later. Right: zoom in the rates near the resume of the N_2 flux.*

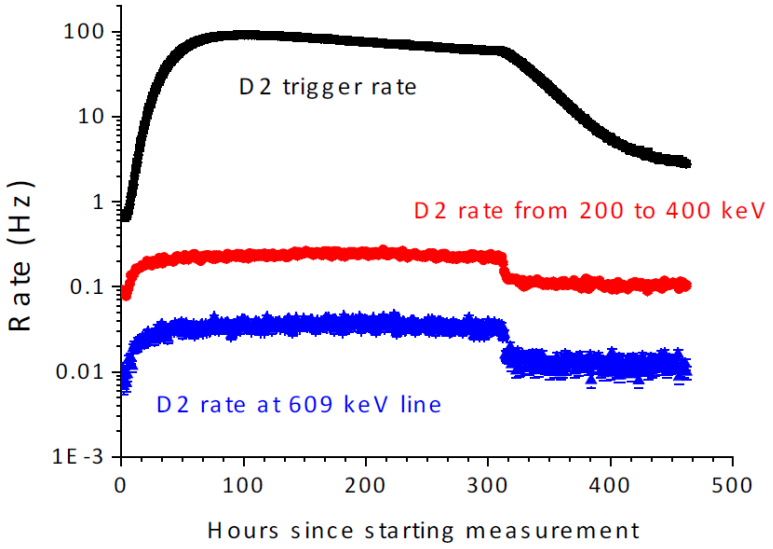

Figure 2.30: *Total trigger rate in D2 together to partial rates corresponding to regions from 200 to 400 keV and the 609 keV line where radon is expected to contribute. Different behaviour can be observed.*

2.9.5 A37D3

Alpha Spectra latest received module, D3 in the following, consists of a crystal made with a more purified powder (WIMPScint-III quality), which should have a lower potassium content than previous AS crystals (D0, D1 and D2 modules).

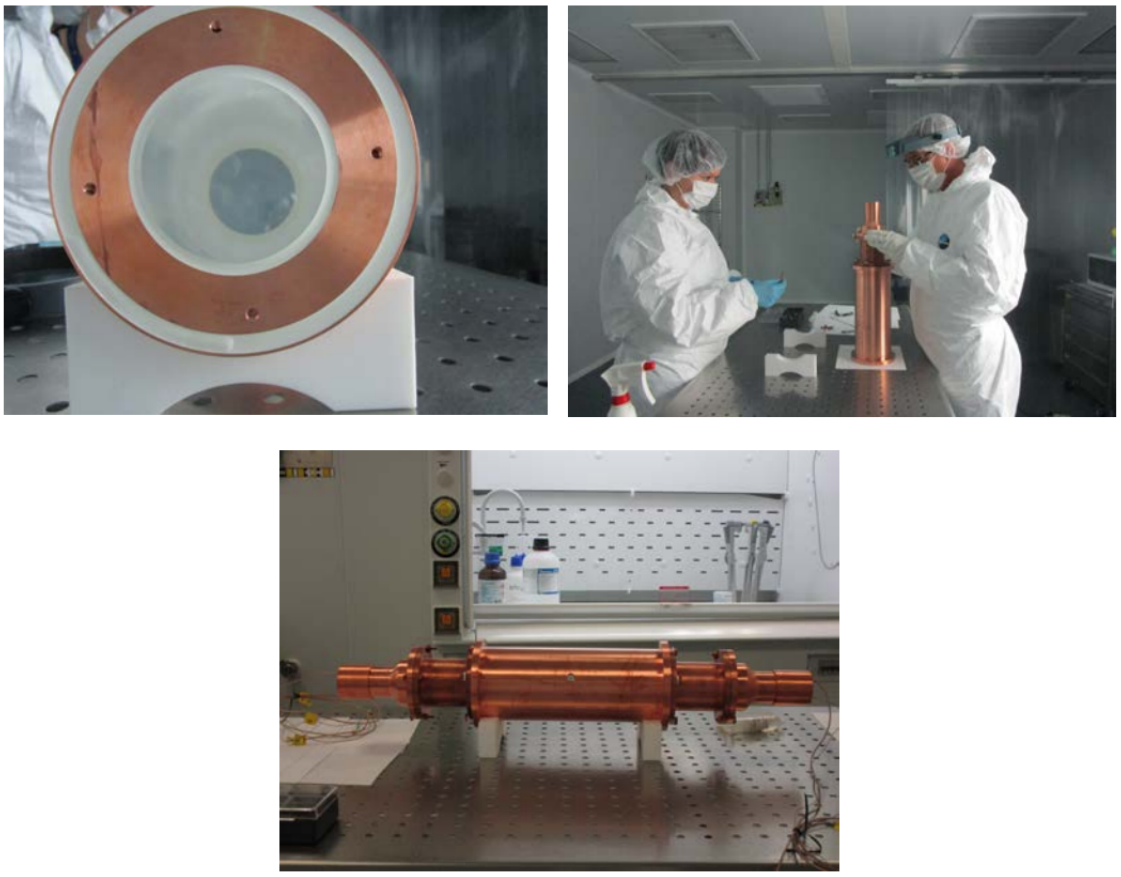

Figure 2.31: *The new Alpha Spectra module, D3, at LSC clean room.*

The crystal was encapsulated following similar protocols and using same materials to those from previous AS modules. An aluminized Mylar window was also built to allow low energy calibrations. The crystal arrived to Barcelona on February 23^{th}, 2016, but the Spanish customs delayed the arrival to Canfranc until March, the 7^{th}. PMTs were coupled to this new module at LSC clean room the 7^{th} of March, 2016 (see figure 2.31) and the mounting in the ANAIS hut at Hall B was done from 7^{th} to 8^{th} March 2016, starting the measurements immediately, profiting from the availability of the ANAIS–37 set–up (see figure 2.32).

This new set-up, A37D3, is very similar to ANAIS–37 in shielding configuration and acquisition parameters, but different in the module layout. The new module (D3) is placed in between D0 (bottom) and D2 (top) modules to maximize the coincidence efficiency for the potassium determination (see figure 2.32).

The preliminary results of D3 characterization will be commented in following chapters; a promising reduction in potassium content seems to be confirmed but in

contrast ^{210}Pb activity seems higher than in D2 module according to the alpha rate measurement and the ^{210}Pb spectral feature at low energy.

Figure 2.32: *A37D3 set–up at LSC.*

2.9.6 AS2K–1 and AS2K–2

Because of the high alpha rate measured in D3 and after discussing the possibility of a surface contamination with AS, two pieces of 1 kg of NaI(Tl) grown from two different ingots were analyzed: sample 1 had as origin the same ingot as D3 module, whereas sample 2 was drawn from a second ingot, grown afterwards. They were sent from AS facilities, in Colorado, to Zaragoza for the measurement of their alpha content.

The pieces arrived to Zaragoza on April the 20^{th}, and one of them (sample 1) was immediately encapsulated and coupled to two PMTs in a glove box at the University of Zaragoza (see figure 2.33) and installed at LSC the following day. After two weeks of measuring, this sample was replaced by sample 2 following the same procedure.

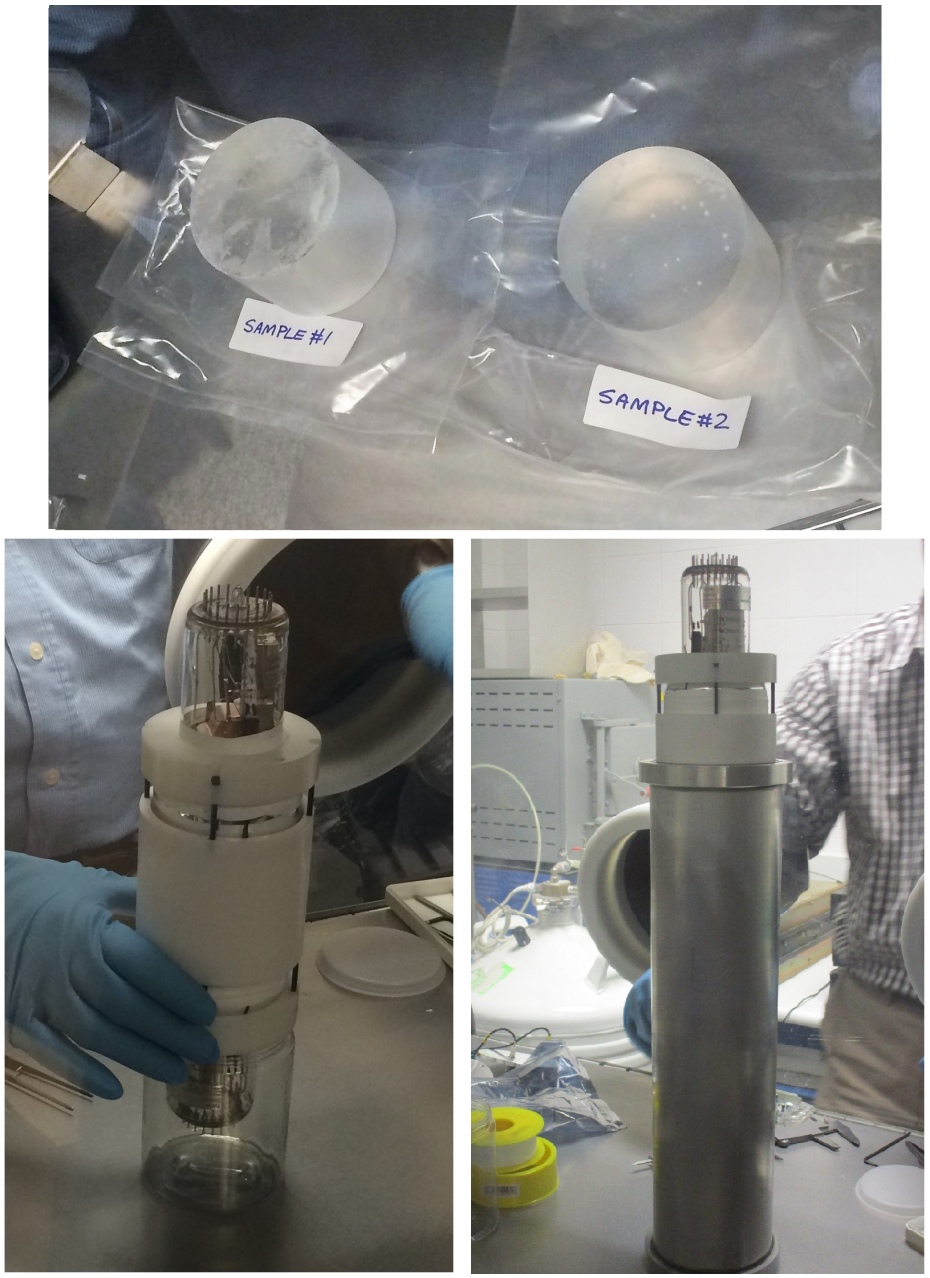

Figure 2.33: *Alpha Spectra samples (AS2K–1 and AS2K–2) being mounted at University of Zaragoza glove box.*

PSA allows easily the identification and quantification of the alpha rate. If the total number of alphas is scaled to the crystal mass, sample 1 shows an alpha rate of about 1.6 mBq/kg. For sample 2, better results have been obtained, at the level of 0.7 mBq/kg (although ^{210}Po activity is still being built) and then, support the suitability of the corresponding ingot to produce more modules for ANAIS.

2.10 Detector performance

AS detectors built for ANAIS have been taking data at LSC since December 2012. Work on their data has been focused on the demonstration of an energy threshold as low as possible with robust efficiency determination (more concretely, to confirm a 1 keVee energy threshold). Main aspects of the detector performance are summarized in this section.

2.10.1 Light Collection

One of the most important features for the ANAIS NaI(Tl) detectors is the optical quality of the crystal. An outstanding light collection must be remarked for D0, D1, D2 and D3 modules, at the level of ∼15 phe/keV [31], which is a factor of 2 larger than that determined for the best DAMA/LIBRA detectors [137]. This much higher light output has a direct impact in both energy resolution and energy threshold, but it also allows to strongly improve the signal vs. noise filtering down to the threshold and hence, to reduce analysis uncertainties.

In table 2.6 all the data derived up to present with the AS modules in the different experimental set–ups are shown. D3 shows very high light collection, similar to that measured for previous AS modules.

Detector	PMT/set–up	Total light collection (phe/keV)
D0	R12669SEL2/ANAIS–25	15.6±0.2
D0	R12669SEL2/ANAIS–37	15.3±0.1
D0	R12669SEL2/A37D3	15.1±0.1
D1	Ham R11065SEL/ANAIS–25	12.6±0.1
D1	R12669SEL2/ANAIS–25–III	15.2±0.1
D1	R12669SEL2/ANAIS–37	14.4±0.1
D2	R12669SEL2/ANAIS–37	15.4±0.1
D3	R12669SEL2/A37D3	15.2±0.5

Table 2.6: *Total light collection derived for all AS modules in the different set–ups.*

2.10.2 Triggering

Triggering strategy must ensure the storage of all relevant events for the experiment but avoiding a too high rate that could increase the dead time. Therefore, two PMTs are coupled to each crystal and trigger is made with the coincidence of the two PMT signals. It is also remarkable that, due to the nature of the low energy events, consisting on few separate photons, trigger must be performed at photoelectron level and can be affected by electric noises; therefore, a baseline characterization was also performed (see [31]).

Coincident events populations at low energy selected for ^{22}Na and ^{40}K events have been used to study trigger efficiency, for energy calibration and background understanding (see figure 2.34).

In figure 2.34 it can be observed that most of the events from ^{22}Na, coincident with 1274 keV in the second detector and expected at 0.9 keV and those from ^{40}K, coincident with 1461 keV and expected at 3.2 keV, are triggering our experiment, allowing to estimate very high trigger efficiencies, almost 100% down to 1 keVee.

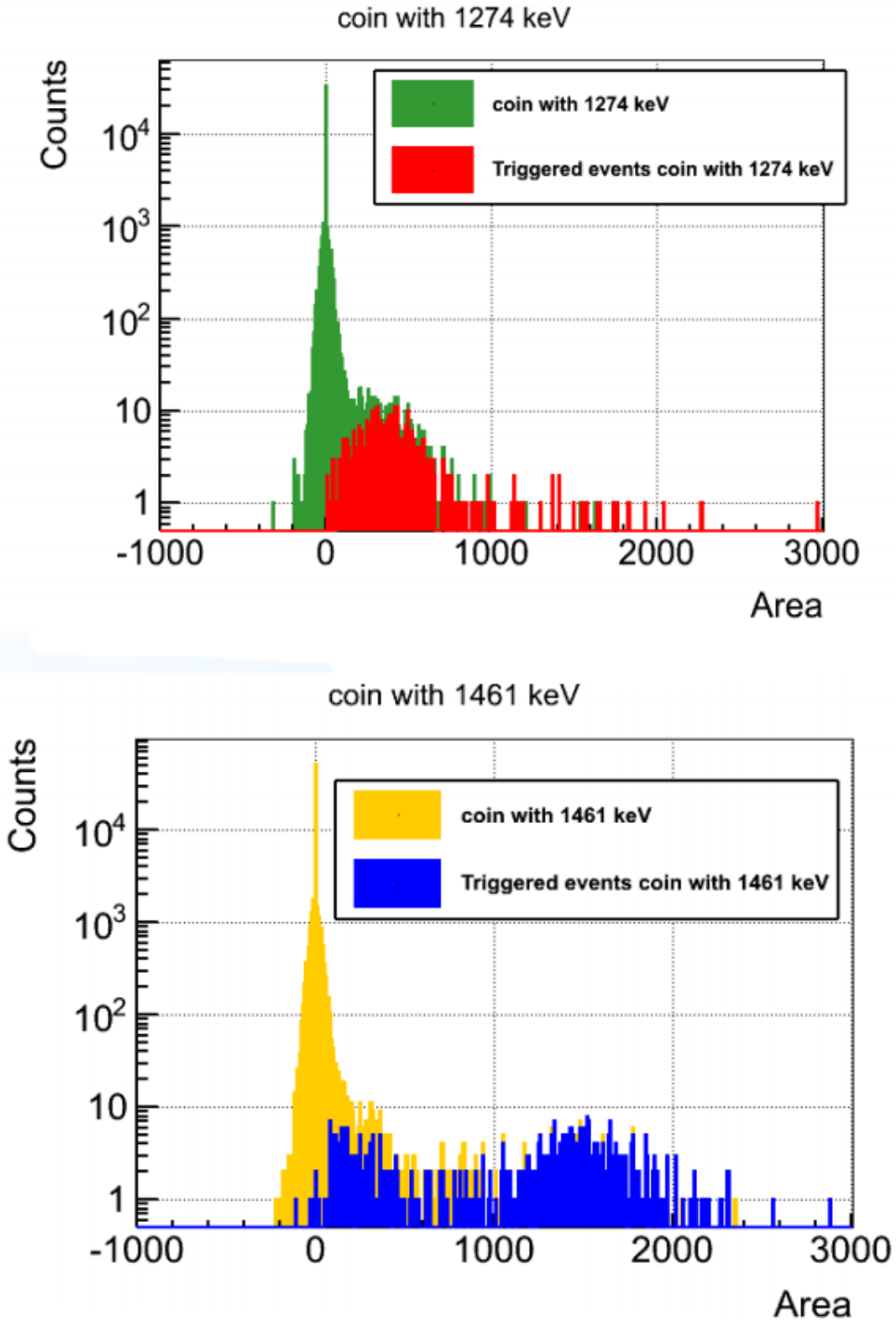

Figure 2.34: *Low energy spectra in one module coincident with a high energy deposition around 1274 keV (top) or 1461 keV (bottom) in a second module. Data shown here correspond to D0 and D1 detectors. The former can be attributed to ^{22}Na in the crystal bulk, the latter to ^{40}K. All events and only triggered events are depicted in different colours.*

2.10.3 Asymmetric events

Since ANAIS–0 prototype, asymmetric events have been observed in the background and calibration data by looking at the different energy sharing between the channels of the two PMTs, PMT0 and PMT1, coupled to each module.
Two types of asymmetric events have been identified in the data.

- *Bulk scintillation events:* These kind of events produce different sharing of the light collected in the two PMT channels depending on the energy release position along the crystal length. These events are originated in the NaI(Tl) crystal.

- *Low energy very asymmetric events:* These kind of events show a much larger pulse area in one PMT than in the other, being not compatible with scintillation events from the bulk. Their origin is probably found at the PMTs.

In order to understand the behaviour of the bulk asymmetric events, the spatial dependence of the light collected for every PMT channel was studied and characterized (see [32]) with a ^{137}Cs source placed in different positions along the axis in ANAIS–0 prototypes. Same procedure was followed with ANAIS–25 modules, D0 and D1 (see figure 2.35).

The spatial dependence was characterized by studying the A parameter, defined as:

$$A = \frac{Q_0 - Q_1}{Q_0 + Q_1} \tag{2.1}$$

where Q_0 and Q_1 are the mean channel associated to the 662 keV gamma line from ^{137}Cs seen by PMT0 and PMT1, respectively. It has to be remarked that parameter A is not distributed around zero because of the different gain in the PMTs and it has to be corrected by subtracting the mean value. Finallly, parameter $A - < A >$ is plotted as a function of the source position along the axis.

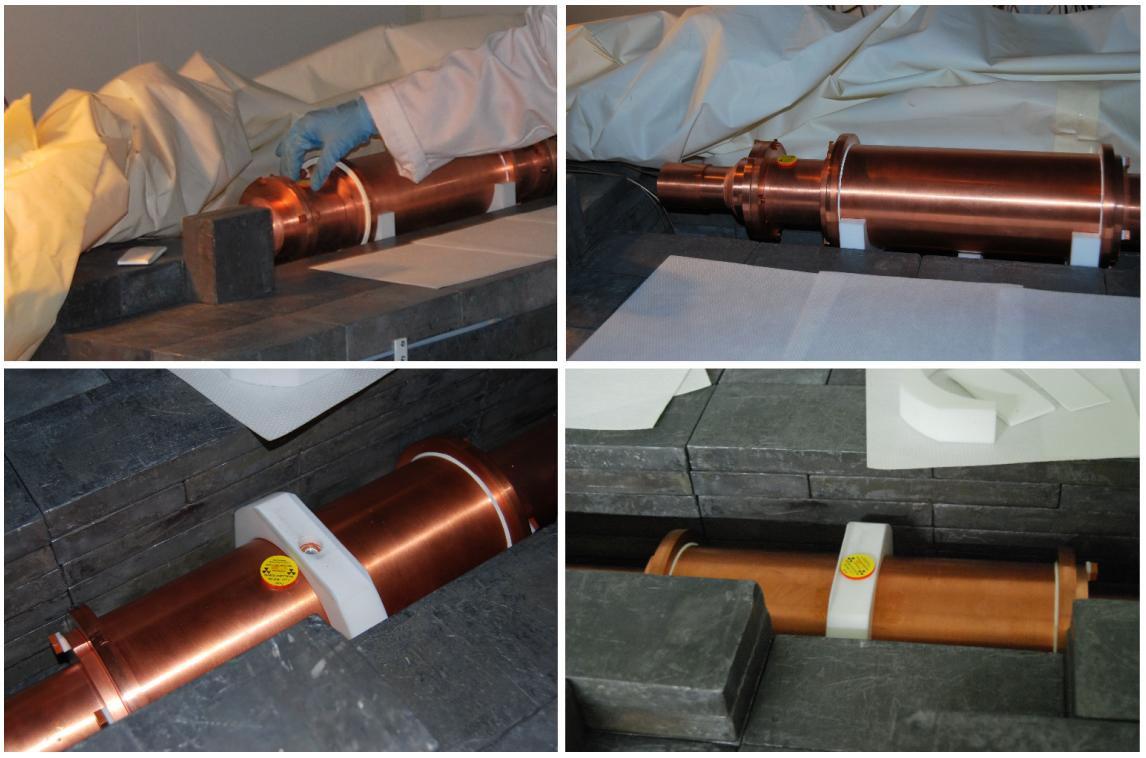

Figure 2.35: ^{137}*Cs calibration source in different positions along the axis in ANAIS–25 modules.*

The quantification of this asymmetry effect for bulk scintillation events has allowed to fix the cut values in the asymmetry parameter in the ANAIS filtering protocols.

Figure 2.36 shows the parameter A for ANAIS–0, PIII, D0 and D1 modules. In this plot, the 0 value is the central position, that is, on the Mylar calibration window, while negative (positive) values mean positions near PMT0 (PMT1). ANAIS–0, D0 and D1 detectors present variations below 2% in the light collected in each PMT. PIII anomalous behaviour might be related to the less coverage of the crystal base by the PMT, but no clear explanation has yet been found in order to understand this issue.

2.10.4 Filtering protocols

Regarding the analysis of the data acquired in ANAIS, the rejection of non–bulk scintillation events is required in order to reduce the energy threshold below 2 keVee [27]. A compromise between high acceptance of NaI scintillation events and also a high

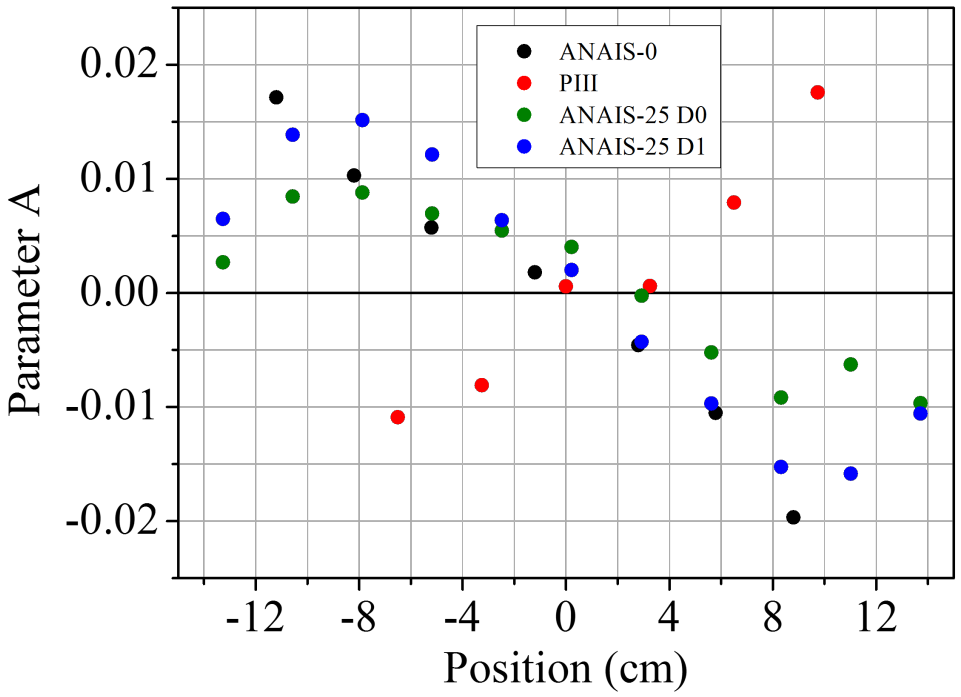

Figure 2.36: *Parameter A, after substracting $< A >$, calculated as a function of the ^{137}Cs source position for ANAIS–0 (black), PIII (red), D0 (green) and D1 (blue).*

rejection factor of other, non–bulk origin events must be established through the filtering. There exist a few aspects on the nature of the signal to consider in the filtering of the data as, among others, dark matter events should not:

- be correlated with muon interactions in vetoes.
- appear in coincidence between two or more modules.
- accumulate in short periods of time.
- show anomalous scintillation time constants in the pulse shape.

As it has been explained before, residual muons are tagged by plastic scintillators covering the shielding, thus, muon related events, coincident with a plastic veto signal can be easily rejected from data.

Due to the slow NaI(Tl) scintillation constant [26], when a very energetic particle interacts in ANAIS set–up, photons at the tail of the pulse can trigger again the acquisition leading to a wrong trigger rate. For this reason, events arriving 0.5 s

after a high energy event are discarded and their live time discounted. Also an algorithm has been developed to count and store the number of peaks in a single pulse. This algorithm requires two parameters: a threshold voltage and the width of the peak. The established criterion is to reject events with less than three peaks in any of the PMTs. Most of these events come from chance coincidences and PMT origin events, and they produce a similar signal to that of the SER, but with a different amplitude/area of that of bulk NaI origin events.

Other filtering criterion is to reject events faster than typical NaI(Tl) bulk scintillation pulses. In order to apply this filter, a few parameters have been studied in the different ANAIS set–ups. Presently there are two main ones in different time–bases:

$$p1 = \frac{area(t_0 + 100\ ns, t_0 + 600\ ns)}{area(t_0, t_0 + 600\ ns)} \tag{2.2}$$

and

$$p2 = \frac{area(t_0 + 500\ ns)}{area(t_0, t_0 + 100\ ns)} \tag{2.3}$$

where t_0 is the time where the pulse overtakes the analysis threshold.

The acceptance efficiency when filtering data as described above must be quantified. It is evaluated from ^{109}Cd calibrations (see figure 2.37); the acceptance efficiency curves obtained for the different detectors are shown in figure 2.38. These curves are used to correct the filtered spectra in order to obtain the final background data; figure 2.39 presents for D3 detector the comparison of raw spectrum and those after the application of this filtering and correction by the corresponding acceptance estimated for bulk scintillation events.

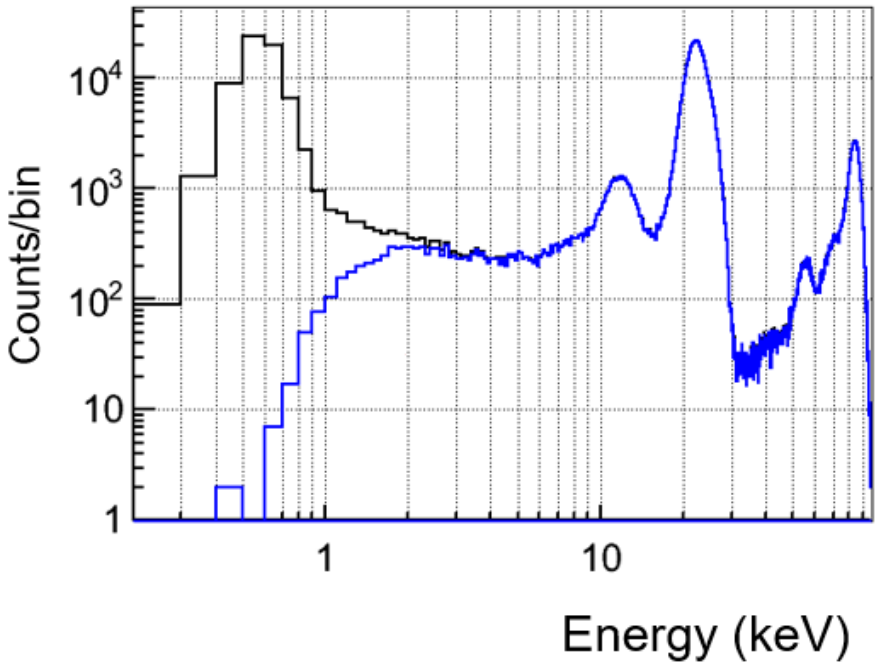

Figure 2.37: ^{109}*Cd calibration before (black) and after (blue) applying the filtering protocols.*

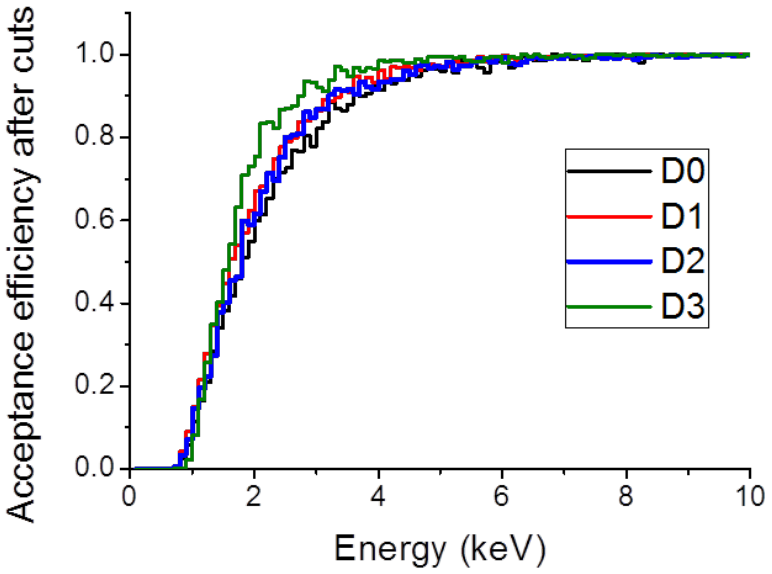

Figure 2.38: *Acceptance efficiency after cuts for D0, D1, D2 and D3 detectors.*

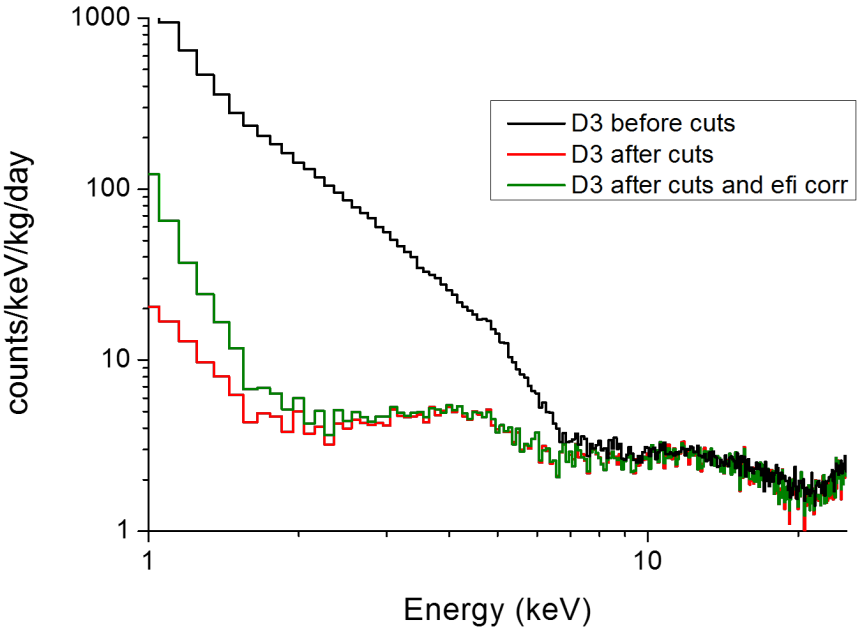

Figure 2.39: *D3 background before (black) and after (red) applying the filtering protocols. Background after filtering and efficiency correction is shown in green.*

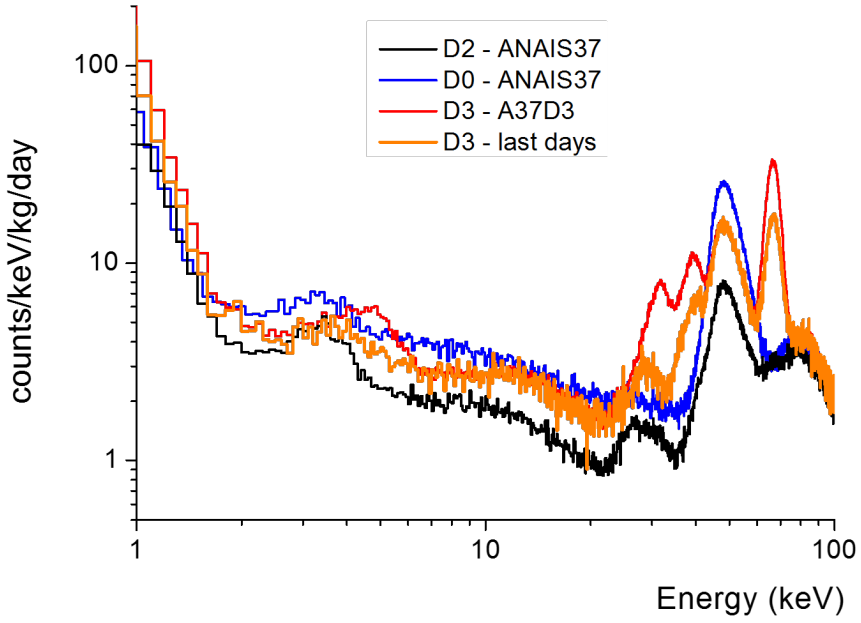

Figure 2.40: *Comparison of the filtered spectra in D0, D2 and D3 detectors in different set–ups.*

Figure 2.40 compares the filtered spectra of D0, D2 and D3 detectors. Cosmogenics has completely decayed in D0, and almost completely in the case of D2, whereas D3 background has still a strong contribution from cosmogenic isotopes, especially in the regions from 30 to 75 keV and 4 to 6 keV. In the region from about 6 to 20 keV the background in D3 is higher than in D2, probably by the effect of the ^{210}Pb content. But on the other hand, the reduced peak from ^{40}K at 3 keV measured for D3 is very promising. Work is still ongoing in order to improve the filtering and the acceptance efficiency estimate, probably underestimated at present [19].

Chapter 3

Background model of ANAIS detectors

A thorough background understanding is a must in experiments searching for a dark matter signal, allowing that the background can be reduced as much as possible, that estimates of the experiment sensitivity are robust, and that any possible time–dependent background is under control. In the frame of the ANAIS experiment, background characterization of the different prototypes and set–ups has always been a main focus, as it is also the case for other projects [182–187]. In this chapter, detailed background models developed for the first three detectors produced by Alpha Spectra company (described in section 2.3.1) and operated at the LSC are presented. First, the background sources considered and the details of their simulation are reviewed in sections 3.1 and 3.2. Validation of the code and the search of an optimum design for the full ANAIS set–up is also discussed in sections 3.3 and 3.4. Then, the quantified background contributions and the comparison with data at different energy ranges and experimental conditions for the different set–ups are presented in sections 3.5, 3.6 and 3.7.

3.1 Background sources

Regarding the possible background sources that can contribute to the experimental background, a distinction between sources in the NaI crystal and those in external components is considered.

3.1.1 External components

Activities of most of the external components were measured by HPGe spectrometry at LSC before being installed in the set-up. A summary of the measured activities of the components of ANAIS–25 and ANAIS–37 are shown in table 3.1. Usually, the most important external contribution to the background comes from the photomultipliers. Every PMT unit to be used in the full experiment has been already screened, finding compatible levels of activity among them; values quoted in table 3.1 correspond to the six units used in the ANAIS–25 and ANAIS–37 set–ups and to the mean of all screened units.

Component	Unit	^{40}K	^{232}Th	^{238}U	^{226}Ra	Others
PMTs (R12669SEL2)	mBq/PMT	97±19	20±2	128±38	84±3	
		133±13	20±2	150±34	88±3	
		108±29	21±3	161±58	79±5	
		95±24	22±2	145±29	88±4	
		136±26	18±2	187±58	59±3	
		155±36	20±3	144±33	89±5	
mean activity all units	mBq/PMT	111±5	20.7±0.5	157±8	82.5±0.8	
Copper encapsulation	mBq/kg	<4.9	<1.8	<62	<0.9	^{60}Co: <0.4
Quartz windows	mBq/kg	<12	<2.2	<100	<1.9	
Silicone pads	mBq/kg	<181	<34		51±7	
Archaeological lead	mBq/kg		<0.3	<0.2		^{210}Pb: <20
Inner volume air	Bq/m^3					^{222}Rn: 0.6

Table 3.1: *Activities of the external components considered as background sources in the simulation of the different ANAIS prototypes and set–ups. Except for the inner volume air (see text for details), the values have been measured by HPGe spectrometry at the LSC. Upper limits are given at 95% C.L.*

There are not direct measurements of most of the materials used in the housing of the AS crystals, but upper limits and values for similar quality copper and synthetic quartz, for instance, from ANAIS–0 prototype have been considered (see table 3.1). For archaeological lead, upper limits on ^{210}Pb, ^{232}Th and ^{238}U activities in table 3.1 and presented in [188] have been used in the model.

Radon activity in the laboratory air is being continuously monitored, but for

radon content in the air filling the inner volume of the shielding, there is no direct measurement. The inner volume of the shielding is flushed with boil–off nitrogen, to guarantee its radon–free quality. Therefore, a value for the radon content in the inner volume air of about one hundredth of the external one has been assumed in our background model (0.6 Bq/m^3), compatible with the absence of lines coming from radon daughter isotopes in the measured background.

Contribution from fast neutrons and environmental gamma background has also been estimated, being negligible at the present sensitivity level of the experiment.

On the other hand, contribution from muons interacting in the crystal (and other muon related events) are vetoed by the coincidence with a signal in the plastic scintillators covering the top and lateral faces of the shielding. Even though the active veto was not in operation during the whole data taking this work refers to, the muon induced background is negligible [27] and thus, it has not been considered in the ANAIS background model.

3.1.2 NaI crystal

Background coming from inside the NaI(Tl) crystals is the dominant background contribution and thus, it has to be studied in a much thorough depth. The most relevant radionuclides activity has been directly measured for ANAIS crystals applying different techniques [178]. ^{40}K bulk content is estimated by searching for the coincidences between 3.2 keV energy deposition in one detector (following electron capture, EC) and the 1460.8 keV gamma line escaping from it and being fully absorbed in another detector [25]. ^{210}Pb, ^{232}Th and ^{238}U chains activities are determined on the one hand, by quantifying Bi/Po and alpha-alpha sequences, and on the other, by comparing the total alpha rate, determined through PSA, with the low energy depositions attributable to ^{210}Pb, which are fully compatible. The potassium concentration and alpha activity reported by the KIMS collaboration for similar crystals produced also by Alpha Spectra [189] are of the same order than those measured for ANAIS detectors.

Data taking for ANAIS AS detectors started very soon after their arrival at the LSC. This allowed the observation of short–life isotopes activated during their stay on surface. Despite transportation is done by boat, in order to avoid higher

activation rates associated to air travel, relevant cosmogenic activation has been observed in all the ANAIS AS modules.

3.1.2.1 ^{40}K activity

^{40}K bulk contamination is typically the most relevant radioactive contribution for NaI(Tl) detectors. It is specially important its contribution to the background in the very low energy region, and thus, a very good knowledge of the ^{40}K contamination is required to properly estimate the sensitivity prospects achievable for ANAIS.

The technique used to estimate the ^{40}K activity in the bulk of ANAIS crystals is the measurement in coincidence: one detector measures the energy released by the X–ray/Auger electrons emissions of argon, amounting a total energy release of 3.2 keV, following the K–shell EC of ^{40}K, while another detector measures the high energy gamma at 1460.8 keV, escaping from the former, and being fully absorbed in the latter. In figure 3.1 a simplified ^{40}K decay diagram is shown. From the measured coincidence rates and the corresponding efficiencies estimated with Geant4 package, the ^{40}K activity in the crystal can be deduced.

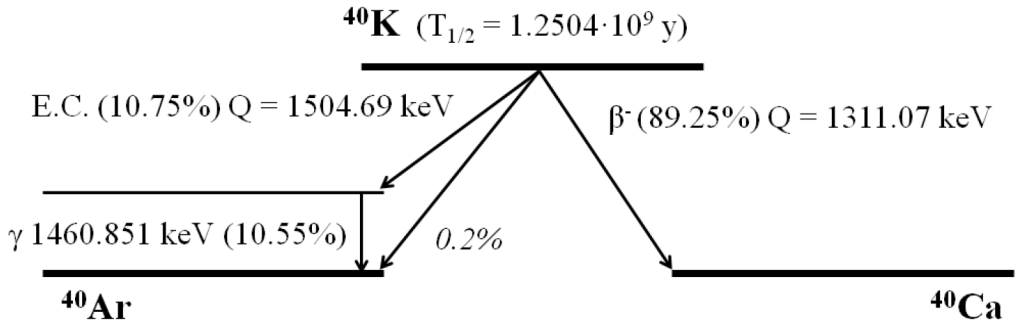

Figure 3.1: *Simplified ^{40}K decay diagram.*

The contribution at 3.2 keV after K–shell EC in ^{40}K is the most worrisome background in the search for dark matter, falling in the region of interest, below 6 keVee. A part of these events is moved to higher energies by the simultaneous interaction of the high energy gamma in the same detector, another part is vetoed by an interaction of the high energy gamma in another detector, however, a residual peak at 3.2 keV can jeopardize the search for dark matter if ^{40}K content is not at a few ppb level. It is worth noticing that the rate of the direct decay of ^{40}K to the ground state of ^{40}Ar through EC (at the 0.2% level) has not been yet experimentally measured, and hence, the uncertainty on the corresponding branching ratio is really

high [190] [191]. This decay is important for the ANAIS background because those events can not be rejected by the coincidence method.

The results obtained for ANAIS–25 detectors, D0 and D1 (see table 3.2) evidenced a moderate contamination of ^{40}K, still above the initial goal of ANAIS (20 ppb[1] of K) but acceptable. The potassium content of D2 was analyzed using the same technique applied to previous prototypes, obtaining a value compatible with those of D0 and D1, whereas the preliminary value obtained for D3 is clearly lower.

Detector	Unit	^{40}K	^{232}Th	^{238}U	^{210}Pb
D0	mBq/kg	1.4±0.2	(4±1) 10^{-3}	(10±2) 10^{-3}	3.15±0.10
D1	mBq/kg	1.1±0.2	(4±1) 10^{-3}	(10±2) 10^{-3}	3.15±0.10
D2	mBq/kg	1.1±0.2	(0.7±0.1) 10^{-3}	(2.7±0.2) 10^{-3}	0.70±0.10
D3	mBq/kg	0.57±0.06	(0.6±0.3) 10^{-3}	(4±1) 10^{-3}	1.8±0.1

Table 3.2: *Measured activity in NaI(Tl) crystals for D0, D1 and D2 detectors using ANAIS–25 and ANAIS–37 data and combining different analysis techniques. Preliminary results for D3 detector from A37D3 set–up are also shown.*

3.1.2.2 The ^{210}Pb problem

PSA in NaI(Tl) scintillators allows to powerfully discriminate the alpha origin energy depositions in the bulk and, hence, to identify and quantify the presence of different isotopes from the ^{238}U and ^{232}Th chains. Bi/Po and alpha–alpha sequences have been also studied in order to better quantify the upper segments on the ^{238}U and ^{232}Th chains.

A specific digitization line for high energy events has allowed to select alpha origin events by PSA. Alpha energy depositions produce in NaI(Tl) a faster scintillation than that corresponding to beta–gamma–muon events, and thus, events can be distinguished by comparing the area and the amplitude of the pulse. Red events in figure 3.2 correspond to alpha particles depositions (faster) and those marked in black to beta–gamma–muon events. Total alpha rate in all the studied AS modules is mostly attributed to ^{210}Po decay, as a result of the crystal contamination in the parent, ^{210}Pb.

[1] 1 ppm K = 31 mBq/kg ^{40}K

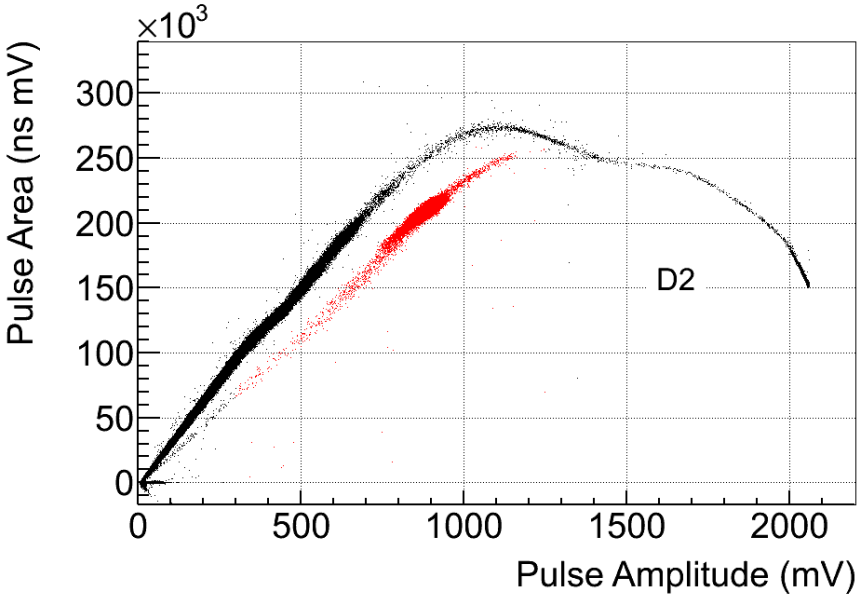

Figure 3.2: *Pulse area as a function of the pulse amplitude in detector D2. Alpha events are shown in red while beta–gamma–muon interactions are shown in black.*

Testing the crystals manufactured by Alpha Spectra for ANAIS, it was found that ^{232}Th and ^{238}U activities were low enough but an out–of–equilibrium activity of ^{210}Pb at the mBq/kg level was observed (see table 3.2), precluding the fulfilment of the background goal of the ANAIS experiment. The lower part of the ^{238}U chain (see figure 3.3) can be frequently found out of equilibrium, being one possible origin of such contamination the entrance of radon during growing and/or machining of the detectors. After a few weeks, only ^{210}Pb would remain. ^{210}Pb content has been quantified by the total alpha rate (determined by PSA and attributed to the daugther, ^{210}Po) and the low energy spectrum, dominated by the decay of the ^{210}Pb itself (see figure 3.4).

The origin of this large ^{210}Pb contamination found in ANAIS–25 crystals was identified with the timing information of the procedures followed by the company (see section 2.9.2). It is compatible with a contamination at the end of the purification process and growing of the crystal (see figure 3.5). This conclusion was addressed by Alpha Spectra and the company modified its procedures in order to reduce the ^{210}Pb content in the next crystals produced for ANAIS. D2 crystal showed a significantly reduced ^{210}Pb content in comparison with previous D0 and D1 crystals: total alpha rate is a factor 5 lower (see table 3.2).

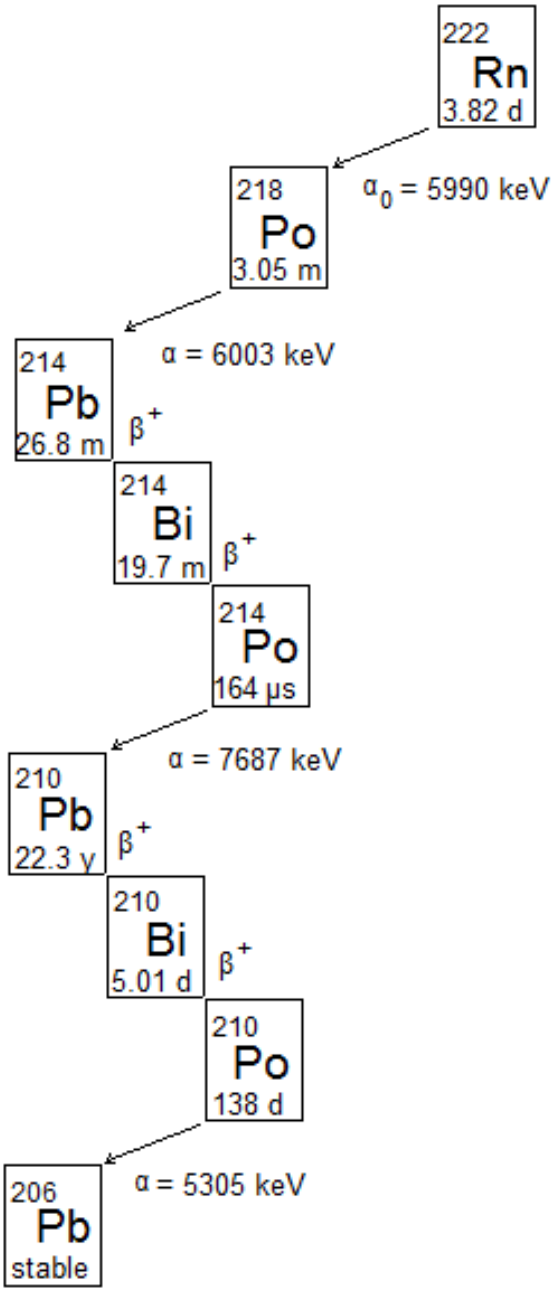

Figure 3.3: ^{222}Rn *decay chain.* ^{210}Pb *is the isotope with the longest half–life.*

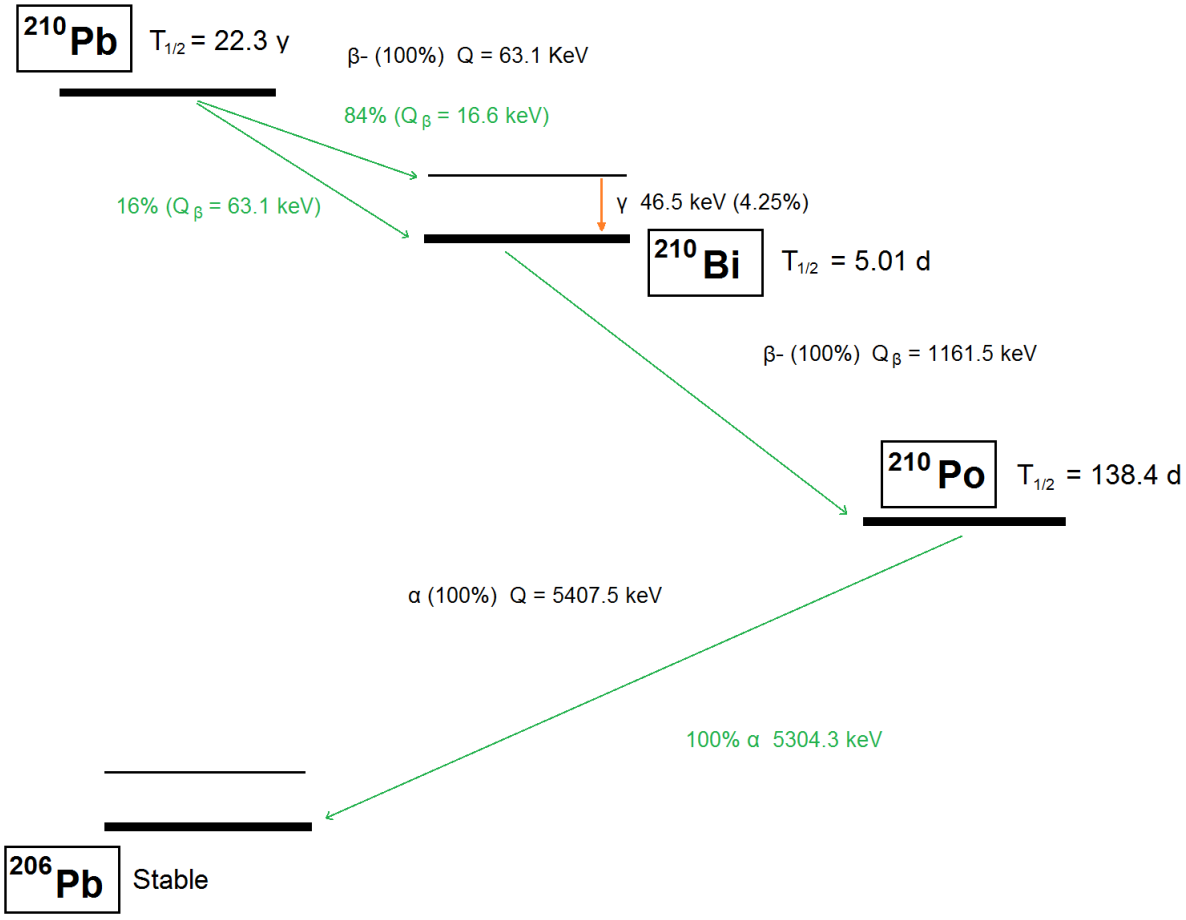

Figure 3.4: ^{210}Pb *decay scheme.*

At the alpha region of the energy spectra measured for the detectors, the prominent peak due to the ^{210}Po decay does not show the pure structure expected from a crystal bulk ^{210}Pb contamination (see figure 3.6) [32]. The double peak structure is not fully understood yet. It is worth noting that sharing of events between these populations is very similar for D0 and D1 modules, but different from those corresponding to D2 and D3. Therefore, the possibility of a surface deposition was carefully analyzed, as it will be shown in section 3.5.1.

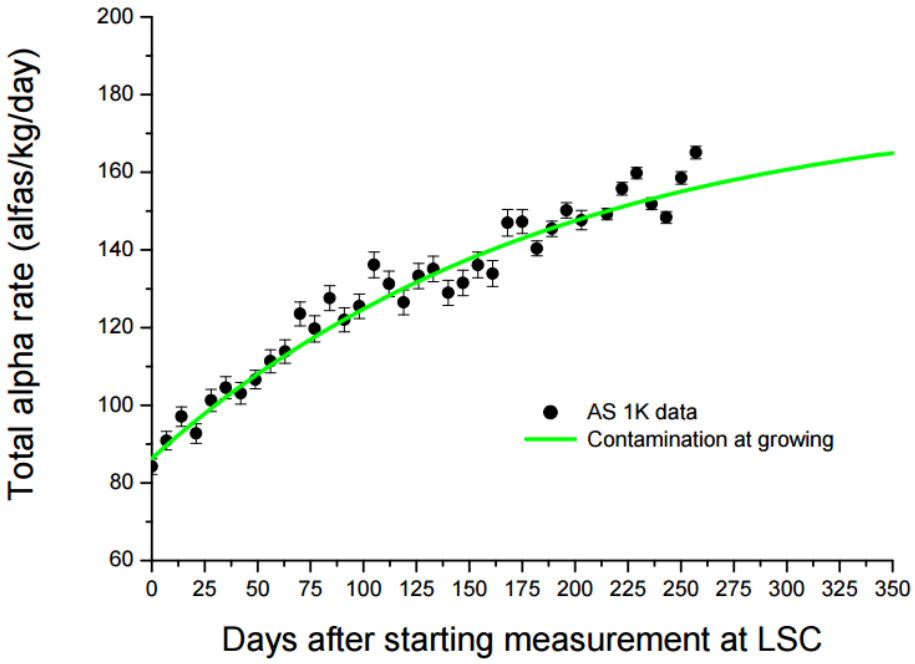

Figure 3.5: *Total alpha rates in AS1K module weekly averaged. Green: expectation of the rate evolution if a contamination in ^{210}Pb entered along the growing procedure.*

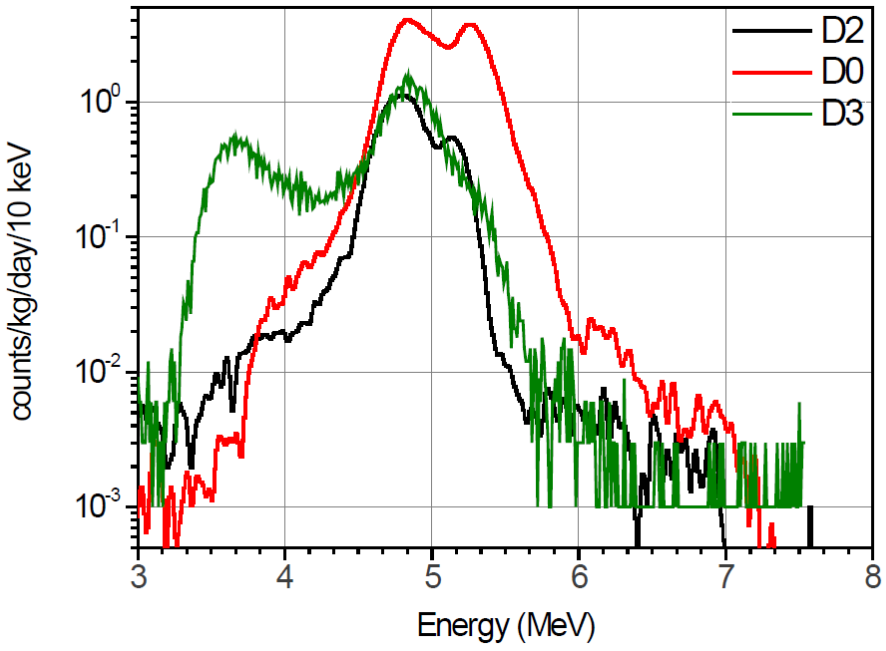

Figure 3.6: *Alpha region of the measured spectra for D0 (similar to that of D1), D2 and D3 detectors.*

3.1.2.3 Cosmogenic activation

Thanks to the very good performance of ANAIS detectors and the prompt data taking starting after storing the detectors underground, a detailed study of cosmogenic radionuclide production in NaI(Tl), due to the exposure time spent while being the detectors manufactured and transported, has been performed using mainly data from ANAIS–25 set-up [192]. The initial activity, A_0, corresponding to the moment of storing crystals underground at LSC was derived, studying the exponential decay of the identifying signature produced by each isotope; production rates at sea level were derived considering the exposure history of the crystals. The crystal growth and detector manufacture took place at Alpha Spectra facilities in Grand Junction, CO (US) and detectors were shipped from US to Spain by boat.

Most of the cosmogenically induced isotopes dissapeared and their decay was observed along the first months of data taking, but some others with larger lifetime remain and must be included in the background models. The production of some induced I, Te and Na isotopes was well characterized and it was considered also as a background source of the detectors; table 3.3 shows the list of all identified products and their half-lives, together with the measured initial activities. ^{22}Na could be specially worrisome for dark matter searches because the binding energy of the K–shell of its daughter Ne is 0.87 keV, falling the corresponding energy deposition in the region of interest, and having a long enough half–life to compromise the first years of data taking. A direct estimate of ^{22}Na activity in D2 crystal was carried out by analyzing coincidences from data corresponding to 111.4 days from a special set-up from October 2015 to February 2016 where only D0 and D2 detectors and a blank module were used. In particular, profiting from the reduced cosmogenics in this period, D2 spectrum in coincidence with 1274.5 keV depositions in D0 was analyzed. It is worth noting that the ^{22}Na initial activity in D0 deduced from the equivalent analysis is in perfect agreement with the first estimate in [192]. The obtained value for the initial activity in D2, A_0=(70.2 $\pm$ 3.9) kg^{-1}d^{-1}, is more than a factor of two lower than the one deduced for D0 and D1 detectors. This result is compatible with a lower time of exposure to cosmic rays, taking into account the ^{22}Na half–life, longer than that corresponding to I and Te products.

As it will be discussed later, there are hints of the production of other isotopes like ^{3}H, ^{109}Cd and ^{113}Sn in the NaI(Tl) crystals, even if they could not be directly identified in the first analysis of cosmogenic activation presented in [192]. Apart

from this, ^{129}I can be present in the NaI crystals, produced either as residual product of uranium spontaneous fission, or by cosmic rays reactions, having a broad range of activity values in iodine compounds depending on the ore origin. Due to its long lifetime and the difficulty to disentangle its signal from other background contributions, the amount of ^{129}I in D0, D1 and D2 crystals could not be quantified. Because of that, the ^{129}I contribution considered in the background model of these modules has been assumed to be the same as estimated by DAMA/LIBRA (^{129}I/^{nat}I = (1.7 ± 0.1) 10^{-13}) [137], corresponding to an activity of 0.94 mBq/kg.

Table 3.3: *Measured initial activities underground (A_0) for the identified cosmogenic isotopes in NaI(Tl) crystals using ANAIS–25 data [192]. Half-lives of the products are also indicated [193].*

Isotope	$T_{1/2}$ (d)	A_0 (kg^{-1}d^{-1})
^{126}I	12.93±0.05	430±37
^{125}I	59.407±0.009	621.8±1.6
^{127m}Te	107±4	32.1±0.8
^{125m}Te	57.40±0.15	79.1±0.8
^{123m}Te	119.3±0.1	100.8±0.8
^{121m}Te	154±7	76.9±0.8
^{121}Te	19.16±0.05	110±12
^{22}Na	(2.6029±0.0008) y	159.7±4.9

3.2 Background modeling

The contribution of all the background sources considered (and detailed in section 3.1) to the background levels of the ANAIS prototypes has been simulated by Monte Carlo using the Geant4 package [194]. A detailed description of the set–ups was implemented: NaI crystals, Teflon wrapping, copper encapsulation, quartz windows, silicone pads, Mylar window, photomultipliers and the shielding made of archaeological and standard low activity lead. Figure 3.7 shows the views of the Geant4 geometry for ANAIS–25 and ANAIS–37 set-ups.

Simulation of the decay of radioactive contaminations, after carefully checking the energy conservation in the decay of all considered isotopes, has been made with

the Geant4 Radioactive Decay Module. The low energy models based on Livermore data libraries were considered for α, β and γ emissions. In the components, a uniformly distributed bulk contamination was assumed and activities (or derived upper limits) given in tables 3.1, 3.2 and 3.3 considered. For each simulated event, defined considering an energy integration time of 1 μs, the energy deposited at each detector by different types of particles has been recorded separately in order to be able to build the energy spectrum afterwards, filtering alpha deposits above 2.5 MeV (as it can be made in real data by PSA) and correcting each component with the corresponding relative scintillation efficiency factor. In this work, a constant value of 0.6 has been taken as relative efficiency factor for alpha particles in the building of the electron equivalent energy spectra and energy from nuclear recoils has been neglected. Energy spectra at different conditions have been constructed to allow direct comparison with data obtained from detectors. Production of scintillation at the NaI(Tl) crystals and the subsequent light propagation and collection have not been simulated here.

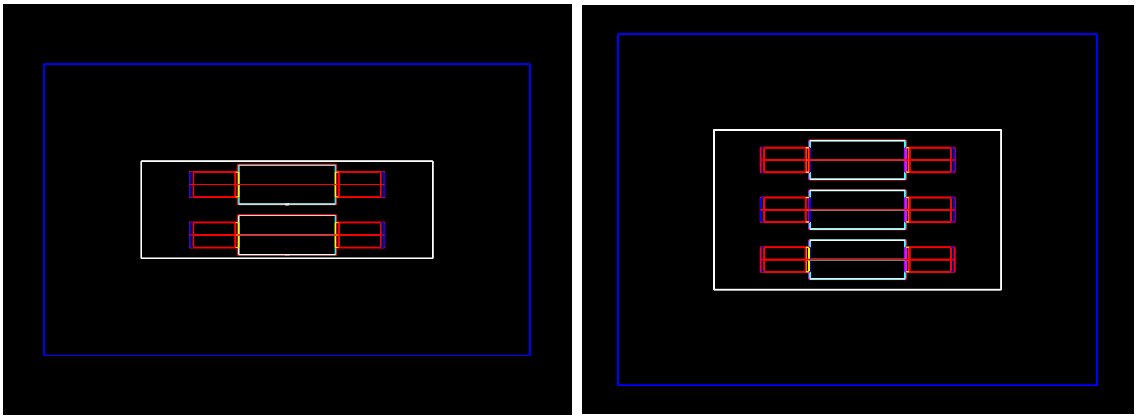

Figure 3.7: *Geometry of the ANAIS–25 (left) and ANAIS–37 (right) set-ups implemented in the Geant 4 simulations.*

3.3 Code validation

The reliability of a background model lies on an accurate quantification of the different sources (shown in section 3.1 for ANAIS detectors), a careful computation of their contribution to the experiment (typically made by Monte Carlo simulations, presented in section 3.2) and a continuous validation of the code by comparing the model with experimental data at all energy ranges (as it will be made in sections 3.5.1 and 3.6.1).

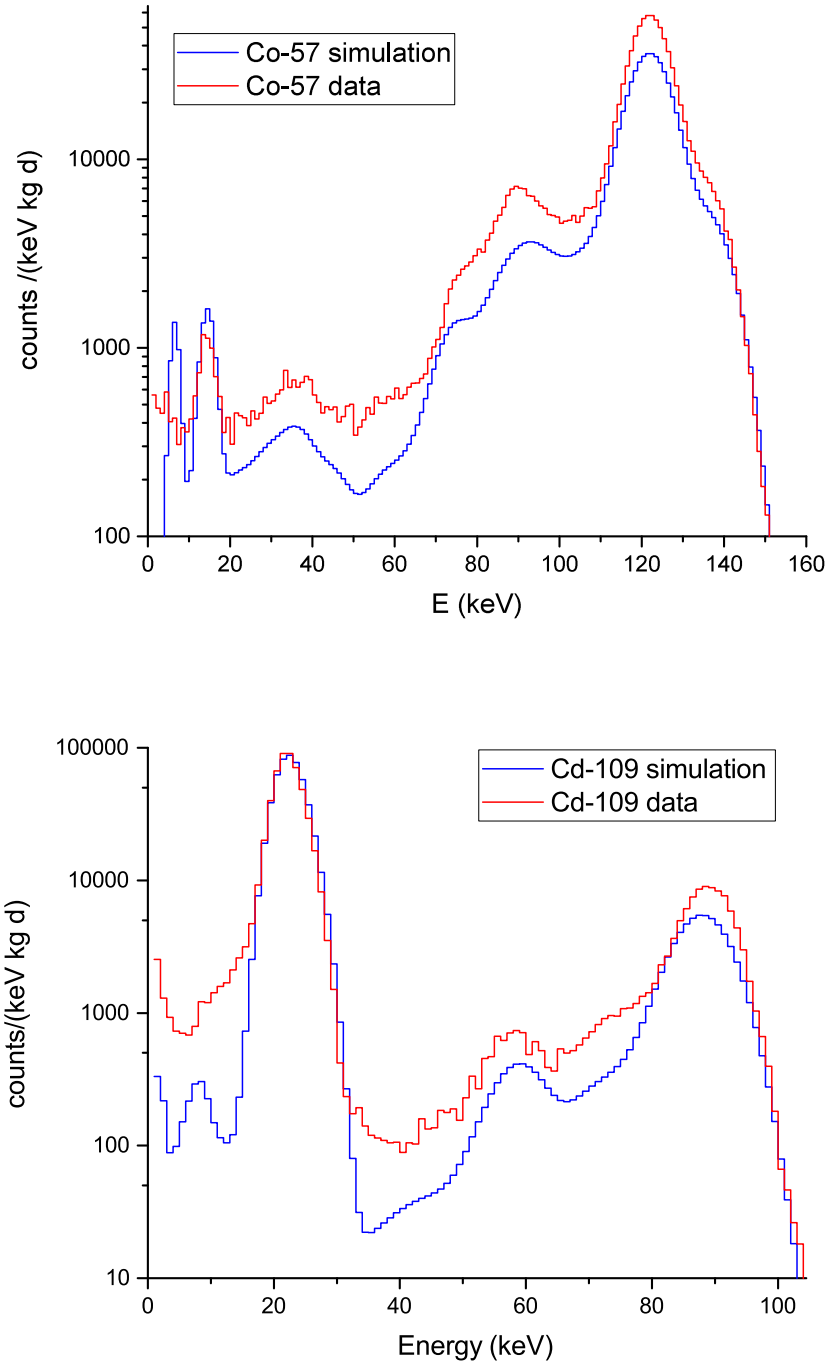

Figure 3.8: *Measured and simulated spectra for* ^{57}Co *(top) and* ^{109}Cd *(bottom) calibration sources in the low energy range. Simulations have been normalized considering the activity of the sources.*

In ANAIS–25 set–up, an additional code validation using experimental calibration spectra has been made in the same way it was done in ANAIS–0 prototype [24]. Energy spectra for ^{57}Co and ^{109}Cd calibration sources with their present activity (0.017μCi for ^{57}Co and 0.1 μCi for ^{109}Cd) have been simulated to validate the code, specially at the region of interest. Experimental and simulated spectra for these two radioactive sources measured at ANAIS–25 set-up have been compared (see figure 3.8). In an attempt to quantify the agreement, table 3.4 presents different ratios between measured and simulated areas of some peaks or integral regions.

From the comparison between simulations and experimentally measured data, it can be concluded that Geant4 simulation reproduces qualitatively well all the spectral features above 10 keV. The observed discrepancies, specially at the lowest energies, could be due to some systematics which could be related with the imprecise knowledge of the sources geometry and possible misplacement of the source with respect to the Mylar window.

Source	Initial activity	Ratio area (a)	Ratio area (b)	Ratio area (c)
^{57}Co	(1.0 $\pm$ 0.1) μCi	1.50	0.91	1.50
^{109}Cd	(1.0 $\pm$ 0.1) μCi	1.07	0.99	1.57

Table 3.4: *Nominal activities of the ^{57}Co and ^{109}Cd sources and ratio between the areas (measured and simulated) for an energy range from 0 to 160 keV (a), for 14.4 keV line in ^{57}Co and 22.1 keV line in ^{109}Cd (b) and for 122.1 keV line in ^{57}Co and 88.0 keV line in ^{109}Cd (c) at 1σ window width. Activities at the time of the measurement were considered for the simulation.*

3.4 Optimization of ANAIS design

Several parameters in the module geometry were analyzed in order to optimize the rejection power of the experiment, profiting from the multiple detector design. For this purpose, rejection power for ^{40}K events in ANAIS–25 layout was studied. The measured ^{40}K activity in ANAIS–25 crystals (see table 3.2) meant an improvement of almost an order of magnitude with respect to ANAIS–0 potassium content and although close to the ANAIS goal of 20 ppb of potassium, a factor of two could be decisive to jeopardize the feasibility of the experiment. While Alpha Spectra was

trying to further purify the NaI powder, and get lower potassium content, simulation of this ^{40}K rejection factor by coincidence between modules when modifying the design parameters was faced. High modularity is usually considered an asset in these issues, but the large size of the crystals is also an advantage, preventing the high energy gamma of ^{40}K from escaping without interaction and thus, removing the dangerous low energy events from the region of interest.

Some examples of the geometries considered, using D0 and D1 detectors, in an experimental layout similar to that of ANAIS–25, are shown in figure 3.9.

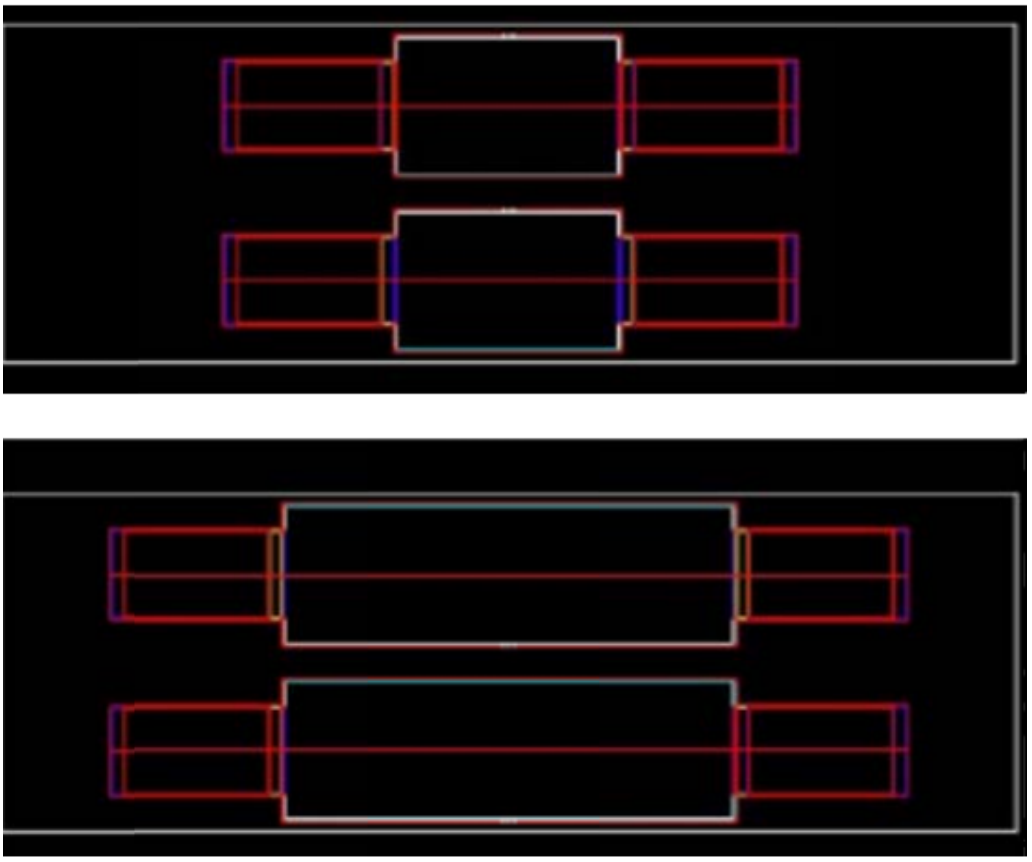

Figure 3.9: *Two module geometries considered for the analysis of the ^{40}K rejection factor by coincidences between modules in ANAIS–25 layout: NaI(Tl) crystal lengths of 198.45 mm (top) and of 398.45 mm (bottom), having the same crystal radius, whereas AS crystals length is 298.45 mm.*

Different parameters have been analysed in this study: length and radius of the crystals (giving different detection mass per module), distance between adja-

cent modules, and thickness of the copper encapsulation. For this study, only the 1460.8 keV gamma following ^{40}K EC decay has been simulated. The percentage of gammas escaping without interacting in any of the two NaI(Tl) crystals (and originating therefore an event in the low energy region of interest) has been used as indicator of the rejection factor achievable.

The existence of a small percentage of ^{40}K decays that cannot be vetoed due to the lack of coincident high energy gamma (see figure 3.1) has a negligible effect on the conclusions derived using this approximation.

The dependence of escape probability for the 1460.8 keV gamma on copper encapsulation thickness, distance between modules (defined as the distance between the outer parts of the copper encapsulation), detector radius and detector length is shown from figure 3.10 to 3.13. Only one parameter is changed each time, keeping the other ones as in the real AS modules (see table 3.5). The relative error in the escape probability due to the number of simulated histories is of the order of 0.1% in all cases. Notice that mass crystal per module is different when modifying detector radius and length.

Radius	60.32	mm
Length	298.45	mm
Mass	12.52	kg
Copper thickness[2]	2	mm
Distance between adjacent modules	30	mm

Table 3.5: *Alpha Spectra modules dimensions and distance between adjacent modules as in ANAIS-25 set-up.*

[2]Although in this study the reference value of the copper thickness was considered as 2 mm, the company, in later conversations, gave 1.5 mm as the correct value. Therefore, the latter has been used in following simulations.

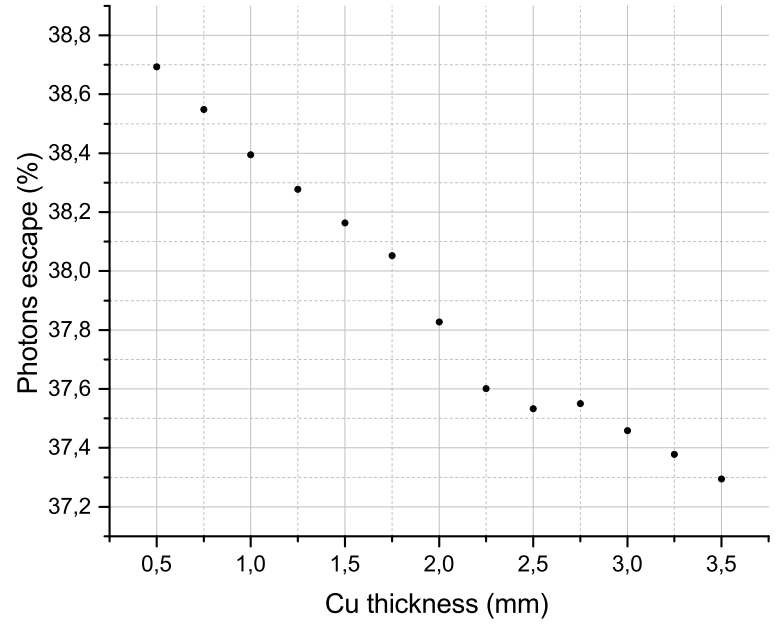

Figure 3.10: *1460.8 keV escape probability without interaction in any module as a function of the copper encapsulation thickness in the ANAIS–25 configuration.*

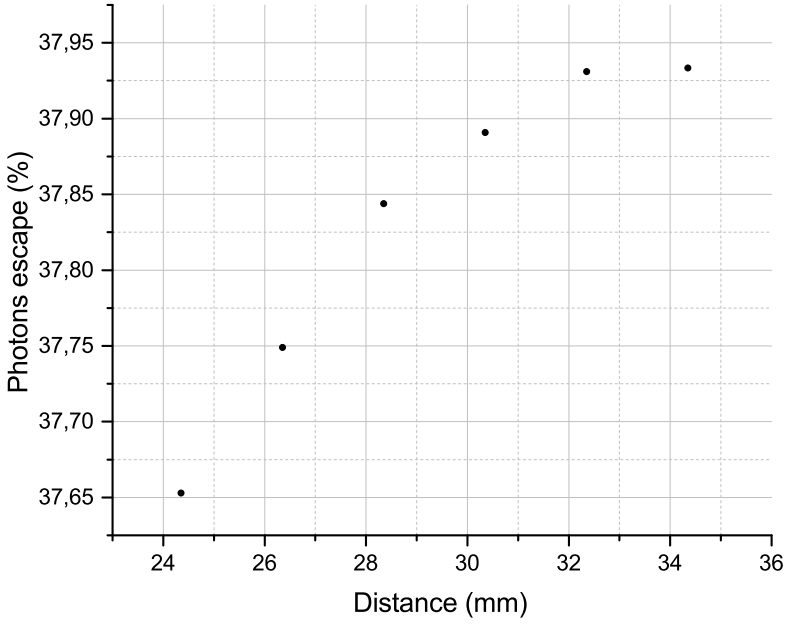

Figure 3.11: *1460.8 keV escape probability without interaction in any module as a function of the distance between adjacent modules in the ANAIS–25 configuration.*

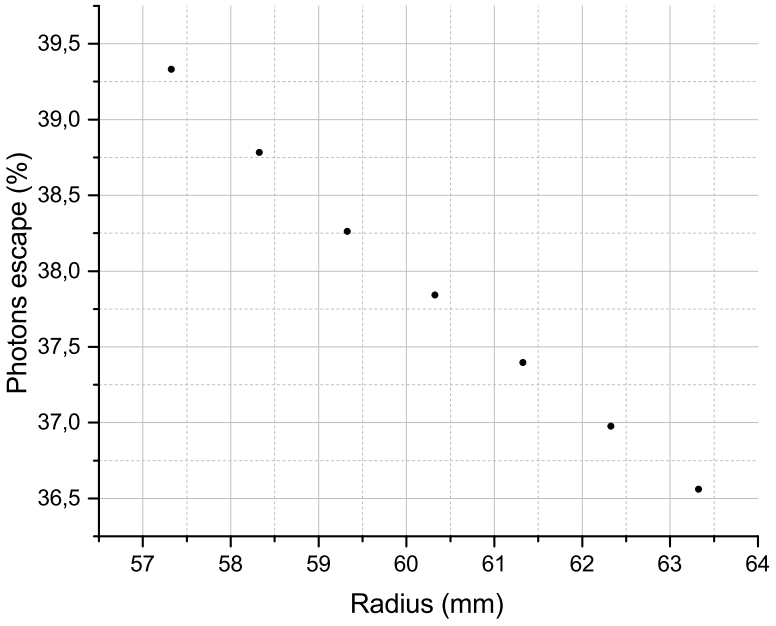

Figure 3.12: *1460.8 keV escape probability without interaction in any module as a function of the crystal radius in the ANAIS–25 configuration.*

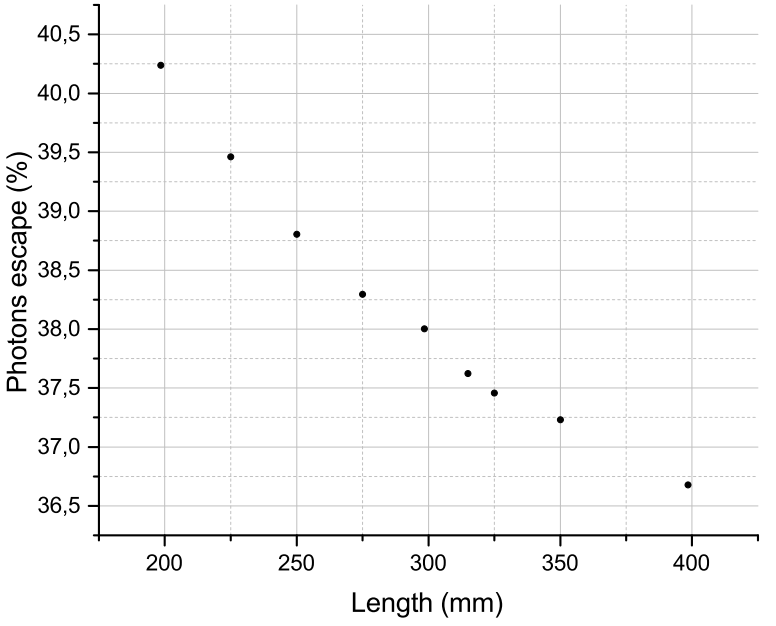

Figure 3.13: *1460.8 keV escape probability without interaction in any module as a function of the crystal length in the ANAIS–25 configuration.*

Simulations with more than two modules were carried out in order to explore the improvement in rejection power with the full ANAIS experiment in different hypothetical module configurations. At first, a configuration of 20 modules, 12.5 kg each in a 5 × 4 matrix (ANAIS–250) was considered (see figure 3.14). Only the 1460.8 keV gamma following the ^{40}K EC decay has been simulated and again, the percentage of gammas escaping without interacting in any of the 20 NaI modules has been taken as indicator of the rejection factor achievable. Photons were uniformly distributed over all the crystals and emitted with random directions. Figures 3.15 to 3.18 show the dependence of the escape probability with the analyzed parameters.

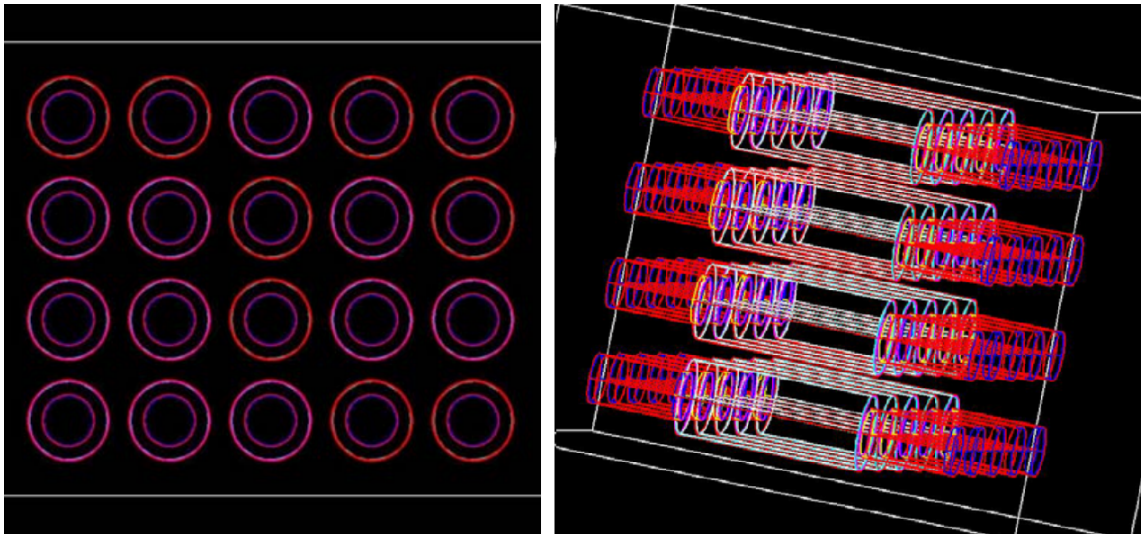

Figure 3.14: *Different views of the complete geometry developed for the simulations of the ANAIS–250 setup in a 5 × 4 configuration (20 modules).*

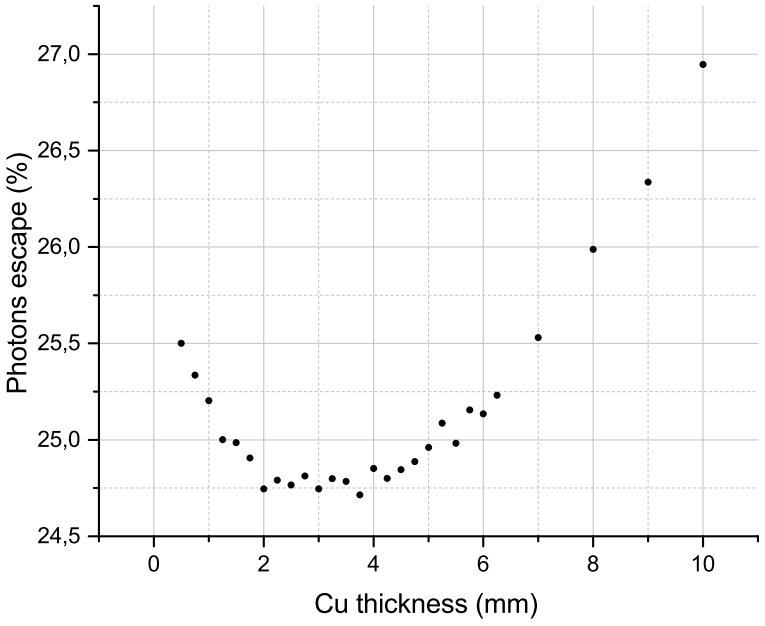

Figure 3.15: *1460.8 keV escape probability without interaction in any module as a function of the copper encapsulation thickness in the ANAIS–250 configuration.*

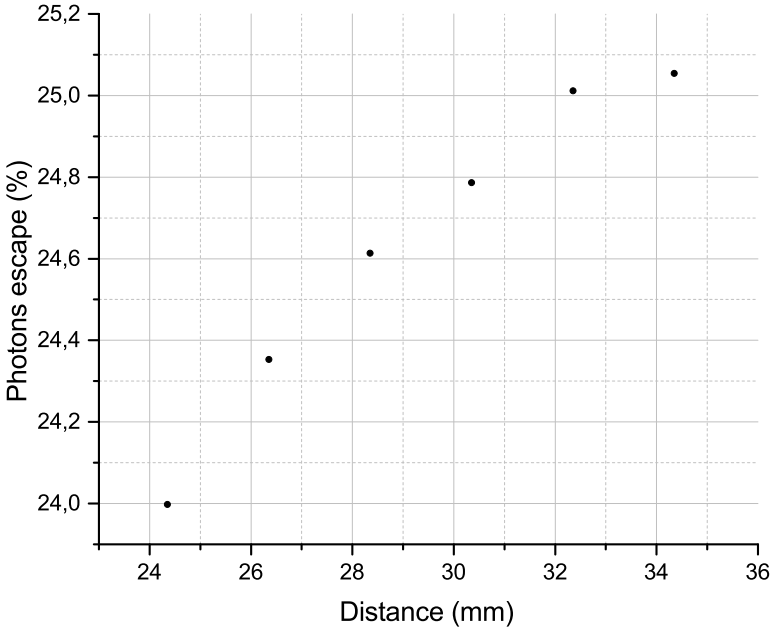

Figure 3.16: *1460.8 keV escape probability without interaction in any module as a function of the distance between adjacent modules in the ANAIS–250 configuration.*

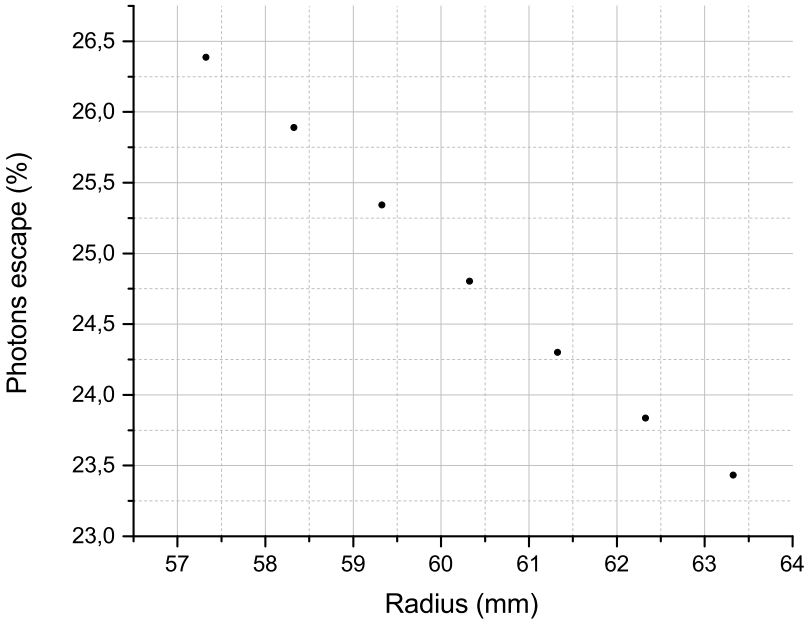

Figure 3.17: *1460.8 keV escape probability without interaction in any module as a function of the detector radius in the ANAIS–250 configuration.*

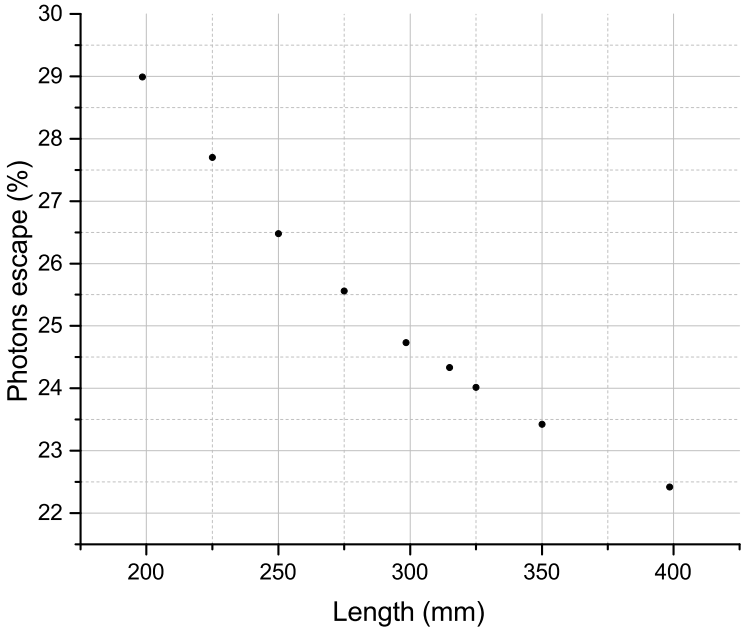

Figure 3.18: *1460.8 keV escape probability without interaction in any module as a function of the detector length in the ANAIS–250 configuration.*

The results point to a reduction of the 1460.8 keV gamma escape probability, going down from $\approx 38\%$ at ANAIS–25 set-up until $\approx 25\%$ in ANAIS–250 studied configuration.

From this study it can be concluded that:

- Rejection factors evaluated as one less the probability of escape of the 1460.8 keV photon, larger than 60% have been obtained for all the geometries tested.
- Larger and closer crystals offer a better rejection factor while for the copper encapsulation thickness a best value between 2 and 4 mm has been found (see figure 3.13). Two opposite trends in photon interaction can be induced by the variation of the copper encapsulation thickness. Total absorption in copper increases with copper thickness and then the escape probability should be higher; but Compton scattering probability also increases, and can make the escape probability reduce due to detection of the backscattered photons. Given the copper mean free path for 1460.8 keV energy gammas, for low copper thickness (below 2 mm) absorption is not yet important, dominating the backscattering contribution to the escape probability.
- Variations of just a few per cent at most observed in the rejection factor by modifying the module design parameters in a reasonable range do not justify the modification of such a design, as the improvement in sensitivity is not significant, and the larger crystal size is expected to produce a worsening of the optical quality and total light collection. On the other hand, copper thickness value is in the present design close to the optimum range (see figure 3.15).

It can be concluded that, although only a small improvement in the rejection power can be achieved by modifying the modules design parameters, it has been quantified the rejection power in a high modular matrix (5×4). Being the improvement significant, nevertheless to achieve an order of magnitude improvement, a liquid scintillator veto system has to be implemented (see sections 4.2 and 4.3).

As result of this analysis, ANAIS modules design parameters were fixed and kept to the values of first AS modules (given in table 3.5), and thus, these are the parameters considered in all the following simulations.

3.5 Background model of D0 and D1

Background models developed for D0 and D1 detectors taking into account all the background contributions are presented in this section together with the comparison with measured data.

3.5.1 Comparison with data

Figures 3.19 and 3.20 compare the energy spectra obtained by summing all the simulated contributions described previously with the measured data obtained for D0 and D1 detectors, in the ANAIS–25 set-up, considering anticoincidences or coincidences between the detectors. These data were taken from June 2014 to March 2015, corresponding to 231.55 d (live time); in these data most of the cosmogenic isotopes had already decayed. Only data for D1 detector are shown since those corresponding to D0 are analogous. From this comparison it can be said that a good agreement among simulated and experimental data is found at high energies. However, in the very low energy region some relevant contributions seem to be missing. Background could be overestimated in some energy regions since upper limits on radionuclide activity have been used for several components. The addition of cosmogenically produced isotopes to the background model was essential to reproduce, in particular, coincidence data.

The region from about 100 to 200 keV is not well reproduced by simulations; but when adding to the model the ^{235}U activity at the PMTs, which corresponds to the measured ^{238}U value and assuming the natural isotopic abundances of uranium, $\sim$7.2 mBq/PMT [2], this mismatching between data and simulation seems partly solved (see figure 3.21).

In addition, the overestimation of the simulation around 92 keV can be controlled by reducing the ^{238}U upper limit for the copper vessel and quartz windows to that of ^{226}Ra (see figure 3.21). The upper limits on the activity of isotopes derived from gamma spectroscopy at the upper part of the ^{238}U chain are typically much larger than those at the lower part starting on ^{226}Ra (as it can be seen in table 3.1) because of the very low intensity of the gamma emissions at that chain segment.

[2] This value is very similar to that reported at [195]

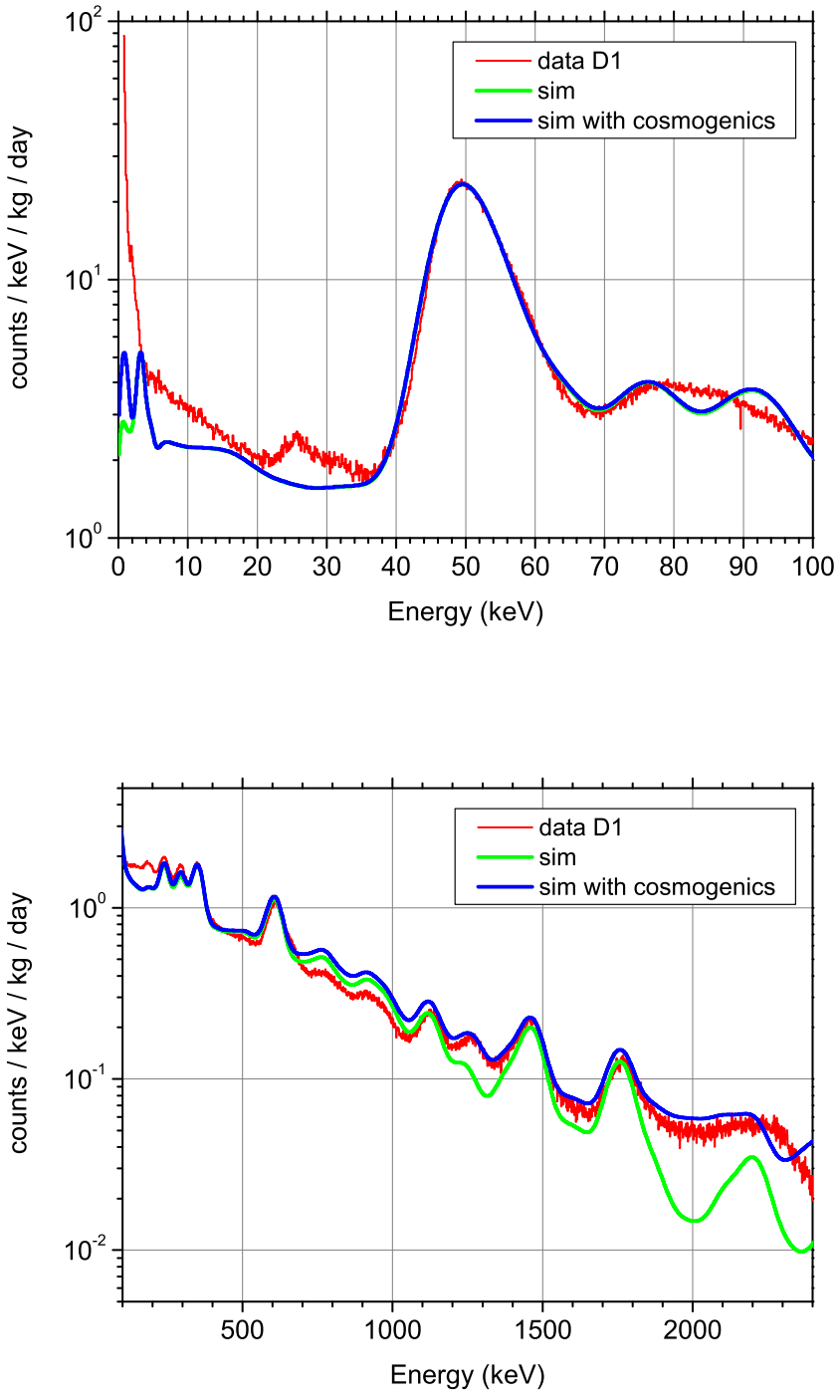

Figure 3.19: *Comparison of the energy spectra summing all the simulated contributions (before and after adding the cosmogenics) with the measured data for ANAIS–25 D1 detector considering anticoincidence data at low energy (top) and high energy (bottom).*

In order to find out the origin of the missing contributions at the very low energy region, different hypotheses have been analysed.

The unexplained peak around 25 keV, observed in figure 3.19, could be due to the cosmogenic production of ^{109}Cd. This isotope decays by electron capture to the 88–keV isomeric state of the daughter, having a half-life of 461.9 d, and therefore the peak may correspond to the binding energy of the K-shell of Ag. The observed peak can be reproduced using different exposure conditions and production rates of the order of the estimates made by convoluting production cross-sections with the cosmic neutron spectrum (see for instance [196], where a calculated rate of 4.8 kg^{-1}d^{-1} is reported). It is worth noting that, being the case, an additional peak around 3.5 keV (Ag L-shell binding energy) is also expected, being 5.4 the ratio between K and L-shell EC probabilities [193].

Figure 3.21 compares again for anticoincidence data the measured ANAIS–25 spectra with the simulated ones including the described hypotheses and two other ones, which are very relevant: the presence of ^{3}H in the crystal and the surface location of part of the ^{210}Pb contamination. These two hypotheses are discussed in detail in this section. The final model still produces an overestimation in the event rate in the energy range from 0.6 to 1 MeV, since upper limits have been considered for several contaminations, and an underestimation from 100 to 200 keV. The inclusion of both ^{3}H and ^{109}Cd contributions significantly improves the agreement in the lowest energy region. The additional inclusion of ^{210}Pb partly on surface helps to reproduce the region from 30 to 40 keV.

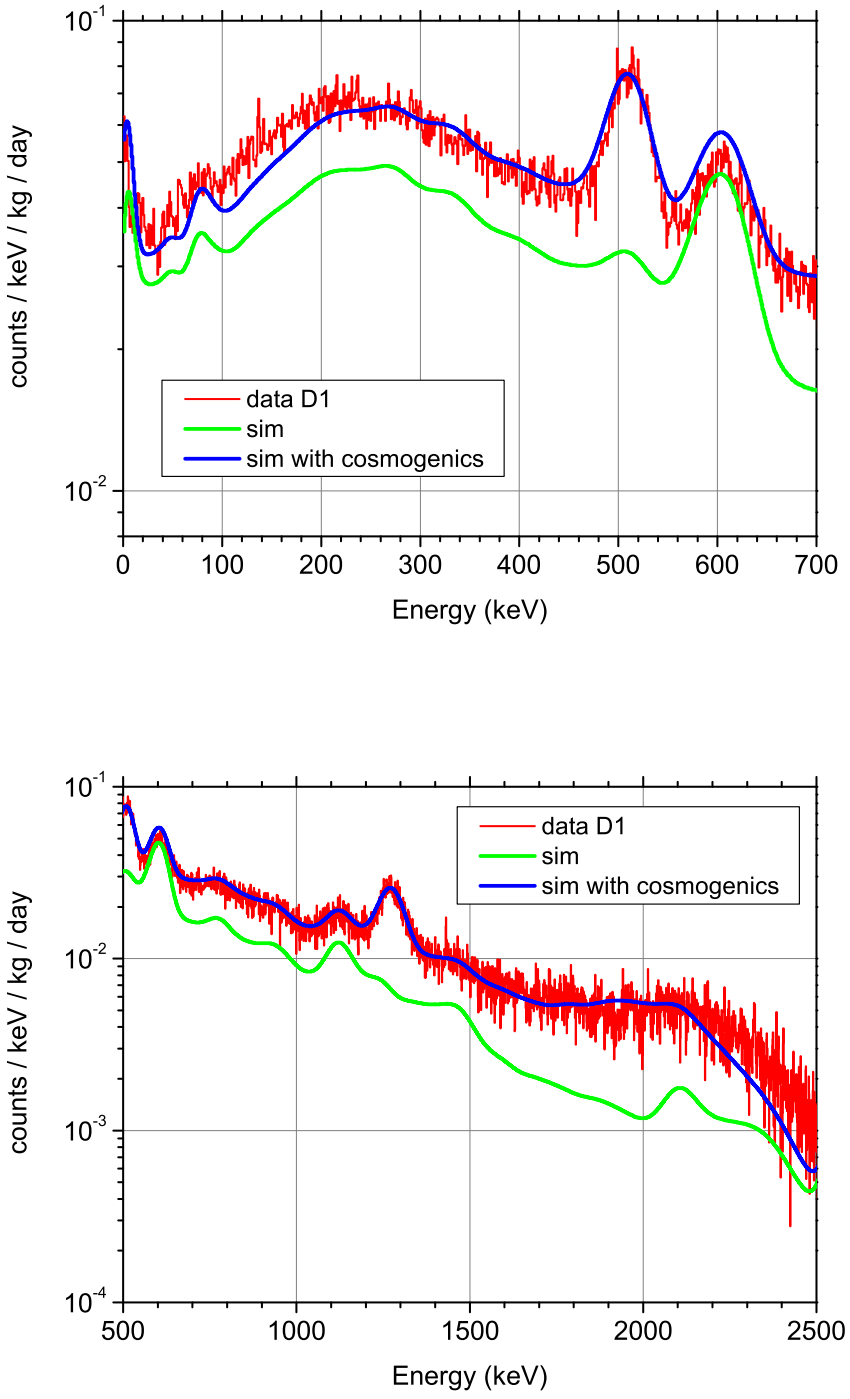

Figure 3.20: *Comparison of the energy spectra summing all the simulated contributions (before and after adding the cosmogenics) with the measured data for ANAIS–25 D1 detector considering coincidence data at low energy (top) and high energy (bottom).*

3.5.1.1 The ^{3}H hypothesis

When comparing the simulated spectrum with the measured spectrum, a very good agreement is obtained when including all the well–known contributions except for the very low energy region. This problem could be solved if an activity of ∼0.2 mBq/kg of ^{3}H homogeneously distributed in the NaI crystal is added to the model, as shown in figure 3.21. Tritium disintegrates 100% by beta-minus decay directly to the ground state of ^{3}He, with a half–life of 12.31 y and a transition energy of 18.59 keV [193].

This required activity is about twice the upper limit set for DAMA/LIBRA crystals [137] but lower than the saturation activity predicted assuming the production rate of ^{3}H in NaI(Tl) of 31.1 kg^{-1}d^{-1} calculated in [197] using production cross–section estimated with TALYS 1.0 code [198] or the rate of 42.9 kg^{-1} d^{-1} obtained in [199] using Geant4 as described in [200].

In order to quantify this production rate in ^{23}Na and ^{127}I (both having 100% natural isotopic abundance) an attempt, using the same approach followed for the cosmogenic isotopes identified in ANAIS–25 [192], has been carried out. First, available information on the excitation function by nucleons was collected, as shown in figure 3.22: only one experimental result was found in the EXFOR database [201] and cross sections were taken from the TENDL–2013 (TALYS–based Evaluated Nuclear Data Library) library [202] up to 200 MeV and from the HEAD-2009 (High Energy Activation Data) library [203] from 150 to 1000 MeV. Then, the production rate was computed convoluting a selected excitation function with the energy spectrum of cosmic neutrons at sea level, using the parameterization from [204]. Table 3.6 summarizes the rates for several descriptions of the cross sections. The total rate considering data from TENDL–2013 library below 150 MeV reproduces the value obtained in [197], since the library is also based on TALYS code. Although information on the excitation function is very limited, it seems that the contribution to the production rate from energies above 150 MeV is not negligible. Assuming that in this high energy range neutron and proton cross–sections are comparable and that production from ^{23}Na and ^{127}I is similar (as for energies below 150 MeV, see table 3.6) the production rate could be of ≈ 50 kg^{-1}d^{-1} summing the contributions in table 3.6. For such a rate, an exposure of 1.9 y to the neutron flux at Grand Junction, Colorado, would produce the required ^{3}H activity in ANAIS–25 crystals. Therefore, the asssumed ^{3}H hypothesis in the background model seems reasonable.

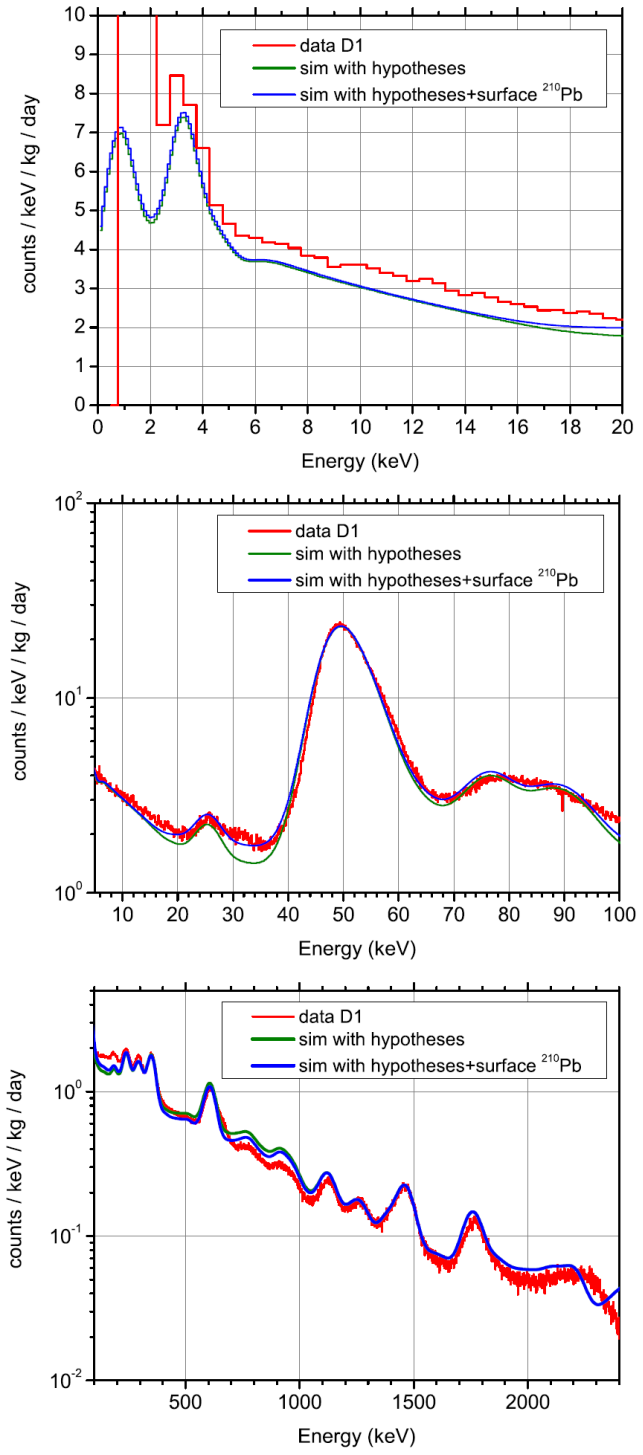

Figure 3.21: *Effect of the consideration of some background hypotheses in the spectra of ANAIS–25 D1 detector at all energy ranges for anticoincidence data (see text). The inclusion of some reduced ^{238}U upper limits, ^{235}U at PMTs and ^{3}H and ^{109}Cd at crystals has been considered (green line); the additional assumption of half of the ^{210}Pb emission from a depth of 100 µm on the crystal surface is separately shown (blue line). The considered hypotheses allow to significantly improve the overall agreement with measured data.*

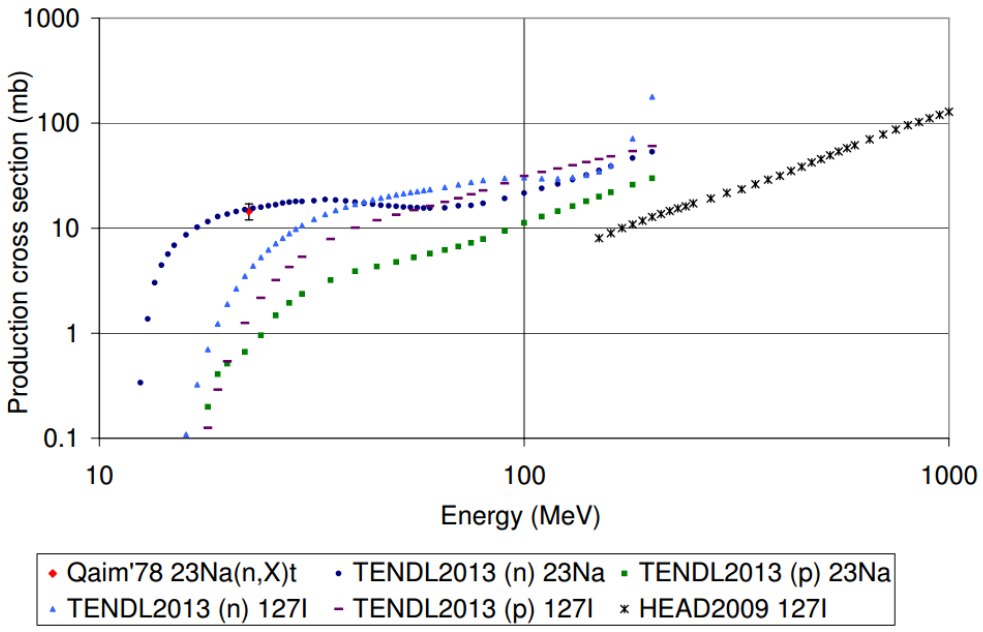

Figure 3.22: *Comparison of excitation functions for production of ^{3}H on ^{23}Na and ^{127}I by nucleons (n for neutrons and p for protons) taken from different sources.*

Isotope	Library	Energy range	Production rate ($kg^{-1}d^{-1}$)
^{23}Na	TENDL–2013	$<$ 150 MeV	14.3
^{127}I	TENDL–2013	$<$ 150 MeV	15.4
^{127}I	HEAD–2009	150 MeV–1000 MeV	10.9

Table 3.6: *Production rates (per kg of NaI) of ^{3}H in NaI isotopes obtained considering different excitation functions.*

3.5.1.2 The ^{210}Pb on surface hypothesis

Because of the structure of the peak due to ^{210}Po in the alpha region of the energy spectra shown in figure 3.6, the possibility of a surface deposition has been analyzed. Figure 3.23 compares the low energy spectra simulated assuming ^{210}Pb in bulk or in surface; since the surface contamination profile is unknown, different constant depths all around the crystal have been considered. The alpha emission is fully absorbed and only a small continuum appears at the left side of the peak for depths at or below 30 μm in the simulation as the range of a 5–MeV alpha particle in NaI

is 29 μm, following NIST data [205]. The need to reproduce the low energy region of the measured spectrum dominated by ^{210}Pb emissions excludes surface contaminations at a very small depth.

The best option to reproduce the whole range of data was found when considering half of the ^{210}Pb content in bulk and the other half on surface from a constant depth of 100 μm; the bulk and surface proportion was fixed following the observed almost symmetric double structure of the ^{210}Po peak for D0 and D1 detectors.

This result has to be taken very cautiously, energy conversion into visible signal is assumed to be constant throughout the crystal in our simulation, but there should be a difference between energy depositions for alpha particles in two regions, as we are indirectly assuming when interpreting the double structure in the alpha peak as due to ^{210}Po. These two regions could be surface and bulk. However, simple tests, including a similarly reduced energy conversion for beta/gamma energy depositions having the same distribution than alpha contamination can be discarded, because it affects so much at the low energy events that it should have been clearly observed in the data. Nevertheless, we cannot discard some spatial dependence of the energy conversion at sub-micrometer scale, that could affect differently alpha particles than beta/gammas and then, it could affect too the energy depositions at the lowest energies (below 10 keV but not in the 50 keV energy scale).

3.5.2 Background contributions

Figure 3.24, summarizes the different contributions from the explained background model of ANAIS–25 detectors, for anticoincidence data, to the rate in the region from 1 to 6 keVee. The energy spectra expected from different background sources in the very low energy region for anticoincidence data are plotted in figure 3.25, together with the sum of all contributions. In the region of interest ^{210}Pb and ^{3}H continua together with ^{40}K, ^{22}Na and ^{109}Cd peaks are the most significant contributions.

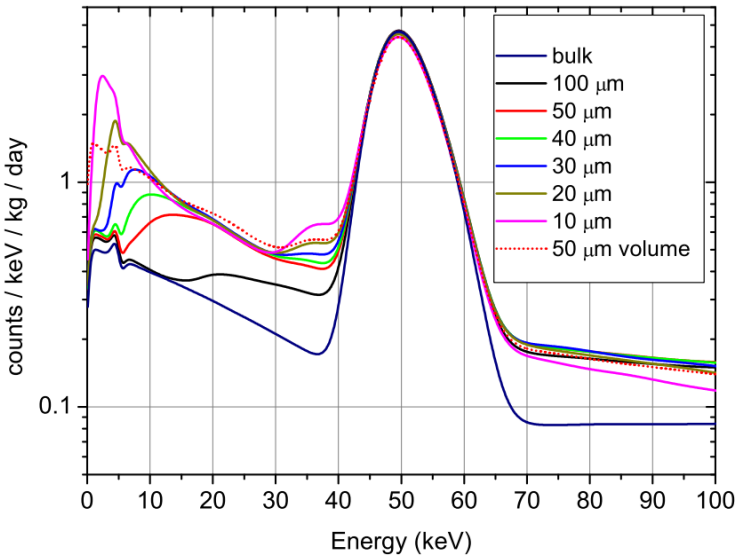

Figure 3.23: *Comparison of the low energy spectra simulated for ^{210}Pb emissions from the crystal bulk or from the surface, considering different constant depths all around the crystal; results for uniform emissions from a 50–μm–thick layer are presented too. All simulations are normalized for an activity of 0.7 mBq/kg.*

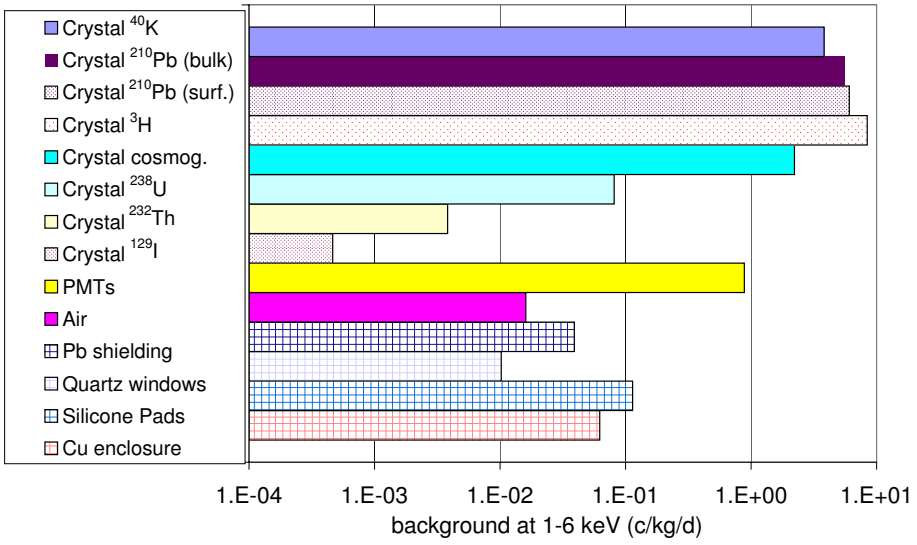

Figure 3.24: *ANAIS–25 background model: expected rates from different background sources in the region of 1–6 keVee . Some contributions have been estimated from a directly quantified activity (filled bars), but others from upper limits (plaid bars) or hypothesized activities (dotted bars).*

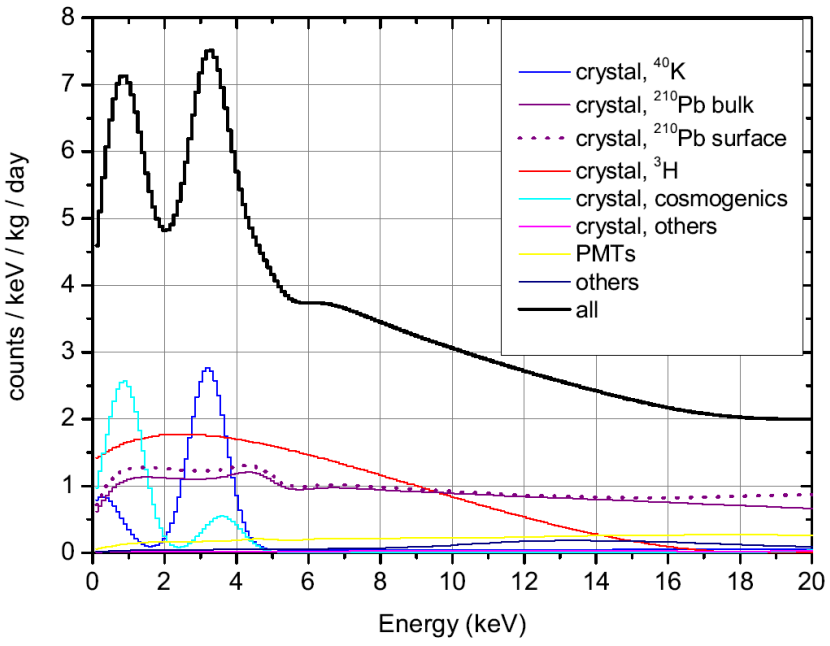

Figure 3.25: *ANAIS–25 background model: anticoincidence spectra from different background sources at the low energy region.*

3.6 Background model for D2

Similarly to D0 and D1, the background model developed for D2 taking into account all the background contributions is presented in this section together with the comparison with measured data.

3.6.1 Comparison with data

The same procedure followed for D0 and D1 detectors in the ANAIS–25 set–up has been applied to build the background model of D2. Figure 3.26 compares the energy spectrum measured for D2 detector at the ANAIS–37 set–up (see section 2.9.3) with the corresponding simulation. The data taken with this set-up from May to September 2015 for 89.5 d have been considered here, where the cosmogenic activation has significantly, but not completely, decayed. For the simulation, the input activities given in tables 3.1 and 3.2 for D2 have been assumed. The same initial activity of I and Te products cosmogenically induced in the NaI crystal, as determined for D0 and D1 detectors, has been taken; although the previous exposure history of the D0, D1 and D2 detectors is not the same and some differences could be expected in other longer half–life isotopes, in the case of I and Te products saturation should have been reached nonetheless.

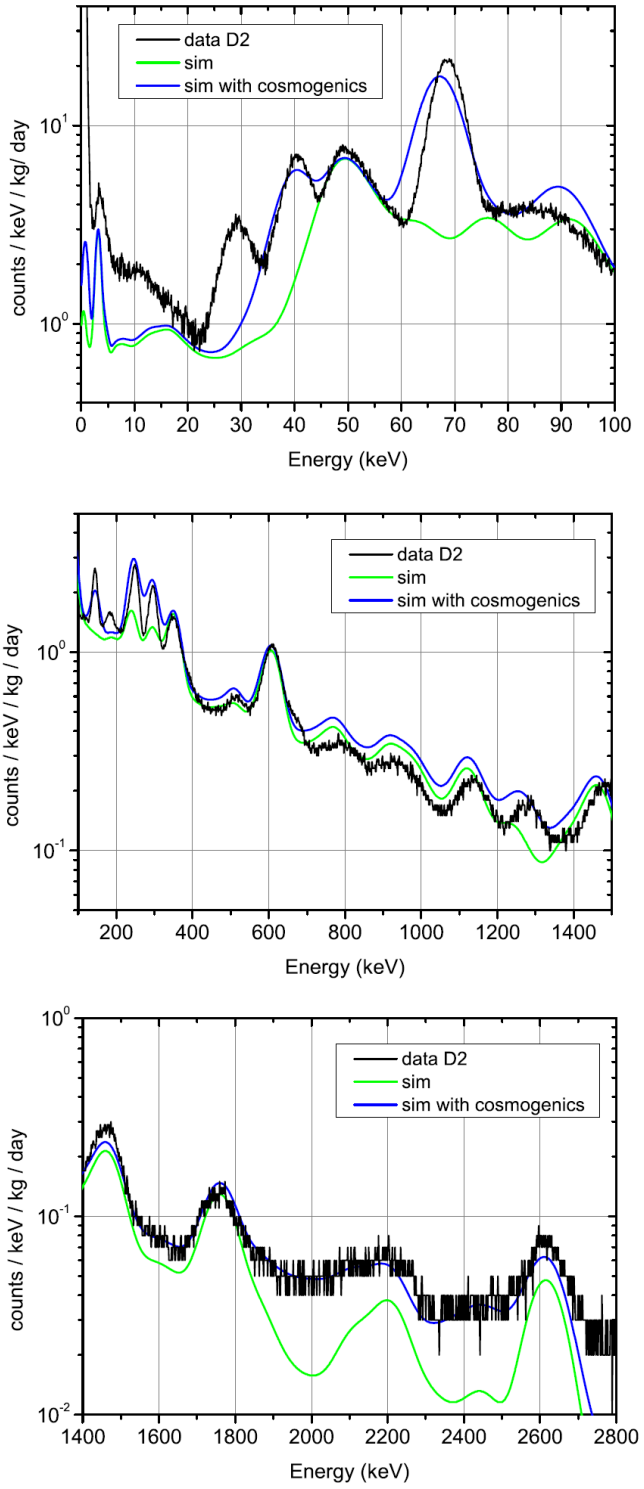

Figure 3.26: *Comparison of the energy spectrum measured for D2 detector at the ANAIS–37 set-up with the corresponding simulation summing all contributions (before and after adding the cosmogenics) at low (top) and high (bottom) energy regions. Anticoincidence data are shown in the low energy region.*

For ^{22}Na, the initial activity quantified specifically for D2 detector and presented in section 3.1.2.3 has been considered. The overall agreement between data and simulation in figure 3.26 is quite satisfactory except for some energy regions. As it was observed in D0 and D1 detectors, ^{210}Pb emissions at low energy are well reproduced by the simulation assuming the activity deduced from the alpha rate (see figure 3.27). At medium energies (around 1 MeV), it can be stated that the simulation is clearly overestimated; this could be due again to the fact that upper limits on radionuclide activity have been used for several components in the code.

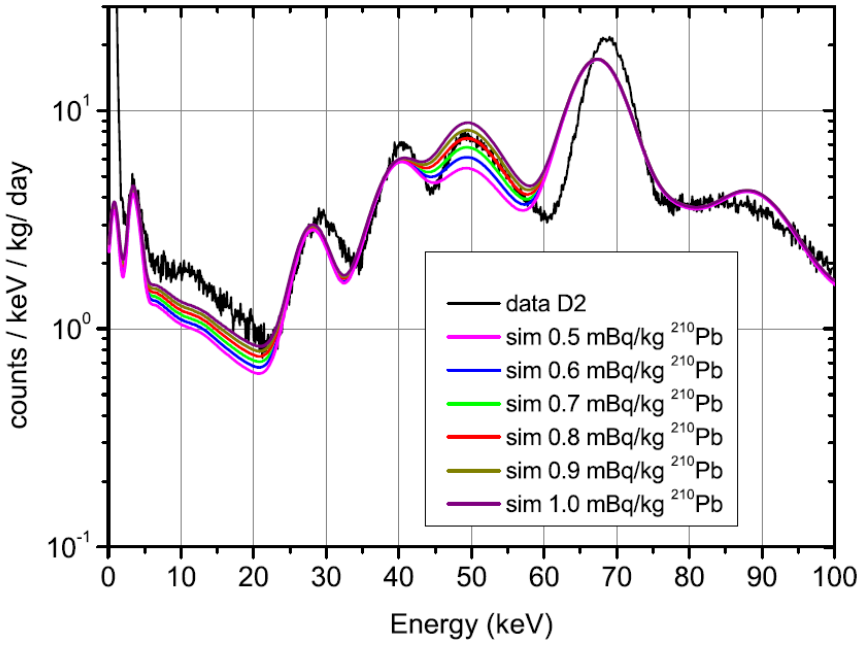

Figure 3.27: *Effect on the low energy region of varying the ^{210}Pb activity in the NaI(Tl) crystal in the background model of D2 detector. Values around that deduced from the alpha rate have been considered.*

The observed peak around 185 keV in D2 data and not reproduced by simulation, as well as the underestimation at ∼145 keV, could be justified by the content of ^{235}U from the photomultipliers also considered for D0/D1 detectors. Again, as for ANAIS–25, the overestimation of the simulation around 92 keV can be partially suppressed by reducing the ^{238}U upper limit for the copper vessel and quartz windows to that of ^{226}Ra.

In this direction, some plausible hypotheses have been analysed in order to find an explanation to the relevant discrepancies between data and simulation in the low energy region:

- The prominent line registered at ∼28 keV is not explained by the cosmogenic isotopes identified in ANAIS–25 data. ^{113}Sn, having a half–life of 115.1 d and decaying by electron capture mainly to a 391.7 keV isomeric state of the daughter, could justify this spectral feature as binding energy of In K–shell and cosmogenic activation of the isotope is possible. As for ^{109}Cd, the observed peak can be reproduced by using different exposure conditions and production rates of the order of the estimates made by convolving production cross-sections with the cosmic neutron spectrum (at [196], a production rate of 9 kg^{-1}d^{-1} is reported and a measured value of 16 kg^{-1}d^{-1} presented). A peak around 4 keV is expected from ^{113}Sn as the binding energy of the L-shell of In, being 7.4 the ratio between the probabilities of EC at K and L shells for the decay to the isomeric state [193], but since the half-life of ^{113}Sn is not too large, it should not be a problem in the long term. ^{113}Sn induced in D0/D1 detectors should have decayed in the data analysed here. No hint of the presence of ^{109}Cd, as seen in ANAIS–25 detectors, has been observed in D2 data; as for ^{22}Na, the initial activity of this isotope, having a longer half-life than ^{113}Sn, could be lower than in ANAIS–25 detectors due to the different time spent at Colorado.

- The spectrum shape and rate observed below 20 keV in D2 data is not completely reproduced by simulation. Several possibilities have been explored:

  - Considering the amount of ^{3}H deduced for D0 and D1, the spectral shape of its beta emission does not fully explain the observed background below 20 keV in D2; therefore, D2 ^{3}H content has been fixed to the upper limit set by DAMA/ LIBRA (0.09 mBq/kg [137]). Due to the fact that D2 had shorter exposure to cosmic rays in Colorado in comparison to D0 and D1, a lower ^{3}H activity is expected.

  - The possibility of ^{210}Pb emissions on the crystal surface instead of in bulk has been deeply studied too. As shown in figure 3.6, the double structure of the ^{210}Po peak observed at the alpha region of the energy spectra of D2 detector is more asymmetric than that measured for ANAIS–25 detectors; according to the structure of this peak, a fourth of the ^{210}Pb contamination has been considered in the crystal bulk and three fourths on the surface. For D2 detector, and considering all the possibilities analysed (see figure 3.23), the best option to reproduce the low energy region of the spectra, dominated by ^{210}Pb emissions, was a surface contamination from a depth of 30 μm.

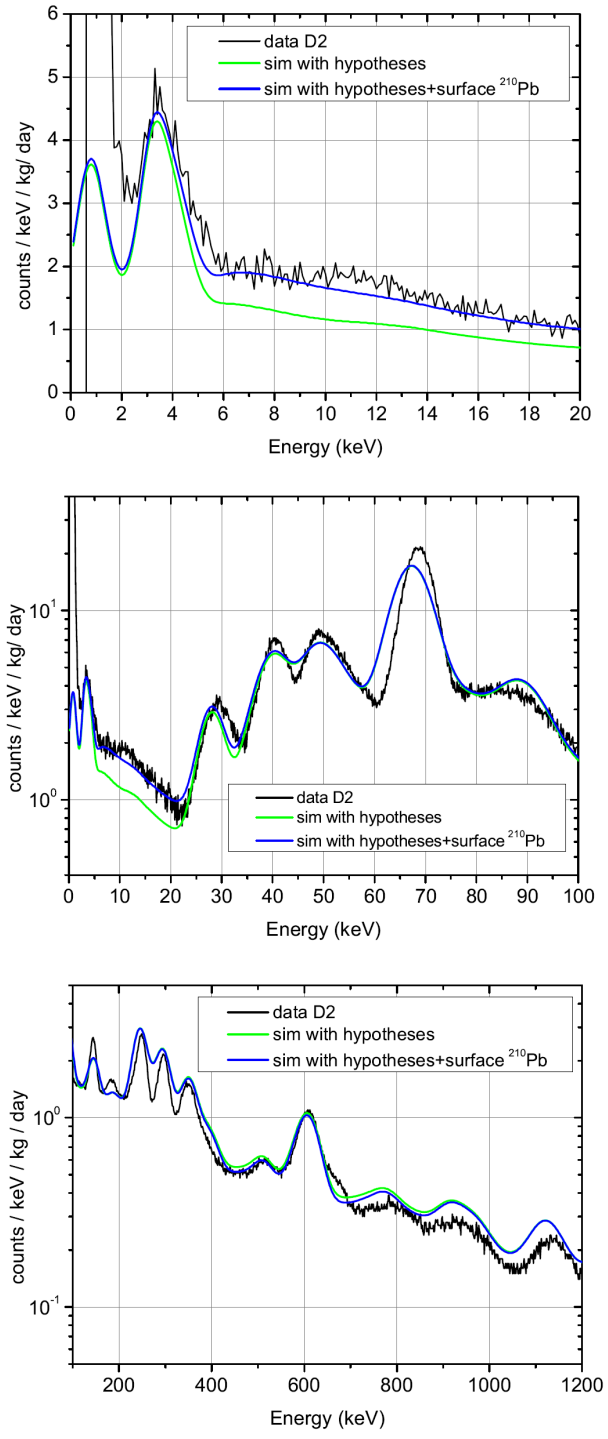

Figure 3.28: *Effect of the consideration of the plausible analysed background hypotheses (see text) in the spectra of D2 detector at different energy ranges (at the highest energies the hypotheses have no effect). The inclusion of some reduced ^{238}U upper limits, ^{235}U at PMTs and ^{3}H and ^{113}Sn at crystal has been considered (green line); the additional assumption of part of the ^{210}Pb emission from a depth of 30 μm on the crystal surface is separately shown (blue line). The considered hypotheses are essential to improve the overall agreement with measured data.*

Figure 3.28 compares the measured D2 spectra with the simulated ones taking into account all these described hypotheses, which significantly improve the agreement. It is remarkable that the inclusion of ^{3}H in the model is necessary since only surface and bulk ^{210}Pb emissions cannot reproduce the registered spectrum shape. The higher continuum level below 40 keV produced by the ^{210}Pb surface emission in comparison with the bulk contamination helps to improve the agreement between the model and the measured data (see figure 3.23).

3.6.2 Background contributions

Figure 3.29, summarizes the different contributions from the proposed background model of D2 at the ANAIS–37 set-up, for anticoincidence data, to the rate in the region from 1 to 6 keVee. The energy spectra expected from different background sources in the very low energy region for anticoincidence data are plotted in figure 3.30, together with the sum of all contributions. In this region of interest it has been verified that ^{210}Pb contribution has been significantly reduced in comparison to D0 and D1; but it is worth pointing out that emissions from surface make a larger contribution than from bulk. Peaks from ^{113}Sn and, to a lesser extent, ^{22}Na will be decreasing in the next future.

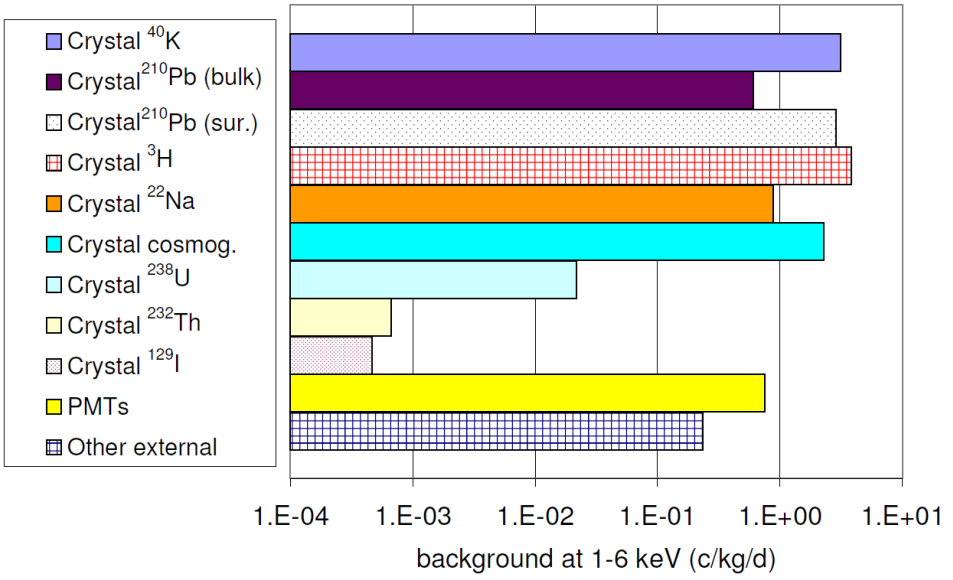

Figure 3.29: *Background model for D2 at the ANAIS–37 set-up: expected rates from different background sources in the region of 1-6 keVee. Some contributions have been estimated from a directly quantified activity (filled bars), but others from upper limits (plaid bars) or hypothesized activities (dotted bars). Contribution from cosmogenic isotopes has been evaluated for the period corresponding to the real data taking.*

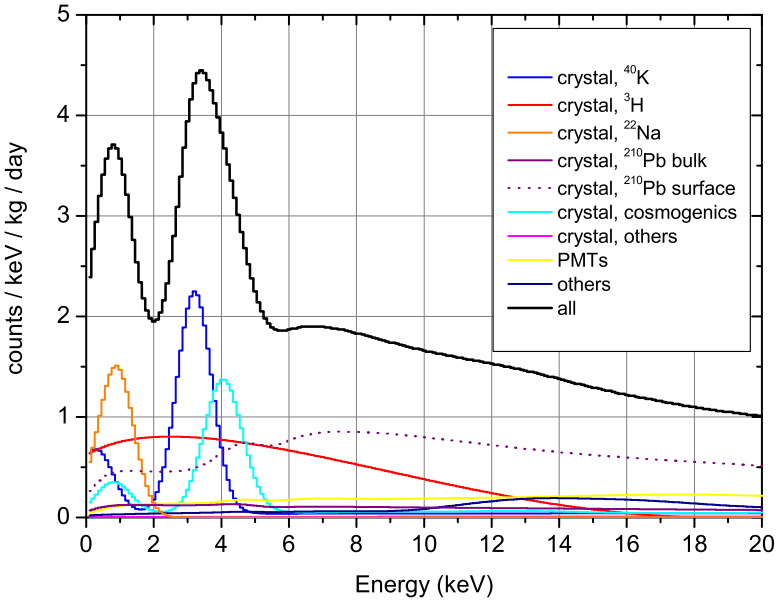

Figure 3.30: *Background model for D2 at the ANAIS–37 set-up: spectra from different background sources at the very low energy region. Contribution from cosmogenic isotopes has been evaluated for the period corresponding to the real data taking.*

As conclusion, and according to our background model, surface contamination in ^{210}Pb is needed to reproduce low energy spectra of D0/D1 and D2 modules, even though in a different amount and in different depth profile. Although some important assumptions are required to estimate the contribution of surface contaminants to the energy spectra, and then, the contaminations depths for ^{210}Pb derived from our analysis should not be firmly taken as stated, we can conclude that a fraction of the total contamination in ^{210}Pb could be due to the treatment of the surfaces while the building of D0/D1 and D2 modules. In [206] and [207], diffusion lengths for radon–induced surface contamination which could happen due to exposure to air during assembly phase and storage of detectors are estimated below 1 μm, depending on radon concentration, exposure time and features of material surface; the required depths deduced for ANAIS crystals cannot then be explained by diffusion from radon surface deposition, but they would point to other mechanisms allowing the contamination from radon (or even directly ^{210}Pb) at the production phase of the crystals or at the treatment of surfaces. This issue is being further investigated in collaboration with AS company.

3.7 Preliminary background model for D3

As explained in section 2.9.5, A37D3 set–up is very similar to ANAIS–37 in shielding configuration and acquisition parameters. A preliminary analysis of D3 background in A37D3 set–up is presented here.

3.7.1 Background contributions

The total alpha rate of the new module D3 has been determined by PSA. The observed alpha rate is increasing, pointing at the building of ^{210}Po activity in the detector (see figure 3.31). An average value of 1.3 mBq/kg can be reported by August 2016, although saturation of the alpha activity is expected at a level of 1.8 mBq/kg, which is more than a factor of two higher than the alpha rate observed in D2 module (0.7 mBq/kg), although better than that in D0 and D1 (3.15 mBq/kg). As shown in figure 3.32, a ^{210}Pb activity around 1.8 mBq/kg could explain the low energy region of the measured spectrum.

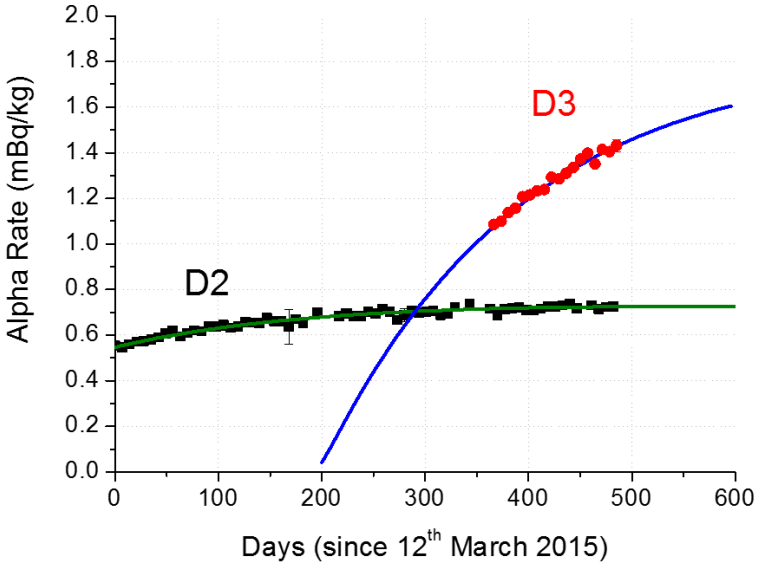

Figure 3.31: *Evolution of the alpha rate in D2 and D3 detectors.*

In figure 3.6 the corresponding spectrum for alpha selected events in D3, compared to those measured for D0 and D2 modules is shown. Calibration has been done by using alpha–alpha sequences from ^{232}Th chain, having a very low number

of events, which limits the accuracy of the calibration. Although statistics for D3 alpha events is much lower, it can be confirmed a qualitative difference between D3 spectrum shape and those from D0 and D2. A plausible hypothesis is that contamination of the crystal surface occurred while building this detector, and work is ongoing exploring this possibility in collaboration with Alpha Spectra.

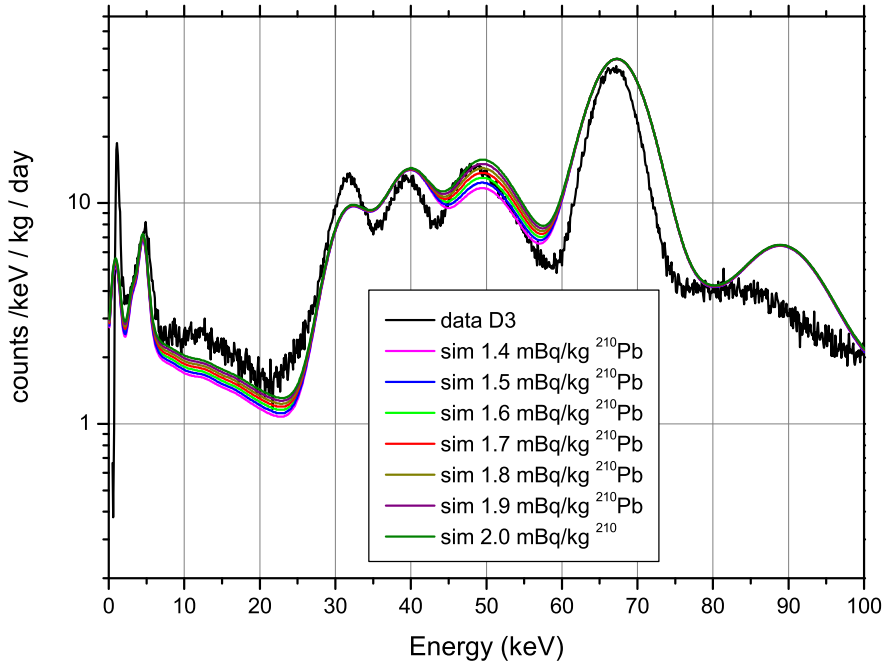

Figure 3.32: *Effect on the low energy region of varying the ^{210}Pb activity in the NaI(Tl) crystal in the background model of D3 detector. Values around that deduced from the alpha rate have been considered. D3 spectrum shown here corresponds to first data taken with this detector in March and April 2016.*

Coincidences between the three modules in order to determine the potassium content in the D3 module have been studied. Energy windows at $\pm$ 1.4 σ of the 1460.8 keV lines in D0 and D2 modules have been chosen and searched for energy depositions at very low energy in D3. Results are shown in figure 3.33. A value around 19 ppb can be derived for the content of potassium in the D3 crystal, assuming that all the events in the region from 2 to 5 keV are due to ^{40}K.

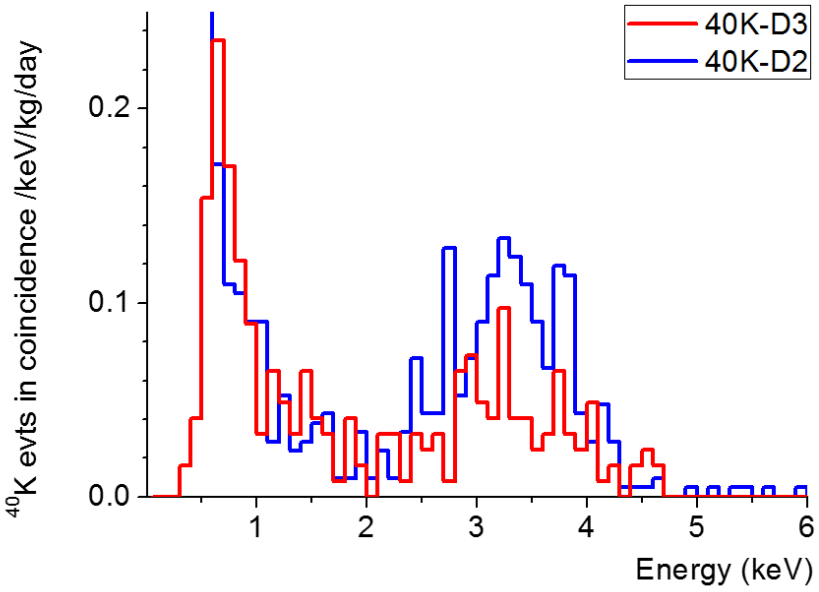

Figure 3.33: *Events in D3 in coincidence with energy windows around 1460.8 keV gamma line in D0 and D2 modules. Same spectrum obtained for D2 module is also shown (in ANAIS–37 set–up, having the same geometry and then, efficiency for the coincidence).*

Table 3.2 includes the previously commented determinations of potassium content and ^{210}Pb, but also the content in the radioactive natural chains (^{238}U and ^{232}Th), determined by looking at the ^{212}Bi-Po and ^{214}Bi-Po sequences and the alpha-alpha decay sequences: ^{220}Rn- ^{216}Po- ^{212}Pb. Clear improvement in radiopurity is observed in the last modules made at AS.

3.7.2 Comparison with data

The background model built for D0, D1 and D2 modules has been preliminary adapted to D3. Measured activities for D3 crystal (reported in table 3.2) have been considered and cosmogenics properly included, for initial activities of ^{3}H and ^{22}Na as in D2. The same hypotheses considered in D2 have been assumed too, but including 50% of ^{210}Pb activity on surface. The simulation has been compared with 24 d of data taken from June to July 2016 in the A37D3 set–up and the result can be seen in figure 3.34. Remarkable agreement between simulation and measurement can be observed.

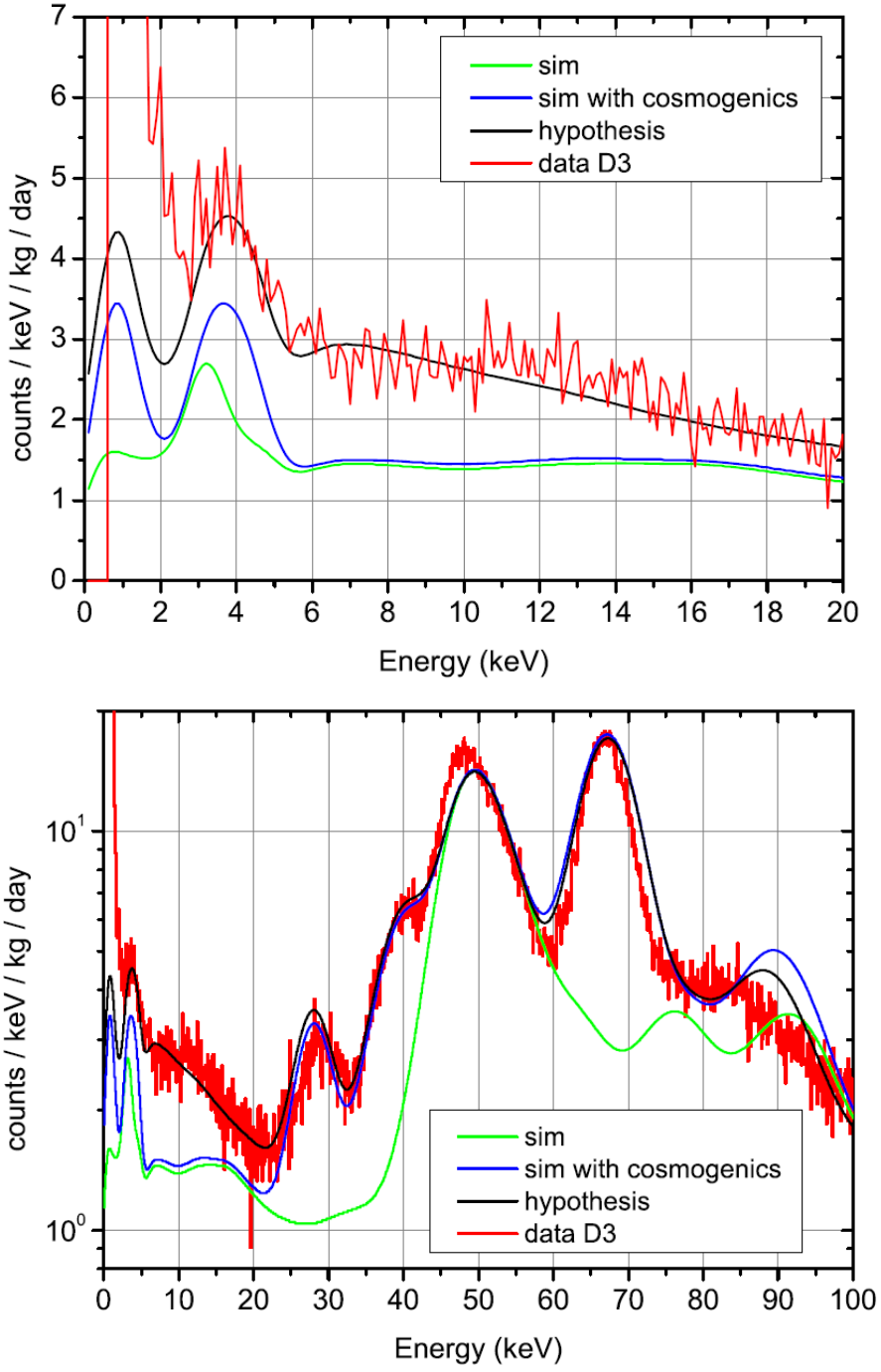

Figure 3.34: *Low energy background of D3 module together with the estimates of the background model adapted to the measured contaminations (see table 3.2) and estimated contribution from cosmogenic isotopes. Results from the background model without and with hypotheses (see text) are depicted.*

3.8 Conclusions

Using the same simulation framework developed for studying the background of ANAIS detectors, the dependence of the escape probability of high energy photons has been evaluated as a function of some detector parameters to assess a possible reduction of crystal ^{40}K contribution. The dependence found did not justify a change of the original detector parameters.

The background models constructed for D0, D1 and D2 modules provide a good description of measured data at all energy ranges and at different analysis conditions (coincidence and anticoincidence). Preliminary results for D3 are also satisfactory.

The measured activity in external components and in crystal roughly explains the observed background, but the inclusion of some additional hypotheses, like the presence of cosmogenic isotopes which cannot be directly quantified or partial crystal surface ^{210}Pb contamination, significantly improves the agreement between model and real data. Crystal bulk contamination is the dominant background source in the region of interest: ^{210}Pb, ^{40}K, ^{22}Na and ^{3}H give the most relevant contributions. An acceptable potassium content has been reached in all detectors but the high activity of ^{210}Pb is a problem, which is being addressed by means of dedicated tests and measurements in collaboration with Alpha Spectra. Surface contamination in ^{210}Pb is needed to reproduce the low energy background, even though in a different amount and in different depth profile for different crystals; the required depths for ANAIS crystals would point to some surface treatment at the production phase as the origin of the contamination. Cosmogenics should be reduced in future AS modules thanks to the use of a shelter for cosmic rays in Alpha Spectra facilities in Colorado.

At present, the best measured background at low energy in ANAIS prototypes is that of D2: 2 counts/(keV kg day) at 6 keVee, being ^{210}Pb and ^{3}H continua contributions at the level of some tenths of counts/(keV kg day) each, PMTs and other external components amounting less than 0.2 counts/(keV kg day). The most relevant contribution from ^{40}K and ^{22}Na peaks amounts to 4 counts/(kg day) from 1 to 6 keVee in D2, but it could be strongly reduced by anticoincidence in a detector matrix set–up (and even more with a Liquid Scintillator Veto System), see section 4.3, and an improved control of radiopurity in the building of the modules. For instance, for D3, with a reduced K content, contribution from ^{40}K and ^{22}Na peaks is of 2.6 counts/(kg day) in the 1–6 keVee region.

Chapter 4

ANAIS background prospects: towards a final design

ANAIS in collaboration with AS is strongly pursuing an improvement of the radiopurity of the subsequent 12.5 kg modules, required to complete the goal of 112.5 kg total detection mass, trying to focus in further reduction of the powder ^{40}K content by increasing the purification steps, in reducing ^{22}Na and ^{3}H activation by using convenient shieldings while storing at surface, and avoiding ^{210}Pb contamination, whose origin is still unknown, although could be related to radon. In parallel, background rejection power of coincidences has been analyzed in different experimental scenarios for ANAIS: present configuration with 3×3 modules (112.5 kg, ANAIS–112) and also the original configuration using 4×5 modules (250 kg, ANAIS–250). An additional Liquid Scintillator Veto (LSV) surrounding the NaI(Tl) detectors has been also considered in order to improve the rejection power of the experiment. Monte Carlo simulations, as those carried out for the AS modules already operated in Canfranc and described in chapter 3, have been developed for all the considered configurations in order to quantify the achievable background levels.

Background sources considered in the simulation of the NaI modules and a possible LSV are explained in section 4.1. In section 4.2, the study of two different configurations for the geometry of the final ANAIS set–up, ANAIS–112 and ANAIS–250, is presented. The results of the inclusion of a LSV, considering two different designs, are exposed in section 4.3.

4.1 Background sources

The following background sources have been taken into consideration, although not all of them have been simulated for all the ANAIS configurations analyzed. Details about the contributions not considered for every configuration will be given in the corresponding sections.

For the NaI modules, measured primordial activities from PMTs and crystals, mainly as for D2 module (0.7 mBq/kg of bulk ^{210}Pb and 1.25 mBq/kg of ^{40}K) have been included (see table 4.1). The cosmogenic initial activity of ^{22}Na (estimated at the beginning of the underground measurements) and possible tritium contribution have been also taken into account, at the levels deduced for D2 at the ANAIS–37 set–up, but conveniently reduced as corresponds to the time spent underground. In the case of PMTs, the mean activity from all the screened units at LSC by HPGe spectrometry has been considered (see table 3.1).

	Unit	^{40}K	^{232}Th	^{238}U	^{226}Ra	^{210}Pb	^{22}Na	^{3}H
Crystal	mBq/kg	1.25±0.11	(0.7±0.1) 10^{-3}	(2.7±0.2)		0.7±0.1	0.81±0.05	0.09
PMTs	mBq/PMT	111±5	20.7±0.5	157±8	82.5±0.8			

Table 4.1: *Activities considered for the NaI modules in the simulation of the different ANAIS configurations. For the rest of components, such as copper, silicone pads, quartz, etc., values from table 3.1 have been assumed.*

Concerning the activities of the different components of the LSV system itself, values from the literature have been considered (see table 4.2): from NEXT for stainless steel container [208], from SNOlab for PMTs [209] and from JUNO for LAB scintillator [210]. For the stainless steel container, results for 316Ti stainless steel from the Nironit company obtained by the NEXT experiment are similar to those obtained by the GERDA collaboration for the same material [211]. This is the cleanest stainless steel we are aware of from the radiopurity point of view. For the Hamamatsu R5912 PMTs, U, Th and K concentrations obtained by the UKDM collaboration [212] for the same PMT model give similar activities to those from SNOlab. For the liquid scintillator, values from JUNO are of the same order than those considered as target also by the SNO+ experiment [213].

	Unit	^{40}K	^{232}Th	^{238}U	^{226}Ra	^{60}Co
Container	mBq/kg	<0.96	<0.54	<21	<0.57	2.8 ±0.8
PMTs	mBq/PMT	2150 ±126	339 ±11	346±105	652±18	
LAB scintillator	mBq/kg	0.0031	$4.1 \cdot 10^{-6}$	$1.2 \cdot 10^{-5}$		

Table 4.2: *Activities considered for the LSV components in the simulation of the different ANAIS configurations. For those materials where only upper limits are available, they have been taken as simulated activity values.*

For the environmental gamma background, the value of the flux determined at Hall B of LSC using a 3" × 3" NaI(Tl) detector has been assumed [214]. Table 4.3 includes also equivalent results obtained at Hall A for comparison [215]. Gamma emissions having intensities above 1% from the radioactive isotopes shown in table 4.3, assuming secular equilibrium in the natural chains, have been simulated from a spherical surface containing the whole set–up.

For the ANAIS configurations without a LSV a 30–cm–thick lead shielding is simulated (as in the ANAIS–25, ANAIS–37 and A37D3 set–ups installed in LSC) and therefore, gamma background contribution is expected to be negligigle and has not been simulated; but for ANAIS configurations with a LSV, the implementation of a lead shielding is much more complicated and gamma background has been simulated to evaluate its need and suitability, as it will be shown in section 4.3.

Location	Unit	^{40}K	^{232}Th	^{238}U
LSC, Hall B (2006)	γ cm^{-2}s^{-1}	0.33 ± 0.01	0.85 ± 0.07	0.71±0.12
LSC, Hall A (2010)	γ cm^{-2}s^{-1}	0.15 ± 0.04	0.36 ± 0.23	0.55±0.22

Table 4.3: *Gamma flux data at LSC [214] [215].*

Similarly, the muon background has been also taken into account for ANAIS configurations with a LSV; without a LSV, the foreseen use of plastic scintillator vetos all around the set–up will reduce muon background contribution to negligible levels and it has not been considered. The muon flux determined at LSC using plastic scintillator detectors [214] has been assumed (see table 4.4). In the simulation,

muons have been generated at the surface of a semisphere containing the whole set-up. The muon energy spectrum has been sampled from Lipari [216] distributions evaluated for the Canfranc depth (with mean energy of 216 GeV) while an angular distribution proportional to $cos^{3.6}\theta$ has been considered [217], corresponding to a depth of 850 m of standard rock.

Location	Muon flux
LSC, Hall B	$(5.04 \pm 0.06\ (\text{stat}) \pm 0.25\ (\text{sys})) \cdot 10^{-3}\ \mu\ \text{m}^{-2}\text{s}^{-1}$
LSC, Hall A	$(4.71 \pm 0.06\ (\text{stat}) \pm 0.24\ (\text{sys})) \cdot 10^{-3}\ \mu\ \text{m}^{-2}\text{s}^{-1}$

Table 4.4: *Muon flux data at LSC [214].*

4.2 ANAIS–112 and ANAIS–250

A study of the expected background for the full ANAIS set-up using several modules similar to D2, was undertaken in order to quantify the power of the anticoincidence rejection in the full experiment and thus, to be able to estimate the experiment sensitivity. The 3 × 3 crystal matrix planned (ANAIS–112) has been studied (see figure 4.1) as well as the originally considered configuration with 5 × 4 detectors (ANAIS–250) (see figure 3.14).

It must be noted that the 3 × 3 modules set–up without a LSV system has not been independently simulated. As it will be shown in section 4.3, for the assumed geometry and radiopurity of the different system components, the contribution to the background level of the LSV components is negligible (two orders of magnitude lower) in comparison to that of the NaI(Tl) crystals. Therefore, simulations for ANAIS–112 shown in this section are the same presented in section 4.3, without profiting from the LSV veto effect.

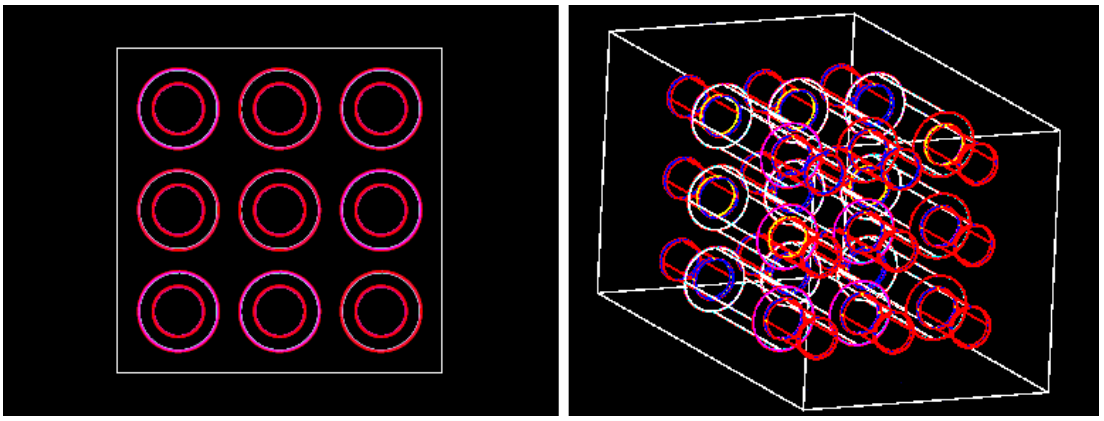

Figure 4.1: *Geometry of the ANAIS–112 set–up as implemented in Geant4 simulations: 3 × 3 NaI(Tl) crystals matrix.*

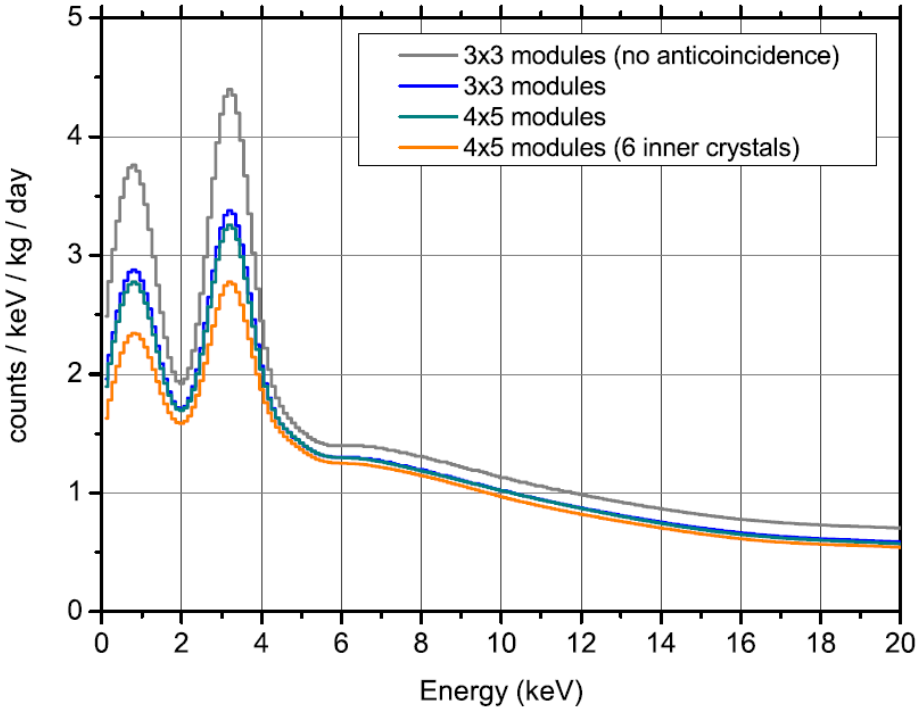

Figure 4.2: *Energy spectra at the very low energy region expected from all the considered background sources in the ANAIS–112 and ANAIS–250 set-ups. For the 3×3 modules configuration the spectrum before anticoincidence rejection is also shown for comparison. For the 5×4 configuration, the result when considering only the six inner crystals (see text) is presented too.*

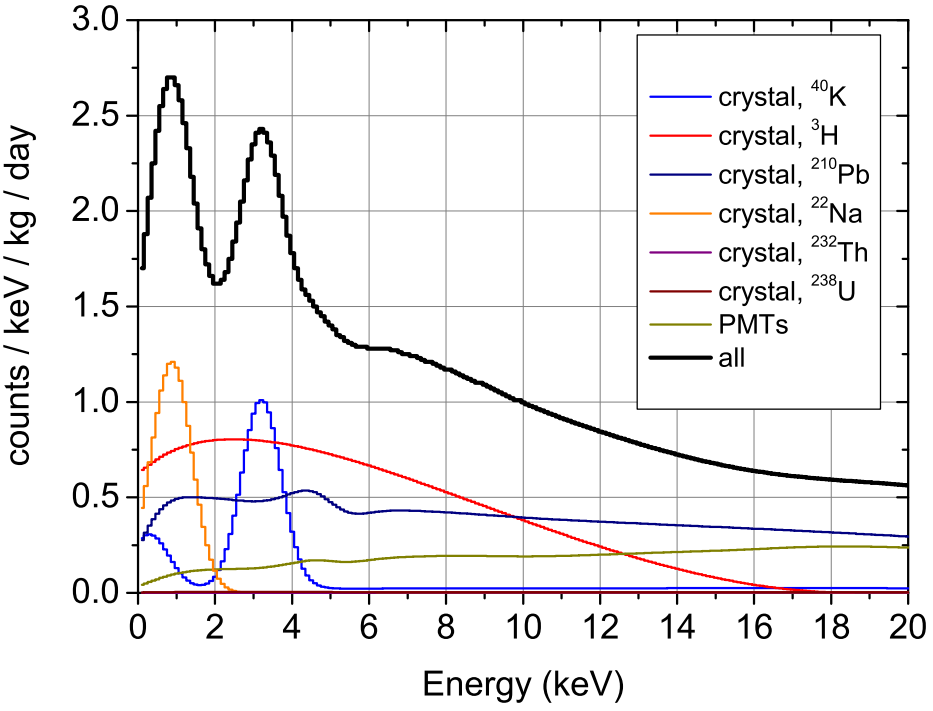

Figure 4.3: *Energy spectra of the different contributions to the background in the low energy region for a 3×3 matrix configuration (ANAIS–112) when assuming the same input activities and hypotheses than for D2 except for a reduced ^{40}K content (0.65 mBq/kg), at the level of that obtained in D3 detector.*

Figure 4.2 presents the obtained energy spectra at the very low energy region for ANAIS–112 and ANAIS–250 set–ups, when adding all the simulated background sources and after rejecting coincidences. The spectrum without profit from coincidence rejection is also depicted for the 3×3 modules configuration to show the obtained reduction; reduction factors in the region of interest will be quantified and discussed in section 4.3 (see table 4.9) together with the results using the LSV system.

As described in section 4.1, to estimate the expected background level for ANAIS–112, D2 measured activities have been mainly assumed. However, the potassium content achieved in D3 detector is significantly lower (see section 3.7). Consequently, the background level which could be obtained considering the lowest ^{40}K and ^{210}Pb activities measured for AS modules (those from D3 and D2 respectively, see table 3.2) has been evaluated; the corresponding energy spectra are shown in figure 4.3.

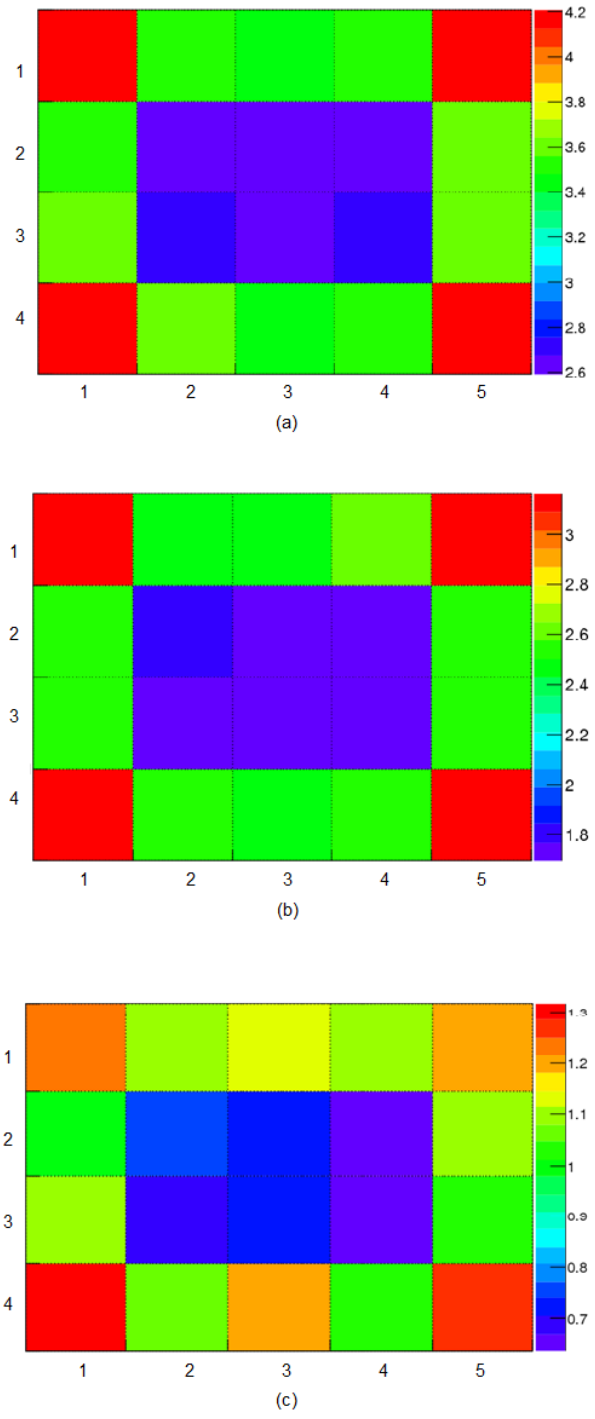

Figure 4.4: *Distribution of the background level (expressed in counts/kg/d) registered in the 1–6 keVee region in anticoincidence at each crystal over a matrix of 4 (vertical) by 5 (horizontal) detectors, for ^{40}K (a) and ^{22}Na (b) from the NaI(Tl) crystals and ^{226}Ra from the PMTs (c). These plots indicate that the analysis of only the six inner modules could be advantageous.*

For ANAIS–250 set–up, it is clear that rejection power will be much more effective for the six inner detectors, as demonstrated in figure 4.4; thus, results for this set–up are shown in the following separately for both, the whole detection mass, and only the six inner modules.

Source	counts/kg/d	(%) of total
Crystal ^{40}K	2.74	26.23
Crystal ^{232}Th	<0.01	<0.01
Crystal ^{238}U	0.02	0.21
Crystal ^{210}Pb	2.45	23.47
Crystal ^{3}H	3.82	36.65
Crystal ^{22}Na	0.71	6.77
PMTs	0.70	6.67
Total	10.44	

Table 4.5: *Expected rate in anticoincidence from different background sources for the ANAIS–112 set–up in the 1–6 keVee energy region.*

Source	counts/kg/d	(%) of total
Crystal ^{40}K	2.00	21.62
Crystal ^{232}Th	<0.01	<0.01
Crystal ^{238}U	0.02	0.23
Crystal ^{210}Pb	2.42	26.18
Crystal ^{3}H	3.82	41.36
Crystal ^{22}Na	0.48	5.16
PMTs	0.50	5.45
Total	9.25	

Table 4.6: *Expected rate in anticoincidence from different background sources for the ANAIS–250 set–up in the 1–6 keVee energy region considering the six central modules only.*

Tables 4.5 and 4.6 summarize the expected rates in the 1-6 keVee region from all the background contributions as well as the total expected rate in anticoincidence for ANAIS-112 and ANAIS-250 (considering the six inner modules), respectively. As expected, the reduction by anticoincidence is more modest in a 3 × 3 matrix than in a 5 × 4 configuration.

4.3 ANAIS–112 with a liquid scintillator veto

The ANAIS set-up for an array of 3 × 3 detectors has been modified by including a LSV. The goal is to evaluate the effective improvement in the background of ANAIS considering the reduction thanks to the rejection of coincidence events, not only between the NaI crystals but also with the veto, and taking into account the contribution from the radioactivity of the main components used in the veto system.

Some of the parameters of the design have been considered as variables and some particular materials or components have been assumed following the work of KIMs [21][189] and SABRE [22] collaborations. For ANAIS LSV system, two different possible designs have been considered (see figure 4.5):

LSVc: A large cylinder for the liquid scintillator (LS) container where NaI modules (including PMTs and crystals) are suspended inside the liquid scintillator.

LSVb: A smaller LS container could be installed in a configuration very similar to that designed for ANAIS-112: the LS would fill the present lead shielding space (10 cm of archaeological lead plus 20 cm of low activity lead surrounding the modules, see figure 4.5) and external 15 cm lead shielding could be added. This design would be easier to be implemented at LSC.

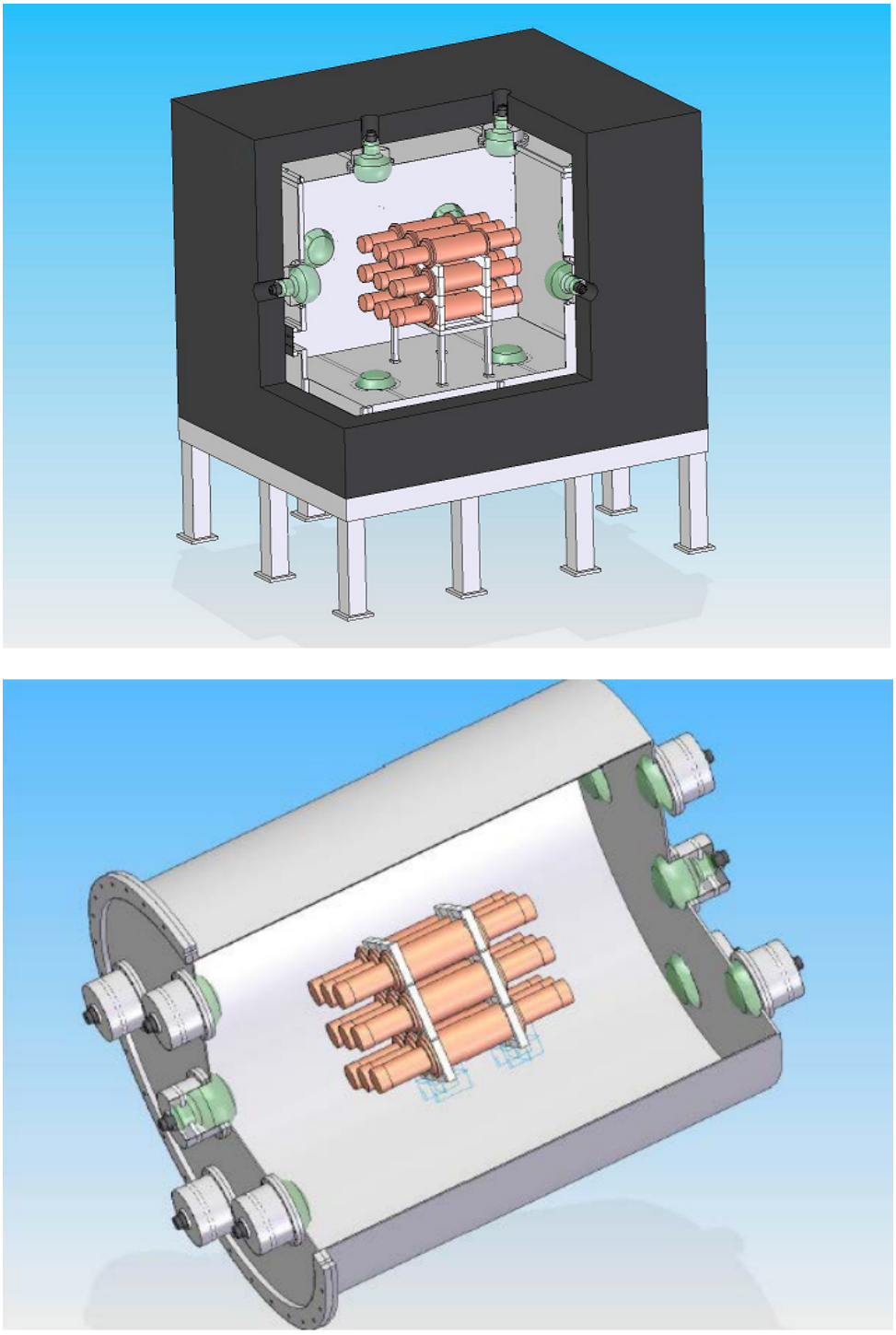

Figure 4.5: *ANAIS–112 set–up artistic view with a liquid scincintillator veto considering two possible designs: LSVb (top) and LSVc (bottom).*

4.3.1 Simulation

The components of the set–ups included in the corresponding Geant4 simulation (see figures 4.6 and 4.7) are:

- *Vessel:*

  – For LSVc, a stainless steel cylinder, 5–mm–thick, has been defined. It allows to contain a thickness [1] of scintillator of 60 cm; this value has been chosen after studying the escape probability [2] of the 1460.8 keV photons from ^{40}K (after emission in one of the NaI crystals) as a function of the liquid scintillator thickness. In figure 4.8 it can be observed that for values of the thickness beyond 60 cm there is not a significant improvement in the escape probability.

  – For LSVb, a 1.5–mm–thick stainless steel box has been defined, as that prepared to house the ANAIS–112 set–up, having external dimensions of 1150 $\times$ 1125 $\times$ 1550 mm^3.

- *Reflector:* 0.5–mm–thick reflector Lumirror has been considered. It is a polyester produced by Japanese Toray company.

- *Liquid scintillator medium:* Linear AlkylBenzene (LAB) has been considered. The total mass of scintillator is estimated to be 3.8 tons for LSVc and 1.7 tons for LSVb. Although it has not been considered in the simulation, 2 g/l 2.2-diphenyloxazole (PPO) will be added to the LAB as a wavelength shifter.

- *Photomultipliers:* PMT model Hamamatsu R5912, with 8" diameter, has been chosen. A simplified description of each PMT unit as a 0.5–mm–thick cylinder made of borosilicate with vacuum inside, having approximately the diameter and length of the R5912 PMT, has been implemented. In both cases, 10 units are used, five units at each end of the vessel for LSVc and one unit at each small face and two units at the four large faces for LSVb.

[1] This thickness is considered as the increase both in radius and half–height of a minimum cylinder with radius 30 cm and height 62 cm containing the 3×3 crystals matrix

[2] At each condition, the escape probability of the 1460.8 keV photon has been evaluated as the probability of null energy depositions in the active detector volumes (either the 9 NaI crystals, or the LSV). For ^{40}K decays, this probability can be multiplied by the probability of K–shell EC to the excited state of the daughter nucleus in order to quantify the residual events at the 3.2 keV peak. This peak has in addition the unavoidable contribution of the direct decay to the fundamental state.

- *Shielding:* no shielding has been considered for LSVc, but for LSVb, a 15–cm–thick layer of lead outside the stainless steel vessel has been included in the simulation.

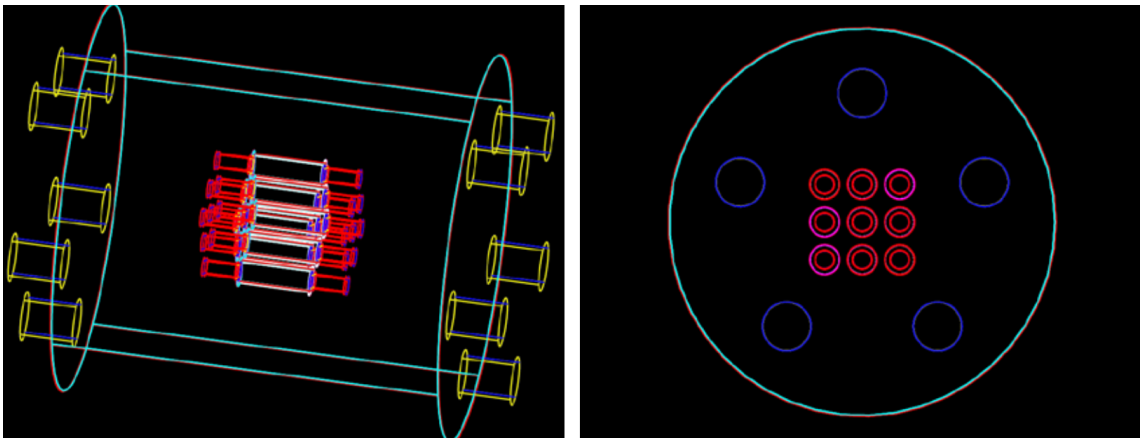

Figure 4.6: *LSVc geometry for the Geant4 simulation.*

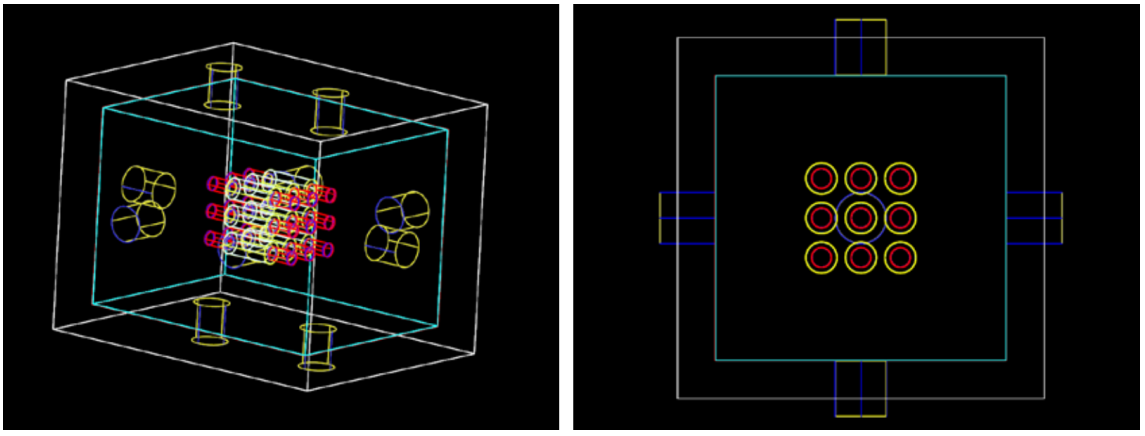

Figure 4.7: *LSVb geometry for the Geant4 simulation.*

Energy deposited at each one of the 3 × 3 NaI crystal matrix and in the LSV is registered for each simulated event to perform coincidence analysis afterwards. An energy threshold for event detection in the LSV can be applied for analysis.

Energy spectra for the following conditions have been derived:

- Spectra at the LSV (without including the effect of the energy resolution of the detector).
- Total spectra (t), summing the contributions from the 9 NaI(Tl) modules.

- Anticoincidence spectra (a), summing the contributions from the 9 NaI(Tl) modules and rejecting coincidences between them.
- Anticoincidence vetoed spectra, summing the contributions from the 9 NaI(Tl) modules and rejecting coincidences between them and with the LSV. No threshold in LSV (av) and a 500 keV energy threshold ($av500$) conditions have been evaluated.

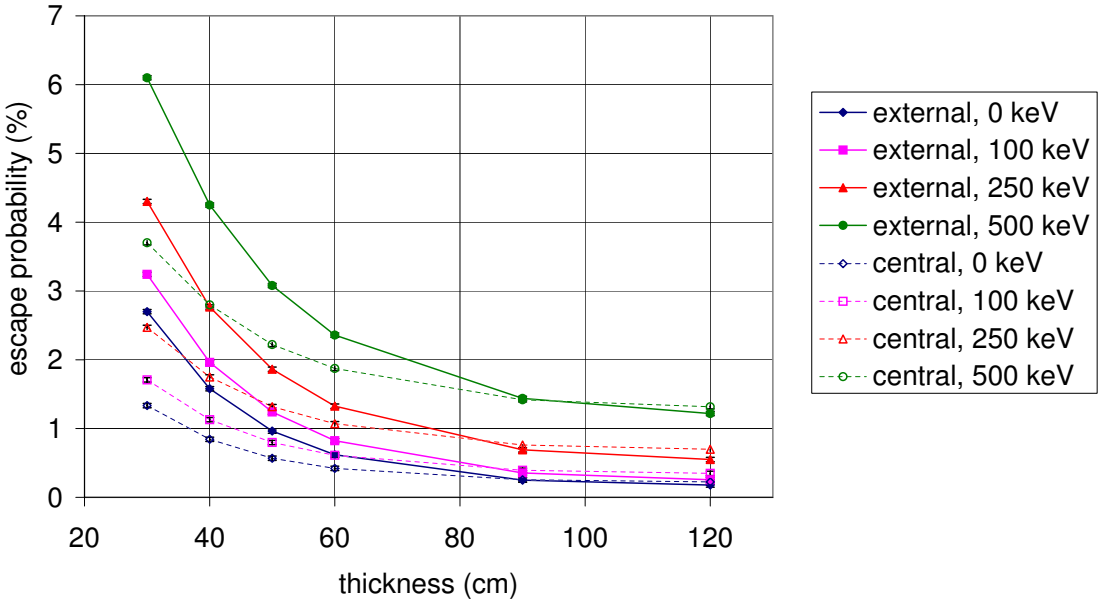

Figure 4.8: *Escape probability of the 1460.8 keV photon as a function of the liquid scintillator thickness, for both external and central detectors and for different energy threshold values of the LSVc system. The curves show that the reduction of the escape probability softens for thickness above 60 cm.*

4.3.2 Results for the LSV detector

Plots in figure 4.9 show the energy spectra registered at the LSV for the different simulated background contributions, for LSVc (the larger cylindrical veto without lead shielding) and LSVb (the smaller box veto with a 15–cm–thick lead shielding). Note that contributions from muons and the LSV system have not been simulated yet for the LSVb configuration because their effect is negligible in the NaI detectors background, as it will be shown later (see subsection 4.3.3).

In the simulation of the LSVc, the external gamma flux contribution to the energy depositions in the LSV is about three orders of magnitude higher than the

other contributions, while that of muons is 3–4 orders of magnitude lower. From the detection system, photomultipliers and container are the dominant sources, while emissions from crystals are much less relevant. In the case of LSVb, even though the external gamma background still dominates the counting, its contribution is significantly reduced (see figure 4.9).

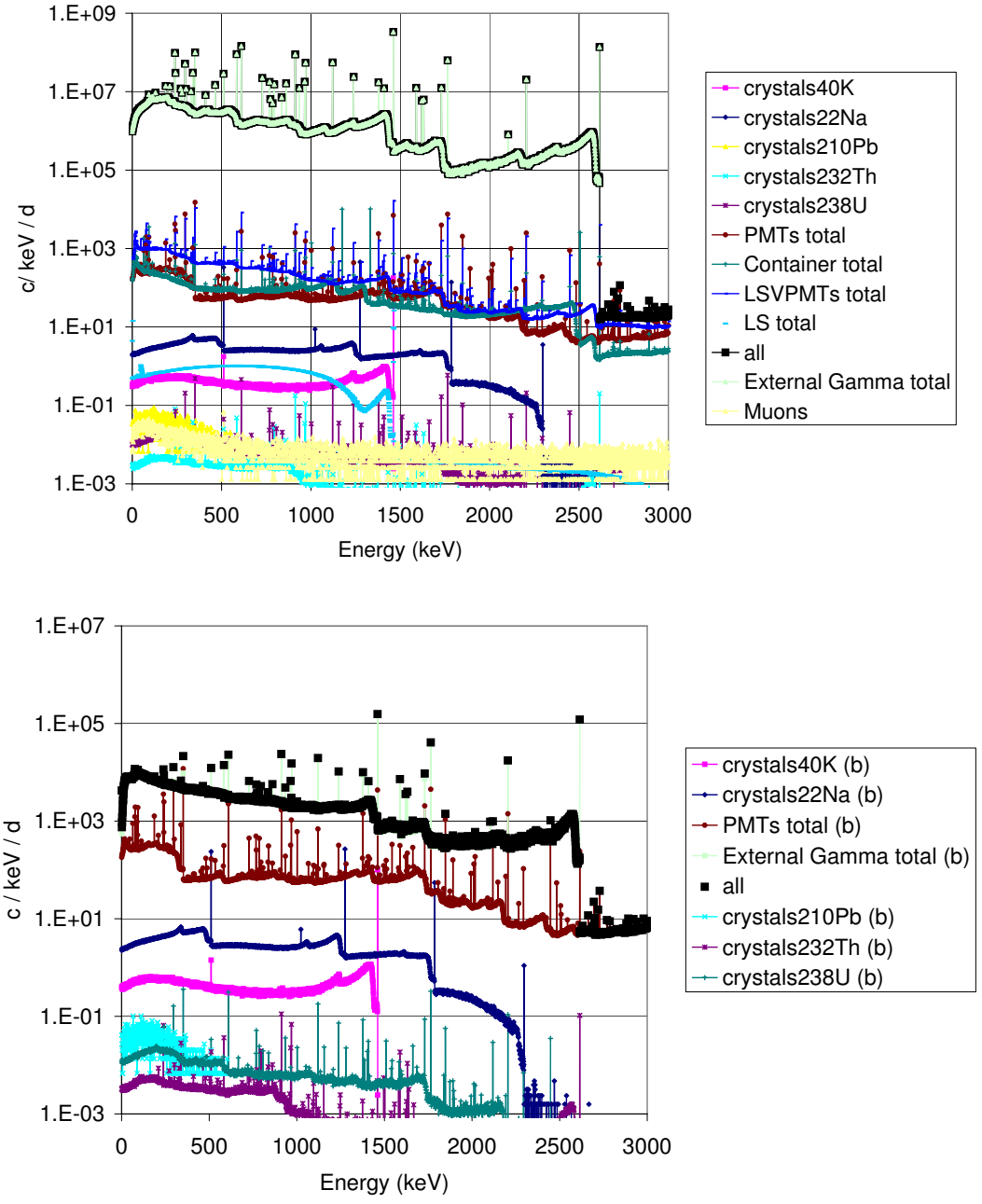

Figure 4.9: *Energy spectra registered at the LSV for different simulated background contributions in the case of LSVc (top) and LSVb (bottom). Note that some sources (muons and contaminations of LSV components) have not been simulated for LSVb.*

The total trigger rate below 3 MeV for the LSV is of the order of 65 kHz in the LSVc (simulated without shielding) while it is below 100 Hz in the case of LSVb (see tables 4.7 and 4.8). Different energy thresholds for the LSV trigger have been considered in the simulation: a 500 keV threshold reduces the trigger rate in a factor of 2 for both designs. Anyhow, it is clear that a shielding for the LSVc should be included in the experimental implementation of the veto system in order to be able to veto real coincidences and not being overcome by the veto rate.

Threshold (keV)	Rate from NaI modules (Hz)	Rate from LSV (Hz)	Rate from muons (mHz)	Rate from external gammas (kHz)	Total rate (kHz)
0	3.2	11.2	0.24	64.5	64.5
100	2.8	9.5	0.21	60.1	60.1
250	2.2	7.4	0.18	47.5	47.5
500	1.6	5.5	0.14	35.3	35.3

Table 4.7: *Detection rates below 3 MeV at the LSV assuming different energy thresholds and for different simulated background contributions in LSVc.*

Threshold (keV)	Rate from NaI modules (Hz)	Rate from external gammas (Hz)	Total rate (Hz)
0	3.2	72.3	75.5
100	2.8	64.2	67.0
250	2.2	51.9	54.1
500	1.6	38.4	40.0

Table 4.8: *Detection rates below 3 MeV at the LSV assuming different energy thresholds and for different simulated background contributions in LSVb. Note that some sources (muons and contaminations of LSV components) have not been simulated for LSVb.*

4.3.3 Results for energy depositions at the NaI(Tl) crystals

Figure 4.10 compares the energy spectra corresponding to energy depositions at the very low energy region in the NaI(Tl) modules, considering all the background sources as explained in section 4.1 and in different situations, to illustrate the effect of anticoincidence between crystals and also with the LSV. Spectra have been evaluated for the 3×3 detectors set-up considering anticoincidence only between crystals, also with an ideal LSV and with a LSV having a 500 keV energy threshold. Spectra obtained in anticoincidence in the 5 × 4 modules set–up (ANAIS–250) are also shown for comparison. Environmental gamma background is assumed to be properly suppressed thanks to the implementation of a lead or water shielding.

Table 4.9 summarizes the reduction factors obtained in the considered situations at the 1–6 keVee region, for all the contributions altogether and separately for some background sources, those for which high reduction is expected: ^{40}K and ^{22}Na at crystals and PMT contaminations. The reduction factor is computed from the ratio between the rates in the 1–6 keVee after coincidence events rejection and before any rejection and therefore corresponds to the percentage of remaining background.

For comparison, the values of the reduction factors obtained by anticoincidence at the ANAIS–250 set–up (5 × 4 crystals, without LSV system) are also reported, both for the whole crystal matrix or considering only the six inner detectors. The veto by the LSV is very effective for the ^{40}K and ^{22}Na peaks, but since it is useless for the other relevant background sources at the region of interest (^{3}H and ^{210}Pb) the estimated overall reduction factor is in the end of 55.6% for the ideal LSVc and 59.1% considering a 500 keV threshold. For the assumed background model, about 70% of the background obtained in anticoincidence for the 3 × 3 crystals configuration remains even after the vetoing effect of the LSV. Comparing the reduction for the two veto systems, the loss of effectiveness in the small box veto is more important for ^{22}Na; the ^{40}K contribution is in both systems dominated by the EC decays to the ground state of the daughter, which cannot be vetoed.

The background rates in the 1–6 keVee region for the considered contributions in the ideal *av* situation for the two veto systems are summarized in tables 4.10 and 4.11. In figure 4.11, the low energy spectra from different contributions for the *av* situation (assuming that the external gamma background has been properly suppressed) are shown for the two designs. The effective reduction of the ^{40}K and

^{22}Na peaks can be seen, becoming tritium the dominant contribution.

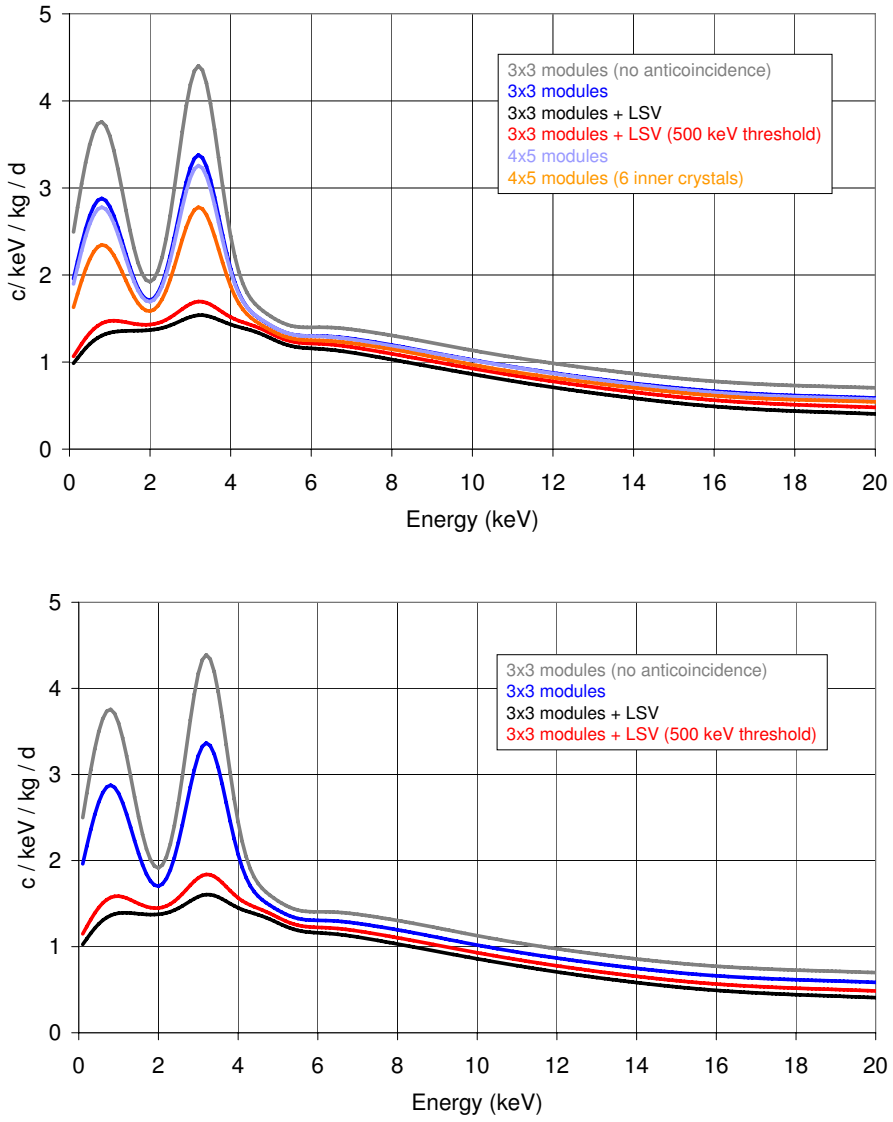

Figure 4.10: *Energy spectra at the very low energy region expected from all the considered background sources in different set-ups and anticoincidence conditions (see text). Results are shown for LSVc (top) and LSVb (bottom).*

Concerning the contribution at the region of interest from ^{210}Pb in crystals, it is worth noting that it could be higher in case of a surface contamination (see sections 3.5 and 3.6). Assuming all the ^{210}Pb was on surface at a depth of 30 μm, the increase in the rate in the 1–6 keV region in comparison to a pure bulk contamination would be of a factor 1.6.

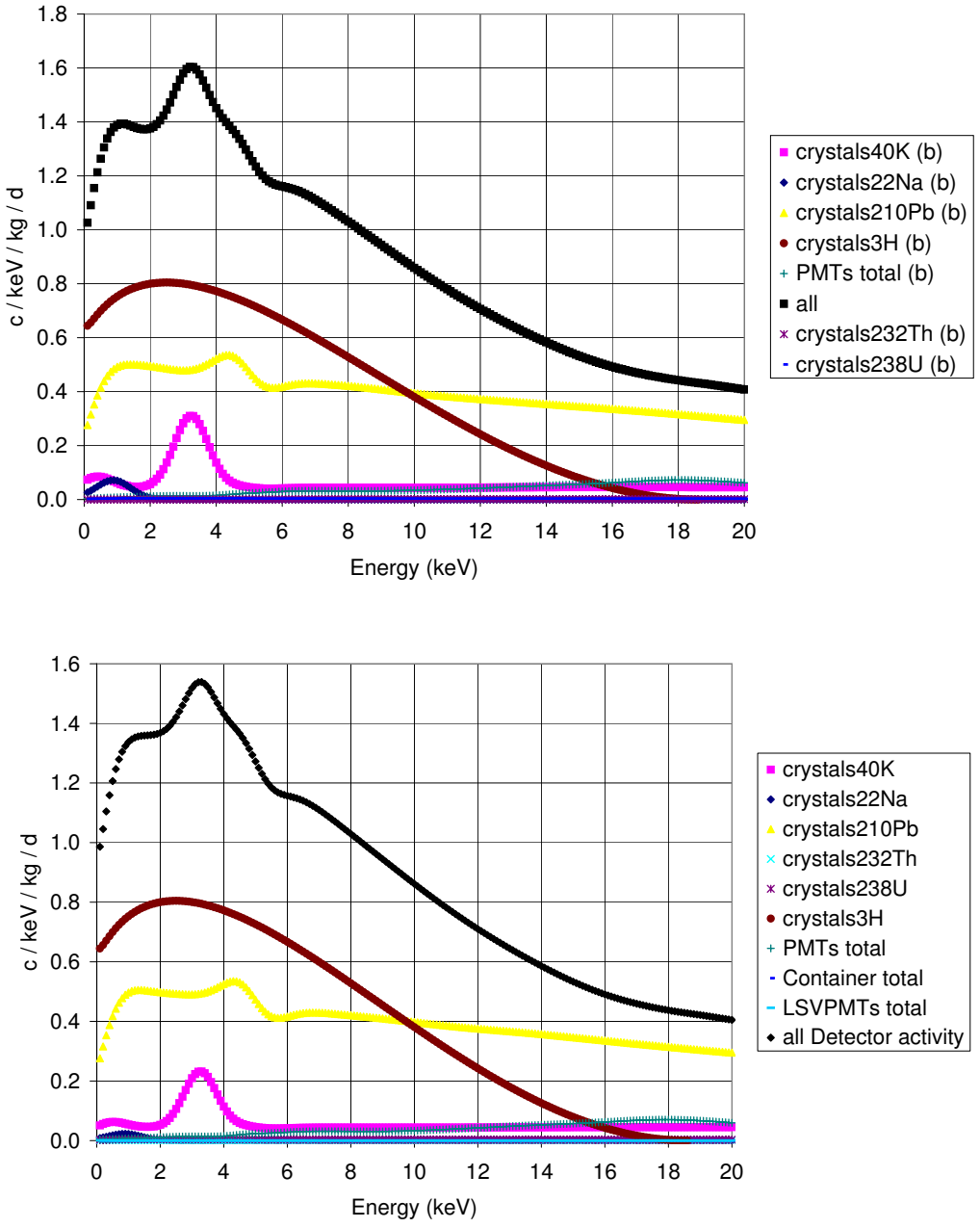

Figure 4.11: *Energy spectra from the simulated background sources registered at the NaI(Tl) detectors for LSVc (top) and LSVb (bottom) designs in the av conditions.*

Set-up	R.F.(%) ^{40}K from crystals	R.F.(%) ^{22}Na from crystals	R.F.(%) PMTs	R.F.(%) Total
3×3 modules	69.0	62.4	62.3	83.7
3×3 modules + LSVc	11.9	1.2	7.3	55.6
3×3 modules + LSVc (500 keV threshold)	15.5	5.7	29.3	59.1
3×3 modules + LSVb	14.5	3.7	7.3	56.6
3×3 modules + LSVb (500 keV threshold)	20.5	11.0	31.1	61.3
5×4 modules	62.7	55.1	45.9	77.9
5×4 modules (6 inner crystals)	48.6	39.8	32.5	70.3

Table 4.9: *Reduction factor (R.F.), defined as percentage of background remaining after anticoincidence in the 1–6 keVee region, computed for several set–ups and applying anticoincidence rejection only between crystals or also with the LSV (see text). It has been evaluated separately for some background sources and for the overall background in different experimental scenarios.*

From the simulation of LSVc, we can conclude that the contribution of the emissions produced in the LSV (container, PMTs and liquid scintillator) is negligible for the assumed activities and geometry, since it is at least two orders of magnitude lower than the contribution from the NaI(Tl) crystals and their PMTs.

The contribution from muons is also negligible and completely disappears when considering anticoincidence with LSVc. For these reasons, these contributions (emissions from the LSV system and muons) have not been simulated for the moment for LSVb. It must be noted that no upper cut has been considered in the detection energy of the LSV for the moment, although it could affect the efficiency of the veto effect for muons.

In the present LSVc configuration (without shielding), the contribution of the external gamma background is about 2 orders of magnitude higher than the total contribution from the detection system activity without considering anticoincidence

with the LSV. The same is observed at higher energies. The anticoincidence with the LSV allows a very effective reduction of this gamma background contribution, but its dependence on the energy threshold of the LSV is very important; for a 500 keV threshold, the external gamma flux gives a rate still comparable to, or significantly higher, than the total contribution from the detection system activity. Therefore, operation of the LSV without a shielding against the environmental gamma background seems to be problematic. For the LSVb, the 15–mm–thick lead shielding efficiently suppresses the external gamma contribution.

With respect to the evaluated contribution from the crystals and their PMTs, there is no difference between the two veto systems when considering total spectra (t) or anticoincidence between crystals (a), but, as expected, the anticoincidence with the veto (av) is less effective for the small box LSV, although the difference is not very significant.

4.4 Conclusions

From the simulation of the most relevant background sources for the full ANAIS set–up considering different configurations, the following conclusions can be drawn:

- Assuming the activities of the best characterized detector (D2), for 9 crystals with total mass of 112.5 kg of NaI(Tl), the expected background rate is below 2 counts/(keV kg d) above 4 keVee and of 2.5 counts/(keV kg d) in the region from 1 to 4 keVee, which could be reduced at 1.4 counts/(keV kg d) by using a LSV. Following the obtained results, the implementation of a LSV system at the 3×3 matrix set–up is more effective that the increase of NaI modules, for fixed radiopurity levels, in order to reduce the intrinsic background level. However, it is worth noticing (see chapter 5) that the expected signal increases with the total detection mass, and thus both effects have to be considered in the sensitivity analysis.

- Operation of a LSV system without a lead (water) shielding is precluded due to the non–negligible contribution of the environmental gamma background at the region of interest and the high counting rate generated at the LSV. The inclusion of a 15–cm–thick lead shielding allows to reduce the environmental gamma background contribution in the 1–6 keVee below 0.04 counts/(keV kg d) for

an ideal LSV and to 0.11 counts/(keV kg d) considering a 500 keV threshold for the LSV.

- The increase in the rate at the region of interest when considering a small box instead of a larger cylindrical LSV is not very significant for the dominant background sources and it seems that it could be tolerated. Reduction factors are virtually the same for both LSV systems (see table 4.9).
- Expected contribution from the activity of the LSV system itself seems to be unimportant for the assumed values, being two orders of magnitude lower than that from the NaI detectors.
- The effect of the energy threshold of the LSV is not very relevant in the very low energy region of interest.

Source	counts/kg/d	(%) of total
Crystal ^{40}K	$4.7\ 10^{-1}$	6.83
Crystal ^{232}Th	$5.6\ 10^{-4}$	0.01
Crystal ^{238}U	$2.1\ 10^{-2}$	0.31
Crystal ^{210}Pb	2.4	35.72
Crystal ^{3}H	3.8	55.78
Crystal ^{22}Na	$1.3\ 10^{-2}$	0.19
PMTs	$8.0\ 10^{-2}$	1.16
LSV PMTs	$1.5\ 10^{-5}$	0.0002
Container	$4.1\ 10^{-6}$	0.0001
LS	0	0
Muons	0	0
Total	6.9	

Table 4.10: *Expected rate from different background sources for the LSVc set–up for the av condition in the 1–6 keVee energy region.*

Source	counts/kg/d	(%) of total
Crystal ^{40}K	5.7 10^{-1}	8.19
Crystal ^{232}Th	5.6 10^{-4}	0.01
Crystal ^{238}U	2.1 10^{-2}	0.31
Crystal ^{210}Pb	2.4	34.88
Crystal ^{3}H	3.8	54.85
Crystal ^{22}Na	4.2 10^{-2}	0.60
PMTs	8.2 10^{-2}	1.17
LSV PMTs	not simulated	
Container	not simulated	
LS	not simulated	
Muons	not simulated	
External gamma	< 0.19 (90% C.L.)	
Total	7.0	

Table 4.11: *Expected rate from different background sources for the LSVb set–up for the av condition in the 1–6 keVee energy region.*

Chapter 5

Sensitivity projections in different scenarios

In the absence of a distinctive signal, as is the observation of an annual modulation effect in the interaction rate, it is very difficult to distinguish interactions produced by the dark matter particles from those corresponding to backgrounds in a given experiment. In these cases, results are usually presented in exclusion curves of the WIMP–nucleon interaction cross-section vs. WIMP mass.

Exclusion curves are obtained by comparing the measured rate in a given experiment and the expected rate of nuclear recoils due to the interaction of WIMPs (see section 1.4.2.1), as shown in figures 1.13 and 1.14 for SI and SD interactions, respectively. In these plots, for a fixed WIMP mass, all cross–sections remaining above the curve are excluded, as they would produce interaction rates large enough to be incompatible with the measured one. In the most conservative approach, all the measured rate is attributed to dark matter. If some of the backgrounds are really well understood, they can be taken into account in order to improve the derived limits.

However, this is not the goal of the ANAIS experiment, devoted to the search for the annual modulation signal (described in section 1.4.2.3). To evaluate the sensitivity of a given experiment in this search, the so–called sensitivity plots were introduced in [218]. A brief explanation about how these plots are derived will be given in section 5.1 and the projections obtained assuming different scenarios for ANAIS will be discussed in section 5.2.

5.1 Sensitivity plots

5.1.1 Extraction of the modulation signal

In order to study any seasonal modulation in a given experiment, data have to be grouped in convenient energy and time intervals. N_{ik} represents the number of events collected in the i–th time bin and k–th energy bin and for a given exposure $W_{ik} = M\Delta t_i \Delta E_k \epsilon_k$, being M the detector mass, Δt_i the effective live time in the i-th time bin, centered in t_i, ΔE_k the amplitude of the k-th energy bin and ϵ_k the efficiencies that have to be taken into account whenever some subtraction or filtering method is used with the data. In the following ϵ_k have been taken as 1, except when explicitly stated.

The mean value of N_{ik} can be expressed as the expected background in the k-th energy bin (b_k) plus the dark matter expected event rate as:

$$< N_{ik} > \equiv \mu_{ik} = [b_k + S_{0,k} + S_{m,k} \cdot cos\omega(t_i - t_0)] \cdot W_{ik} \tag{5.1}$$

where $\omega = \frac{2\pi}{T}$ with T=1 y and t_0 corresponds to 2^{nd} June (see section 1.4.2.3). For simplicity t_0 is omitted in the following equations as far as this only implies a re-definition of the time origin. $S_{0,k}$ and $S_{m,k}$ parameters (constant and modulated amplitude of the dark matter expected event rate, respectively, as seen in subsection 1.4.2.3) depend on the WIMP–nucleus cross–section and the WIMP mass.

The procedure to extract a modulated signal with a given period and phase from a set of measured events has been discussed by several authors [85] [220–222].

The maximum–likelihood estimation method is the most commonly used procedure when comparing theory with the measured data. Assuming that N_{ik} follow a Poisson distribution with mean values μ_{ik}, the combined–probability function of all the collected N_{ik} is given by:

$$L = \prod_{ik} e^{-\mu_{ik}} \frac{\mu_{ik}^{N_{ik}}}{N_{ik}!} \tag{5.2}$$

The most probable values of m_W and the cross–section, σ, maximize equation 5.2,

this is, minimize the following function:

$$y(m_W, \sigma) \equiv -2logL - C = 2\mu - 2\sum_{ik} N_{ik} log[b_k + S_{0,k} + S_{m,k} \cdot cos\omega t_i] \qquad (5.3)$$

where $\mu \equiv \sum_{ik} \mu_{ik}$ and, for simplicity, those terms not depending on m_W or σ are included in the constant, C, as they are irrelevant for the minimization of equation 5.3.

The function y is minimized in two steps: first with respect to the time independent parts, $b_k + S_{0,k}$, and second with respect to m_W and σ. In the first minimization, b_k are free parameters, only constrained to be positive.

Following standard procedures [219], a region of n standard deviations around the minimum in the plane (σ, m_W) can be found by imposing the condition $y(\sigma, m_W) - y_{min} \leq n^2$.

In reference [218] it is shown that the likelihood function y behaves asymptotically like the χ^2 function:

$$\chi^2(\sigma, m_W) \equiv \sum_k \frac{(S_{m,k}(m_W, \sigma) - X_k)^2}{Var(X_k)} \qquad (5.4)$$

where

$$X_k \equiv \frac{\sum_i N_{ik} cos\omega t_i - N_k \beta_k}{W_k(\alpha_k - \beta_k^2)} \qquad (5.5)$$

$$\beta_k = \frac{\sum_i W_{ik} cos\omega t_i}{W_k} \qquad \alpha_k = \frac{\sum_i W_{ik} cos^2 \omega t_i}{W_k} \qquad (5.6)$$

$$N_k \equiv \sum_i N_{ik} \qquad W_k \equiv \sum_i W_{ik} \qquad < X_k >= S_{m,k} \qquad (5.7)$$

When the maximum of the likelihood function has been found, a positive result excludes the absence of modulation at some confidence level probability. In order to test the goodness of the null hypothesis, the quantity

$$\delta^2 = y(\sigma = 0) - y(m_W, \sigma)_{min} \qquad (5.8)$$

can be evaluated, due to its asymptotic behaviour as:

$$\delta^2 \simeq \chi^2(\sigma = 0) - \chi^2_{min} \qquad (5.9)$$

5.1.2 Statistical significance

Following this procedure, two different situations could be found:

- Absence of a modulation effect; in this case, numerical simulations show that δ^2 belongs asymptotically to a χ^2 distribution with two degrees of freedom (once the cross–section is set to zero, the L function no longer depends on m_W as all the S_0 and S_m functions vanish).

- Presence of a modulation effect; in this case, δ^2 has an asymptotic distribution of a non–central χ^2 with one degree of freedom and with a mean value given by:

$$< \delta^2 >= \frac{1}{2} \sum_k \frac{S_{m,k}(\sigma, m_W)^2 \Delta E_k}{b_k + S_{0,k}} MT\alpha + 2 \tag{5.10}$$

  where the factor of merit α, has been considered as $\alpha = \frac{2}{T} \sum_i cos^2 \omega t_i$ ($\alpha = 1$ in case of a full period of data taking). The same time of measuring has been assumed for all the energy bins and the approximations

$$< \sum_i N_{ik} cos^2 \omega t_i > \simeq < N_{ik} > \sum cos^2 \omega t_i \tag{5.11}$$

  and

$$< N_{ik} > \simeq W_k (b_k + S_0) \tag{5.12}$$

  have been considered.

The statistical interpretation of the sensitivity plot is obtained from the degree of overlapping between the δ^2 distributions in the two cases, absence and presence of modulation.

The needed exposure $MT\alpha$ in order to observe a modulation effect with a given probability can be estimated through equation 5.10: for instance, $< \delta^2 > = 14.9$ (5.6) corresponds to a 90% (50%) probability to see an effect at least at the 95% (90%) C.L. Therefore, once a required $< \delta^2 >$ is chosen, a sensitivity plot can be obtained by showing the curves of constant $MT\alpha$ in the plane $m_W - \sigma$. Other situations are summarized in table 5.1, where $< \delta^2 >$ is tabulated as a function of the fraction of experiments where absence of modulation can be excluded (rows), at a

given confidence level (columns). This procedure would allow to see the masses and exposures needed to explore each different region of the WIMP m_W–σ parameter space in a compact way.

	90%	**95**%	**99** %	**99.5**%	**99.9**%
50%	5.6	7.0	10.2	11.6	14.8
60%	6.8	8.3	11.8	13.3	16.8
70%	8.1	9.9	13.7	15.3	19.0
80%	9.9	11.8	16.0	17.8	21.8
90%	12.8	14.9	19.6	21.6	26.0
95%	15.4	17.8	22.9	25.0	29.8
99%	21.0	23.8	29.7	32.2	37.5

Table 5.1: *Parameter* $< \delta^2 >$ *as a function of the confidence level required to exclude the absence of modulation (columns) and the fraction of successful experiments (rows). From [218].*

5.2 Prospects for ANAIS

The projected sensitivity of ANAIS to dark matter annual modulation assuming SI interactions has been evaluated in different scenarios following the procedure presented in [218] and summarized in section 5.1.

In the calculation of the sensitiviy plots, Helm form factors have been considered, as well as a standard halo model (isothermal sphere) with ρ=0.3 GeV/cm^3, v_0=220 km/s and v_{esc}=650 km/s, quenching factors 0.3 for Na and 0.1 for I. All sensitivity plots have been obtained requiring 90% CL and 90% of successful experiments and assuming 5 years of data taking.

First, a conservative scenario of background, assuming that already achieved for D2 (see section 3.6.1) with two active masses (112 and 250 kg of NaI(Tl)) is shown in figure 5.1. The modulated signal is searched for in an analysis energy window from 1 to 6 keVee.

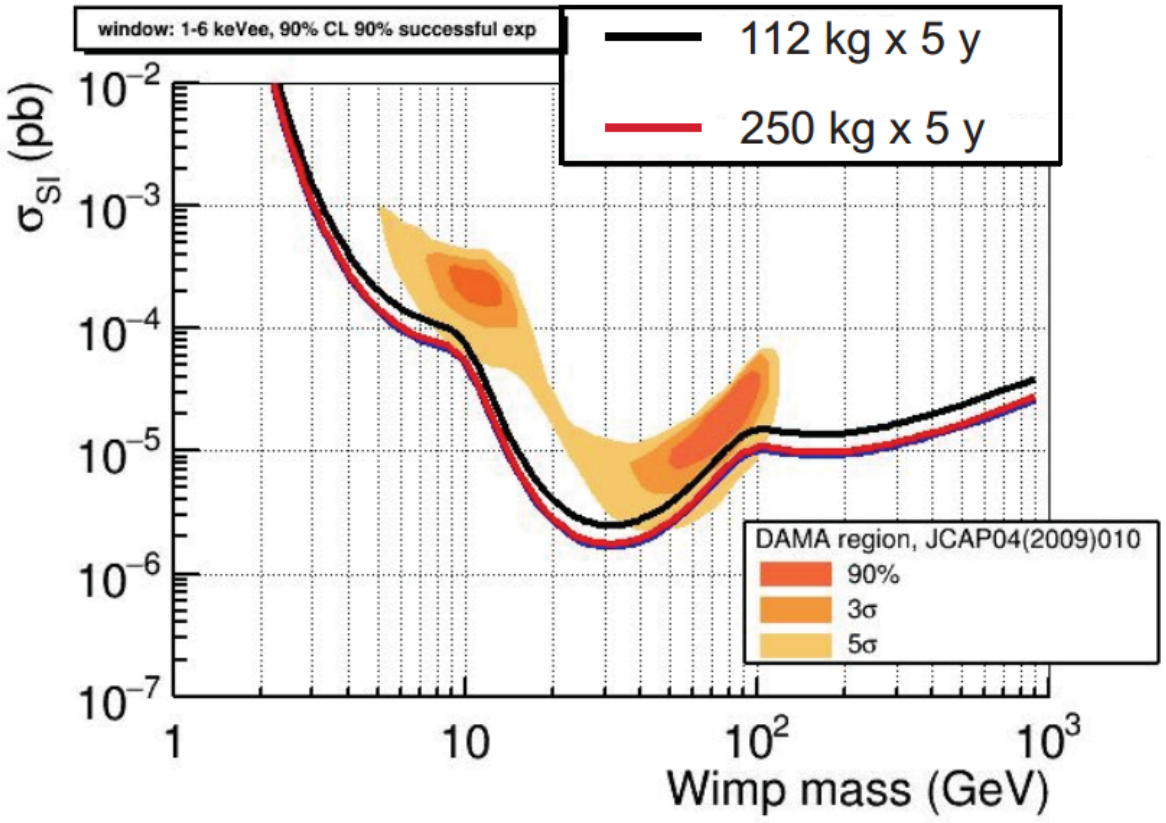

Figure 5.1: *Sensitivity plot in the $\sigma^{SI}_{Wn} - m_W$ plane for ANAIS full experiment. Background level achieved in D2 detector has been assumed in the 1-6 keVee energy region for 112 kg and 250 kg of NaI(Tl). Orange areas represent DAMA modulation regions at 90%, 3σ and 5σ levels.*

Then, the effect of considering different energy regions for the analysis in ANAIS–112, without LSV and for 5 years of data taking is shown in figure 5.2. The simulated background depicted in figure 4.2 has been assumed.

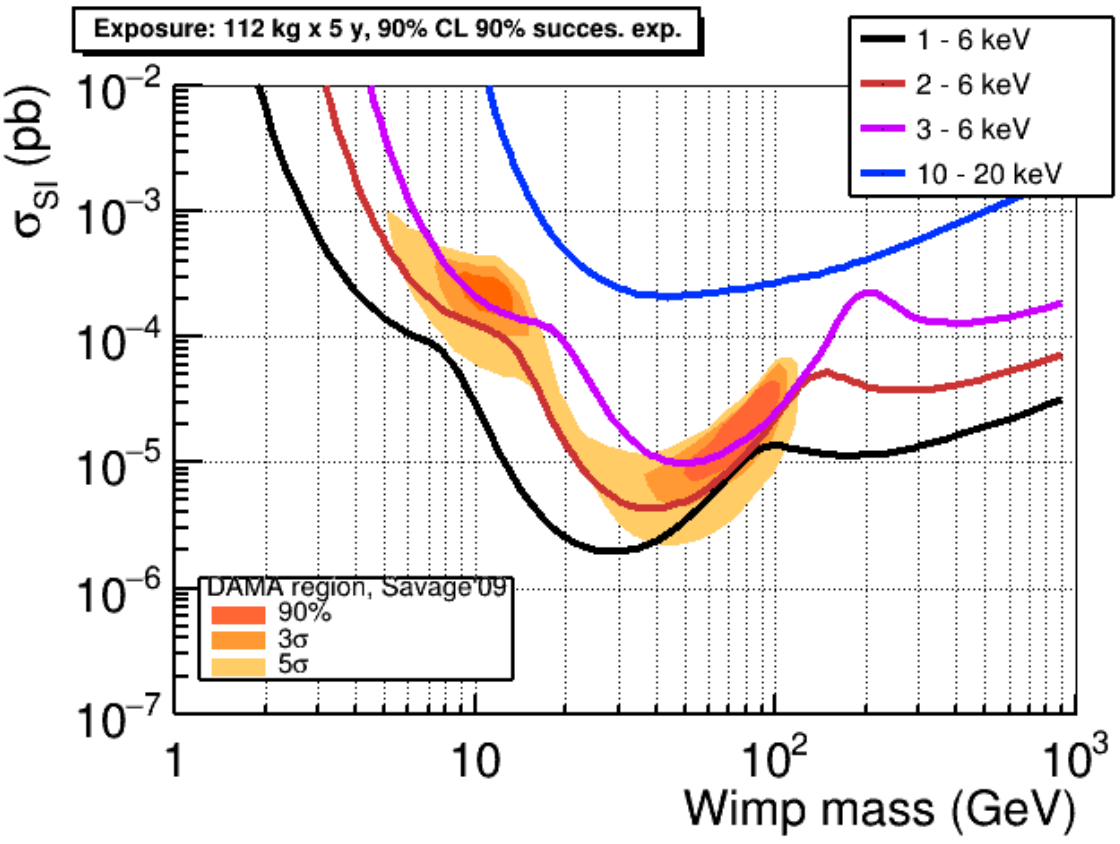

Figure 5.2: *Sensitivity plot in the $\sigma^{SI}_{Wn} - m_W$ plane for ANAIS-112 experiment considering different energy regions in the analysis for 112 kg of NaI(Tl) and the background simulated for ANAIS-112 without LSV (shown in figure 4.2).*

The sensitivity plot for ANAIS–112 with LSV, ANAIS-250 and considering only the six central crystals in the 5×4 configuration for 5 years of data taking is shown in figure 5.3. The simulated backgrounds shown in figure 4.10 (top) have been assumed.

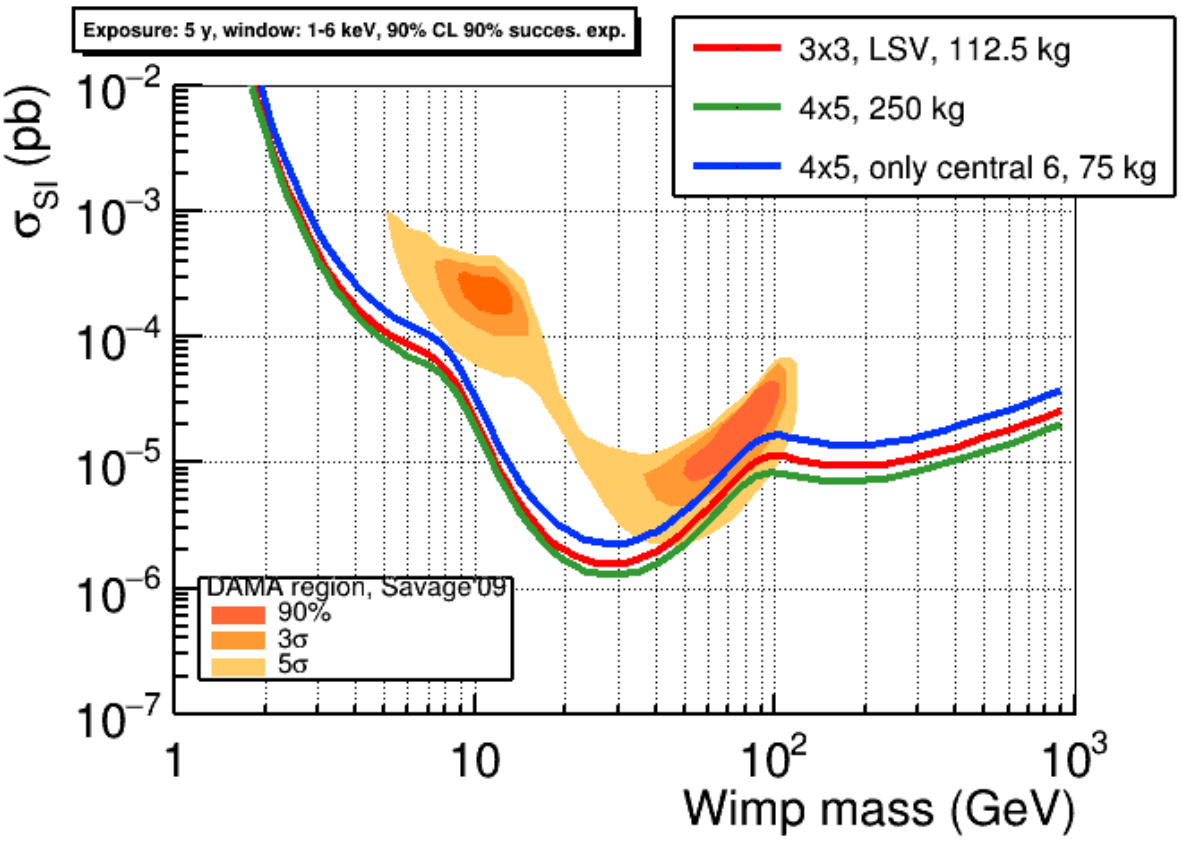

Figure 5.3: *Sensitivity plot in the $\sigma^{SI}_{Wn} - m_W$ plane for ANAIS-112 + LSV, ANAIS-250 and considering only the six central crystals in the 5 ×4 configuration. The simulated backgrounds shown in figure 4.10 (top) have been assumed in the 1–6 keVee energy region.*

In figure 5.4 it is shown the sensitivity corresponding to ANAIS–112 with and without LSV (spectra from figure 4.10) (top) and to ANAIS–112 with an improved background (by reducing ^{40}K contamination to the level of D3, as estimated in figure 4.3) in the 1–6 keVee region.

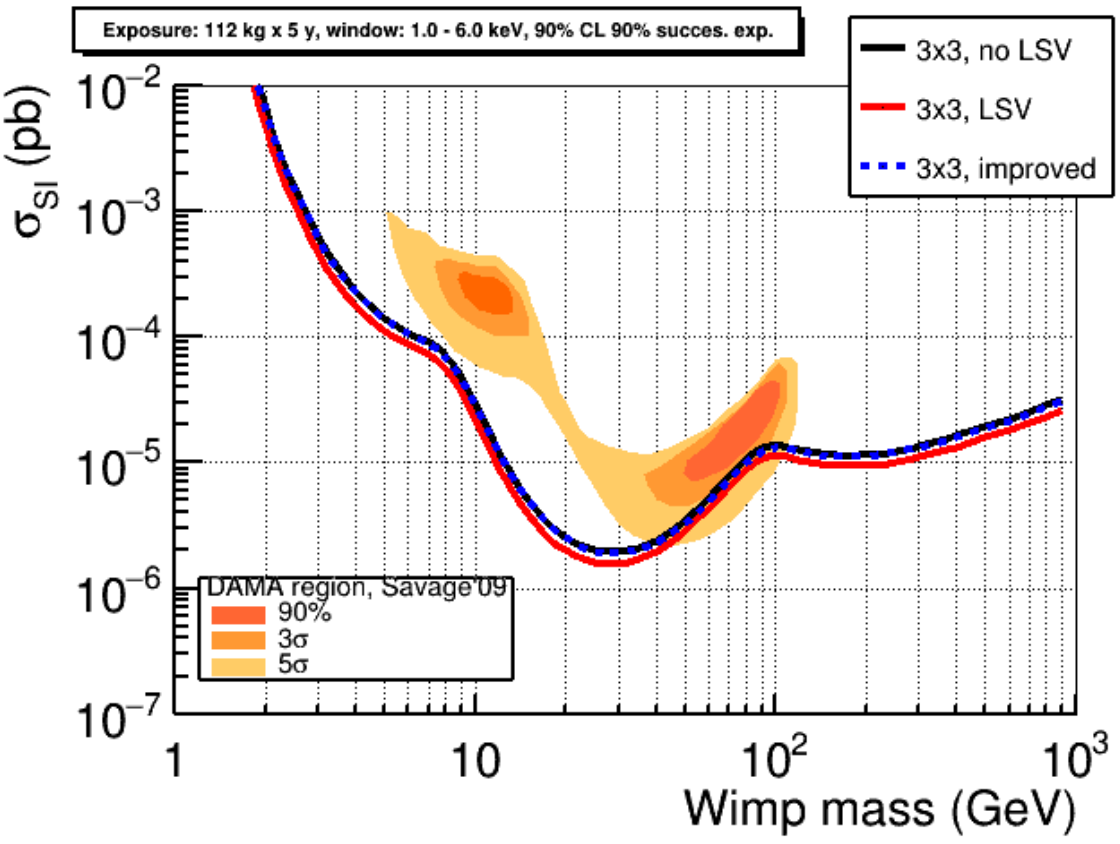

Figure 5.4: *Sensitivity plot in the $\sigma^{SI}_{Wn} - m_W$ plane for ANAIS–112 with and without LSV together with a reduction of the background (^{40}K at the level of D3 and ^{210}Pb at the level of D2) in the 1-6 keVee energy region for 112 kg of NaI(Tl).*

Finally, the effect of including a filtering acceptance efficiency lower than 1 near the threshold has been studied and it is shown in figure 5.5. Two cases are compared with that corresponding to efficiency 1 from 1 to 6 keVee: efficiency of 0.1 from 1 to 2 keVee and 1 from 2 to 6 keVee and an efficiency linearly increasing from 0.1 at 1 keVee till 1 at 3 keVee and constant above 3 keVee. Background level in a 3×3 configuration set–up without LSV, shown in figure 4.2, has been assumed.

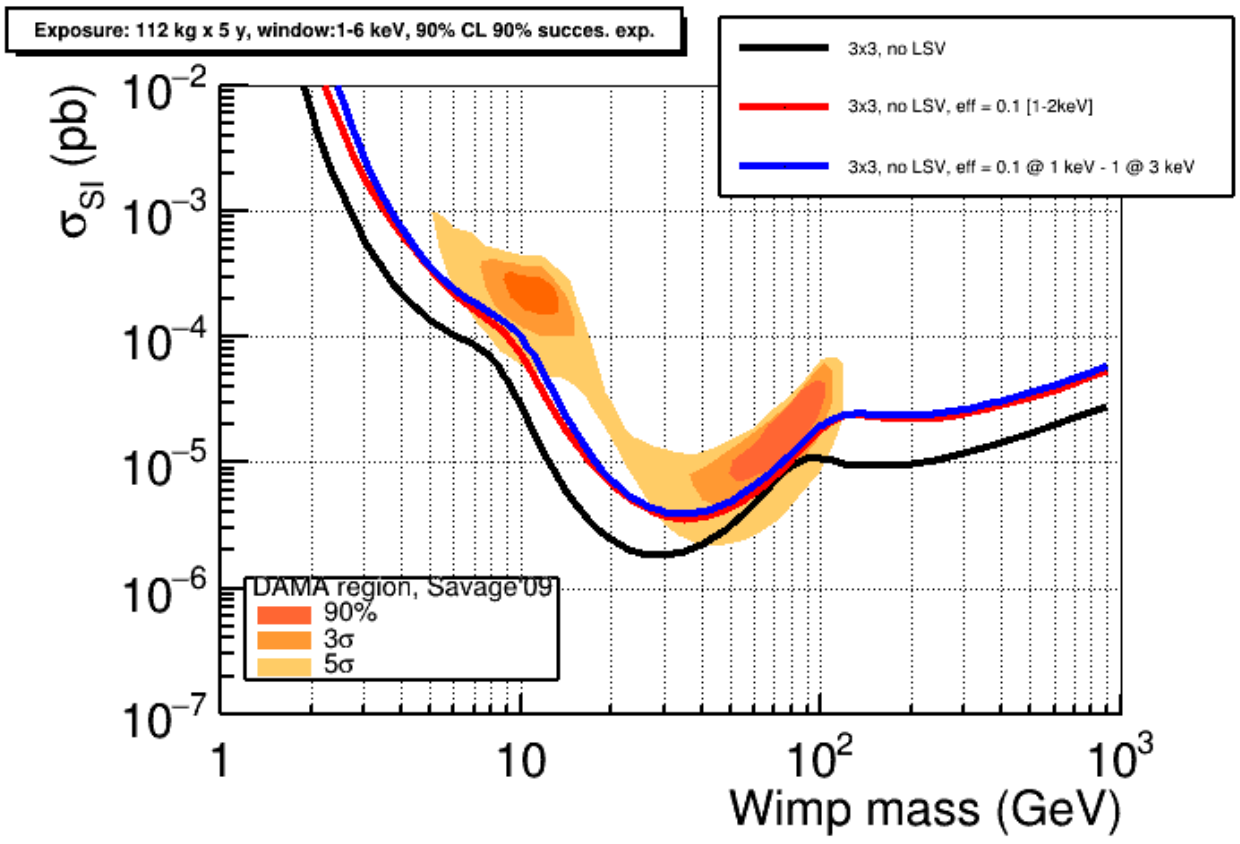

Figure 5.5: *Sensitivity plot in the $\sigma^{SI}_{Wn} - m_W$ plane for ANAIS–112 without LSV including a filtering acceptance efficiency lower than 1 near the threshold in different situations (see text).*

Summarizing, from this sensitivity analysis it can be concluded:

- A significative improvement in sensitivity is observed when lowering the energy threshold down to 1 keVee (see figure 5.2).
- On the other hand, a clear sensitivity improvement can be appreciated in figure 5.3 when increasing the total NaI(Tl) mass up to 250 kg, being this effect much more significant than the background improvement achieved by applying a LSV, or by analyzing only the six central crystals.
- Although the most sensitive of the ANAIS configurations analyzed in this work corresponds to the 5 × 4 matrix of NaI(Tl) detectors, ANAIS-112, as it is designed, covers in a reasonable way DAMA/LIBRA region, even in the more conservative scenario, with the background level achieved for D2 detector (see figure 5.1).

Summary and conclusions

The detection of the dark matter in the Universe and the understanding of its nature represent one of the largest challenges of Cosmology, Astrophysics and Particle Physics of the modern era. There exist many hints, from galactic to cosmological scales, pointing to the existence of this particular kind of matter. These evidences restrict the nature of dark matter, requiring it to be very weakly interacting and non–relativistic at the time of decoupling from the rest of the Universe contents (cold dark matter), leading to the search of a particle beyond the Standard Model of Particle Physics.

Several experiments have been devoted to the dark matter direct detection with different targets and techniques since the mid–eighties. Among the targets used, germanium, xenon, argon, and sodium iodide can be highlighted; among the techniques, semiconductor devices, scintillators, cryogenic hybrid detectors, and noble liquids TPCs have played a relevant role in the development of the field and the continuous improvement in sensitivity. Up to date, only DAMA/LIBRA experiment, at the LNGS, Italy, has claimed to have detected a positive signal of annual modulation in single–hit events in the 2–6 keVee energy region. This result is not compatible neither with conventional backgrounds, nor with any systematic effect proposed. However, it has not been confirmed yet by any other experiment.

The DAMA group has carried out several studies of the model independent annual modulation effect in different dark matter scenarios. Here, the DAMA/LIBRA measured signal has been analyzed in terms of symmetric mirror dark matter, assuming that a fraction, f, of the dark matter halo in the Milky Way is composed by mirror atoms of different species that interact with target nuclei in the detector via Rutherford–like scattering induced by kinetic mixing between mirror and ordinary photons. Many different possible scenarios for the

mirror matter chemical composition, its density profile and velocity distribution in the Milky Way were considered. Allowed physical intervals compatible with the DAMA/LIBRA positive annual modulation signal for the parameter $\sqrt{f}\epsilon$ have been derived in various situations. The results obtained with this study demonstrate that $\sqrt{f}\epsilon$ values compatible with cosmological bounds are able to reproduce the DAMA/LIBRA positive signal for many different experimental parameters configurations and halo models.

The ANAIS project has been a long–time effort developed by the University of Zaragoza in order to carry out an experiment searching for dark matter annual modulation with very low background NaI(Tl) detectors at the LSC. ANAIS experiment aims at the confirmation of the DAMA/LIBRA positive signal using the same target and technique. Very stringent requirements are mandatory, in order to have enough sensitivity to detect an annual modulation signal in the very low energy region: very low energy threshold, a background as low as possible in the region of interest, high target mass, very stable operation conditions and control of environmental parameters. ANAIS–112, an experiment of more than one hundred kilograms of ultrapure NaI(Tl), has been conceived as the conclusion of previous ANAIS prototypes, having enough sensitivity to test the DAMA/LIBRA signal, and it is being commissioned at the LSC.

An extensive work has been carried out to characterize and quantify the different background contributions and develop a satisfactory background model for sodium iodide detectors, that was lacking. In this work, the different set–ups including AS detectors, operated at LSC within the ANAIS project, have been considered.

- ANAIS–25: two detector prototypes (named D0 and D1), amounting 25 kg NaI(Tl), took data from December 2012 to March 2015. D0 and D1 presented an excellent light collection at the level of 15 phe/keV, and an acceptable K bulk content, around 40 ppb, but an unacceptable ^{210}Pb activity of 3.15 mBq/kg.
- AS1K: a 1–kg NaI(Tl) crystal prepared by Alpha Spectra confirmed the contamination on ^{210}Pb, and the building of the ^{210}Po activity allowed to establish the contamination time at the end of the purification procedures

or crystal growing. A thorough investigation of the possible mechanism responsible of the contamination was carried out at AS and changes were implemented in their protocols.

- ANAIS–37: a new detector, D2, was placed in between the two ANAIS–25 modules. It was grown using new protocols to prevent radon contamination and presented a reduction of the ^{210}Pb content down to 0.7 mBq/kg maintaining an excellent light collection and similar ^{40}K activity than the D0 and D1 detectors.

- Blank Module: a module built like the AS ones but without crystal, silicone pads and quartz windows was prepared and mounted in the ANAIS–37 set–up replacing the D1 detector. The goal of this set–up was to accumulate a population of pure photomultiplier events and to test the filtering protocols. This module has allowed to confirm the presence of light coming from the PMTs and being able to trigger the ANAIS acquisition. However, the suitability of the filtering protocols could be tested, and most of those events were efficiently rejected. Some events survive this filtering procedure, being anomalously slow, and they are still under study, trying to improve the selection criteria to get rid of them.

- A37D3: very similar to ANAIS–37 set–up in shielding configuration and acquisition parameters, but different in module layout in order to incorporate the latest received module, D3, made of a crystal grown with a more purified powder. This new module (D3) is placed in between D0 (bottom) and D2 (top) modules; preliminary results point to a significantly reduced K content of 19 ppb in comparison to previous modules but a ^{210}Pb activity higher than in D2, which could reach 1.8 mBq/kg. D3 has also shown excellent light collection, similar to that of previous AS modules.

- AS2K-1 and AS2K-2: due to the high alpha rate measured in D3 and after discussing the possibility of a surface contamination with AS, two pieces of 1 kg of NaI(Tl) (AS1K-1 grown from the same ingot than D3 and AS2K-2 from the same ingot than the following detectors in preparation) were received and have been measured along the summer 2016. Preliminary results confirm the ^{210}Pb activity measured for D3 in the sample from its ingot, but point to a lower value at the level of 0.7 mBq/kg

for the other one. From this second ingot are being built the last four ANAIS–112 modules.

The background models constructed for D0 and D1 detectors at the ANAIS–25 set–up and for D2 module at ANAIS–37 provide a good description of measured data from energy threshold to high energy at different analysis conditions. Preliminary results for the model of D3 detector in A37D3 set–up are also satisfactory. The measured activity in external components and in crystal, including cosmogenic products, quantified combining different analysis techniques, roughly explains the observed background. But the inclusion of some additional hypotheses, like the presence of cosmogenic isotopes which cannot be directly quantified or partial crystal surface ^{210}Pb contamination, significantly improves the agreement between model and real data. It can be concluded that at the region of interest, crystal bulk contamination is the dominant background source. Contributions from ^{210}Pb and ^{3}H continua and ^{40}K and ^{22}Na peaks are the most relevant ones. The best measured background, corresponding to D2 module, is already about 2 counts/(keV kg day) at 6 keVee, but reduction is still possible thanks to the increase of the background rejection power in a detector matrix set–up and an improved control of radiopurity in the ANAIS modules under preparation. D2 background in the region from 1 to 2 keVee increases steeply. Work is ongoing to improve PMT–origin events filtering and better estimate of the corresponding acceptance efficiencies.

Together with the background models of the already operated Alpha Spectra detectors, an evaluation of the background prospects for the full experiment has been developed, taking into account the planned ANAIS–112 design as well as several other hypothetical scenarios, like a matrix of NaI(Tl) crystals corresponding to a total mass of 250 kg (ANAIS–250), or the use of a Liquid Scintillator Veto (LSV) in the 3×3 modules configuration.

– Reduction factors for the background at the very low energy region thanks to the rejection of coincident events have been computed for all these situations, confirming that contributions from ^{40}K and ^{22}Na could be efficiently suppressed thanks to anticoincidence operation in a crystals matrix or inside the LSV. However, since the other relevant background sources at the region of interest (^{3}H and ^{210}Pb) are fully absorbed at each

detector and anticoincidence operation is useless for them, the estimated overall reduction factor could be in the end of a factor 2 in the best case.

- With the radiopurity levels achieved in D2 detector, for the 3 × 3 matrix of crystals amounting to 112.5 kg of mass, a background rate below 2 counts/(keV kg day) above 4 keVee is expected; the foreseen rate is 2.5 counts/(keV kg day) in the region from 1 to 4 keVee, which could be reduced at most to 1.4 counts/(keV kg day) by using a LSV. In terms of background, the use of a LSV is clearly a better alternative than the increase of the total mass up to 250 kg. In this situation, the fully absorbed emission from ^{3}H could become the main contribution in the region of interest; therefore, a shielding against cosmogenic activation has been procured for the production of the new ANAIS NaI(Tl) crystals at Alpha Spectra facilities. Additionally, a further reduction of ^{210}Pb and ^{40}K in Alpha Spectra detectors could be possible thanks to improved purification and surface machining protocols. In this direction, detector D3 already confirmed a clear improvement in the potassium content, attributed to the WIMPScint-III grade powder used. The additional reduction in ^{210}Pb content is expected to be confirmed after measuring D4 and D5 modules, on their way to Canfranc at the moment of writing this memory.

- Concerning the design of the possible implementation of the LSV in ANAIS, different options have been analyzed, concluding that a shielding against the environmental gamma background is mandatory, being 15 cm of lead enough to reduce its contribution to non-relevant levels. The box holding the shielding of the ANAIS–112 set–up filled instead with liquid scintillator offers reduction factors in the region of interest for the dominant ^{22}Na and ^{40}K crystal emissions similar to a larger LSV system with a 60–cm–thick liquid scintillator. Contribution from the radioactive contaminants of the LSV, assuming typical activities from the literature, is unimportant as it is two orders of magnitude lower than that from NaI modules. It has been checked that the effect of a non-zero energy threshold in the LSV is not relevant for the background in the region of interest.

The sensitivity of ANAIS in the search for the annual modulation effect in the dark matter signal has been evaluated in different experimental configurations

(for 112.5 or 250 kg of NaI(Tl), using or not a LSV) and background conditions (taking into account the background models developed).

- It can be concluded that a significative improvement in sensitivity is observed when lowering the energy threshold down to 1 keVee.
- A clear sensitivity improvement can be appreciated when increasing the total NaI(Tl) mass up to 250 kg, being this effect much more significant than the background improvement achieved by applying a LSV, or by analyzing only the six central crystals.
- Finally, although the most sensitive of the ANAIS configurations analyzed in this work corresponds to the 5×4 matrix of NaI(Tl) detectors, it is important to highlight that ANAIS-112, as it is designed, covers in a reasonable way the region of parameters compatible with DAMA/LIBRA positive result, even in the more conservative scenario, with the background level achieved for D2 detector.

In the immediate future, detectors D4 and D5 will be characterized at the LSC following the same procedures applied to the previous modules. Reception of the last three detectors completing ANAIS–112 set–up is expected for beginning of 2017.

Resumen y conclusiones

La detección de la materia oscura del Universo y la comprensión de su naturaleza se encuentran desde hace décadas entre los mayores desafíos que afrontan la Cosmología, la Astrofísica y la Física de Partículas. Existen muchas evidencias, desde la escala galáctica a la cosmológica, que apoyan la existencia de materia que interacciona muy débilmente, masiva y no relativista en la época del desacoplo del resto de componentes del Universo: la materia oscura fría. El Modelo Estándar de la Física de Partículas no contiene ningún candidato capaz de explicar todas estas evidencias, por lo que hay que buscarlos en nuevas teorías que, ampliando dicho modelo, incorporan nuevas partículas con propiedades adecuadas.

Desde mediados de los años ochenta se han llevado a cabo diversos experimentos dedicados a la detección directa de la materia oscura con diferentes blancos y técnicas. De entre los blancos utilizados, destacan el germanio, xenon, argon e yoduro de sodio; y de entre las técnicas, semiconductores, centelleadores, detectores híbridos criogénicos y TPCs de líquidos nobles han jugado un papel fundamental en el desarrollo de un campo que ha mejorado en varios órdenes de magnitud la sensibilidad de los experimentos. Hasta la fecha, sólo el experimento DAMA/LIBRA, en el LNGS, Italia, ha reivindicado haber detectado una señal positiva de modulación anual para eventos que depositan energía en un único detector en la región de 2 a 6 keVee, como la que se espera que produzcan las partículas de materia oscura que constituyen el halo de nuestra galaxia. Este resultado no es compatible ni con fondos convencionales ni con los variados efectos sistemáticos propuestos. Sin embargo, todavía no ha sido confirmado por ningún otro experimento.

La colaboración DAMA/LIBRA ha llevado a cabo diversos estudios del efecto (independiente del modelo) de modulación anual en diferentes escenarios de

materia oscura. En esta tesis, la señal medida por DAMA/LIBRA ha sido analizada en términos de materia oscura "mirror" simétrica, asumiendo que una fracción, f, del halo de materia oscura en la Vía Láctea está compuesta por átomos *espejo* de diferentes especies. Estos átomos "mirror" interaccionarían con los núcleos blanco en el detector vía dispersión Rutherford inducida por la mezcla cinética entre los fotones ordinarios y los fotones "mirror", caracterizada por un parámetro de acoplo ϵ. Se han considerado diferentes situaciones para la composición química de la materia mirror, su perfil de densidad, temperatura y velocidad neta del halo de materia oscura respecto a la velocidad de la Tierra, obteniéndose intervalos permitidos para el parámetro $\sqrt{f}\epsilon$, compatibles con la señal positiva de la modulación anual medida por DAMA/LIBRA. Los resultados obtenidos con este estudio demuestran que valores de $\sqrt{f}\epsilon$ compatibles con los límites cosmológicos son capaces de reproducir la señal positiva de DAMA/LIBRA para diferentes configuraciones de parámetros experimentales y modelos de halo.

El proyecto ANAIS es la culminación de un gran esfuerzo desarrollado por la Universidad de Zaragoza para llevar a cabo un experimento de búsqueda de la modulación anual de la materia oscura con detectores de NaI(Tl) de muy bajo fondo en el LSC. El experimento ANAIS tiene como objetivo la confirmación de la señal positiva de DAMA/LIBRA usando el mismo blanco y técnica de detección. Para lograr este objetivo, ANAIS debe cumplir los siguientes requisitos: umbral en energías inferior a 2 keVee, fondo radiactivo lo más bajo posible en la región de interés (de 1 a 6 keVee), gran masa de detección y control de los parámetros ambientales. ANAIS–112 es un experimento de más de cien kilogramos de NaI(Tl) ultrapuro que ha sido concebido como conclusión del estudio de prototipos previos, teniendo suficiente sensibilidad para probar la señal de DAMA/LIBRA. El montaje de ANAIS–112 en el LSC está prácticamente listo, pendiente de completar la masa de detección de NaI(Tl) con los últimos 5 módulos.

Se ha llevado a cabo un extenso trabajo para caracterizar y cuantificar las contribuciones al fondo radiactivo de los diferentes prototipos considerados en el marco del proyecto ANAIS. En este trabajo se presentan resultados de todos los montajes que han incluido detectores fabricados por Alpha Spectra en el LSC.

– ANAIS–25: dos prototipos (denominados D0 y D1), con un total de 25 kg de NaI(Tl), estuvieron tomando datos desde diciembre de 2012 hasta marzo de 2015. D0 y D1 presentaron una excelente recogida de luz, del orden de 15 phe/keV, y un contenido interno de K aceptable, alrededor de 40 ppb, pero una actividad inaceptable de 3.15 mBq/kg de ^{210}Pb.

– AS1K: un cristal de 1 kg de NaI(Tl) preparado por Alpha Spectra confirmó la contaminación de ^{210}Pb y la evolución del ^{210}Po permitió establecer el momento de la contaminación al final de los procesos de purificación o crecimiento del cristal. AS llevó a cabo una exhaustiva investigación del posible mecanismo responsable de la contaminación y se implementaron mejoras en sus protocolos.

– ANAIS–37: un nuevo detector, D2, se instaló entre los dos módulos de ANAIS–25. Fue crecido usando protocolos mejorados para la prevención de la contaminación con radón y presentó una reducción del contenido de ^{210}Pb a 0.7 mBq/kg manteniendo una excelente recogida de luz y una actividad de ^{40}K similar a la de los detectores D0 y D1.

– Módulo *blank*: un módulo similar a los de AS, pero sin cristal, láminas de silicona y ventanas de cuarzo, se preparó y montó en ANAIS–37 reemplazando al detector D1. El objetivo de este montaje era acumular una población de sucesos puros de fotomultiplicador y poner a prueba los protocolos de filtrado. Este módulo ha permitido confirmar la presencia de luz procedente de los fotomultiplicadores, capaz de disparar la adquisición de datos de ANAIS. Sin embargo, se confirmó la adecuación del procedimiento de selección debido a que la mayoría de estos sucesos pudieron ser rechazados eficientemente. Algunos eventos pasan estos filtros, siendo anómalamente lentos, y son todavía objeto de estudio, intentando mejorar el criterio de selección para poder eliminarlos.

– A37D3: muy similar al montaje de ANAIS–37 en la configuración del blindaje y parámetros de adquisición, pero diferente en el diseño para incorporar el último módulo recibido, D3, fabricado con cristal crecido con un polvo más purificado. Este nuevo módulo (D3) está situado entre los detectores D0 (abajo) y D2 (arriba); los resultados preliminares

apuntan a una significativa reducción en el contenido de K hasta 19 ppb en comparación con módulos previos, pero una actividad mayor de ^{210}Pb que en D2, que podría alcanzar 1.8 mBq/kg. D3 ha mostrado también una excelente colección de luz, similar a la de los módulos anteriores de AS.

– AS2K-1 y AS2K-2: debido al alto ritmo alfa medido en D3 y después de discusiones acerca de la posibilidad de una contaminación superficial con AS, dos piezas de 1 kg de NaI(Tl) (AS2K-1 crecida del mismo lingote que D3 y AS2K-2 del lingote de los módulos restantes en preparación) fueron recibidas y han estado midiendo desde el verano de 2016. Resultados preliminares confirman la actividad de ^{210}Pb medida en D3 en la muestra de este lingote, pero apuntan a una reducción a nivel de 0.7 mBq/kg para la otra muestra.

Los modelos de fondo construidos para los detectores D0 y D1 en ANAIS–25 y para el detector D2 en ANAIS–37 dan una buena descripción de los datos medidos desde la energía umbral hasta la alta energía en diferentes condiciones de análisis. Los resultados preliminares para el modelo del detector D3 en A37D3 son también satisfactorios. La actividad medida en los componentes externos y en el cristal, incluyendo los isótopos activados cosmogénicamente, cuantificados combinando diferentes técnicas de análisis, explica a grandes rasgos el fondo observado. Pero la inclusión de algunas hipótesis adicionales, como la presencia de isótopos cosmogénicos que no pueden ser cuantificados directamente o la contaminación parcial de ^{210}Pb en la superficie, mejoran significativamente la concordancia del modelo con los datos reales. Se puede concluir que en la región de interés, la contaminación en el propio cristal es la fuente de fondo dominante. Las contribuciones de ^{210}Pb y ^{3}H, y las de los picos de ^{40}K y ^{22}Na son las más relevantes. El mejor fondo medido hasta la fecha, el del detector D2, es de aproximadamente 2 cuentas/(keV kg día) en 6 keVee, pero se espera mejorar dicho fondo en ANAIS–112 gracias al incremento del poder de rechazo en un montaje multimodular, que permite eliminar coincidencias, y un mayor control de la radiopureza de los módulos restantes. El fondo de D2 en la región de 1 a 2 keVee crece rápidamente. Se está trabajando en mejorar el proceso de filtrado de los sucesos originados en los fotomultiplicadores y la estimación de las eficiencias de aceptación de sucesos de centelleo en el cristal de NaI(Tl).

Junto con los modelos de fondo de los detectores de Alpha Spectra ya operativos, se han evaluado las perspectivas de fondo para el experimento completo, teniendo en cuenta el diseño planeado para ANAIS–112, así como otros escenarios hipotéticos, como una matriz de detectores de NaI(Tl) correspondiente a 250 kg (ANAIS–250), o el uso de un veto de centelleo líquido (LSV) en la configuración de 3 × 3 módulos.

- Se han calculado factores de reducción para el fondo en la región de muy baja energía gracias al rechazo de los eventos en coincidencia para todas estas situaciones, confirmando que las contribuciones de ^{40}K y ^{22}Na pueden ser suprimidas eficientemente gracias a la anticoincidencia entre los cristales de la matriz o con el LSV. Sin embargo, dado que otras fuentes de fondo relevantes en la región de interés (^{3}H y ^{210}Pb) producen depósitos energéticos en un único detector y la anticoincidencia no permite su rechazo en ningún caso, el factor de reducción total estimado podría ser un factor 2 en el mejor de los casos.

- Con los niveles de radiopureza alcanzados en el detector D2, para la matriz 3 × 3 de cristales, que corresponde a 112.5 kg de masa, se espera un ritmo de fondo menor que 2 cuentas/(keV kg día) por encima de 4 keVee; la perspectiva es de un ritmo de 2.5 cuentas/(keV kg día) en la región de 1 a 4 keVee, que podría ser reducida como máximo a 1.4 cuentas/(keV kg día) usando un LSV. En términos de fondo, el uso de un LSV es claramente mejor alternativa que el incremento de masa a 250 kg. En esta situación, ^{3}H se podría convertir en la mayor contribución en la región de interés; por tanto, se ha instalado un blindaje frente a la activación cosmogénica en la producción de nuevos cristales de NaI(Tl) para ANAIS en las instalaciones de Alpha Spectra. Además, las mejoras implementadas en los procesos de purificación y tratamiento superficial de los cristales hacen viable una mayor reducción del contenido en ^{210}Pb y ^{40}K en los siguientes módulos fabricados por AS. En esta dirección, el detector D3 ya ha confirmado una clara mejora en el contenido de potasio, atribuído al mayor grado de purificación del polvo de NaI de calidad WIMPScint-III. La reducción adicional en el contenido de ^{210}Pb se espera que se confirme tras medir los módulos D4 y D5, viajando a Canfranc en el momento de redacción de esta memoria.

– En cuanto al diseño de la posible implementación de un LSV en ANAIS, se han analizado diferentes opciones, concluyendo que un blindaje contra el fondo gamma ambiental es imprescindible, siendo suficientes 15 cm de plomo para reducir su contribución a niveles aceptables. La caja contenedora del blindaje diseñada para su uso en ANAIS-112 llena de líquido centelleador ofrece unos factores de reducción para las emisiones dominantes de ^{22}Na y ^{40}K en la región de interés similares a un LSV mayor con un espesor de 60 cm de centelleador líquido. La contribución de los contaminantes radiactivos del LSV, asumiendo actividades típicas de la literatura, no es importante ya que es dos órdenes de magnitud menor que la de los módulos de NaI. Se ha comprobado que el efecto de un umbral energético distinto de cero en el LSV no es relevante para el fondo en la región de interés.

La sensibilidad de ANAIS en la búsqueda de la modulación anual de la señal de materia oscura ha sido evaluada en diferentes configuraciones experimentales (para 112.5 o 250 kg de NaI(Tl), usando o no un LSV) y condiciones de fondo (teniendo en cuenta los modelos de fondo desarrollados).

– Se puede concluir que se observa una mejora significativa al reducir el umbral energético hasta 1 keVee.

– Se puede apreciar una mejora en la sensibilidad al incrementar la masa total de NaI(Tl) a 250 kg, siendo este efecto mucho más significativo que la mejora alcanzada en el fondo al aplicar un LSV, o analizando sólo los seis cristales centrales.

– Finalmente, aunque las configuraciones más sensibles de ANAIS analizadas en este trabajo corresponden a matrices de detectores 5 $\times$ 4, es importante destacar que la sensibilidad de ANAIS-112 al efecto de modulación anual cubre de manera razonable la región de parámetros compatible con el resultado positivo de DAMA/LIBRA, incluso en el escenario más conservador, con el nivel de fondo alcanzado en el detector D2.

En un futuro inmediato, los detectores D4 y D5 serán caracterizados siguiendo los mismos procedimientos aplicados para módulos previos. La recepción de los tres detectores restantes y la operación del experimento completo ANAIS–112 está prevista para 2017.

Agradecimientos

En primer lugar me gustaría dar las gracias a mis directoras, Mª Luisa Sarsa y Susana Cebrián por su consejo, dedicación, paciencia y apoyo durante estos años, especialmente en esta última etapa. Por haberme guiado en este trabajo y haber compartido conmigo una pequeña parte de su extenso conocimiento en la Física de Astropartículas y la búsqueda de la materia oscura del Universo.

Me gustaría dar las gracias también a Eduardo García, mi director de trabajo fin de máster y quien me introdujo en la detección directa de materia oscura con detectores de germanio, por su constante apoyo y consejo. A Jorge Puimedón, por su interés por mi trabajo durante estos años, así como por su trabajo con las medidas de radiopureza de materiales. A Alfonso, por hacer tan amenos los viajes a Canfranc a pesar de los pesados montajes y desmontajes de ANAIS. A Miguel Ángel, por enseñarme y guiarme en la electrónica del experimento. A Clara, por iniciarme en el experimento ANAIS y guiarme en los primeros pasos con su funcionamiento, a Ysrael, por sus consejos y las animadas charlas de despacho en este último periodo y a María Martínez por su ayuda tanto en Zaragoza como en Roma, te lo agradezco de verdad. A todos los demás profesores y compañeros del departamento, compañeros de pasillo, despacho, cafés, a todos con los que he coincidido en algún momento de estos años de tesis. De estos años me llevo un gran grupo de amigos.

Vorrei ringraziare il gruppo di DAMA e tutti a Roma e Gran Sasso per la sua gentileza e per avermi fatto sentire come a casa. Grazie da cuore a tutti quanti. Voglio dare un ringraziamento especiale a la Prof. Rita Bernabei per la sua aiuta e gentileza con me e per avermi dato la possibilità di lavorare nel suo gruppo qualche mese. Grazie mille.

Gracias también a todo el staff del Laboratorio Subterráneo de Canfranc, por

su colaboración y ayuda.

Finalmente, en el terreno más personal, me gustaría dar las gracias a mi familia; en especial a mi hermano y mejor amigo, por estar siempre ahí, sin condiciones; a mis padres, pilares fundamentales de mi vida, por su apoyo incondicional y por la educación que me han brindado, especialmente a mi padre por haberme inculcado su pasión por la ciencia y el "lado oscuro del Universo".

Y por supuesto, a tí, por creer siempre en mí, por estar siempre a mi lado y por tu apoyo constante, no puedo sentirme más afortunada.

A todos quienes de una u otra forma han aportado su granito de arena para esta tesis, GRACIAS.

Patricia Villar Gómez,
Octubre de 2016

Acknowledgments

This work and the ANAIS experiment development have been supported by the Spanish Ministerio de Economía y Competitividad, the European Regional Development Fund (MINECO-FEDER) (FPA2011-23749, FPA2014-55986-P), the Consolider-Ingenio 2010 Programme under Grant MultiDark CSD 2009-00064 and the Gobierno de Aragón and the European Social Fund (Group in Nuclear and Astroparticle Physics). Support from LSC and GIFNA staff through all stages of this work is also worth of acknowledgement. Finally, the warm hospitality received from the DAMA group during the research stage is gratefully acknowledged.

This PhD dissertation has been possible thanks to the MINECO Subprograma de Formación de Personal Investigador BES-2012-056299 and the research stage at University of Rome "Tor Vergata" to the MINECO Subprograma Estatal de Movilidad EEBB-I-15-10012.

Bibliography

[1] Planck Collaboration, P. A. R. Ade et al., Planck 2015 results. XIII. Cosmological parameters, Astronomy and Astrophysics **594**, A13 (2016).

[2] K. Fushimi et al., Limits on the annual modulation of WIMPs nucleus scattering with large–volume NaI(Tl) scintillators, Astropart. Phys. **12**, 185 (1999).

[3] R. Bernabei et al., Performances of the 100 kg NaI (Tl) set-up of the DAMA experiment at Gran Sasso, Riv. Nuovo Cim. A **112**, 545 (1999).

[4] R. Bernabei et al., New limits on WIMP search with large mass low radioactivity NaI(Tl) set–up at Gran Sasso, Phys. Lett. B **389**, 757 (1996).

[5] G. Gerbier et al., Pulse shape discrimination with NaI(Tl) and results from a WIMP search at the Laboratoire Souterrain de Modane, Astropart. Phys. **11**, 287 (1999).

[6] G.J. Alner et al., Limits on WIMP cross-sections from the NAIAD experiment at the Boulby Underground Laboratory, Phys. Lett. B **616**, 17 (2005).

[7] M. Sarsa et al., Searching for annual modulations of WIMPs with NaI scintillators, Phys. Lett. B **386**, 458 (1996).

[8] M. Sarsa et al., Results of a search for annual modulation of WIMP signals, Phys. Rev. D **56**, 1856 (1997).

[9] R. Bernabei et al., Final model independent result of DAMA/LIBRA-phase 1, Eur. Phys. J. C **73**, 2648 (2013).

[10] R. Bernabei el al., Dark Matter search, Riv. Nuovo Cim. **26**, 1 (2003).

[11] R. Agnese et al., New Results from the Search for Low-Mass Weakly Interacting Massive Particles with the CDMS Low Ionization Threshold Experiment, Phys. Rev. Lett. **116**, 071301 (2016).

[12] CRESST Collaboration, G. Angloher et al., CRESST Results on light dark matter particles with a low-threshold CRESST-II detector, Eur. Phys. J. C **76**, 25 (2016).

[13] EDELWEISS Collaboration, E. Armengaud et al., Constraints on low–mass WIMPs from the EDELWEISS-III dark matter search, Journal of Cosmology and Astropart. Phys. **05**, 019 (2016).

[14] H.S. Lee et al., A Search for Low-Mass Dark Matter with CsI(Tl) Crystal Detectors, Phys. Rev. D **90**, 052006 (2014).

[15] D.S. Akerib et al. (LUX Collaboration), Results on the Spin–Dependent Scattering of Weakly Interacting Massive Particles on Nucleons from the Run 3 Data of the LUX Experiment, Phys. Rev. Lett. **116**, 161302 (2016).

[16] C. Amole et al., Dark Matter Search Results from the PICO–60 CF_3I Bubble Chamber, Phys. Rev. D **93**, 052014 (2016).

[17] C. Amole, et al., Improved Dark Matter Search Results from PICO–2L Run–2, Phys. Rev. D **93**, 061101 (2016).

[18] XENON Collaboration, E. Aprile et al., XENON Search for Event Rate Modulation in XENON100 Electronic Recoil Data, Phys. Rev. Lett. **115**, 091302 (2015).

[19] J. Amaré et al., Status of the ANAIS Dark Matter Project at the Canfranc Underground Laboratory, Journal of Physics: Conference Series **718**, 042052 (2016).

[20] J. Cherwinka et al., First data from DM-Ice17, Phys. Rev. D **90**, 092005 (2014).

[21] K.W. Kim et al., Tests on NaI(Tl) crystals for WIMP search at the Yangyang Underground Laboratory, Astropart. Phys. **62**, 249 (2014).

[22] E. Shields et al., SABRE: A new NaI(Tl) dark matter direct detection experiment, Physics Procedia **61**, 169 (2015).

[23] COSINE Collaboration, Status of the COSINE–100 experiment at Yangyang underground laboratory, SUSY2016, https://indico.cern.ch/event/443176/contributions/2162787/attachments/1302993/1946070/SUSY2016_KIMS-NaI_NYKim_v2.0.pdf

[24] S. Cebrián et al., Background model for a NaI (Tl) detector devoted to dark matter searches, Astropart. Phys. **37**, 60 (2012).

[25] C. Cuesta et al., Analysis of the ^{40}K contamination in NaI(Tl) crystals from different providers, Int. J. Mod. Phys. A **29**, 1443010 (2014).

[26] C. Cuesta et al., Slow scintillation time constants in NaI(Tl) for different interacting particles, Opt. Mat. **36**, 316 (2013).

[27] C. Cuesta et al., Bulk NaI(Tl) scintillation low energy events selection with the ANAIS–0 module, Eur. Phys. J. C **74**, 3150 (2014).

[28] J. Amaré et al., Study of scintillation in natural and synthetic quartz and methacrylate, Opt. Mat. **36**, 1408 (2014).

[29] Alpha Spectra Inc. Home Page. http://www.alphaspectra.com/

[30] J. Amaré et al., ANAIS: Status and prospects, EPJ Web of Conferences **121**, 06008 (2016).

[31] M.A. Oliván, Design, scale-up and characterization of the data acquisition system for the ANAIS dark matter experiment, PhD thesis, Universidad de Zaragoza, (2016), https://arxiv.org/abs/1601.07312.

[32] C. Cuesta, ANAIS–0: Feasibility study for a 250 kg NaI(Tl) dark matter search experiment at the Canfranc Underground Laboratory, PhD thesis, Universidad de Zaragoza (2013), http://www.multidark.es/images/tesiscuesta.pdf.

[33] P. J. E. Peebles, Discovery of the hot Big Bang: What happened in 1948, Eur. Phys. J. H **39**, 205 (2014).

[34] A. A. Penzias and R. W. Wilson, A Measurement of Excess Antenna Temperature at 4080 Mc/s., The Astrophysical Journal, **142**, 419 (1965).

[35] P. J. E. Peebles and B. Ratra, The cosmological constant and dark energy, Rev. Mod. Phys. **75**, 559 (2003).

[36] G. Hinshaw et al., Nine-Year Wilkinson Microwave Anisotropy Probe (WMAP) Observations: Cosmological Parameter Results, Astrop. J. Suppl. Series **208**, 19 (2013).

[37] `http://sci.esa.int/home/`

[38] K. A. Olive and B. D. Fields, Big Bang Nucleosynthesis, Nucl. Phys. A **777**, 208 (2006).

[39] Richard H. Cyburt et al., Big Bang Nucleosynthesis: Present status, Rev. Mod. Phys. **88**, 015004 (2016).

[40] F. Zwicky, Die Rotverschiebung von extragalaktischen Nebeln, Helvetica Physica Acta **6**, 110 (1933).

[41] V. C. Rubin. The rotation of spiral galaxies. Science **220**, 1339 (1983).

[42] G. Bertone et al., Particle dark matter: Evidence, candidates and constraints, Physics Reports **405**, 279 (2005).

[43] K. Begeman, A. Broeils, and R. Sanders, Extended rotation curves of spiral galaxies: Dark haloes and modified dynamics, Monthly Notices of the Royal Astronomical Society **249**, 3, 523 (1991).

[44] `http://www.Hubblesite.org`

[45] G. F. Smoot et al., Structure in the COBE diferential microwave radiometer first-year maps, The Astrophysical Journal **396**, L1 (1992).

[46] X–ray: NASA/CXC/CfA/M.Markevitch et al.; Optical: NASA/STScI; Magellan/ U.Arizona/D.Clowe et al.; Lensing Map: NASA/STScI; ESO WFI; Magellan/ U.Arizona/D.Clowe et al., -Light and X-Ray Composite Image of Galaxy Cluster 1E 0657-556, 2006. `http://hubblesite.org/newscenter/archive/releases/2006/39/image/a/`.

[47] J. Beringer et al., Review of particle physics, Phys. Rev. D **86**, 010001 (2012).

[48] K. S. Dawson et al., The baryon oscillation spectroscopic survey of SDSS–III, The Astronomical Journal **145**, 10 (2012).

[49] B. Famaey and S. S. McGaugh, Modified Newtonian Dynamics (MOND): Observational Phenomenology and Relativistic Extensions, Living Rev. Relativity, **15**, 10 (2012).

[50] M. Milgrom, A modification of the Newtonian dynamics as a possible alternative to the hidden mass hypothesis, The Astrophysical Journal **270**, 365 (1983).

[51] G. R. Blumenthal et al., Formation of galaxies and large scale structure with cold dark matter, Nature **311**, 517 (1984).

[52] H. P. Nilles, Supersymmetry, supergravity and particle physics, Physics Reports **110**, 1 (1984).

[53] S. A. Malik et al., Interplay and characterization of Dark Matter searches at colliders and in direct detection experiments, Physics of the Dark Universe, **9- 10**, 51 (2015).

[54] L. Baudis, Dark matter detection, J. Phys. G: Nucl. Part. Phys. **43**, 044001 (2016).

[55] R. D. Peccei and H. R. Quinn, Constraints imposed by CP conservation in the presence of pseudoparticles, Phys. Rev. D **16**, 1791 (1977).

[56] P. Sikivie, "Axions", Particle dark matter: observations, models and searches, G. Bertone (ed.), Cambridge University Press, 204 (2010).

[57] S. Gardner and G. M. Fuller, Dark matter studies entrain nuclear physics, Progress in Particle and Nuclear Physics **71**, 167 (2013).

[58] P. Gondolo and G. Gelmini, Cosmic abundances of stable particles: Improved analysis, Nuclear Physics B **360**, 145 (1991).

[59] M. Battaglia and M. E. Peskin, "Supersymmetric dark matter at colliders", Particle dark matter: observations, models and searches, G. Bertone (ed.), Cambridge University Press, 276 (2010).

[60] CDF Collaboration, Search for Dark Matter in Events with One Jet and Missing Transverse Energy in $p\bar{p}$ Collisions at $\sqrt{s}$=1.96 TeV, Phys. Rev. Lett. **108**, 211804 (2012).

[61] CMS Collaboration, S. Chatrchyan et al., Search for dark matter and large extra dimensions in monojet events in $p\bar{p}$ collisions at $\sqrt{s} = 7$ TeV, J. High Energ. Phys. **94**, 1-37 (2012).

[62] CMS Collaboration, Search for Dark Matter and Large Extra Dimensions in $p\bar{p}$ Collisions Yielding a Photon and Missing Transverse Energy, Phys. Rev. Lett. **108**, 261803 (2012).

[63] ATLAS Collaboration, G. Aad et al., Search for dark matter candidates and large extra dimensions in events with a jet and missing transverse momentum with the ATLAS detector, J. High Energ. Phys. **4**, 1 (2013).

[64] ATLAS Collaboration, Search for Dark Matter Candidates and Large Extra Dimensions in Events with a Photon and Missing Transverse Momentum in $p\bar{p}$ Collision Data at $\sqrt{s}$ =7 TeV with the ATLAS Detector, Phys. Rev. Lett. **110**, 011802 (2013).

[65] ATLAS Collaboration, Search for Dark Matter in Events with a Hadronically Decaying W or Z Boson and Missing Transverse Momentum in $p\bar{p}$ Collisions at $\sqrt{s}$ =8 TeV with the ATLAS Detector, Phys. Rev. Lett. **112**, 041802 (2014).

[66] ATLAS Collaboration, Charged–particle distributions at low transverse momentum in $\sqrt{s}$ = 13 TeV $p\bar{p}$ interactions measured with the ATLAS detector at the LHC, Eur. Phys. J. C **76**, 502 (2016).

[67] H.E.S.S. Collaboration: A. Abramowski et al., Search for dark matter annihilation signatures in H.E.S.S. observations of Dwarf Spheroidal Galaxies, Phys. Rev. D **90**, 112012 (2014).

[68] J. Aleksic et al., Optimized dark matter searches in deep observations of Segue 1 with MAGIC, Journal of Cosmology and Astropart. Phys. **02**, 008 (2014).

[69] E. Aliu et al., VERITAS deep observations of the dwarf spheroidal galaxy Segue 1, Phys. Rev. D **85**, 6, 062001 (2012).

[70] The CTA consortium, Design concepts for the Cherenkov Telescope Array CTA: an advanced facility for ground based high–energy gamma–ray astronomy. Exp. Astron. **32**, 193 (2011).

[71] C. Weniger, A Tentative Gamma–Ray Line from Dark Matter Annihilation at the Fermi Large Area Telescope, Journal of Cosmology and Astropart. Phys. **08**, 007 (2012).

[72] E. Tempel et al., Fermi 130 GeV gamma–ray excess and dark matter annihilation in sub–haloes and in the Galactic centre, Journal of Cosmology and Astropart. Phys. **09**, 032 (2012).

[73] Fermi–LAT Collaboration, Search for gamma–ray spectral lines with the Fermi Large Area Telescope and dark matter implications, Phys. Rev. D **88**, 082002 (2013).

[74] F. Halzen and D. Hooper, "High-energy neutrinos from WIMP annihilations in the Sun", Particle dark matter: observations, models and searches, G. Bertone (ed.), Cambridge University Press, 507 (2010).

[75] IceCube Collaboration: M. G. Aartsen, et al., Search for Dark Matter Annihilation in the Galactic Center with IceCube–79, Eur. Phys. J. C **75** (10) 49212 (2015).

[76] J. Alcaraz et al., Leptons in near earth orbit, Phys. Lett. B **484**, 1, 10 (2000).

[77] O. Adriani et al., Cosmic–Ray Positron Energy Spectrum Measured by PAMELA, Phys. Rev. Lett. **111**, 081102 (2013).

[78] AMS Collaboration, Electron and Positron Fluxes in Primary Cosmic Rays Measured with the Alpha Magnetic Spectrometer on the International Space Station, Phys. Rev. Lett. **113**, 121102 (2014).

[79] M. Di Mauro et al, Dark matter vs. astrophysics in the interpretation of AMS–02 electron and positron data, Journal of Cosmology and Astropart. Phys. **05**, 031 (2016).

[80] P. Sikivie, Experimental tests of the invisible axion, Phys. Rev. Lett. **51**, 1415 (1983).

[81] E. Armengaud et al., Conceptual design of the International Axion Observatory (IAXO), Journal of Instrumentation **9**, T05002 (2014).

[82] The ADMX Collaboration, SQUID–Based Microwave Cavity Search for Dark–Matter Axions, Phys. Rev. Lett. **104**, 041301 (2010).

[83] D. Cerdeño and A. Green, "Direct detection of WIMPs", Particle dark matter: observations, models and searches, G. Bertone (ed.), Cambridge University Press, 347 (2010).

[84] R. Catena, Dark matter directional detection in non–relativistic effective theories, Journal of Cosmology and Astropart. Phys. **7**, 026 (2015).

[85] K. Freese et al., Signal modulation in cold dark matter detection, Phys. Rev. D **27**, 3388 (1988).

[86] S. Ahlen, et al., The case for a directional dark matter detector and the status of current experimental efforts, International Journal of Modern Physics A **25**, 1 (2010).

[87] P. F. Smith and J. D. Lewin, Dark matter detection, Phys. Rep. **187**, 203 (1990).

[88] P. F. Smith, Discrimination of a small dark matter signal from residual nuclear recoil background by means of two target elements, New Astr. Rev. **49**, 303 (2005).

[89] P. Gondolo, Trends in WIMP direct detection, Talk at the IBS-MultiDark Joint Focus Program: WIMPs and Axions. `https://indico.ibs.re.kr/event/7/contribution/11/material/slides/0.pdf`.

[90] J. Collar, Quenching and channeling of nuclear recoils in NaI (Tl): Implications for dark–matter searches, Phys. Rev. D **88**, 035806 (2013).

[91] H. Chagani et al., Measurement of the quenching factor of Na recoils in NaI(Tl), Journal of Instrumentation **3**, P06003 (2008).

[92] V. I. Tretyak, Semi–empirical calculation of quenching factors for ions in scintillators. Astropart. Phys, **33**, 40 (2010).

[93] T. Marrodán and L. Rauch, Dark matter direct-detection experiments, J. of Phys. G: Nuclear and Particle Physics **43**, 013001 (2015).

[94] N. Spooner et al., The scintillation eficiency of sodium and iodine recoils in a NaI(Tl) detector for dark matter searches, Phys. Lett. B **321**, 156 (1994).

[95] K. Fushimi et al., Application of a large volume NaI scintillator to search for dark matter, Phys. Rev. C **47**, R425 (1993).

[96] D. R. Tovey et al., Measurement of scintillation efficiencies and pulse-shapes for nuclear recoils in NaI(Tl) and CaF_2(Eu) at low energies for dark matter experiments, Phys. Lett. B **433**, 150 (1998).

[97] J. Xu et al., Scintillation efficiency measurement of Na recoils in NaI(Tl) below the DAMA/LIBRA energy threshold, Phys. Rev. C **92**, 015807 (2015).

[98] N. E. Booth et al., Low–temperature particle detectors, Annual review of nuclear and particle science **46**, 471 (1996).

[99] R. Agnese et al., Silicon detector dark matter results from the final exposure of CDMS–II, Phys. Rev. Lett. **111**, 251301 (2013).

[100] R. Agnese et al. (SuperCDMS Collaboration), New Results from the Search for Low–Mass Weakly Interacting Massive Particles with the CDMS Low Ionization Threshold Experiment, Phys. Rev. Lett. **116**, 071301 (2016).

[101] R. Agnese et al., Search for low–mass WIMPs with SuperCDMS, Phys. Rev. Lett. **112**, 241302 (2014).

[102] D. Cerdeño, SuperCDMS: Recent results on low mass WIMPs and future perspectives, Talk at the IBS–MultiDark Joint Focus Program: WIMPs and Axions. `https://indico.ibs.re.kr/event/7/contribution/14/material/slides/0.pdf`.

[103] E. Armengaud et al., Final results of the EDELWEISS–II WIMP search using a 4–kg array of cryogenic germanium detectors with interleaved electrodes, Phys. Lett. B **702**, 329 (2011).

[104] G. Angloher et al., Results from 730 kg days of the CRESST–II Dark Matter Search, Eur. Phys. J. C **72**, 1 (2012).

[105] G. Angloher et al., Results on low mass WIMPs using an upgraded CRESST–II detector, Eur. Phys. J. C **74**, 3184 (2014).

[106] The EURECA Collaboration G. Angloher et al., EURECA Conceptual Design Report, Physics of the Dark Universe **3**, 41 (2014).

[107] P. Barbeau, J. Collar, and O. Tench, Large–mass ultralow noise germanium detectors: performance and applications in neutrino and astroparticle physics, Journal of Cosmology and Astropart. Phys. **09**, 009 (2007).

[108] C. E. Aalseth et al., Search for an annual modulation in a p–type point contact germanium dark matter detector, Phys. Rev. Lett. **107**, 141301 (2011).

[109] C. Aalseth et al., Search for an annual modulation in three years of CoGeNT dark matter detector data, `https://arxiv.org/abs/1401.3295` (2014).

[110] C. Aalseth et al., Maximum Likelihood Signal Extraction Method Applied to 3.4 years of CoGeNT Data, `https://arxiv.org/abs/1401.6234` (2014).

[111] J. H. Davis, C. McCabe, and C. Boehm, Quantifying the evidence for Dark Matter in CoGeNT data, Journal of Cosmology and Astropart. Phys. **08**, 014 (2014).

[112] E. Aprile and L. Baudis, "Liquid noble gases", Particle dark matter: observations, models and searches, G. Bertone (ed.), Cambridge University Press, 413 (2010).

[113] D.S. Akerib et al. (LUX Collaboration), Improved Limits on Scattering of Weakly Interacting Massive Particles from Reanalysis of 2013 LUX Data, Phys. Rev. Lett. **116**, 161301 (2016).

[114] XENON100 Collaboration: E. Aprile, et al., XENON100 Dark Matter Results from a Combination of 477 Live Days, `https://arxiv.org/abs/1609.06154` (2016).

[115] XENON100 Collaboration: E. Aprile et al., Limits on spin–dependent WIMP–nucleon cross sections from 225 live days of XENON100 data, Phys. Rev. Lett. **111**, 021301 (2013).

[116] XENON100 Collaboration: E. Aprile et al., Dark Matter Results from 225 Live Days of XENON100 Data, Phys. Rev. Lett. **109**, 181301 (2012).

[117] The XENON collaboration: E. Aprile, et al., Physics reach of the XENON1T dark matter experiment, Journal of Cosmology and Astropart. Phys. **4**, 027 (2016).

[118] The PandaX Collaboration, Andi Tan et al., Dark Matter Search Results from the Commissioning Run of PandaX–II, Phys. Rev. D **93**, 122009 (2016).

[119] A. Badertscher et al., ArDM: first results from underground commissioning, Journal of Instrumentation **8**, C09005 (2013).

[120] C. E. Aalseth et al., The DarkSide Multiton Detector for the Direct Dark Matter Search, Advances in High Energy Physics **2015**, 541362 (2015).

[121] P. Agnes; DarkSide Collaboration, Results from the first use of low radioactivity argon in a dark matter search, Phys. Rev. D **93**, 081101 (2016).

[122] K. Rielage, et al., Update on the MiniCLEAN Dark Matter Experiment, Physics Procedia **61**, 144 (2015).

[123] The DEAP Collaboration, Bei Cai et al., The DEAP–3600 Dark Matter Experiment, `https://arxiv.org/abs/1511.00949` (2015).

[124] The XMASS Collaboration, K. Abe, et al., Direct dark matter search by annual modulation in XMASS–I, Phys. Lett. B **759**, 272 (2016).

[125] M. Felizardo et al., The SIMPLE Phase II Dark Matter Search, Phys. Rev. D **89**, 072013 (2014).

[126] E. Behnke et al., First dark matter search results from a 4-kg CF_3I bubble chamber operated in a deep underground site, Phys. Rev. D **86**, 052001 (2012).

[127] S. Archambault et al., Constraints on low–mass WIMP interactions on ^{19}F from PICASSO, Phys. Lett. B **711**, 153 (2012).

[128] S. C. Kim, et al., New Limits on Interactions between Weakly Interacting Massive Particles and Nucleons Obtained with CsI(Tl) Crystal Detectors, Phys. Rev. Lett. **108**, 181301 (2012).

[129] H.S. Lee,et al., A Search for Low–Mass Dark Matter with CsI(Tl) Crystal Detectors, Phys. Rev. D **90**, 052006 (2014).

[130] G. Angloher et al., The COSINUS project - perspectives of a NaI scintillating calorimeter for dark matter search, Eur. Phys. J. C **76**, 441 (2016).

[131] K. Fushimi et al., Dark matter search project PICO–LON, J. Phys.: Conf. Ser. **718**, 042022 (2016).

[132] K. Freese, M. Lisanti, and C. Savage, Annual modulation of dark matter: a review, Reviews of Modern Physics **85**, 1561 (2012).

[133] M. Martínez, Diseño de un prototipo para un experimento de detección directa de materia oscura mediante modulación anual con centelleadores de ioduro de sodio. PhD thesis, Universidad de Zaragoza (2006).

[134] E. Fernández–Martínez and R. Mahbubani, The Gran Sasso muon puzzle, Journal of Cosmology and Astropart. Phys. **07**, 029 (2012).

[135] J. H. Davis, Fitting the annual modulation in DAMA with neutrons from muons and neutrinos, Phys. Rev. Lett. **113**, 081302 (2014).

[136] J. Klinger and V.A. Kudryavtsev, Muon–Induced Neutrons Do Not Explain the DAMA Data, Phys. Rev. Lett. **114**, 151301 (2015).

[137] R. Bernabei et al., The DAMA/LIBRA apparatus, Nucl. Instrum. Meth. A **592**, 297 (2008).

[138] R. Bernabei, P. Belli, F. Cappella et al., Final model independent results of DAMA/LIBRA-phase 1 and perspectives of phase 2, Phys. Part. Nuclei **46**, 138 (2015).

[139] Bernabei et al., No role for muons in the DAMA annual modulation results, Eur. Phys. J. C **72**, 2064 (2012).

[140] R. Bernabei et al., No role for neutrons, muons and solar neutrinos in the DAMA annual modulation results, Eur. Phys. J. C **74**, 3196 (2014).

[141] `https://www.saint-gobain.com/`

[142] A. Addazi et al., DAMA annual modulation effect and asymmetric mirror matter, Eur. Phys. J. C **75**, 400 (2015).

[143] R. Bernabei et al., Investigating electron interacting dark matter, Phys. Rev. D **77**, 023506 (2008).

[144] R. Bernabei et al., Investigation on light Dark Matter, Mod. Phys. Lett. A **23**, 2125 (2008).

[145] R. Bernabei et al., Investigating halo substructures with annual modulation signature, Eur. Phys. J. C **47**, 263 (2006).

[146] R. Bernabei et al., Investigating Earth shadowing effect with DAMA/LIBRA–phase1, Eur. Phys. J. C **75**, 239 (2015).

[147] R. Cerulli et al., DAMA annual modulation and mirror dark matter, Submmited to Eur. Phys. J. C (2016).

[148] T. D. Lee and C. N. Yang, Question of Parity Conservation in Weak Interactions, Phys. Rev. **104**, 254 (1956).

[149] I. Yu. Kobzarev, L. B. Okun and I. Ya. Pomeranchuk, Vacua, Vacuum: The physics of nothing, Sov. J. Nucl. Phys. **3**, 837 (1966).

[150] R. Foot, H. Lew and R. R. Volkas, A model with fundamental improper spacetime symmetries, Phys. Lett. B **272**, 67 (1991).

[151] M. Y. Khlopov et al., Observational Physics of Mirror World, Sov. Astron. **35**, 21 (1991).

[152] H. M. Hodges, Mirror baryons as the dark matter, Phys. Rev. D **47**, 456 (1993).

[153] Z. Berezhiani, D. Comelli and F. L. Villante, The early mirror universe: inflation, baryogenesis, nucleosynthesis and dark matter, Phys. Lett. B **503**, 362 (2001).

[154] A. Y. Ignatiev and R. R. Volkas, Mirror dark matter and large scale structure, Phys. Rev. D **68**, 023518 (2003).

[155] Z. Berezhiani, Mirror world and its cosmological consequences, Int. J. Mod. Phys. A **19**, 3775 (2004).

[156] Z. Berezhiani, P. Ciarcelluti, D. Comelli and F. L. Villante, Structure formation with mirror dark matter: CMB and LSS, Int. J. Mod. Phys. D **14**, 107 (2005).

[157] P. Ciarcelluti, Cosmology with mirror dark matter. 2. Cosmic microwave background and large scale structure, Int. J. Mod. Phys. D **14**, 223 (2005).

[158] Z. G. Berezhiani, A. D. Dolgov and R. N. Mohapatra, Asymmetric Inflationary Reheating and the Nature of Mirror Universe, Phys. Lett. B **375**, 26 (1996).

[159] Z. G. Berezhiani, Astrophysical Implications of the Mirror World with Broken Mirror Parity, Acta Phys. Polon. B **27**, 1503 (1996).

[160] R. N. Mohapatra and V. L. Teplitz, Structures in the mirror Universe, Astrophys. J. **478**, 29 (1997).

[161] S. L. Glashow, Positronium versus the mirror universe, Phys. Lett. B **167**, 35 (1986).

[162] S. N. Gninenko, Limit on "disappearance" of orthopositronium in vacuum, Phys. Lett. B **326**, 317 (1994).

[163] A. Badertscher et al., An Improved Limit on Invisible Decays of Positronium, Phys. Rev. D **75**, 032004 (2007).

[164] E. D. Carlson and S. L. Glashow, Nucleosynthesis versus the mirror universe, Phys. Lett. B **193**, 168 (1987).

[165] Z. Berezhiani and A. Lepidi, Cosmological bounds on the "millicharges" of mirror particles, Phys. Lett. B **681**, 276 (2009).

[166] B. Holdom, Two U(1)'s and ϵ charge shifts, Phys. Lett. B **166**, 196 (1986).

[167] R. Foot, Implications of the DAMA and CRESST experiments for mirror matter-type dark matter, Phys. Rev. D **69**, 036001 (2004).

[168] R. Foot, Hidden sector dark matter explains the DAMA, CoGeNT, CRESST–II and CDMS/Si experiments, Phys. Rev. D **88**, 025032 (2013).

[169] D. Arnett, Supernovae and Nucleosynthesis (First ed.). Princeton, New Jersey: Princeton University Press. ISBN 0-691-01147-8. OCLC 33162440 (1996).

[170] R. Bernabei et al., Technical aspects and dark matter searches, J. Phys.: Conf. Ser. 203, 012040 (2010). `http://taup2009.lngs.infn.it/slides/jul3/nozzoli.pdf`, talk given by F. Nozzoli

[171] A. B. Migdal, Ionization of atoms accompanying α and β decay, J. Phys. USSR **4**, 449 (1941).

[172] G. Baur, F. Rosel and D. Trautmann, Ionisation induced by neutrons, J. Phys. B: Atom. Mol. Phys. **16**, L419 (1983).

[173] R. Bernabei et al., Possible implications of the channeling effect in NaI(Tl) crystals, Eur. Phys. J. C **53**, 20 (2008).

[174] L. Baudis, Direct dark matter detection: the next decade, Physics of the Dark Universe **1**, 94 (2012).

[175] M. Sarsa et al., Dark matter searches at the Canfranc tunnel, Nuclear Physics B Proceedings Supplements **35**, 154 (1994).

[176] S. Cebrián, Estudio del fondo radioactivo en experimentos subterráneos de búsqueda de sucesos poco probables: CUORE (Cryogenic underground Observatory for Rare Events) y ANAIS (Annual Modulation with NaI(Tl)). PhD thesis, Universidad de Zaragoza (2002).

[177] G. F. Knoll, Radiation detection and measurement. John Wiley and Sons (2010).

[178] J. Amaré et al., Preliminary results of ANAIS–25, Nucl. Instrum. Meth. A **742**, 197 (2014).

[179] Hamamatsu Photonics, `http://www.hamamatsu.com`.

[180] J. Amaré et al., Background analysis and status of the ANAIS dark matter project, AIP Conference Proceedings **1672**, 100001 (2015).

[181] J. Amaré et al., Status of the ANAIS Dark Matter Project at the Canfranc Underground Laboratory DESY-PROC-2015-02, published by Verlag Deutsches Elektronen-Synchrotron, 88 (2015). ISBN: 978-3-935702-43-0.

[182] E. Aprile et al., Study of the electromagnetic background in the XENON100 experiment, Phys. Rev. D **83**, 082001 (2011).

[183] H.M. Araujo et al., Radioactivity backgrounds in ZEPLIN-III, Astropart. Phys. **35**, 495 (2012).

[184] E. Armengaud et al., Background studies for the EDELWEISS dark matter experiment, Astropart. Phys. **47**, 1 (2013).

[185] M. Agostini et al., The background in the neutrinoless double beta decay experiment GERDA, Eur. Phys. J. C **74**, 2764 (2014).

[186] D.S. Akerib et al., Radiogenic and Muon-Induced Backgrounds in the LUX Dark Matter Detector, Astropart. Phys. **62**, 33 (2015).

[187] J.B. Albert et al., Investigation of radioactivity-induced backgrounds in EXO–200, Phys. Rev. C **92**, 015503 (2015).

[188] S. Cebrián et al. Performances and prospects of the ROSEBUD dark matter search experiment. Astropart. Phys. **10**, 361 (1999).

[189] P. Adhikari et al., Understanding internal backgrounds of NaI(Tl) crystals toward a 200 kg array for the KIMS-NaI experiment, Eur. Phys. J. C **76**, 185 (2016).

[190] J. Pradler et al., On an unverified nuclear decay and its role in the DAMA experiment, Phys. Lett. B **720**, 399 (2013).

[191] J. Pradler et al., Addendum to *On an unverified nuclear decay and its role in the DAMA experiment* [Phys. Lett. B 720, 399 (2013)], Phys. Lett. B **723**, 168 (2013).

[192] J. Amaré et al., Cosmogenic radionuclide production in NaI(Tl) crystals, Journal of Cosmology and Astropart. Phys. **02**, 046 (2015).

[193] Decay Data Evaluation Projet, `http://www.nucleide.org/DDEP_WG/DDEPdata.htm`.

[194] S. Agostinelli et al., Geant4 – a simulation toolkit, Nucl. Instrum. Meth. A **506**, 250 (2003).

[195] R. Bernabei et al., Performances of the new high quantum efficiency PMTs in DAMA/LIBRA, Journal of Instrumentation **7**, P03009 (2012).

[196] W.C. Pettus, Cosmogenic Activation in NaI Detectors for Dark Matter Searches, PhD thesis, University of Wisconsin-Madison (2015).

[197] D.M. Mei et al., Cosmogenic production as a background in searching for rare physics processes, Astropart. Phys. **31**, 417 (2009).

[198] `http://www.talys.eu/`

[199] C. Zhang et al., Cosmogenic Activation of Materials Used in Rare Event Search Experiments, Astropart. Phys. **84**, 62 (2016).

[200] J. Amaré et al, Production and relevance of cosmogenic radionuclides in NaI(Tl) crystals, AIP Conference Proceedings **1672**, 140001 (2015).

[201] Experimental Nuclear Reaction Data (EXFOR) http://www.nndc.bnl.gov/exfor/exfor.htm, `http://www-nds.iaea.org/exfor/exfor.htm`

[202] A. J. Koning and D. Rochman, Nuclear Data Sheets **113**, 2841 (2012), `http://www.talys.eu/tendl-2013.html`

[203] Y. A. Korovin et al., High Energy Activation Data Library (HEAD–2009), Nucl. Instrum. Meth. A **624**, 20 (2010).

[204] M. S. Gordon et al., Measurement of the flux and energy spectrum of cosmic–ray induced neutrons on the ground, IEEE Trans. Nucl. Sci. **51**, 3427 (2004).

[205] National Institute of Standards and Technology, `http://physics.nist.gov/PhysRefData/Star/Text/ASTAR.html`

[206] M. Clemenza et al., Radon–induced surface contaminations in low background experiments, Eur. Phys. J. C **71**, 1805 (2011).

[207] S. Cooper et al., Radon–implanted ^{214}Pb and anomalous pulses in sodium iodide detectors for dark matter, Phys. Lett. B **490**, 6 (2000).

[208] V. Álvarez et al., Radiopurity control in the NEXT– 100 double beta decay experiment: procedures and initial measurements, Journal of Instrumentation **8**, T01002 (2013).

[209] I. Lawson and B. Clevenland, Low Background Counting At SNOLAB, AIP Conf. Proc. **1338**, 68 (2011).

[210] X. Li et al, Simulation of natural radioactivity backgrounds in the JUNO central detector, Chinese Physics C **40**, 026001 (2016).

[211] W. Maneschg et al., Measurements of extremely low radioactivity levels in stainless steel for GERDA, Nucl. Instrum. Meth. A **593**, 448 (2008).

[212] `http://radiopurity.in2p3.fr`

[213] The SNO+ Collaboration, S. Andringa et al., Current Status and Future Prospects of the SNO+ Experiment, Advances in High Energy Physics, **2016**, 6194250 (2016).

[214] G. Luzón et al., Characterization of the Canfranc Underground Laboratory: status and future plans, Proc. of the Sixth International Workshop on Identification of Dark matter (IDM) 2006, 514 (2007).

[215] Data from I. Bandac private communication.

[216] P. Lipari and T. Stanev, Propagation of multi–TeV muons, Phys. Rev. D **44**, 3543 (1991).

[217] C. T. Stockel, A study of muons deep underground: I. Angular distribution and vertical intensity, J. Phys. A (Gen. Phys.) **2**, 639 (1969).

[218] S. Cebrián et al., Sensitivity plots for WIMP direct detection using the annual modulation signature, Astropart. Phys. **14**, 339 (2001).

[219] C. Caso et al. (Particle Data Group), Review of Particle Properties, Eur. Phys. J. C **3**, 1 (1998).

[220] R. Bernabei et al., Searching for WIMPs by the annual modulation signature, Phys. Lett. B **424**, 195 (1998).

[221] R. Bernabei et al., On a further search for a yearly modulation of the rate in particle Dark Matter direct search, Phys. Lett. B **450**, 448 (1999).

[222] Y. Ramachers, M. Hirsch and H.V. Klapdor-Kleingrothaus, Limitations of modulation analysis for dark matter direct detection experiments, Eur. Phys. J. A **3**, 93 (1998).